The Dissertation Committee for David Gogichaishvili
certifies that this is the approved version of the following dissertation:

Linear and nonlinear processes in magnetohydrodynamic shear flows: their special nature, interplay and consequences

Committee:

Philip J. Morrison, Supervisor

Claude Wendell Horton Jr., Co-supervisor

Linda Reichl

Francois Waelbroeck

Gary Hallock

Linear and nonlinear processes in magnetohydrodynamic shear flows: their special nature, interplay and consequences

by

David Gogichaishvili,

DISSERTATION

Presented to the Faculty of the Graduate School of

The University of Texas at Austin

in Partial Fulfillment

of the Requirements

for the Degree of

DOCTOR OF PHILOSOPHY

THE UNIVERSITY OF TEXAS AT AUSTIN

December 2018

Acknowledgments

I would like to start by thanking my parents for always caring about my focus on education, and also approved my hobbies in sports and music.

My interest towards physics was strengthened by my high-school teacher Nikoloz Chkhaidze, who also happened to be the head coach of the high-school physics team of Georgia I became part of and participated in numerous international Olympiads. In 2008 at International Physics Olympiad (IPHO) in Vietnam, I managed to get a bronze medal.

I am thankful for my advisor Dr. George Chagelishvili in Tbilisi State University, where I completed my bachelor studies, for guiding me throughout my undergraduate years. Also, among other professors I would like to thank Dr. George Mamatsashvili for making his classes very easy to understand and helping me with other questions I had outside the class material he taught. George Mamatsashvili and George Chagelishvili also happen to have been my collaborators since then.

And finally of course I have to mention my last 6 years in the University of Texas at Austin. My advisors, Prof. Wendell Horton and Prof. Philip J. Morrison were always helpful, gave me a very clear guidance, and at the same time I always felt I had all the necessary freedom to work in a stress free environment.

I also learned a lot from interacting with undergraduate students as I taught them mechanics and electricity & magnetism labs as a teaching assistant, and I would like thank Prof. Linda Reichl and a head TA at the time Henry Shreiner for sharing their knowledge in the beginning when I lacked the teaching experience.

I am thankful to Prof. Francois Waelbroeck who helped me a lot with a numerous administrative issues in Institute for fusion studies (IFS), and Prof. John Keto and Matthew Ervin in graduate affairs.

Linear and nonlinear processes in magnetohydrodynamic shear flows: their special nature, interplay and consequences

Publication No. _____

David Gogichaishvili, Ph.D.
The University of Texas at Austin, 2018

Supervisor: Philip J. Morrison

In the 1990s it was rigorously revealed by the hydrodynamic community non-normal nature of operators of the modal analysis of linear processes in shear flows – so, called "shear flow non-normality". The non-normality ensures finite-time, or transient, growth of perturbations in spectrally stable shear flows that is essentially anisotropic in spectral space and, in turn, leads to anisotropy of nonlinear processes in spectral space – the dominant nonlinear process turns out to be not a direct/inverse, but a transverse cascade, that is, a transverse/angular redistribution of perturbation harmonics in spectral space. The investigation of the linear transient growth and nonlinear transverse cascade in magnetohydrodynamic (MHD) unbounded constant shear flows – their special nature, interplay and consequences – is the goal of the present thesis.

Initially, in Chapter 2, is investigated in detail the transient linear dynamics in the form of overreflection of pseudo- and shear-Alfvén waves (P-AWs and S-AWs) in spectrally stable MHD plane constant shear flow. We show that: (1) the linear coupling of counter-propagating waves determines the overreflection, (2) counter-propagating P-AWs are coupled with each other, while counter-propagating S-AWs are not coupled with each other, but are asymmetrically coupled with P-AWs; S-AWs do not participate in the linear dynamics of P-AWs, (3) the transient growth of S-AWs is somewhat smaller compared with that of P-AWs, (4) the linear transient processes are highly anisotropic in wave number space, (5) the waves with small streamwise wavenumbers exhibit stronger transient growth and become more balanced.

Further, in the thesis is investigated MHD turbulence in spectrally stable two dimensional (2D) plane shear flows (Chapter 3) and three dimensional (3D) Keplerian disk flows, threaded by a non-zero azimuthal (Chapter 4) and vertical (Chapter 5) net magnetic flux. In order to gain a deeper insight into the underlying dynamical balances and sustaining mechanism, we performed a set of numerical simulations in the shearing box model and based on the simulation data, analyzed in detail the turbulence dynamics in Fourier space.

2D MHD plane shear flow, considered in Chapter 3, is spectrally stable, so the turbulence is subcritical by nature and hence it can be energetically supported just by a transient growth mechanism due to shear flow non-normality. We focus on analysis of the character of nonlinear processes and the underlying self-sustaining scheme of the turbulence, i.e., on the interplay between

linear transient growth and nonlinear processes, in the spectral plane. The study, being concerned with a new type of energy-injecting process for turbulence - the transient growth - represents an alternative to the main trends of magnetohydrodynamic (MHD) turbulence research.

In the case of Keplerian disk flows with a net azimuthal field, classical exponential/modal instabilities are absent and linear growth of perturbations (shearing waves) has a transient nature, also referred to as nonmodal growth. Particularly, in the case of disk flows with azimuthal field and rotation, magnetorotational instability (MRI), being only available source of energy for turbulence, has transient nature and by itself, cannot ensure a long-term sustenance of the perturbations, i.e. is imperfect in this sense. A necessary positive nonlinear feedback is required to regenerate new transiently growing modes. In other words, the role of nonlinearity becomes crucial: it lies at the heart of the sustenance of turbulence. The detailed analysis of the dynamics in apextral/Fourier space, allows to demonstrate existence of the positive feedback. Specifically, main novelties of the findings are the following:

I. The nonmodal growth process is strongly anisotropic in Fourier space that, in turn, leads to anisotropy of nonlinear processes in this space. As a result, the main nonlinear process appears to be not an usual direct/inverse, but rather a new type of transverse/angular redistribution of perturbation modes in Fourier space, when their wavevector mainly changes orientation during nonlinear mode interactions – *nonlinear transverse cascade*.

II. Both the linear nonmodal growth and nonlinear transverse cascade

mainly operate at large length scales, comparable to the box/system size. Consequently, the central, small wavenumber area of Fourier space, is crucial in the turbulence sustenance process and is called the *vital area*.

III. The turbulence is sustained by a subtle interplay of the linear non-modal growth (transient MRI in the case of Keplerian disks) and the nonlinear transverse cascade. Analyzing this interplay, it is revealed the basic subcycle of the sustenance scheme that clearly shows synergy of the linear and nonlinear processes in the self-organization of the magnetized flow system.

In the case of net vertical field, there is exponential growth of axisymmetric channel modes, and hence no deficit in energy supply. Due to this, the role of the transverse cascade in the turbulence sustenance is not as crucial as in the case of the azimuthal field. But it still shapes the dynamics, sets the saturation level, and determines the overall "design" of the net vertical field MRI-turbulence. In particular, it accounts for the transfer of energy among the "building blocks" of this turbulence: the axisymmetric channel mode, zonal flow, to a broad spectrum of nonaxisymmetric (parasitic) modes.

The analyzed refined interplay of linear and nonlinear processes should be relevant to the understanding of subcritical turbulence in other sheared and magnetized complex environmental and engineering flows (e.g., sheared $\mathbf{E} \times \mathbf{B}$ plasma fusion flows).

Table of Contents

List of Tables

List of Figures

Chapter 1

Introduction

Nonuniform/shear flows are ubiquitous both in nature and in laboratory. They occur in atmospheres, oceans, solar wind, stars, astrophysical disks, pipe flows, tokamak reactors, etc. Complex dynamics of these systems is, in many respects, a consequence of their nonuniform kinematics.

Developments in understanding the physics of the causes of turbulence in spectrally stable shear flows have been irregular and taken considerable time.The delay was due to some inadequacy of the canonical/modal/spectral approach to study linear stability of smooth shear flows, which ultimately led to the change of paradigm to a different, so-called, nonmodal approach (Schmid & Henningson, 2001). Now the phrases: shear flow nonnormality, nonmodal approach, transient growth, bypass concept of turbulence, shearing sheet and etc. are already a common parlance in the fluid dynamical, atmospheric and astrophysical disk communities. Although, retrospectively a thinking inertia pretty long was clutching on the modal approach – eigenfunctions and eigenvalues – and delayed the legitimation of these concepts in studies of dynamical processes in disks.

In the beginning of the 1990s, the non-normal nature of shear flows and

its consequences became well understood and extensively studied by the hydrodynamic community (Reddy & Henningson (1993), Trefethen et al. (1993), Schmid & Henningson (2001)).Shortcomings of traditional modal analysis (spectral expansion of perturbations in time and subsequent analysis of eigenfunctions) for shear flows have been revealed. Operators in the mathematical formalism of the modal analysis are non-normal and the corresponding eigenmodes are nonorthogonal (Reddy & Henningson (1993), Trefethen & Embree (2005), Schmid (2007)). The nonorthogonality leads to strong interference among the eigenmodes. Consequently, a proper approach should fully analyze this interference. While being in principle possible, this is in practice a formidable task. On this issue colorfully expressed (Trefethen, 1991): "For non-normal systems eigenvalues may still be used to a greater degree, like a nail file when a screwdriver can't be found, but they are rarely exactly right". As a result, the mathematical approach was shifted from the 1990s to the nonmodal approach and a breakthrough in the understanding and precise description of linear transient phenomena ensued. In spectrally stable hydrodynamic shear flows, it became clear that vortex and wave mode perturbations of certain spatial characteristics/orientation undergo linear transient growth (Gustavsson (1991), Farrell & Ioannou (1993a), Chagelishvili et al. (2003)), leading to short perturbation life times. However, in certain favorable circumstances, the perturbations are sustained for long time by the shear flow. Specifically, the imperfect linear transient growth, which is the only source of energy for turbulence in such flows, must be compensated by the nonlinear positive feedback,

i.e., the role of nonlinear processes becomes crucial: they lie at the heart of sustenance of the turbulence – close the feedback loop ensuring the sustaining dynamics. On the basis of this interplay between linear transient growth and nonlinear positive feedback, the hydrodynamic community described in detail transient growth types and formulated the concept of bypass transition to explain the onset and sustenance of turbulence in spectrally stable shear flows (Gebhardt & Grossmann (1994); Baggett et al. (1995); Grossmann (2000); Chapman (2002)).

One type of linear transient growth – overreflection of pseudo- and shear-Alfvén waves (P-AWs and S-AWs) – in spectrally stable MHD plane constant shear flow is investigated in (Gogichaishvili et al., 2014) and represent the content of Chapter 2.

As for the bypass concept, it was initially illustrated on toy model of Trefethen et al. (1993). It's natural that Trefethen's bypass turbulence model as a toy one has limitations. Afterwards phenomenological bypass concept was elaborated by (Waleffe, 1995). The concept relates to bounded hydrodynamics nonuniform flows and operates in physical space. This model showed limitations of the flow non-normality for the hydrodynamic bounded flow turbulence (see: Lectures of Summer program in Geophysical Fluid Dynamics, Walsh Cottage Woods Hole Oceanographic Institution, June 20 – August 26, 2011, Codirectors: Norman Lebovitz and Phil Morrison). Issues addressed in this thesis differ from the above case – we address (i) MHD, (ii) unbounded/free, (iii) constant shear flows where Maxwell (and not Reynolds) stress is dom-

inant. The action of boundaries on the dynamics is absent (as the flow is free). The flow profile is linear (and not curved). It appears that, in such situations, the flow non-normality induced transient growth is the dominant energy supplying linear phenomenon. So, we consider the simplest/constant shear flow and analyze the interplay of the linear transient and nonlinear feedback processes in spectral (**k**-)space. First, a constant shear flow is not a idealization, but quite a realistic/useful model. For instance, the well-known shearing sheet approximation for investigation of local dynamics in astrophysical disks is based on the background flow configuration with constant shear of velocity. Second, canonical nonlinear processes, such as direct/inverse cascade, are analyzed in spectral space. Therefore, it is natural to investigate how enriched the canonical nonlinear processes are by flow shear, whether the direct and inverse cascades are modified, or a new type of cascade process appears. The following thoughts can contribute to the clarification of these questions. Actually, the shear-induced linear nonmodal growth of a perturbation harmonic mainly depends on its wave vector orientation and, to a lesser degree, on the value (e.g., Farrell, 1988; Butler & Farrell, 1992; Farrell & Ioannou, 1993a; Jimenez, 2013): the spatial Fourier harmonics that have a certain orientation of the wave vector with respect to shear flow draw energy from it and grow, whereas harmonics with other orientation of the wave vector give energy to the flow and decay. This anisotropy of the linear energy-exchange processes with respect to wave vector orientation (angle), in turn, leads to anisotropy of nonlinear processes in **k**-space. Specifically, as revealed in (Hor-

ton et al., 2010; Mamatsashvili et al., 2014, 2016), in HD and MHD plane shear flows, the main nonlinear process is not a direct or inverse, but rather, so-called, nonlinear transverse cascade, that is angular (transverse) redistribution of perturbation harmonics in **k**-space. The *nonlinear transverse cascade* represents an alternative to the canonical direct and inverse cascades in the presence of flow velocity shear. Such angular redistribution of harmonics in **k**-space has been suggested in the context of the problem of hydrodynamic shear turbulence in non-magnetized Keplerian disks. In fact, differentially rotating disks represent special case of shear flows and hence the effects of nonnormality inevitably play a key role in their dynamics (e.g., Chagelishvili et al., 2003; Mukhopadhyay et al., 2005; Zhuravlev & Razdoburdin, 2014; Razdoburdin & Zhuravlev, 2017). Chagelishvili et al. (2003) first showed the applicability/relevance of the findings of the hydrodynamic community for spectrally stable shear flows, the nonorthogonality of linear operators and the nonmodal approach, the mechanism of perturbation amplification and the bypass concept of onset of turbulence for the dynamics of disks. Then, a simple sketch of the bypass scenario in wavenumber (k_x, k_y)-plane was presented (see figure A.1 of Chagelishvili et al. (2003)), which schematically describes the nonlinear angular redistribution of harmonics, i.e., the transverse cascade. Subsequently, a key character of the transverse cascade was confirmed and refined interplay of linear transient growth and nonlinear transverse cascade analyzed in detail for magnetized Keplerian disks by (Gogichaishvili et al. (2017, 2018)). In these papers are investigated Keplerian disk flows, threaded by a non-zero az-

imuthal and vertical net magnetic flux, respectively. The detail description of the specificity of these cases and the existing knowledge of similar research – magnetized disk flows – are presented in the related Chapters (4 and 5) of this theses.

1.1 Vivid example of nonlinear transverse cascade – dynamics of coherent vorticies in 2D plane shear flows

The nonlinear transverse cascade and its interplay with the linear transient growth can be clearly demonstrated in (k_x, k_y)-plane by analyzing the dynamics of coherent cyclonic and anticyclonic vorticies in 2D homogeneous constant shear flow, $U_0(x) = (0, Ax)$, with the shear parameter $A > 0$ (Horton et al. (2010)). The nonlinear dynamical equation for the stream function of perturbations, ψ, is

$$\left[\frac{\partial}{\partial t} + U_0(x)\frac{\partial}{\partial y}\right]\Delta\psi + J(\psi, \Delta\psi) - \nu\Delta^2\psi = 0, \tag{1.1}$$

where the spatial operators $J(.,.)$ and Δ are, respectively, 2D Jacobian and Laplacian and ν is the viscosity. The velocity and energy density of perturbations are defined through ψ and density ρ, respectively, as

$$v_x = -\frac{\partial\psi}{\partial y}; \quad v_y = \frac{\partial\psi}{\partial x}, \quad e(x,y,t) = \frac{1}{2}\rho\left[\left(\frac{\partial\psi}{\partial y}\right)^2 + \left(\frac{\partial\psi}{\partial x}\right)^2\right].$$

Initially we impose coherent vortices with Gaussian shape of stream function in the (x, y)-plane:

$$\psi(x,y,t)|_{t=0} = nb\exp\left(-\frac{x^2+y^2}{l^2}\right). \tag{1.2}$$

where $n = -1$ corresponds to cyclonic and $n = 1$ to anticyclonic vortex perturbations and $b > 0$ is their amplitude. Introduce non-dimensional parameters,

$$\tau \equiv At, \quad (X, Y) \equiv \frac{(x, y)}{l}, \quad B \equiv \frac{b}{Al^2}, \quad \Psi \equiv \frac{\psi}{Al^2}, \quad E \equiv \frac{2e}{\rho A^2 l^2}, \quad Re \equiv \frac{Al^2}{\nu},$$

and perform Fourier transform with respect to the coordinates X and Y,

$$\Psi = \int dk_x dk_y \Psi_{\mathbf{k}} \exp(ik_x X + ik_y Y). \tag{1.3}$$

Substituting Eq. (2.3) into Eqs. (2.1) and (2.2), one can obtain the evolution equation for $\Psi_{\mathbf{k}}$:

$$k^2 \frac{\partial \Psi_{\mathbf{k}}}{\partial \tau} - k_y \frac{\partial (k^2 \Psi_{\mathbf{k}})}{\partial k_x} + \frac{k^4}{Re} \Psi_{\mathbf{k}} = \sum_{\mathbf{k}=\mathbf{k}'+\mathbf{k}''} (k'_x k''_y - k''_x k'_y) k'^2 \Psi_{\mathbf{k}'} \Psi_{\mathbf{k}''}, \tag{1.4}$$

with the corresponding initial condition in Fourier plane

$$\Psi_{\mathbf{k}}|_{\tau=0} = nB \exp\left(-\frac{k_x^2 + k_y^2}{4\pi^2}\right),$$

where $k^2 \equiv k_x^2 + k_y^2$. The nonlinear term on the right hand side (rhs) of this equation describes three-wave interactions. Equation (2.4) forms the basis of the numerical study to explore quantitatively the dynamics of the stream function, spectral energy density, and total energy of cyclonic and anticyclonic vorticies. However, to investigate the physics of the phenomena, one has to analyze the dynamical equation for the spectral kinetic energy density, $E_{\mathbf{k}} = k^2 |\Psi_{\mathbf{k}}|^2$, which follows from Eq. (2.4),

$$\frac{\partial E_{\mathbf{k}}}{\partial \tau} = k_y \frac{\partial E_{\mathbf{k}}}{\partial k_x} + \frac{2k_x k_y}{k^2} E_{\mathbf{k}} - \frac{k^2}{Re} E_{\mathbf{k}} + N_{\mathbf{k}}, \tag{1.5}$$

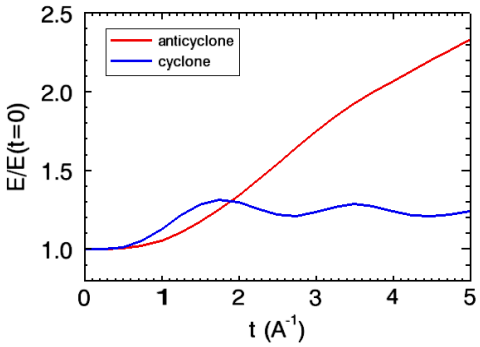

Figure 1.1: Normalized total energy vs. time for coherent anticyclonic (red) and cyclonic (blue) vortex perturbations for $Re = 1000$ and $B = 3$. The energy of the anticyclonic vortex increases monotonically, while the energy of the cyclonic one initially increases and then oscillates weakly around a constant value.

where $N_{\mathbf{k}}$ is the nonlinear term:

$$N_{\mathbf{k}} = \sum_{\mathbf{k}=\mathbf{k}'+\mathbf{k}''} (k'_x k''_y - k''_x k'_y) k'^2 (\Psi^*_{\mathbf{k}} \Psi_{\mathbf{k}'} \Psi_{\mathbf{k}''} + \Psi_{\mathbf{k}} \Psi^*_{\mathbf{k}'} \Psi^*_{\mathbf{k}''}).$$

The terms on the rhs of Eq. (2.5) represent four – three linear and one nonlinear – basic phenomena: 1. The linear flux of the spectral kinetic energy parallel to the k_x-axis, 2. The energy exchange between the perturbation harmonics and the background flow, 3. The viscous dissipation, 4. The nonlinear processes that redistribute the energy of perturbation harmonics in $\mathbf{k}$-plane, but do not change their total energy. The interplay of these basic phenomena defines $\partial E_{\mathbf{k}}/\partial\tau$. Solving numerically Eq. (2.4), or equivalently Eq. (2.5), one can get full information on all the physical quantities and the basic phenomena.

The evolution of the perturbation energy normalized to the initial value

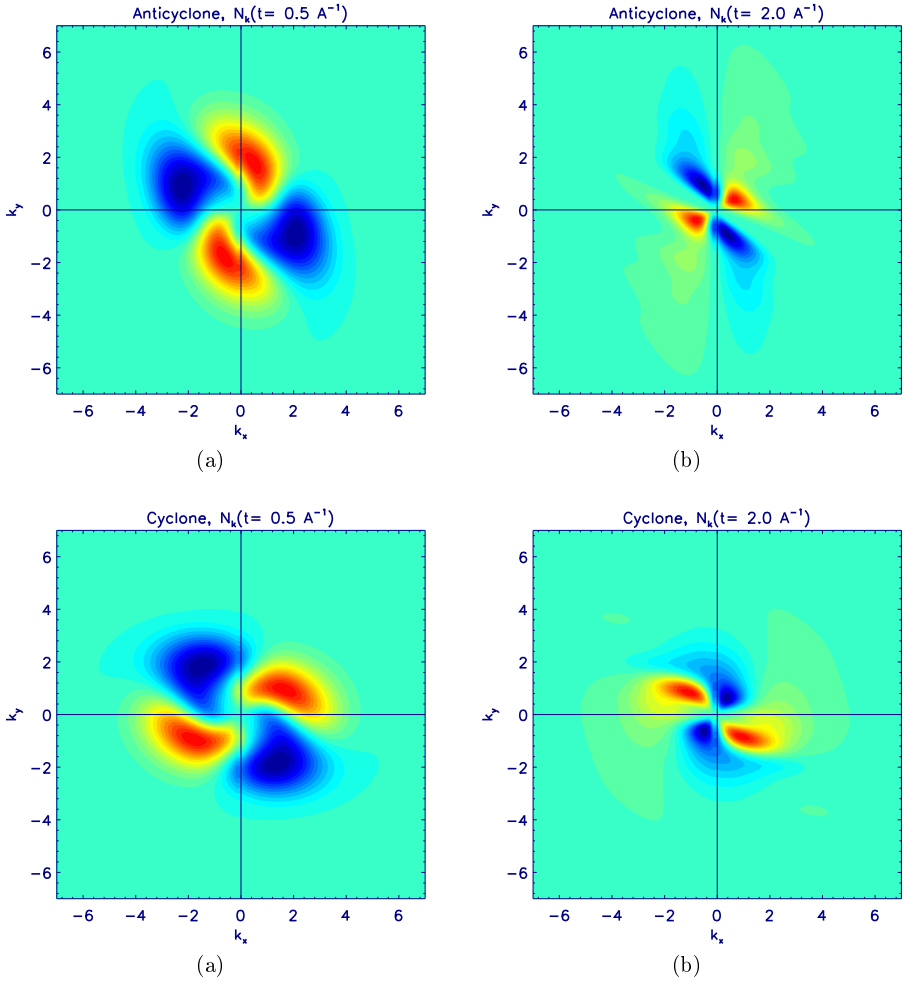

Figure 1.2: The spectrum of the nonlinear term $N_{\mathbf{k}}(k_x, k_y, \tau)$ for the coherent anticyclonic (upper two plots) and cyclonic (lower two plots) vorticies with $Re = 1000$ and $B = 3$ at times $\tau = 0.5$ and 2, respectively. The nonlinearity redistributes the perturbation harmonics energy from the blue areas (where $N_{\mathbf{k}} < 0$) to the red ones (where $N_{\mathbf{k}} > 0$) – the nonlinear transverse cascade is strongly pronounced.

E/E_0 for the coherent anticyclonic and cyclonic perturbations are presented in Fig. 1. The energy of the anticyclonic vortex increases monotonically, while

the energy of the cyclonic one initially increases and then oscillates weakly around a constant value. Since, the linear dynamics of the perturbations are identical, the difference in the energy evolutions is due to the nonlinear phenomena described in (k_x, k_y)-plane by $N_{\mathbf{k}}$. This term for the anticyclonic vortex (with $B = 3$ and $Re = 1000$) is presented in upper plots of Fig. 2 at $\tau = 0.5$ and 2. The nonlinearity redistributes the perturbation energy from the blue areas (where $N_{\mathbf{k}} < 0$) to the red ones (where $N_{\mathbf{k}} > 0$). The green refers to areas where $N_{\mathbf{k}} \simeq 0$. As one can see, the nonlinear interactions redistribute energy from quadrants II and IV (where $N_{\mathbf{k}}$ is predominantly negative), to quadrants I and III (where $N_{\mathbf{k}}$ is predominantly positive). This nonlinear angular redistribution, or transverse cascade, repopulates the growing harmonics, which extract shear flow energy and are amplified in quadrants I and III of $\mathbf{k}$-plane, where $k_x k_y > 0$ (see Eq. 2.5). This nonlinear feedback mechanism leads to the growth of the total energy of the coherent anticyclonic perturbations (the red curve in Fig.1), i.e., – to the sustenance of anticyclonic perturbations. Also, one can see that the domain of significant nonlinear activity shrinks in time towards lower wave numbers: an inverse cascade is also at work. However, the dominant nonlinear process is the transverse cascade.

The lower plots of Fig. 2 show that the transverse cascade is also strongly pronounced for coherent cyclonic vortices. However, in this case the nonlinear dynamics is more complicated. Positive and negative feedbacks alternate in time. Indeed, we see that nonlinear interactions redistribute energy mainly over wavenumber angle, from quadrants II and IV to quadrants I and

III at $\tau = 0.5$ and vice versa at $\tau = 2$. Hence, the transverse cascade repopulates growing harmonics (for which $k_x k_y > 0$) at $\tau = 0.5$, contributing to an increase in the cyclonic vortex total energy. By contrast, the repopulation of decaying harmonics by the transverse cascade leads to a decrease in the total energy at $\tau = 2$ (see variation of the blue curve in Fig. 1). So, in the case of the cyclonic vortex, the transverse cascade does not ensure a continuous positive feedback.

Chapter 2

Nature and dynamics of overreflection of Alfvén waves in MHD shear flows

2.1 Introduction

Nonuniform flows are ubiquitous both in nature and in laboratory. They occur in atmospheres, oceans, solar wind, stars, astrophysical disks, pipe flows, tokamak reactors, etc. Complex dynamics of these systems is, in many respects, a consequence of their nonuniform kinematics. One of the basic manifestations of flow shear is wave overreflection phenomenon – substantial growth of counter-propagating wave perturbations – that occurs universally whenever flow has non-zero shear. For instance, in astrophysical discs, there is the overreflection of spiral-density waves, in the atmosphere – internal-gravity waves, in the solar wind – MHD waves, and in laboratory plasmas.

The essence of the overreflection is the following. If initially in a shear flow exist just waves having definitely directed group velocity and, consequently, propagating in one direction (i.e. counter-propagating waves are absent initially), in the course of time, there appears the growth of counter-propagating waves, i.e., waves that have oppositely (to the initial waves) directed group velocities. Of course, if the initial/incident waves are localized in

the flow shear direction, the overreflection phenomenon has visual manifestation – it appears reflected (also localized in the shear direction) waves having larger, then incident waves, amplitude. However, in the non-modal approach, investigating the dynamics of spatial Fourier harmonics of waves (so called, Kelvin waves) that are not localized in the physical space, the visual manifestation is absent and one can mathematically describe the overreflection by the appearance and increase of counter-propagating waves, i.e. – waves having oppositely directed group velocity. We aim to go deeper into the physical mechanism responsible for this overreflection in an incompressible MHD shear flow.

The overreflection phenomenon is usually analysed on the basis of a single second-order ordinary differential (wave) equation (e.g., see seminal papers on overreflection Goldreich & Tremaine, 1978, 1979; Lindzen & Barker, 1985; Farrell & Ioannou, 1993b). This approach describes counter-propagating waves by a single/physical variable and, consequently, possible dynamical processes between these waves (e.g., their coupling) are, in fact, left out of consideration. To fill this gap – to reduce the perturbation equations to the set of first order differential equations for individual counter-propagating wave – we propose, at first, to find "eigen-variable" for each wave component. I.e., to find variables for which the linear matrix operator is diagonal in the shearless limit. Then, one have to generalize the eigen-variables for plasmas with non-zero shear case. The generalization is not unique possible procedure. But the optimal one is quite easily findable. In the considered MHD flow, the generalized

variables are the renormalized Elsässer variables (derived in equations 2.12). Resulting first order ordinary differential equations (written for the generalized variables) separate from each other different physical processes, making it possible to grasp their interplay and to understand the basic physics of the overreflection phenomenon. In the renormalized Elsässer variables we get two different types of Alfvén waves in incompressible MHD flows with linear shear of mean velocity, $\mathbf{U}_0 = (Sy, 0, 0)$. As stated in the abstract, these waves are reduced to pseudo- and shear-Alfvén waves when the wavenumber along Z-axis equals zero (i.e., when $k_z = 0$). Therefore, for simplicity, we labelled these waves as: P-Alfvén and S-Alfvén waves (Pseudo-Alfven and shear-Alfven waves). We carried out analytical (Kelvin mode) and numerical analysis of the linear dynamics of P-AWs and S-AWs. Our analysis has clearly demonstrated linear coupling between these waves. We describe in detail transient growth of counter-propagating components of P-AWs and S-AWs when only one of them exists initially in the flow. The amplification of these (so-called, transmitted and reflected) waves, i.e. *the wave overreflection phenomenon*, is determined by the linear coupling of the waves induced by shear flow non-normality.

Historically, the non-normality of shear flows considerably delayed the full understanding of their behavior. In fact, this feature and its dynamical consequences only became well understood by the hydrodynamic community in the 1990s (e.g., see Reddy & Henningson, 1993; Trefethen et al., 1993; Schmid, 2007). Shortcomings of the traditional modal analysis (i.e., spectral expansion of perturbations in time and then analysis of eigenfunctions) for shear flows

have been revealed and an alternative Kelvin wave approach – a special kind of the non-modal approach – has become well established and has been extensively used since the 1990s. Kelvin waves represent the basic "elements" of dynamical processes at constant shear rate (Chagelishvili et al., 1996; Yoshida, 2005) and greatly help to understand finite-time transient phenomena in shear flows. In particular, non-modal analysis reveals a channel of linear coupling among different branches/modes of perturbations in shear flows (Chagelishvili et al., 1997b,a), leading to energy exchange between vortex and wave modes and between different wave branches.

A new, *bypass transition*, concept was also formulated by the the hydrodynamic community to explain the onset of turbulence in spectrally stable shear flows (e.g., see Baggett et al., 1995; Grossmann, 2000; Eckhardt et al., 2007, and references therein) on the basis of the interplay between linear transient growth and nonlinear positive feedback. The bypass scenario differs fundamentally from the classical turbulence scenario, which is based on exponentially growing perturbations in a system that supplies turbulent energy. In the classical case, the nonlinearity is not vital to the existence of the perturbations. Instead, it merely determines their scales, via the direct and inverse cascades.

This breakthrough led to renewed comprehension of different aspects of shear flow dynamics. This thesis (related to (Gogichaishvili et al., 2014)), aims to provide new insight into the physics of wave overreflection on the example of P-AWs and S-AWs in incompressible MHD flows with linear shear in the

mean velocity profile. Actually, our study can be of wide applicability:
(i) The method of characterizing overreflection presented here is optimal, moreover, canonical, and can be easily applied for deeper understanding of the overreflection phenomenon in other important cases, such as spiral-density waves in astrophysical discs and internal-gravity waves in stably stratified atmospheres;
(ii) The presented overreflection dynamics fits in naturally within the abovementioned bypass concept. This allows us to adopt schemes and ideas of the bypass concept for the understanding of driven turbulence in MHD shear flows.

The Chapter is organized as follows. Section 2.2 is devoted to deriving four first order differential equations (for individual counter-propagating wave) and qualitative analysis of the equations. Section 2.3 – to the numerical analysis in two and three dimensions. Summary and discussion are given in Section 2.4 where we also analyze nonlinear consequences of the described linear dynamics and application of the proposed approach to more complex shear flow systems.

2.2 Physical model and equations

Consider a 3D ideal, incompressible MHD fluid flow with constant/linear shear of velocity, $\mathbf{U}_0 = (Sy, 0, 0)$, and uniform magnetic field, $\mathbf{B}_0 = (B_0, 0, 0)$, directed along the flow. The linearized dynamical equations for small perturbations to the flow are:

$$\left(\frac{\partial}{\partial t}+Sy\frac{\partial}{\partial x}\right)v_x+Sv_y=-\frac{1}{\rho}\frac{\partial p}{\partial x}\ , \tag{2.1}$$

$$\left(\frac{\partial}{\partial t}+Sy\frac{\partial}{\partial x}\right)v_y=-\frac{1}{\rho}\frac{\partial p}{\partial y}+\frac{B_0}{4\pi\rho}\left(\frac{\partial b_y}{\partial x}-\frac{\partial b_x}{\partial y}\right)\ , \tag{2.2}$$

$$\left(\frac{\partial}{\partial t}+Sy\frac{\partial}{\partial x}\right)v_z=-\frac{1}{\rho}\frac{\partial p}{\partial z}+\frac{B_0}{4\pi\rho}\left(\frac{\partial b_z}{\partial x}-\frac{\partial b_x}{\partial z}\right)\ , \tag{2.3}$$

$$\frac{\partial v_x}{\partial x}+\frac{\partial v_y}{\partial y}+\frac{\partial v_z}{\partial z}=0\ ,\qquad \frac{\partial b_x}{\partial x}+\frac{\partial b_y}{\partial y}+\frac{\partial b_z}{\partial z}=0\ , \tag{2.4}$$

$$\left(\frac{\partial}{\partial t}+Sy\frac{\partial}{\partial x}\right)b_y=B_0\frac{\partial v_y}{\partial x}\ , \tag{2.5}$$

$$\left(\frac{\partial}{\partial t}+Sy\frac{\partial}{\partial x}\right)b_z=B_0\frac{\partial v_z}{\partial x}\ , \tag{2.6}$$

where: ρ is the unperturbed density; p, $\mathbf{v}$ and $\mathbf{b}$ are the pressure, velocity and magnetic field perturbations, respectively.

The dynamic equations permit the decomposition of perturbed quantities into Kelvin waves, or spatial Fourier harmonics (SFHs):

$$\Psi(x,y,z,t)=\tilde{\Psi}(k_x,k_y(t),k_z,t)\exp(ik_xx+ik_y(t)y+ik_zz)\ , \tag{2.7}$$

where $\Psi=\{p,\mathbf{v},\mathbf{b}\}$, $\tilde{\Psi}=\{\tilde{p},\tilde{\mathbf{v}},\tilde{\mathbf{b}}\}$ and $k_y(t)=k_{y0}-Sk_xt$.

Introducing the following non-dimensional variables and parameters by taking: $1/S$ as the scale of time; Alfvén velocity, $V_A=B_0/(4\pi\rho)^{1/2}$, as the scale of velocity perturbation; B_0 as the scale of magnetic field perturbation,

$$\tau=St\ ,\quad k_y(\tau)=k_y(0)-k_x\tau\ ,\quad \hat{v}_y=\tilde{v}_y/V_A\ ,$$
$$\hat{v}_z=\tilde{v}_z/V_A\ ,\quad \hat{b}_y=\tilde{b}_y/B_0\ ,\quad \hat{b}_z=\tilde{b}_z/B_0\ , \tag{2.8}$$

the above system of equations reduces to the following first order dynamic equations:

$$\frac{d\hat{v}_y}{d\tau} = 2\chi_p(\tau)\hat{v}_y + i\Omega_A\hat{b}_y \ , \qquad \frac{d\hat{b}_y}{d\tau} = i\Omega_A\hat{v}_y \ , \tag{2.9}$$

$$\frac{d\hat{v}_z}{d\tau} = 2\chi_s(\tau)\hat{v}_y + i\Omega_A\hat{b}_z \ , \qquad \frac{d\hat{b}_z}{d\tau} = i\Omega_A\hat{v}_z \ , \tag{2.10}$$

where

$$\chi_p(\tau) = \frac{k_x k_y(\tau)}{k^2(\tau)} \ , \quad \chi_s(\tau) = \frac{k_x k_z}{k^2(\tau)} \ ,$$
$$k^2(\tau) \equiv k_x^2 + k_y^2(\tau) + k_z^2 \ , \quad \Omega_A \equiv \frac{k_x V_A}{S} \ . \tag{2.11}$$

Ω_A is non-dimensional Alfvén wave frequency.

One can say, that $\hat{v}_y$, $\hat{v}_z$, $\hat{b}_y$ and $\hat{b}_z$ are physical variables, but not eigen ones for the counter-propagating P-AWs and S-AWs. Here we start our optimal route to the description of the overreflection phenomenon the essence of which is outlined in the introduction: initially, one have to define eigen variable for each wave components in the shearless limit (for which the linear matrix operator is diagonal). Then, one have to generalize the eigen variables for non-zero shear case and rewrite the dynamic equations for them. Fortunately, in the considered MHD flow, one can use the Elsässer variables as the generalized ones,

$$Z_p^{\pm} = \hat{v}_y \mp \hat{b}_y \ , \quad Z_s^{\pm} = \hat{v}_z \mp \hat{b}_z \ . \tag{2.12}$$

Inserting the Elsässer variables into equations (2.9) and(2.10), one get the set of the four, first order differential equations describing the dynamics of

P-Alfvén (labelled by the index "p") and S-Alfvén (labelled by the index "s") wave SFHs:

$$\frac{dZ_p^+}{d\tau} = -i\Omega_A Z_p^+ + \chi_p(\tau) Z_p^+ + \chi_p(\tau) Z_p^- \ , \tag{2.13}$$

$$\frac{dZ_p^-}{d\tau} = i\Omega_A Z_p^- + \chi_p(\tau) Z_p^- + \chi_p(\tau) Z_p^+ \ , \tag{2.14}$$

$$\frac{dZ_s^+}{d\tau} = -i\Omega_A Z_s^+ + \chi_s(\tau) Z_p^+ + \chi_s(\tau) Z_p^- \ , \tag{2.15}$$

$$\frac{dZ_s^-}{d\tau} = i\Omega_A Z_s^- + \chi_s(\tau) Z_p^- + \chi_s(\tau) Z_p^+ \ . \tag{2.16}$$

One can see that the linear matrix operator of the equations (written for the eigen variables) is not diagonal in shear flow. I.e. the dynamics of the waves are not separated to each other any more.

2.2.1 Spectral energy

Strictly speaking, the energy of waves should be determined in the framework of nonlinear problems. However, usually, the concept of energy is introduced in solving linearized problems (Stepanyants & Fabrikant, 1989). We also do the same to get a feeling of the dynamics of quadratic forms of physical variables.

The energy of an individual SFH (total spectral energy) is the sum of

kinetic and magnetic ones:

$$E(k_x, k_y(\tau), \tau) = \frac{\rho V_A^2}{2}\left(|\hat{v}_x|^2 + |\hat{v}_y|^2 + |\hat{v}_z|^2 + |\hat{b}_x|^2 + |\hat{b}_y|^2 + |\hat{b}_z|^2\right) =$$
$$= \frac{1}{4}\rho V_A^2\left(1 + \frac{k_y^2(\tau)}{k_x^2}\right)\left(|Z_p^+|^2 + |Z_p^-|^2\right) + \frac{1}{4}\rho V_A^2\left(1 + \frac{k_z^2}{k_x^2}\right)\left(|Z_s^+|^2 + |Z_s^-|^2\right) +$$
$$+\frac{1}{4}\rho V_A^2\frac{k_y(\tau)k_z}{k_x^2}\left(Z_p^+ Z_s^{+*} + Z_p^- Z_s^{-*} + Z_s^+ Z_p^{+*} + Z_s^- Z_p^{-*}\right) =$$
$$= E_p^+ + E_p^- + E_s^+ + E_s^- + E_{int}, \tag{2.17}$$

where:

$$E_i^{\pm} \equiv \frac{1}{4}\rho V_A^2\left(1 + \frac{k_y^2(\tau)}{k_x^2}\right)|Z_i^{\pm}|^2, \quad i = p, s$$

$$E_{int} \equiv \frac{1}{4}\rho V_A^2\frac{k_y(\tau)k_z}{k_x^2}\left(Z_p^+ Z_s^{+*} + Z_p^- Z_s^{-*} + Z_s^+ Z_p^{+*} + Z_s^- Z_p^{-*}\right) \quad .$$

One can say, that $E_p = E_p^+ + E_p^-$ is the spectral energy of P-AWs, $E_s = E_s^+ + E_s^-$ – the spectral energy of S-AWs, and E_{int} – the spectral potential energy connected to the coupling, or interaction between P-AWs and S-AWs. So, the spectral energy, that is the sum of quadratic forms of velocity and magnetic field perturbations, does not reduce to a sum of quadrates of the Elsässer variables – it can be interpreted as the sum of the spectral energies of P-AWs and S-AWs with the additional term, E_{int}. This additional term appears in the framework of the considered linear theory due to the coupling of these two waves and, of course, has not any relation to their nonlinear interaction. Generally, E_{int} is of the order of E_p and E_s (see below figure 2.6). Evaluating the dynamic processes, we will work in terms of the spectral energies of the waves (E_p, E_s, E_p^+, E_s^+, E_p^- and E_s^-).

2.2.2 Qualitative analysis of the dynamic equations: the wave linear coupling as the basis of the overreflection

From equations (2.13)-(2.16) it follows that the dynamics of counter-propagating P-AW SFHs is self-contained – the dynamics is defined by the intrinsic to the P-AWs terms, while the dynamics of S-AW SFHs is defined by the extrinsic to S-AWs terms – the second and third rhs terms of equations (2.15) and (2.16) linearly couple the dynamics of each S-AW SFH to the corresponding SFH of P-AWs. So, the coupling is asymmetric: S-AWs do not participate in the dynamics of P-AWs, while P-AWs do. Somewhat similar investigation, but in compressible case, is performed in Hollweg & Kaghashvili (2012). In compressible flows, the coupling is mutual – slow magnetosonic waves are generated by Alfvén ones and inverse. A physical result of this process is the generation of density perturbations by Alfvén waves.

The dynamics of each (counter-propagating) P-AW SFH is determined by the interplay of three different terms on the right hand side of equations (2.13) and (2.14). The second rhs terms of these equations relate to a mechanism of energy exchange between the mean flow and the SFH. The third rhs terms couple these equations, or physically, linearly couple the counter-propagating P-AWs. These terms relate to another mechanism, which is responsible, in many respects, for P-AW overreflection phenomenon. χ_p is the time-dependent coupling coefficient of counter-propagating P-AWs and, in fact, its value determines the strength of the overreflection of these waves. In the shearless limit, $\chi_p = 0$ and only the first, easily recognizable terms are

left in these equations, which result in oscillations with normalized frequencies Ω_A and $-\Omega_A$, i.e., with Alfvén frequency, $K_x V_A$, in dimensional variables.

As for equations (2.15) and (2.16), the second and third rhs terms describe the growth of S-AWs that occurs due to the linear coupling of P-AWs and S-AWs, i.e. the growth of S-AWs is an indirect consequence of P-AWs growth. Nevertheless, as it follows from the below performed numerical calculations, the growth of P-AWs prevails over the growth of S-AWs for a wide range of the system parameters.

2.2.3 Qualitative analysis of the dynamics of P-Alfvén waves

We analyze the wave dynamics in polar coordinates,

$$Z_i^{\pm}(\tau) = |Z_i^{\pm}(\tau)| \exp(-i\phi_i^{\pm}(\tau)) \ , \quad i = p, s \tag{2.18}$$

and define the degree of imbalance for counter-propagating SFHs of P-AWs and S-AWs as:

$$\alpha_i = 1 - \frac{|Z_i^-|^2}{|Z_i^+|^2} \ , \quad i = p, s. \tag{2.19}$$

For the purpose of the visualization of overreflection phenomenon we introduce "instantaneous frequency" as

$$\Omega_i^{\pm}(\tau) = \frac{d\phi_i^{\pm}(\tau)}{d\tau} \ , \quad i = p, s. \tag{2.20}$$

As it was mentioned above, the dynamics of counter-propagating P-Alfvén waves is self-contained. Let's focus on a qualitative analysis of P-AWs' SFHs amplitude and phase dynamics.

From equations (2.13) and (2.14) it follows:

$$\frac{d}{d\tau}(|Z_p^+|^2 - |Z_p^-|^2) = 2\chi_p(\tau)(|Z_p^+|^2 - |Z_p^-|^2) = \\ = \left[\frac{d}{d\tau}\ln\left(\frac{k_x^2 + k_y^2(0) + k_z^2}{k_x^2 + k_y^2(\tau) + k_z^2}\right)\right](|Z_p^+|^2 - |Z_p^-|^2) \ , \tag{2.21}$$

or, after integration,

$$|Z_p^+(\tau)|^2 - |Z_p^-(\tau)|^2 = \frac{k_x^2 + k_y^2(0) + k_z^2}{k_x^2 + k_y^2(\tau) + k_z^2}(|Z_p^+(0)|^2 - |Z_p^-(0)|^2) \ . \tag{2.22}$$

We see that if the waves are balanced at the beginning, $|Z_p^+(0)| = |Z_p^-(0)|$, they remain balanced. If at the beginning $|Z_p^+(0)| \neq |Z_p^-(0)|$, then the difference of the intensities varies by an algebraic law ($\sim 1/k^2(\tau)$) that is characteristic to transient growth in hydrodynamic shear flows (Farrell & Ioannou, 1993a; Schmid, 2007). This indicates a common basis of transient dynamics in MHD and hydrodynamics shear flows.

Renormalizing the Elsässer variables:

$$|Z_p^\pm(\tau)| = \exp\left(\int_0^\tau d\tau' \chi_p(\tau')\right)|\hat{Z}_p^\pm(\tau)| = \sqrt{\frac{k_x^2 + k_y^2(0) + k_z^2}{k_x^2 + k_y^2(\tau) + k_z^2}}|\hat{Z}_p^\pm(\tau)| \ , \tag{2.23}$$

Equations (2.13) and (2.14) are reduced to

$$\frac{d\hat{Z}_p^+}{d\tau} = -i\Omega_A\hat{Z}_p^+ + \chi_p(\tau)\hat{Z}_p^- \ , \quad \frac{d\hat{Z}_p^-}{d\tau} = i\Omega_A\hat{Z}_p^- + \chi_p(\tau)\hat{Z}_p^+ \ , \tag{2.24}$$

and equation (2.22) to

$$|\hat{Z}_p^+(\tau)|^2 - |\hat{Z}_p^-(\tau)|^2 = |\hat{Z}_p^+(0)|^2 - |\hat{Z}_p^-(0)|^2 \ , \tag{2.25}$$

i.e., in this version of eigen variables, the dynamic equations are simplified (compare 2.13 and 2.14 with 2.24) and, in addition (as it follows from equation 2.25), the difference between the intensities is constant. Equation (2.25) indicates the conservation of action for P-AW harmonics. The similar conservation of wave action for different and more complex configuration is derived in Heinemann & Olbert (1980). The latter considers small-amplitude, toroidal non-WKB (long wavelength) Alfvén waves in a model of axisymmetric ideal MHD solar wind flow neglecting solar rotation. The considered toroidal waves decouple from compressional waves in linear approximation and their amplitudes dynamics can be computed from only two equations without consideration of the other wave modes. I.e. the dynamics of the toroidal Alfvén waves is self-contained as the dynamics of counter-propagating P-AWs considered here. Consequently, the conservation of wave action in the both cases is reduced to the conservation of the wave action for one (counter-propagating, or inward-outward) wave mode independently to the complexity of the flow system and has the simple form.

Equations (2.18) and (2.23) give

$$\hat{Z}_p^{\pm}(\tau) = |\hat{Z}_p^{\pm}(\tau)| \exp(-i\phi_p^{\pm}(\tau)) \ , \tag{2.26}$$

substituting which in (2.24), after simple but cumbersome mathematical manipulations, finally, results in two dynamic equations for the normalized total intensity, $|\hat{Z}_p^{+}(\tau)|^2 + |\hat{Z}_p^{-}(\tau)|^2$, and phases difference, $\Delta\phi_p(\tau) = \phi_p^{+}(\tau) - \phi_p^{-}(\tau)$,

of the counter-propagating P-Alfvén waves:

$$\frac{d\ln(|\hat{Z}_p^+|^2+|\hat{Z}_p^-|^2)}{d\tau}=\Gamma(\tau)\chi_p(\tau)\cos\Delta\phi_p\ , \tag{2.27}$$

$$\frac{d\Delta\phi_p}{d\tau}=2\Omega_A-\frac{\chi_p(\tau)}{\Gamma(\tau)}\sin\Delta\phi_p\ , \tag{2.28}$$

where,

$$\Gamma(\tau)=\frac{2|\hat{Z}_p^+||\hat{Z}_p^-|}{|\hat{Z}_p^+|^2+|\hat{Z}_p^-|^2} \tag{2.29}$$

mathematically is the ratio of the geometrical and arithmetic means of the amplitudes. Of course, this ratio is the maximum when the amplitudes are equal to each other. Consequently, the fastest growth of the total intensity of the counter-propagating waves occurs when the waves are balanced from the beginning, $|\hat{Z}_p^+(0)|=|\hat{Z}_p^-(0)|$. In this case, $\Gamma(\tau)=1$ that contributes to the intensification of the growth. The results of the presented below numerical calculations confirms this.

The growth also depends on sign-varying quantities χ_p and $\cos\Delta\phi_p$. For the optimal growth, the coincidence of their signs during main part of the dynamics is necessary. The sign of $\chi_p(\tau)$ is defined by the sign of $k_xk_y(\tau)$. If initially $k_xk_y(0)>0$, $\chi_p(0)$ is positive. In the course of time, when $\tau>\tau^*\equiv k_y(0)/k_x$, $\chi_p(\tau)$ becomes negative. For the effectivness of the growth, well-timed change of the sign of $\cos\Delta\phi_p$ is necessary to make the rhs of equation (2.27) positive again. So, the growth should depend strongly on the dynamics of $\Delta\phi_p(\tau)$, including the initial value of the phase difference, $\Delta\phi_p(0)$. This fact is also confirmed by the following calculations.

2.3 Numerical analysis

It is seen from equations (2.13)-(2.16) that, S-AWs do not participate in any energy exchange processes in the flow. If initially only S-AWs are excited in the flow, $|Z_s^{\pm}(0)| \neq 0$ and $|Z_p^{\pm}(0)| = 0$, and the dynamics is trivial – any kind of energy exchange process is absent and we simply have the propagation of S-AWs. So, we analyze cases when initially only P-AW SFHs are imposed in the flow. Specifically, we inserted a single unidirectional P-AW harmonic (i.e., with one sign of frequency, $Z_p^+(0) = 1$ and $Z_p^-(0) = 0$) or counter-propagating P-AW harmonics with equal amplitudes but different phases ($Z_p^+(0) = 1$ and $Z_p^-(0) = 1, i, -1$). We present the results of the numerical calculations for $\Omega_A = 0.1; 0.3; 1$ and $k_y(0)/k_x = 100$. We consider two-dimensional ($k_z = 0$), as well as three-dimensional ($k_z/k_x = 1; 10$) cases. A general outcome of the dynamics is the following: the growth of the waves occurs mostly at $\Omega_A < 1$ and $k_y(0)/k_x > 1$; the intensity of the processes increases with the decrease of Ω_A and increase of $k_y(0)/k_x$; it also strongly depends on the value of k_z/k_x.

2.3.1 Two-dimensional case

The transient dynamics of amplitudes of P-AWs (governed by equations 2.13 and 2.14) is shown in figure 2.1 at $\Omega_A = 0.1$ and $k_z = 0$ when initially only unidirectional P-AW harmonic is imposed in the flow. The dynamics of corresponding phases of the two-dimensional P-AW harmonic is presented in figure 2.2. Plotted in figure 2.3 are the variation of the P-AWs' SFH instantaneous frequencies, Ω_p^+ and Ω_p^-, associated with the dynamics of the corresponding

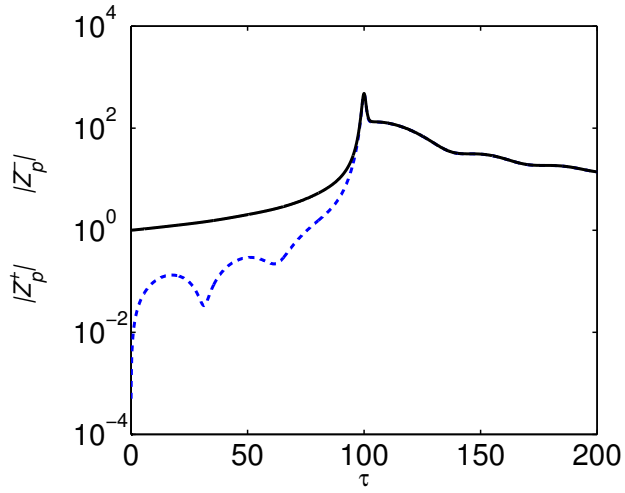

Figure 2.1: $|Z_p^+|$ (solid black) and $|Z_p^-|$ (dashed blue) vs time in log-linear scaling at: $Z_p^+(0) = 1$, $Z_p^-(0) = 0$, $Z_s^+(0) = 0$, $Z_s^-(0) = 0$, $\Omega_A = 0.1$, $k_y(0)/k_x = 100$ and $k_z = 0$.

phases.

With the help of equations (2.13) and (2.14) and Figures 2.1-2.3 one can trace each stage of the evolution of the counter-propagating P-AW harmonic, which in fact, represents the overreflection phenomenon. Initially, as $Z_p^-(0) = 0$, in (2.14) only the last rhs term is nonzero. So, the initial amplification and the dynamics of $Z_p^-(\tau)$ is due to the third term $\chi_p Z^+$. Therefore, the positive "instantaneous frequency" of Z_p^+ results in the positive "instantaneous frequency" of Z_p^- (see figure 2.3). The growth of $|Z_p^-|$ is rapid, but algebraic (nonexponential). In the course of the evolution, $|Z_p^-|$ becomes almost equal to $|Z_p^+|$ (see figure 2.1 at $\tau \simeq \tau^* \equiv k_y(0)/k_x = 100$). At the same time, the influence of the first and second rhs terms of equation (2.14) become appreciable, behavior of ϕ_p^- and Ω_p^- changes at $\tau \simeq \tau^*$ with Ω_p^- becoming negative

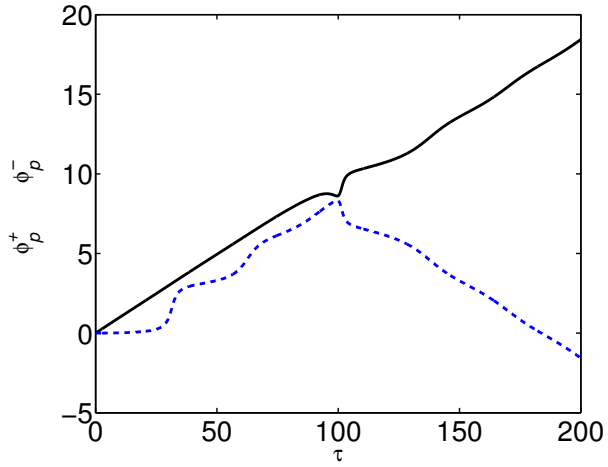

Figure 2.2: ϕ_p^+ (solid black) and ϕ_p^- (dashed blue) vs time for the same parameters as in figure 2.1.

and, as a result of all these, Z_p^- is propagating opposite to Z_p^+. With further increase of time, Ω_p^- tends to $-\Omega_A$ and slightly varies around it. As for the dynamics of Z_p^+, the coupling (the last rhs term of equation 2.13) somewhat modifies its dynamics in the vicinity of $\tau \simeq \tau^*$, where Z_p^- is already large and χ_p is not small too (while at $\tau \gg \tau^*,\ \chi_p \to 0$).

Figure 2.4 shows that, starting with a purely unidirectional P-AW harmonic, $Z_p^-(0) = 0$, the perturbation energy increases and reaches a peak value at time $\tau \simeq \tau^*$. After that, the harmonic undergoes nearly periodic and damping oscillations around some plateau value of the energy. This plateau value increases with decreasing Ω_A.

Figure 2.5 shows that the imbalance degree of the P-AW harmonic decreases with time (with the increase of the amplitudes), i.e., the energy propagating opposite to the X-axis approaches the energy propagating along

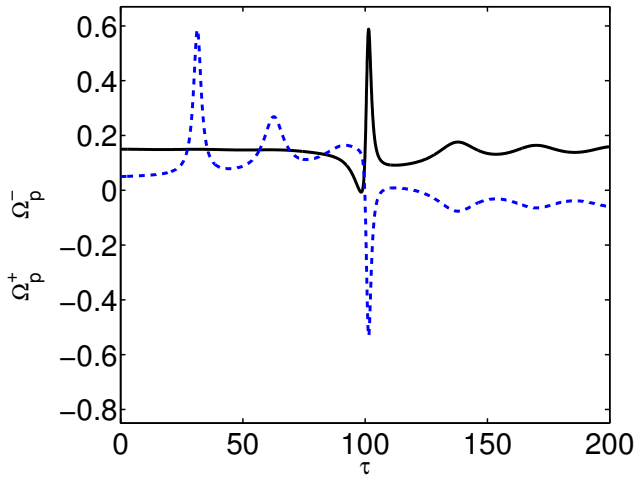

Figure 2.3: Instantaneous frequencies Ω_p^+ (solid black) and Ω_p^- (dashed blue) vs time for the same parameters as in figure 2.1.

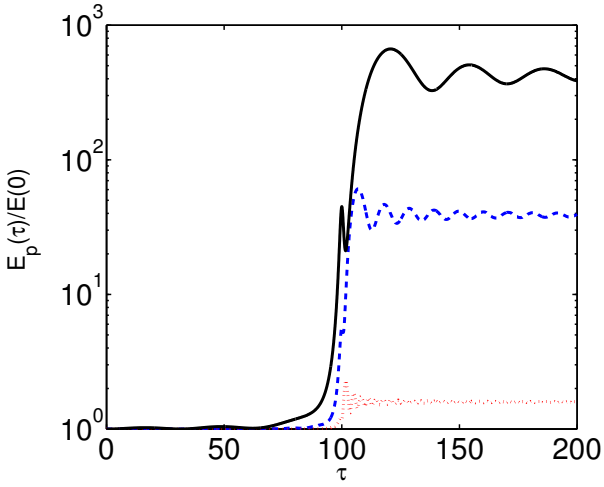

Figure 2.4: Normalized spectral energy of P-AWs, $E_p(\tau)/E(0)$, vs time in log-linear scaling for the same parameters as in figure 2.1, but at $\Omega_A = 0.1$ (solid black), $\Omega_A = 0.3$ (dashed blue) and $\Omega_A = 1$ (dotted red).

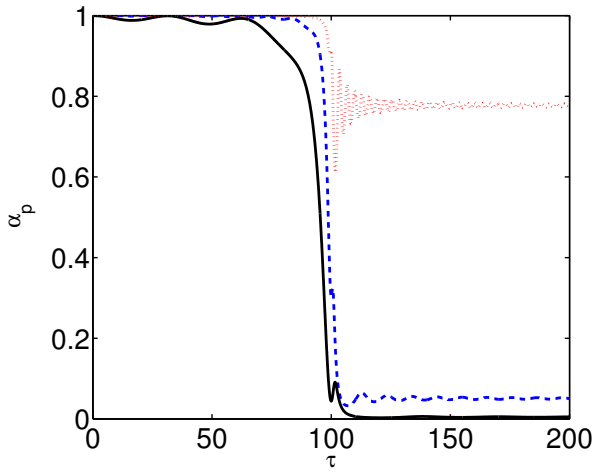

Figure 2.5: The imbalance degree of P-AWs, $\alpha_p = 1 - |Z_p^-|^2|Z_p^+|^2$, vs time for the same parameters as in figure 2.1, but at $\Omega_A = 0.1$ (solid black), $\Omega_A = 0.3$ (dashed blue) and $\Omega_A = 1$ (dotted red).

the X-axis: for the case of $\Omega_A = 1$, the harmonic remains imbalanced, for the case of $\Omega_A = 0.3$ the imbalance degree tends to 0.05, and for the case of $\Omega_A = 0.1$, in fact, the harmonic becomes balanced with time.

When initially counter-propagating P-AW harmonics with equal amplitudes but different phases ($Z_p^+(0) = 1$ and $Z_p^-(0) = 1, i, -1$) are inserted, the dynamics is simpler. Amplitudes of the physical variables are equal to each other, $Z_p^+(\tau) = Z_p^-(\tau)$, according to equation (2.22), i.e., they are balanced from the beginning and their phase dynamics is quite trivial.

Figure 2.6 shows that the transient growth of perturbation energy is smaller in the case of initially imposed unidirectional P-AW harmonic than that in the case when equal amplitude counter-propagating P-AW harmonics are imposed. And, in the latter cases, the energy growth is maximum if the

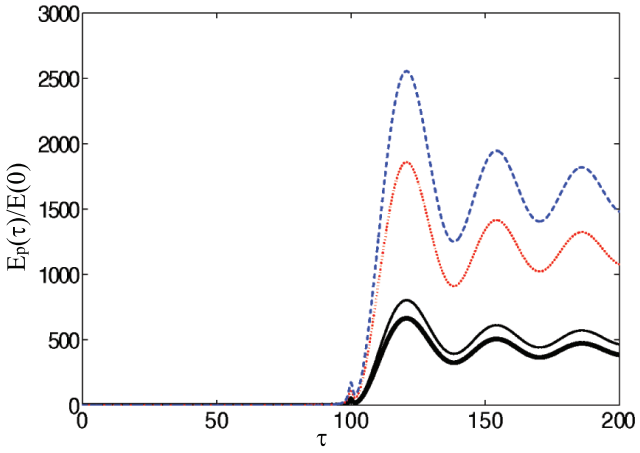

Figure 2.6: Normalized spectral energy of P-AWs, $E_p(\tau)/E(0)$, vs time in two-dimensional case ($k_z = 0$, $Z_s^{\pm} = 0$) at: $\Omega_A = 0.1$, $k_y(0)/k_x = 100$, $Z_p^+(0) = 1$ and $Z_p^-(0) = 0$ (thick solid black), $Z_p^-(0) = 1$ (solid black), $Z_p^-(0) = i$ (dashed blue), $Z_p^-(0) = -1$ (dotted red).

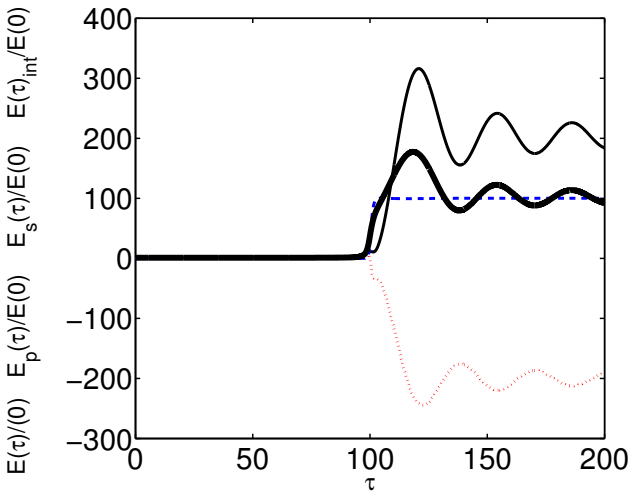

Figure 2.7: Normalized spectral energies: $E(\tau)/E(0)$ (thick solid black), $E_p(\tau)/E(0)$ (solid black), $E_s(\tau)/E(0)$ (dashed blue) and $E_{int}(\tau)/E(0)$ (dotted red) vs time at: $Z_p^+(0) = 1$, $Z_p^-(0) = 0$, $Z_s^{\pm}(0) = 0$, $\Omega_A = 0.1$, $k_y(0)/k_x = 100$ and $k_z/k_x = 1$.

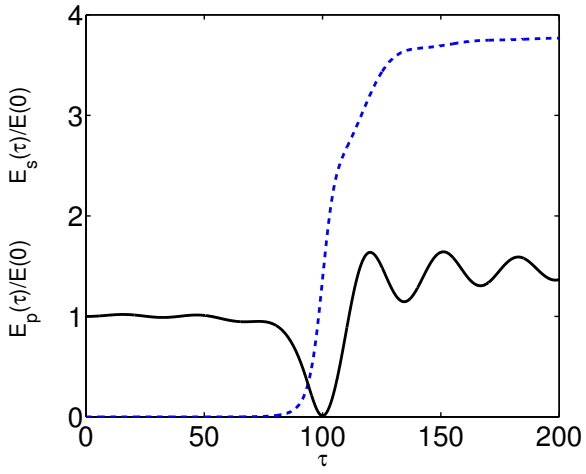

Figure 2.8: Normalized spectral energies of P-AWs and S-AWs, $E_p(\tau)/E(0)$ (solid black) and $E_s(\tau)/E(0)$ (dashed blue), vs time for the same parameters as in figure 2.7, but at $k_z/k_x = 10$.

phases of the inserted harmonics differ from each other by $\pi/2$ $(Z_p^+(0) = 1$ and $Z_p^-(0) = i)$.

2.3.2 Three-dimensional case

Figures 2.7-2.11 correspond to 3D cases when initially just unidirectional P-AW harmonic is imposed in the flow. Figures 2.12 and 2.13 – when initially counter-propagating P-AW harmonics are inserted with equal amplitudes but different phases.

In the 3D case, S-AWs become an active participant in the dynamics, however, the growth of P-AWs remains somewhat larger than the growth of S-AWs. Figure 2.7 shows the prevalence of P-AWs for $k_z/k_x = 1$. (It is natural that this prevalence is more pronounced for $k_z/k_x \ll 1$.) The transient growth

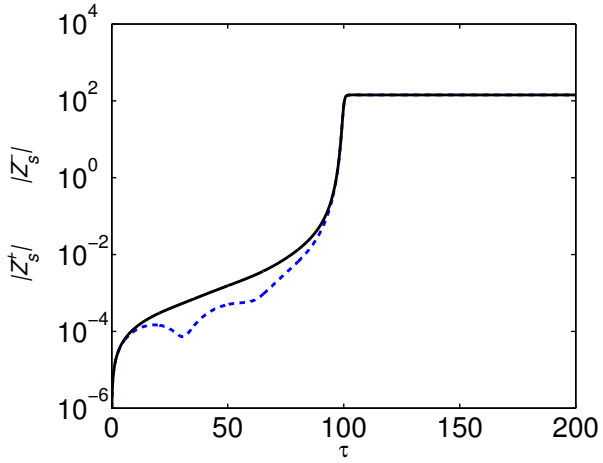

Figure 2.9: $|Z_s^+|$ (solid black) and $|Z_s^-|$ (dashed blue) vs time in log-linear scaling for the same parameters as in figure 2.7.

of both waves substantially reduces with the further increase of the ratio k_z/k_x (see figure 2.8) and, consequently, SFHs with $k_z/k_x \gg 1$ do not play any role in the dynamical processes.

In figure 2.9 we present the dynamics of $|Z_s^+|$ (solid black) and $|Z_s^-|$ (dashed blue) vs time in log-linear scaling for a small value of Ω_A ($\Omega_A = 0.1$) and $k_z/k_x = 1$ when, only $Z_p^+(0)$ is inserted in the flow (i.e., $Z_p^-(0), Z_s^\pm(0) = 0$). In the beginning, $|Z_s^+|$ increases stronger than $|Z_s^-|$. However, in the course of the evolution, $|Z_s^-|$ becomes almost equal to $|Z_s^+|$. Figure 2.10 shows that with increase of the amplitudes, the imbalance degree of the S-AWs decreases with time for small Ω_A as it is for P-AWs (compare figures 2.5 and 2.10). S-AWs are imbalanced already at $\Omega_A \simeq 1$. However, the growth of S-AWs is negligible in the last case.

Figure 2.11 shows that, the growth of the total spectral energy is max-

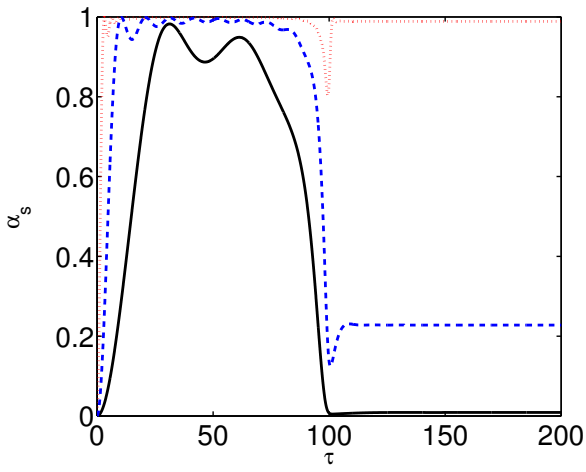

Figure 2.10: The imbalance degree of S-AWs, $\alpha_s = 1 - |Z_s^-|^2/|Z_s^+|^2$, vs time in log-linear scaling for the same parameters as in figure 2.7, but at $\Omega_A = 0.1$ (solid black), $\Omega_A = 0.3$ (dashed blue) and $\Omega_A = 1$ (dotted red).

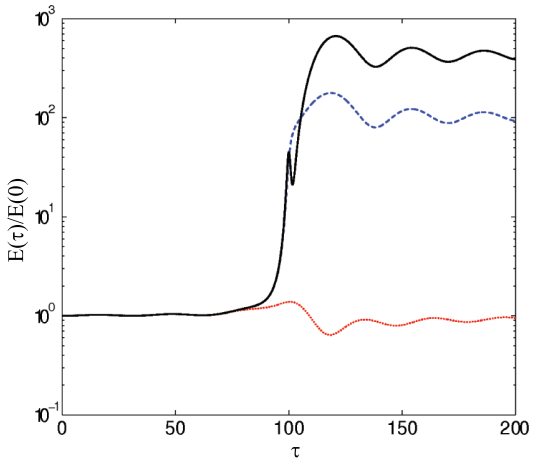

Figure 2.11: Normalized spectral energy, $E(\tau)/E(0)$, vs time in log-linear scaling for 2D and 3D cases for the same parameters as in figure 2.7, but at $k_z/k_x = 0$ (solid), $k_z/k_x = 1$ (dashed) and $k_z/k_x = 10$ (dotted).

imal for 2D case and decreases with the increase of k_z/k_x. This result is somewhat unexpected/surprising, because in non-magnetized flows (i.e., in the simplest incompressible hydrodynamic constant shear flow) the transient growth of three-dimensional perturbations is generally stronger than transient growth of two-dimensional ones (e.g., see Chagelishvili et al., 1996; Moffatt, 1967; Farrell & Ioannou, 1993a; Bakas et al., 2001) and the dynamics of a non-magnetized system is determined by three-dimensional perturbations.

Figures 2.12 and 2.13 show that the energy growth is maximal if the phases of inserted SFHs differ from each other by $\pi/2$ (as in the 2D case). These figures also coincide with 2.7 for cases when phases of the initially inserted SFHs differ from each other – the transient growth of P-AW always prevails over the growth of S-AW. All energy dynamics plots (see figures 2.4,2.6,2.7,2.11-2.13) show that real transient growth takes place in the vicinity of $\tau \simeq \tau^*$ during the time interval $|\tau - \tau^*| \leq \Omega_A^{-1}$.

2.4 Summary and discussion

The proposed formalism provides a deeper insight into the physical mechanism underlying the overreflection phenomenon by allowing us to separate from each other physical processes associated with counter-propagating waves and to follow their interaction during the overreflection. Based on the presented analysis, the path to the overreflection is as follows. Initially an imposed on the shear flow pure Z_p^+ generates Z_p^- due to the shear-induced linear coupling, that at first propagates in the same direction as Z_p^+. With time, Z_p^-

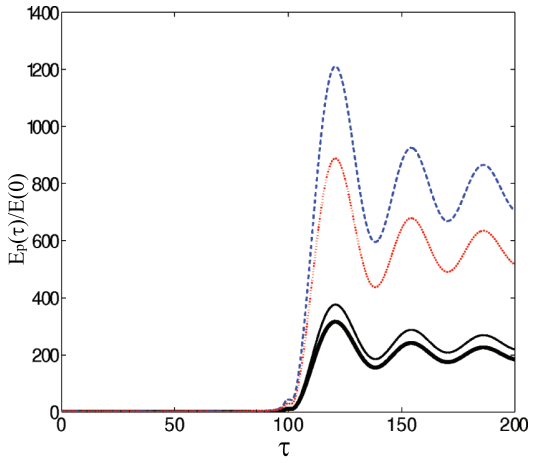

Figure 2.12: Normalized spectral energy of P-AWs, $E_p(\tau)/E(0)$, vs time at: $\Omega_A = 0.1$, $k_y(0)/k_x = 100$, $k_z/k_x = 1$, $Z_s^{\pm}(0) = 0$, $Z_p^{+}(0) = 1$ and $Z_p^{-}(0) = 0$ (thick solid black), $Z_p^{-}(0) = 1$ (solid black), $Z_p^{-}(0) = i$ (dashed blue), $Z_p^{-}(0) = -1$ (dotted red).

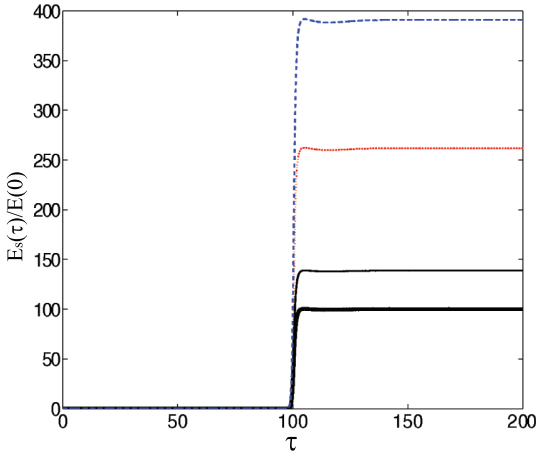

Figure 2.13: Normalized spectral energy of S-AWs, $E_s(\tau)/E(0)$, vs time at: $\Omega_A = 0.1$, $k_y(0)/k_x = 100$, $k_z/k_x = 1$, $Z_s^{\pm}(0) = 0$, $Z_p^{+}(0) = 1$ and $Z_p^{-}(0) = 0$ (thick solid black), $Z_p^{-}(0) = 1$ (solid black), $Z_p^{-}(0) = i$ (dashed blue), $Z_p^{-}(0) = -1$ (dotted red).

grows transiently and in the vicinity of $\tau \simeq \tau^*$ (at which $k_y(\tau^*) = 0$) reverses the direction of propagation and becomes counter-propagating to Z_p^+. Both counter-propagating P-AWs SFHs exhibit transient growth that is appreciable at $\Omega_A < 1$, $k_z/k_x \leq 1$ and $k_y(0)/k_x \gg 1$. As for S-AWs, its transient growth occurs due to the linear coupling of P-AW and S-AW, i.e. – is an indirect consequence of P-AW (i.e. Z_p^+ and Z_p^-) growth. At the same time, the growth of P-AWs somewhat prevails over the growth of S-AWs. It is obvious, that the dynamics has transient nature, as it should be – shear flow non-normality induced energy exchange processes are always transient (e.g., see Schmid, 2007). This statement is correct for constant in time shear flows. However, in periodic shear flows (i.e., when shear parameter is a periodic function of time), wave perturbations may grow exponentially in time. For instance, Zaqarashvili (2000); Zaqarashvili & Roberts (2002) studied the stability of periodic MHD shear flows, showing that the temporal behaviour of spatial Fourier harmonics of magnetosonic waves is governed by Mathieu's equation. Consequently, the harmonics with the half frequency of the shear flow grow exponentially in time. Mathieu's equation represent a single second order ordinary differential (wave) equation and describes counter-propagating waves of a single/physical variable. Consequently, possible dynamical processes between these waves (e.g., their coupling) are, in fact, left out of consideration. To get an additional information about the physics of the growth (e.g., to grasp the coupling between counter-propagating waves) one has to find "eigen-variable" for each wave component and, by this way, reduce Mathieu's equation to the set of first

order differential equations for individual counter-propagating wave (as it is done for the constant shear flows).

Evaluating the linear transient dynamics we use the concept of energy. Of course, when calculating energy - the quantity of the second order in the wave amplitude - causes dissatisfaction associated with the known fact: it is obviously necessary to take into account changes in the mean parameters of the environment and, in particular, the wave-induced flow (Stepanyants & Fabrikant, 1989). In this case, there is an ambiguous field separation of the physical variables in the wave field and the medium field. These issues are rather complicated and analysis continues to this day. For example, in the MHD context, theory for the wave and background stress energy tensors is developed based on the exact Lagrangian map in Webb et al. (2005). We do not go into this debate, but, only aim to get a feeling of the dynamics of quadratic forms of physical variables. Therefore, we introduced the concept of energy in solving the linearized problems as it is usually accepted in hydrodynamic and magnetodynamic flow studies (Stepanyants & Fabrikant, 1989).

Maximal transient growth (and overreflection) of the wave energy occurs in the 2D limit (at $k_z = 0$). Consequently, the dynamics of the MHD flow should be defined mainly by SFHs with $k_z/k_x \ll 1$. At the same time, the transient growth of the both, P- and S-Alfvén wave modes increases with decreasing Ω_A. If initially only unidirectional P-AW harmonic is imposed in the flow, the imbalance degree decreases with the decrease of Ω_A and the waves become already balanced at $\Omega_A = 0.1$. If initially counter-propagating P-AW

harmonics with equal amplitudes are imposed, they maintain the balance irrespective of the initial phase. Because of the condition $\Omega_A \sim k_x$, SFHs having smaller k_x exhibit stronger growth. Finally, one can conclude, that the dynamical processes should be defined by waves having small k_x and k_z, i.e. long streamwise and spanwise wavelengthes, $\lambda_x, \lambda_z \gg V_A/S$.

2.4.1 Impact of the transient growth on the character of nonlinear cascade processes

The described linear dynamics is expected to have significant nonlinear consequences. The point is that the linear transient processes are mainly defined by coefficients χ_p of equations (2.13) and (2.14). The coefficients introduce dependency of the transient growth on the ratio $k_x k_y(\tau)/k^2(\tau)$. Consequently, the transient growth depends not on the value but on the orientation of wavevector and takes place when $|\chi_p(\tau)| \geq \Omega_A$, i.e. when $|k_y(\tau)/k_x| \leq \Omega_A^{-1}$. As it is outlined at the end of the previous section, this happens in the vicinity of $\tau \simeq \tau^*$ during the time interval $|\tau - \tau^*| \leq \Omega_A^{-1}$ (see figures 2.4,2.6,2.7,2.11-2.13). It is obvious, that the linear transient processes are highly anisotropic in wavenumber plane. A similar anisotropy exists in hydrodynamic shear flows Horton et al. (see for details 2010). The anisotropy changes classical view on the nonlinear cascade processes: classically, the net action of nonlinear (turbulent) processes is interpreted as either a direct or inverse cascade. However, as it is shown in Horton et al. (2010), in hydrodynamic nonuniform/shear flows, the dominant process is a nonlinear redistribution over wavevector angles of perturbation spatial Fourier harmonics. This anisotropic transfers of spec-

tral energy in the wavenumber space has been coined as *nonlinear transverse cascade*.

Nonlinear transverse cascade redistributes perturbation harmonics over different quadrants of the wavenumber plane (e.g., from quadrants where $k_x k_y > 0$ to quadrants where $k_x k_y < 0$ or vice versa) and the interplay of this nonlinear redistribution with linear phenomena (transient growth) becomes intricate: it can realize either positive or negative feedback. In the case of positive feedback, the nonlinearity repopulates transiently growing perturbations and contributes to the self-sustenance of perturbations. Consequently, nonlinear transverse cascade naturally appears as a possible cornerstone of the bypass scenario of turbulence.

The similarity of the anisotropy of the transient growth in the hydrodynamic and our MHD cases hints at the similarity of nonlinear processes. In other words, the transverse cascade should also be inherent to MHD shear flows. Therefore, the conventional characterization of MHD turbulence in terms of direct and inverse cascades, which ignores the transverse cascade, can be misleading for MHD shear flow turbulence. In principal, the nonlinear transverse cascade can repopulate the transiently growing wave SFHs in a MHD shear flow and can acquire a vital role of ensuring the self-sustenance of the waves. To verify these, consistent with the bypass concept, processes in MHD shear flows, (Mamatsashvili et al., 2014) is already simulated nonlinear dynamics of the considered here flow system in 2D limit . The performed direct numerical simulations show the existence of subcritical transition to

turbulence even in the 2D case, i.e., show the vitality of the *bypass transition to turbulence* for the simplest (spectrally stable) plane MHD flow. The minimal/critical Reynolds number of the subcritical transition turned out to be about 5000, i.e. larger than for the hydrodynamic Couette flow, where $Re_{cr} \sim 350$. At the same time, in the hydrodynamic case, the transition occurs just in the 3D case, while in the simplest MHD flow, the subcritical transition and self-sustenance of turbulence occurs in the 2D case too.

Discussing the character of nonlinear cascade processes, finally, one has to present the generalizing view.

MHD turbulence phenomenon is ubiquitous in nature and is very important in engineering/industrial applications. So, it is natural that there is an enormous amount of research devoted to it, starting with seminal papers Iroshnikov (1963) and Kraichnan (1965) and their extensions Goldreich & Sridhar (1995); Boldyrev (2005). To date, the main trends, including cases of forced, freely decaying and with background magnetic field MHD turbulence, established over decades are thoroughly analyzed in a number of review articles and books (see e.g., Biskamp, 2003; Mininni, 2011; Brandenburg & Lazarian, 2013). Most of such an analysis commonly focuses on turbulence dynamics in wavenumber/Fourier space. However, the case of MHD turbulence in smooth shear flows involves fundamental novelties: the energy-supplying process for turbulence is the flow nonnormality induced linear transient growth. The latter *anisotropically injects energy into turbulence over a broad range of lengthscales*, consequently, rules out the inertial range of the activity of nonlin-

earity and leads to complex/refined interplay of linear and nonlinear processes (Mamatsashvili et al., 2014). These circumstances give rise to new type of processes in the turbulence dynamics that are not accounted for in the main trends of MHD turbulence research.

The essence of the view is the following: anisotropic linear processes lead to anisotropy of nonlinear processes. Specifically, the nonlinear transverse cascade (that is anisotropic by definition) is the result of only *anisotropic* linear coupling/reflection. For instance, there is a number of papers addressing linear wave reflection that is caused by parallel gradients of density/magnetic field (e.g., Velli et al., 1989; Matthaeus et al., 1999; Dmitruk et al., 2002; Verdini et al., 2012; Perez & Chandran, 2013). However, this kind of reflection, due to the absence of the above noted anisotropy in wavenumber space, should not lead to the nonlinear transverse cascade. A flow configuration, similar to our magnetized shear flow, is considered by Hollweg et al. (2013), addressing the wave reflection. The difference is in the value of beta parameter – we consider incompressible waves in high-beta plasma, while, that paper considers compressible waves in low-beta plasma. The participants of the linear dynamics are different, however, in the both cases, transient liner processes/coupling/growth are anisotropic. Consequently, the nonlinear transverse cascade should also be important for the range of parameters considered in Hollweg et al. (2013).

2.4.2 On application of the proposed approach of the overreflection to more complex shear flow systems

Finally, we would like to stress that the present scenario and mathematical formalism of the overreflection phenomenon is easily applicable to more complex shear flow systems, including widely discussed cases of overreflection of spiral-density waves in astrophysical discs and of internal-gravity waves in stably stratified atmospheres. The proposed approach describes each (counter-propagating) wave component by its generalized eigen variable. In the considered here MHD flow, fortunately, one can use Elsässer variables (see equation 2.12) or its renormalized version (see equation 2.23) as the generalized eigen variables. This fact has actually simplified our analysis. As for more complex shear flow systems, there appears to be some difficulty in finding generalized eigen variable and construction of fist order differential equations for each counter-propagating wave. The difficulty is due to the fact that in complex flow systems "nominal frequency" may depend on the varying/shearwise wavenumber and, consequently, on time (e.g., as the "nominal frequency" of internal-gravity waves), while in our case considered here Alfvén waves, the "nominal frequency" (Alfvén frequency) does not depend on the shearwise wavenumber and is constant. However, this is not a fundamental difficulty – it requires just a bit of complicated calculations and gives somewhat bulky coefficients in dynamical equations. So, to apply the proposed mathematical approach, one has to find eigen variables of the waves in the shearless limit, then generalize these eigen variables for the non-zero shear case and write

dynamic equations for them. This procedure gives the corresponding set of easily foreseeable, *coupled* first order ordinary differential equations for each counter-propagating wave.

Chapter 3

Nonlinear transverse cascade and two-dimensional magnetohydrodynamic subcritical turbulence in plane shear flows

3.1 Introduction

The problem of the onset and self-sustenance of turbulence in spectrally stable nonuniform flows is a challenge to fluid dynamics research. The efforts in this direction significantly increased in the 1990s with the understanding and rigorous description of the nonnormal nature of nonuniform, or shear flows (see e.g., Refs. Reddy et al. (1993); Trefethen et al. (1993); Schmid & Henningson (2001); Criminale et al. (2003); Schmid (2007)) and its direct consequences, such as the possibility of finite-time, or transient growth of perturbations in spectrally stable shear flows (e.g., Refs. Gustavsson (1991); Farrell & Ioannou (1993a); Reddy & Henningson (1993); Farrell & Ioannou (2000)). Classical (direct and inverse) nonlinear cascade processes, even if anisotropic, are in fact unable to provide self-sustenance of perturbations (turbulence) when transiently (non-exponentially) growing modes are present in the flow. In the case of a specific shear flow, however, turbulence can self-organize and be self-sustained through the refined interplay of the linear transient and nonlinear processes, where the flow shear acts, through the Reynolds stress, to contin-

uously supply the turbulence with energy thanks to an essential constructive feedback provided by the nonlinear processes Gebhardt & Grossmann (1994); Henningson & Reddy (1994); Baggett et al. (1995); Grossmann (2000); Chapman (2002); Eckhardt et al. (2007).

The direct (nonlinear) cascade – a central process in Kolmogorov's phenomenology – is a consequence of the existence of the so-called inertial range in spectral (Fourier, or wavenumber) space, which is free from the action of linear energy-exchange processes and, in fact, occupied by nonlinear transfers. Kolmogorov's classical theory of forced turbulence in hydrodynamics (HD) is the following: large scale (long wavelength) perturbations imposed on the flow are transferred by a direct nonlinear cascade, through the inertial range, to short wavelengths and, ultimately, to the dissipation region. So, the direct cascade, together with linear instability and dissipative phenomena, constitute the well-known scheme of forced turbulence in HD. However, in spectrally stable shear flows, where transient growth of perturbations is the only possibility, the balance of processes leading to the self-sustenance of turbulence should be completely different. The shear-induced transient growth mainly depends on the orientation (and, to a lesser degree, on the value) of the perturbation wavevector: the spatial Fourier harmonics of perturbations (SFHs) having a certain orientation of the wavevector with respect to the shear flow, can draw flow energy and get amplified, whereas harmonics having another orientation of the wavevector give energy back to the flow and decay. In other words, the linear energy-exchange processes are strongly anisotropic in

wavenumber **k**-space and occur over a broad range of wavenumbers without leaving a free room (i.e., inertial range) for the action of nonlinear processes only. This might render Kolmogorov's phenomenology inapplicable to spectrally stable shear flows. A strong anisotropy of the linear processes in shear flows, in turn, leads to anisotropy of nonlinear processes in **k**-space. In this case, as revealed in Ref. Horton et al. (2010), even in the simplest HD shear flow with linear shear, the dominant nonlinear process turns out to be not a direct, but a *transverse cascade*, that is, a transverse (angular) redistribution of perturbation harmonics over different quadrants of wavenumber plane (e.g., from quadrants where $k_x k_y > 0$ to quadrants where $k_x k_y < 0$ or vice versa). The interplay of this nonlinear redistribution with linear phenomena (transient growth) becomes intricate: it can provide either positive or negative feedback. In the case of positive feedback, the nonlinearity repopulates transiently growing modes and contributes to the self-sustenance of perturbations. This combined action of anisotropic linear and nonlinear processes can, in turn, give rise to an anisotropic energy spectrum, which, in general, is expected to differ from the Kolmogorovian. As a result, the transverse cascade may naturally appear to be a possible keystone of the *bypass* concept of subcritical turbulence in spectrally stable hydrodynamic shear flows.

In this Chapter (related to (Mamatsashvili et al., 2014)), is extended the above study of nonlinear processes in HD flows to magnetohydrodynamic (MHD) flows and investigate subcritical turbulence in the simplest, spectrally stable shear flow of magnetized plasma. We present the results of direct nu-

merical simulations (DNS) in Fourier plane, demonstrating the dominance of the transverse cascade in MHD shear flows too. Specifically, we consider the dynamics of two-dimensional (2D, with zero spanwise wavenumber, $k_z = 0$) perturbations in unbounded incompressible MHD fluid flow with linear shear of velocity threaded by a uniform background magnetic field directed parallel to the flow. This flow configuration is spectrally stable in the linear regime Stern (1963); Ogilvie & Pringle (1996) and therefore should be dominated by the above-mentioned shear-induced transient phenomena Chagelishvili et al. (1997). Our main goals are:

(i) to examine subcritical transition to turbulence and subsequent self-sustaining dynamics by DNS,

(ii) to describe the general behavior of nonlinear processes (transfers) – transverse cascade – in the presence of shear by carrying out an analysis of these processes in Fourier plane,

(iii) to show that the nonlinear transverse cascade is a keystone of self-sustaining dynamics of the turbulence in this simple open MHD flow system.

The last point will allow us to find out in what form the *bypass* concept of subcritical turbulence can be realized in spectrally stable MHD shear flows.

MHD turbulence phenomenon is ubiquitous in nature and is very important in engineering applications. So, it is natural that there is an enormous amount of research devoted to it, starting with seminal papers Iroshnikov (1963) and Kraichnan (1965) and their extensions Goldreich & Sridhar (1995);

Boldyrev (2005). To date, the main trends, including cases of forced and freely decaying MHD turbulence as well as MHD turbulence with a background magnetic field, established over decades have been thoroughly analyzed in a number of review articles and books (see e.g., Refs. Biskamp (2003); Mininni (2011); Brandenburg & Lazarian (2013) and references therein). Most of these analyses commonly focus on turbulence dynamics in wavenumber space. However, the case of MHD turbulence in smooth shear flows that we study here involves fundamental novelties: an energy-supplying process for turbulence is the flow nonnormality induced linear transient growth. The latter anisotropically injects energy into turbulence over a broad range of lengthscales and, consequently, rules out the inertial range of the sole activity of nonlinearity and leads to a complex/refined interplay of linear and nonlinear processes. These circumstances give rise to new type of processes in turbulence dynamics that are not accounted for in the main trends of MHD turbulence research.

Magnetized shear flows have been considered in a number of papers Kim (2006); Douglas et al. (2008); Newton & Kim (2009). However, the range of target parameters adopted in these studies excludes transient growth effects due to shear and novelties associated with it. So, these investigations still belong to the existing trends of MHD turbulence research. For instance, these studies consider the limit of a strong background magnetic field, $\mathbf{B_0}$, along the flow, where the Alfvén frequency of modes with wavenumber $\mathbf{k}$, $\omega_A = \mathbf{k} \cdot \mathbf{B}_0/(4\pi\rho_0)^{1/2}$ (ρ_0 is the equilibrium density), is larger than shear rate of the mean flow and since transient phenomena responsible for energy

injection from shear flow into perturbation harmonics are inefficient in this case, external forcing (peaked at certain wavenumbers) is included to drive turbulence. In contrast to this, in our case, the magnetic field is weak and the adopted parameters permit an effective transient exchange of energy between the mean flow and the perturbation harmonics; this actually should serve to drive turbulence without any external forcing. In this regard, in Refs. Hawley et al. (1995); Fromang & Papaloizou (2007); Guan et al. (2009); Simon & Hawley (2009); Lesur & Longaretti (2011), the dynamics of MHD turbulence is investigated in a somewhat similar setup – astrophysical (protoplanetary) disk flows with Keplerian shear and an imposed large-scale magnetic field which is typically weak (i.e., usual plasma $\beta \gg 1$ in disks, see e.g. Ref. Armitage (2011)). This means that there exists harmonics whose Alfvén frequency is smaller than shear parameter, as in our case. However, in Refs. Fromang & Papaloizou (2007); Lesur & Longaretti (2011), although turbulence dynamics is analyzed in Fourier space, the magnetic field is directed perpendicular to the flow and consequently shear-induced transient phenomena differ from those studied here. On the other hand, Refs. Hawley et al. (1995); Guan et al. (2009); Simon & Hawley (2009) similarly to our study, consider orientation for the magnetic field along the mean flow (i.e., azimuthal for disk flows). They observe three-dimensional (3D) self-sustained turbulence, which is expected to be governed by transient processes of a type similar to those of the 2D shear turbulence studied here, but since the turbulence dynamics (energy injection and transfers) was not investigated in spectral space in those studies,

identification of shear-induced effects is not straightforward in their analysis.

The Earth's magnetosphere, created by the interaction of the solar wind with the Earth's magnetic field, represents a huge "laboratory" of various MHD turbulence. In different parts of this laboratory (e.g., ion foreshock, magnetosheath, LL magnetopause, polar cusps, ionosphere, magnetotail) characteristic parameters vary greatly from each other. There are shear flows, different orientations of the magnetic field, different values of the plasma β parameter, anisotropic magnetic pressure, magnetic reconnection, etc. (see e.g., Ref. Zimbardo et al. (2010) for a recent review). Evidently, it is hard to seek an immediate realization of the proposed scheme of MHD shear turbulence in the magnetized environment of the Earth. Still, certain areas can be identified where a similar configuration and course of events are realized. This, first of all, implies high-β regions with shear flows and a mean magnetic field parallel to the flow velocity. Generally, such regions are in the magnetotail, magnetosheath and cusp, but a definite view can be obtained after a detailed investigation of the dynamical processes therein.

The specific nature of nonlinear processes, which we will focus on in our study is, in many respects, a consequence of the shear-induced transient linear dynamics described in Refs. Balbus & Hawley (1992); Chagelishvili et al. (1997); Dimitrov et al. (2011); Gogichaishvili et al. (2014). We particularly follow Chapter 2, where the linear dynamics of pseudo-Alfvén waves (P-AWs) and shear-Alfvén waves (S-AWs) is described in a 3D MHD flow with linear shear and parallel magnetic field. Specifically, it is shown there that:

1. Counter-propagating P-AWs are coupled to each other, while S-AWs are not coupled with each other, but are asymmetrically coupled to P-AWs; S-AWs do not participate in the linear dynamics of P-AWs,

2. The linear coupling of counter-propagating waves determines the transient growth (overreflection).

3. The transient growth of S-AWs is somewhat smaller compared with that of P-AWs,

4. Waves with a smaller streamwise wavenumber, k_y, exhibit stronger transient growth,

5. Maximal transient growth (and overreflection) of the wave energy occurs for 2D waves with $k_z = 0$.

These preliminary linear results served as a natural starting point of the present study of nonlinear dynamics of 2D perturbations with $k_z = 0$ and white-noise initial spectrum in $\mathbf{k}$-plane using DNS with a spectral code.

This Chapter is organized as follows. Section 3.2 is devoted to the physical model and derivation of dynamical equations in spectral plane. The DNS of the turbulence dynamics is presented in Section 3.3 In Section 3.4, we perform analysis of the numerical results focusing on the activity of linear and nonlinear processes in spectral plane. A summary and discussion are given in Section 3.5.

3.2 Physical model and equations

The motion of an incompressible conducting fluid with constant viscosity, ν, and Ohmic resistivity, η, is governed by the basic equations of MHD

$$\frac{\partial \mathbf{U}}{\partial t} + (\mathbf{U} \cdot \nabla)\,\mathbf{U} = -\frac{\nabla P}{\rho} + \frac{(\mathbf{B} \cdot \nabla)\,\mathbf{B}}{4\pi\rho} + \nu\nabla^2\mathbf{U}, \tag{3.1}$$

$$\frac{\partial \mathbf{B}}{\partial t} = \nabla \times (\mathbf{U} \times \mathbf{B}) + \eta\nabla^2\mathbf{B}, \tag{3.2}$$

$$\nabla \cdot \mathbf{U} = 0, \tag{3.3}$$

$$\nabla \cdot \mathbf{B} = 0, \tag{3.4}$$

where ρ is the fluid density, $\mathbf{U}$ is the velocity, $\mathbf{B}$ is the magnetic field and P is the total pressure equal to the sum of the thermal and magnetic pressures.

Equations (3.1)-(3.4) have a stationary equilibrium solution – an unbounded plane Couette flow along the $y-$axis with linear shear of velocity in the the x-direction, $\mathbf{U}_0 = (0, -Sx, 0)$, and threaded by a uniform background magnetic field parallel to the flow, $\mathbf{B}_0 = (0, B_{0y}, 0)$. Without loss of generality, the constant shear parameter S and B_{0y} are chosen to be positive, $S, B_{0y} > 0$. The equilibrium density ρ_0 and total pressure P_0 are spatially constant. Such a simple configuration of an unbounded flow with a linear shear of the velocity profile corresponds, for example, to plasma flow in astrophysical accretion disks in the framework of the widely used local shearing box approximation (e.g., Ref. Hawley et al. (1995)) as well as to flows of magnetized plasma in the laboratory (e.g., Refs. Kim (2006); Douglas et al. (2008)). It allows us to

grasp key effects of shear on the perturbation dynamics and, ultimately, on the resulting MHD turbulent state in kinematically nonuniform plasma flows.

Consider 2D perturbations of the velocity, total pressure and magnetic field, $\mathbf{u}, p$ and $\mathbf{b}$, which are independent of the vertical z-coordinate ($\partial/\partial z = 0$), about the equilibrium. In this case, the evolution in the horizontal $(x, y)-$plane is decoupled from that of the $z-$components of the perturbed velocity and magnetic field, so we set them to zero, $u_z = b_z = 0$. Representing the total fields as the sum of the equilibrium and perturbed values, $\mathbf{U} = \mathbf{U}_0 + \mathbf{u}, P = P_0 + p$ and $\mathbf{B} = \mathbf{B}_0 + \mathbf{b}$, substituting these into Eqs. (3.1)-(3.4) and rearranging the nonlinear terms with the help of Eqs. (3.3) and (3.4), we arrive at the following system governing the dynamics of perturbations with arbitrary amplitude

$$\left(\frac{\partial}{\partial t} - Sx\frac{\partial}{\partial y}\right) u_x = -\frac{1}{\rho_0}\frac{\partial p}{\partial x} + \frac{B_{0y}}{4\pi\rho_0}\frac{\partial b_x}{\partial y} + \nu\nabla^2 u_x + \\ + \frac{\partial}{\partial y}\left(\frac{b_x b_y}{4\pi\rho_0} - u_x u_y\right) + \frac{\partial}{\partial x}\left(\frac{b_x^2}{4\pi\rho_0} - u_x^2\right), \quad (3.5)$$

$$\left(\frac{\partial}{\partial t} - Sx\frac{\partial}{\partial y}\right) u_y = Su_x - \frac{1}{\rho_0}\frac{\partial p}{\partial y} + \frac{B_{0y}}{4\pi\rho_0}\frac{\partial b_y}{\partial y} + \nu\nabla^2 u_y + \\ + \frac{\partial}{\partial x}\left(\frac{b_x b_y}{4\pi\rho_0} - u_x u_y\right) + \frac{\partial}{\partial y}\left(\frac{b_y^2}{4\pi\rho_0} - u_y^2\right), \quad (3.6)$$

$$\left(\frac{\partial}{\partial t} - Sx\frac{\partial}{\partial y}\right) b_x = B_{0y}\frac{\partial u_x}{\partial y} + \eta\nabla^2 b_x + \frac{\partial}{\partial y}(u_x b_y - u_y b_x), \quad (3.7)$$

$$\left(\frac{\partial}{\partial t} - Sx\frac{\partial}{\partial y}\right) b_y = -Sb_x + B_{0y}\frac{\partial u_y}{\partial y} + \eta\nabla^2 b_y - \frac{\partial}{\partial x}\left(u_x b_y - u_y b_x\right), \quad (3.8)$$

$$\frac{\partial u_x}{\partial x} + \frac{\partial u_y}{\partial y} = 0, \quad (3.9)$$

$$\frac{\partial b_x}{\partial x} + \frac{\partial b_y}{\partial y} = 0. \tag{3.10}$$

We solve Eqs. (3.5)-(3.10) in a rectangular 2D domain with sizes L_x and L_y, respectively, in the $x-$ and $y-$directions, $-L_x/2 \leq x \leq L_x/2$ and $-L_y/2 \leq y \leq L_y/2$, divided into $N_x \times N_y$ cells. Since we consider an unbounded flow with linear shear, we adopt boundary conditions commonly used in similar cases of MHD simulations of astrophysical disk flows in the local shearing box approximation (e.g., Refs. Hawley et al. (1995); Fromang & Papaloizou (2007); Guan et al. (2009); Lesur & Longaretti (2011); Davis et al. (2010)). Namely, for the perturbations of all quantities, we impose periodic boundary conditions in the $y-$direction and shearing-periodic in the $x-$direction. That is, the $x-$boundaries are initially periodic, but shear with respect to each other as time goes by, becoming again periodic at discrete moments $t_n = nL_y/SL_x$, where $n = 1, 2, ...$ is a positive integer. This can be written as

$$f(x, y, t) = f(x + L_x, y - SL_x t, t) \qquad (x \text{ boundary}),$$

$$f(x, y, t) = f(x, y + L_y, t) \qquad (y \text{ boundary}),$$

where $f \equiv (\mathbf{u}, p, \mathbf{b})$ denotes any of the perturbed quantities. These boundary conditions ensure natural evolution of shearing plane waves within the domain, as it would be in an unbounded constant shear flow.

3.2.1 Energy equation

In this subsection, we derive dynamical equations for kinetic and magnetic energies in order to gain insight into the interplay of the flow shear and

nonlinearity in the self-sustenance of perturbations. The perturbation kinetic and magnetic energies are defined, respectively, as

$$E_K = \frac{\rho_0 \mathbf{u}^2}{2}, \quad E_M = \frac{\mathbf{b}^2}{8\pi}.$$

Using the main Eqs. (3.5)-(3.10) and the above shearing box boundary conditions, after some algebra, we can readily derive the evolution equation for the domain-averaged kinetic and magnetic energies

$$\frac{d}{dt}\langle E_K \rangle = S \langle \rho_0 u_x u_y \rangle + \frac{B_{0y}}{4\pi} \left\langle u_x \frac{\partial b_x}{\partial y} + u_y \frac{\partial b_y}{\partial y} \right\rangle + \\ + \frac{1}{4\pi} \left\langle u_x b_y \frac{\partial b_x}{\partial y} + \frac{u_x}{2} \frac{\partial b_x^2}{\partial x} + \frac{u_y}{2} \frac{\partial b_y^2}{\partial y} + u_y b_x \frac{\partial b_y}{\partial x} \right\rangle - \rho_0 \nu \langle (\nabla u_x)^2 + (\nabla u_y)^2 \rangle, \tag{3.11}$$

$$\frac{d}{dt}\langle E_M \rangle = S \left\langle -\frac{b_x b_y}{4\pi} \right\rangle + \frac{B_{0y}}{4\pi} \left\langle b_x \frac{\partial u_x}{\partial y} + b_y \frac{\partial u_y}{\partial y} \right\rangle + \\ + \frac{1}{4\pi} \left\langle b_x \frac{\partial}{\partial y}(u_x b_y) + \frac{b_x^2}{2} \frac{\partial u_x}{\partial x} + \frac{b_y^2}{2} \frac{\partial u_y}{\partial y} + b_y \frac{\partial}{\partial x}(u_y b_x) \right\rangle - \frac{\eta}{4\pi} \langle (\nabla b_x)^2 + (\nabla b_y)^2 \rangle, \tag{3.12}$$

where the angle brackets denote a spatial average, $\langle ... \rangle = \int \int ... \, dxdy / L_x L_y$, with the integral being taken over an entire domain. Adding up Eqs. (3.11) and (3.12), the cross terms of linear origin, proportional to B_{0y}, and nonlinear terms cancel out due to the boundary conditions and we obtain the equation for the total energy $E = E_K + E_M$,

$$\frac{d\langle E \rangle}{dt} = S \left\langle \rho_0 u_x u_y - \frac{b_x b_y}{4\pi} \right\rangle - \rho_0 \nu \langle (\nabla u_x)^2 + (\nabla u_y)^2 \rangle - \frac{\eta}{4\pi} \langle (\nabla b_x)^2 + (\nabla b_y)^2 \rangle. \tag{3.13}$$

The first term on the right hand side of Eq. (3.13) is the shear parameter, S, multiplied by the total stress in the angle brackets. The total stress is the sum of the Reynolds, $\rho_0 u_x u_y$, and Maxwell, $-b_x b_y/4\pi$, stresses which describe, respectively, the exchange of kinetic and magnetic energies between perturbations and the background flow in Eqs. (3.11) and (3.12). Note that they originate from the linear terms proportional to shear on the right hand sides of Eqs. (3.6) and (3.8). These stresses also determine the rate of momentum transport (see e.g., Refs. Hawley et al. (1995); Balbus (2003); Douglas et al. (2008)) and thus are one of the important quantities characterizing shear flow turbulence. The second and third terms describe energy dissipation due to viscosity and resistivity, respectively. Note that the net contribution from nonlinear terms has canceled out in the total energy evolution Eq. (3.13) after averaging over the domain. Thus, only Reynolds and Maxwell stresses can supply perturbations with energy, extracting it from the mean flow due to shear; the other two terms are negative definite and dissipative. In the case of shear flow turbulence studied below, these stresses ensure energy injection into turbulent fluctuations. The nonlinear terms, not directly tapping into the shear flow energy and therefore not changing the total perturbation energy, serve only to redistribute energy gained by means of the stresses among Fourier harmonics of perturbations with different wavenumbers (see below). In the absence of shear ($S = 0$), the contribution from the Reynolds and Maxwell stresses disappears in Eq. (3.13) and hence the total perturbation energy cannot grow, gradually decaying due to viscosity and resistivity.

3.2.2 Spectral representation of the equations

Before proceeding further, we normalize the variables by taking the shear time, S^{-1}, as the unit of time, the Alfvén speed, $u_A = B_{0y}/(4\pi\rho_0)^{1/2}$, as the unit of velocity, $\ell \equiv u_A S^{-1}$ as the unit of length and B_{0y} as the unit of the magnetic field perturbations,

$$St \to t, \quad \left(\frac{x}{\ell}, \frac{y}{\ell}\right) \to (x, y), \quad \frac{\mathbf{u}}{u_A} \to \mathbf{u},$$

$$\frac{p}{\rho_0 u_A^2} \to p, \quad \frac{\mathbf{b}}{B_{0y}} \to \mathbf{b}, \quad \frac{E_{K,M}}{\rho_0 u_A^2} \to E_{K,M}.$$

Viscosity and resistivity are characterized by hydrodynamic, Re, and magnetic, Rm, Reynolds numbers defined here, for convenience, in terms of u_A and ℓ as

$$\mathrm{Re} = \frac{u_A \ell}{\nu} = \frac{u_A^2}{\nu S}, \qquad \mathrm{Rm} = \frac{u_A \ell}{\eta} = \frac{u_A^2}{\eta S}.$$

These numbers are also referred to, respectively, as viscous and resistive Elsasser numbers (e.g., Ref. Lesur & Longaretti (2011)). The strength of the imposed mean magnetic field is measured by the ratio of the mean flow kinetic energy to the magnetic energy within the domain

$$\beta = \frac{\pi \rho_0 S^2 L_x^2}{3 B_{0y}^2} = \frac{S^2 L_x^2}{12 u_A^2} = \frac{L_x^2}{12 \ell^2}.$$

For further analysis, we need to do a spectral representation of the main equations. We decompose the perturbations into spatial Fourier harmonics (SFHs)

$$f(\mathbf{r}, t) = \int \bar{f}(\mathbf{k}, t) \exp\left(\mathrm{i}\mathbf{k} \cdot \mathbf{r}\right) d^2\mathbf{k} \tag{3.14}$$

where, as before, $f \equiv (\mathbf{u}, p, \mathbf{b})$ denotes the perturbations and $\bar{f} \equiv (\bar{\mathbf{u}}, \bar{p}, \bar{\mathbf{b}})$ is their corresponding Fourier transforms ($k_z = 0$ for $z-$independent 2D perturbations and $d^2\mathbf{k} \equiv dk_x dk_y$). Substituting decomposition (3.14) into Eqs. (3.5)-(3.10) and taking into account the above normalization, we arrive at the following equations governing the dynamics of perturbation SFHs in spectral plane

$$\left(\frac{\partial}{\partial t} + k_y \frac{\partial}{\partial k_x}\right) \bar{u}_x = -\mathrm{i}k_x \bar{p} + \mathrm{i}k_y \bar{b}_x - \frac{k^2}{\mathrm{Re}} \bar{u}_x + \mathrm{i}k_y N_1 + \mathrm{i}k_x N_2, \tag{3.15}$$

$$\left(\frac{\partial}{\partial t} + k_y \frac{\partial}{\partial k_x}\right) \bar{u}_y = \bar{u}_x - \mathrm{i}k_y \bar{p} + \mathrm{i}k_y \bar{b}_y - \frac{k^2}{\mathrm{Re}} \bar{u}_y + \mathrm{i}k_x N_1 + \mathrm{i}k_y N_3, \tag{3.16}$$

$$\left(\frac{\partial}{\partial t} + k_y \frac{\partial}{\partial k_x}\right) \bar{b}_x = \mathrm{i}k_y \bar{u}_x - \frac{k^2}{\mathrm{Rm}} \bar{b}_x + \mathrm{i}k_y N_4, \tag{3.17}$$

$$\left(\frac{\partial}{\partial t} + k_y \frac{\partial}{\partial k_x}\right) \bar{b}_y = -\bar{b}_x + \mathrm{i}k_y \bar{u}_y - \frac{k^2}{\mathrm{Rm}} \bar{b}_y - \mathrm{i}k_x N_4, \tag{3.18}$$

$$k_x \bar{u}_x + k_y \bar{u}_y = 0, \tag{3.19}$$

$$k_x \bar{b}_x + k_y \bar{b}_y = 0, \tag{3.20}$$

where $k^2 = k_x^2 + k_y^2$ (wavenumbers are normalized by ℓ^{-1}). These spectral equations contain the linear as well as the nonlinear, $N_1(\mathbf{k}, t)$, $N_2(\mathbf{k}, t)$, $N_3(\mathbf{k}, t)$ and $N_4(\mathbf{k}, t)$, terms that are the Fourier transforms of corresponding linear and nonlinear terms in the original Eqs. (3.5)-(3.10). The latter are given by

$$N_1(\mathbf{k}, t) = \int d^2\mathbf{k}' \left[\bar{b}_x(\mathbf{k}', t)\bar{b}_y(\mathbf{k} - \mathbf{k}', t) - \bar{u}_x(\mathbf{k}', t)\bar{u}_y(\mathbf{k} - \mathbf{k}', t)\right]$$

$$N_2(\mathbf{k}, t) = \int d^2\mathbf{k}' \left[\bar{b}_x(\mathbf{k}', t)\bar{b}_x(\mathbf{k} - \mathbf{k}', t) - \bar{u}_x(\mathbf{k}', t)\bar{u}_x(\mathbf{k} - \mathbf{k}', t)\right]$$

$$N_3(\mathbf{k}, t) = \int d^2\mathbf{k}' \left[\bar{b}_y(\mathbf{k}', t)\bar{b}_y(\mathbf{k} - \mathbf{k}', t) - \bar{u}_y(\mathbf{k}', t)\bar{u}_y(\mathbf{k} - \mathbf{k}', t)\right]$$

$$N_4(\mathbf{k},t) = \int d^2\mathbf{k}' \left[\bar{u}_x(\mathbf{k}',t)\bar{b}_y(\mathbf{k}-\mathbf{k}',t) - \bar{u}_y(\mathbf{k}',t)\bar{b}_x(\mathbf{k}-\mathbf{k}',t)\right]$$

and describe nonlinear triad interactions among velocity and magnetic field components of SFHs with different wavenumbers in Fourier **k**-plane. Equations (3.15)-(3.20), which are the basis for subsequent analysis, involve two free dissipative parameters Re and Rm. Since we consider a finite domain in physical (x, y)-plane, the perturbation dynamics also depends on the smallest wavenumber available in this domain, or equivalently on its sizes L_x and L_y, which are the other two free parameters of the problem. Given these parameters and specific initial conditions, Eqs. (3.15)-(3.20) fully determine the nonlinear dynamics of the considered system in Fourier plane. These equations form the mathematical basis of our main goal – to investigate the character of nonlinear processes and self-sustaining scheme of the (subcritical) MHD turbulence in **k**-plane in this constant shear flow. Since energy spectra and nonlinear transfers relate to energy equations, following Refs. Chagelishvili et al. (2002); Alexakis et al. (2007); Fromang & Papaloizou (2007); Simon et al. (2009); Horton et al. (2010); Lesur & Longaretti (2011), below we derive equations governing the evolution of kinetic and magnetic spectral energies.

Multiplying Eqs. (3.15) and (3.16), respectively, by $\bar{u}_x^*$ and $\bar{u}_y^*$, combining and adding its complex conjugate, we arrive at the following equation for the nondimensional kinetic spectral energy $\bar{E}_K = |\bar{u}_x|^2 + |\bar{u}_y|^2$,

$$\frac{\partial \bar{E}_K}{\partial t} + \frac{\partial}{\partial k_x}\left(k_y \bar{E}_K\right) = I_K + I_{K-M} + D_K + N_K, \tag{3.21}$$

where

$$I_K = \bar{u}_x\bar{u}_y^* + \bar{u}_x^*\bar{u}_y = -\frac{2k_xk_y}{k^2}\bar{E}_K, \quad D_K = -\frac{2k^2}{\mathrm{Re}}\bar{E}_K,$$

$$I_{K-M} = \mathrm{i}k_y\left(\bar{u}_x^*\bar{b}_x + \bar{u}_y^*\bar{b}_y - \bar{u}_x\bar{b}_x^* - \bar{u}_y\bar{b}_y^*\right),$$

and the nonlinear kinetic transfer function $N_K(\mathbf{k},t)$ is given by

$$N_K(\mathbf{k},t) \;=\; \mathrm{i}(k_y\bar{u}_x^* + k_x\bar{u}_y^*)N_1(\mathbf{k},t) + \mathrm{i}k_x\bar{u}_x^*[N_2(\mathbf{k},t) - N_3(\mathbf{k},t)] + \text{c.c.}\ .$$

Similarly, multiplying Eqs. (3.17) and (3.18), respectively, by $\bar{b}_x^*$ and $\bar{b}_y^*$, combining and adding its complex conjugate, we obtain the evolution equation for the nondimensional magnetic spectral energy $\bar{E}_M = |\bar{b}_x|^2 + |\bar{b}_y|^2$,

$$\frac{\partial\bar{E}_M}{\partial t} + \frac{\partial}{\partial k_x}\left(k_y\bar{E}_M\right) = I_M + I_{M-K} + D_M + N_M, \tag{3.22}$$

where

$$I_M = -\bar{b}_x\bar{b}_y^* - \bar{b}_x^*\bar{b}_y = \frac{2k_xk_y}{k^2}\bar{E}_M,$$

$$I_{M-K} = -I_{K-M}, \quad D_M = -\frac{2k^2}{\mathrm{Rm}}\bar{E}_M$$

and the nonlinear magnetic transfer function $N_M(\mathbf{k},t)$ is given by

$$N_M(\mathbf{k},t) = \mathrm{i}(k_y\bar{b}_x^* - k_x\bar{b}_y^*)N_4(\mathbf{k},t) + \text{c.c.}\ .$$

By inspection of Eqs. (3.21) and (3.22), one can distinguish five basic processes underlying the dynamics of $\bar{E}_K$ and $\bar{E}_M$:

1. The quantities $k_y\bar{E}_K$ and $k_y\bar{E}_M$ in the second terms on the left hand sides of Eqs. (3.21) and (3.22) are, respectively, the fluxes of the kinetic and magnetic spectral energies parallel to the k_x-axis. These terms

are of linear origin, coming from the convective derivative on the left hand sides of the main Eqs. (3.5)-(3.10) and therefore correspond to the advection by the mean flow. In other words, background shear flow makes the spectral energies (Fourier transforms) "drift" in $\mathbf{k}-$plane, and SFHs with $k_y > 0$ and $k_y < 0$ travel, respectively, along and opposite the k_x-axis at a speed $|k_y|$, whereas SFHs with $k_y = 0$ are not advected by the flow. Since $\int d^2\mathbf{k}\partial(k_y\bar{E}_{K,M})/\partial k_x = 0$, this drift only transports SFHs parallel to the k_x-axis, without changing the total kinetic and magnetic energies.

2. The first terms on the right hand sides, I_K and I_M, are associated with shear, i.e., they originate from linear terms proportional to the shear parameter on the right hand side of Eqs. (3.6) and (3.8), and describe energy exchange between the mean flow and individual SFHs. These terms are related to the domain-averaged nondimensional Reynolds and Maxwell stresses entering Eqs. (3.11) and (3.12) through

$$\langle u_x u_y \rangle = \frac{1}{2}\int I_K(\mathbf{k},t)d^2\mathbf{k},$$

$$\langle -b_x b_y \rangle = \frac{1}{2}\int I_M(\mathbf{k},t)d^2\mathbf{k}$$

and therefore serve as a main source of energy for SFHs (with $k_y \neq 0$) at the expense of which they can undergo amplification. This shear-induced growth of perturbation SFHs is in fact linear by nature and has a transient character due to the drift in $\mathbf{k}-$plane Balbus & Hawley (1992); Chagelishvili et al. (1997); Dimitrov et al. (2011); Mamatsashvili

et al. (2013); Pessah & Chan (2012). The SFHs, drifting parallel to the k_x-axis, go through dynamically important regions in spectral plane, where *energy-supplying* linear terms, I_K and I_M, and *redistributing* nonlinear terms, N_K and N_M, are at work from small and intermediate wavenumbers almost up to the dissipation region at large wavenumbers (see e.g., Fig 3.6). In the case of turbulence studied below, I_K and I_M describe the injection, respectively, of kinetic and magnetic energies into turbulent fluctuations as a function of wavenumbers (see also Refs. Fromang & Papaloizou (2007); Lesur & Longaretti (2011)).

3. The second, cross terms on the right hand sides, I_{K-M} and I_{M-K}, describe the exchange between kinetic and magnetic spectral energies. They have opposite signs and therefore cancel out in the total energy budget of SFHs [see Eq. (3.24) below]. These terms are also of linear origin, corresponding to terms proportional to B_{0y} (linearized magnetic tension and electromotive forces) in Eqs. (3.5)-(3.8).

4. The third terms on the right hand sides, D_K and D_M, describe the dissipation of kinetic and magnetic energies due to viscosity and resistivity, respectively. Comparing these dissipation terms with the energy-supplying terms I_K and I_M, we see that viscous and resistive dissipation are important at large wavenumbers $k \gtrsim k_D = \min(\sqrt{\mathrm{Re}}, \sqrt{\mathrm{Rm}})$, where k_D denotes the effective wavenumber for which dissipation effects start to play a role.

5. The fourth terms on the right hand sides, N_K and N_M, describe nonlinear transfers, respectively, of kinetic and magnetic energies among SFHs with different wavenumbers in $\mathbf{k}-$plane. It follows from the definition of N_K and N_M that their sum integrated over an entire wavenumber plane is equal to zero,

$$\int [N_K(\mathbf{k},t) + N_M(\mathbf{k},t)]d^2\mathbf{k} = 0, \tag{3.23}$$

which is, in fact, a direct consequence of the vanishing of the nonlinear terms in the total energy Eq. (3.13) in real plane. This implies that the main effect of nonlinearity is only to redistribute (scatter) energy drawn from the mean flow among kinetic and magnetic components of perturbation SFHs with different wavenumbers, while leaving the total (kinetic plus magnetic) spectral energy summed over all wavenumbers unchanged. In general, nonlinear transfer functions, N_K and N_M, play a central role in MHD turbulence theory – they determine cascades of spectral energies in $\mathbf{k}-$space, leading to the development of their specific spectra. These transfer functions are one of the main focuses of the present analysis. We aim to explore how they operate in the presence of shear, adopting the approach of Refs. Chagelishvili et al. (2002); Horton et al. (2010), which numerically studied the nonlinear dynamics of 2D perturbations in an HD Couette flow by performing a full 2D Fourier analysis of individual terms in the evolution equation for spectral energy, thus allowing for anisotropy of spectra and cascades. In particular, we show below that like that in the HD shear flow, nonlinear transfers

in the quasi-steady MHD shear turbulence result in the redistribution of spectral energy among wavevector angles in $\mathbf{k}-$plane, which we refer to as a nonlinear transverse cascade, in contrast to classical HD or MHD turbulence without background shear flow, where energy cascade processes change only the wavevector magnitude, $k = |\mathbf{k}|$, of SFHs (see e.g., Ref. Biskamp (2003)).

Combining Eqs. (3.21) and (3.22), we obtain the equation for the total spectral energy $\bar{E} = \bar{E}_K + \bar{E}_M$,

$$\frac{\partial \bar{E}}{\partial t} + \frac{\partial}{\partial k_x}\left(k_y \bar{E}\right) = I_K + I_M + D_K + D_M + N_K + N_M. \tag{3.24}$$

As mentioned above, the linear cross terms responsible for kinetic and magnetic energy exchange are absent in this equation. The net effect of the nonlinear terms in the total spectral energy budget over all wavenumbers is zero according to Eq. (3.23). Thus, as follows from Eq. (3.24), the only source for the total perturbation energy is the integral over an entire spectral plane $\int (I_K + I_M) d^2\mathbf{k}$ that extracts energy from a vast reservoir of shear flow and injects it into perturbations. Since the terms I_K and I_M, as noted above, are of linear origin, the energy extraction and perturbation growth mechanisms are essentially linear by nature. The role of nonlinearity is to continually provide, or regenerate those SFHs in $\mathbf{k}-$plane that are able to undergo transient growth, drawing on the mean flow energy, and in this way feed the nonlinear state over long times.

3.3 Nonlinear evolution

We now turn to an analysis of the nonlinear evolution of perturbations employing modern numerical methods. The main emphasis is on the spectral aspect of the dynamics using the mathematical formalism outlined in the previous section. We start a fiducial run by imposing solenoidal random noise perturbations of the velocity and magnetic field with spatially uniform rms amplitudes $\langle \mathbf{u}^2 \rangle^{1/2} = \langle \mathbf{b}^2 \rangle^{1/2} = 0.84$ on top of the equilibrium. The computational domain is a square of size $L_x \times L_y = 400 \times 400$ and resolution $N_x \times N_y = 512 \times 512$. The reason for taking a large domain is to encompass wavenumbers as small as possible at which, as shown below, the effective transient amplification of SFHs and most of dynamical activity take place. The minimum and maximum wavenumbers of the domain are $k_{x,min} = k_{y,min} = 2\pi/L_x = 0.016$ and $k_{x,max} = k_{y,max} = \pi N_x/L_x = 4.02$. The viscous and resistive Reynolds numbers are fixed to the values $\mathrm{Re} = \mathrm{Rm} = 5$ (corresponding to magnetic Prandtl number of unity $\mathrm{Pr} = \mathrm{Rm}/\mathrm{Re} = 1$), so that the dissipation wavenumber, k_D, falls in this range, $k_D = \sqrt{\mathrm{Re}} = 2.24 < k_{x,max}$.[1] Note also that for the domain size $L_x = 400$ the above defined parameter $\beta = L_x^2/12 = 1.33 \times 10^4$ is quite large, indicating that the background magnetic field energy is small compared to the kinetic energy of the mean flow and therefore the flow can be regarded as weakly magnetized.

[1]The usual Reynolds numbers defined in terms of the half domain size $L_x/2$ and the mean flow velocity at the domain boundary, $U_{0,max} = SL_x/2$, $\mathrm{Re}^* = L_x U_{0,max}/2\nu, \mathrm{Rm}^* = L_x U_{0,max}/2\eta$, are related to the Reynolds numbers used here by $\mathrm{Re}^* = L_x^2\mathrm{Re}/4, \mathrm{Rm}^* = L_x^2\mathrm{Rm}/4$. So, for $L_x = 400$ and $\mathrm{Re} = \mathrm{Rm} = 5$, these numbers are actually quite large

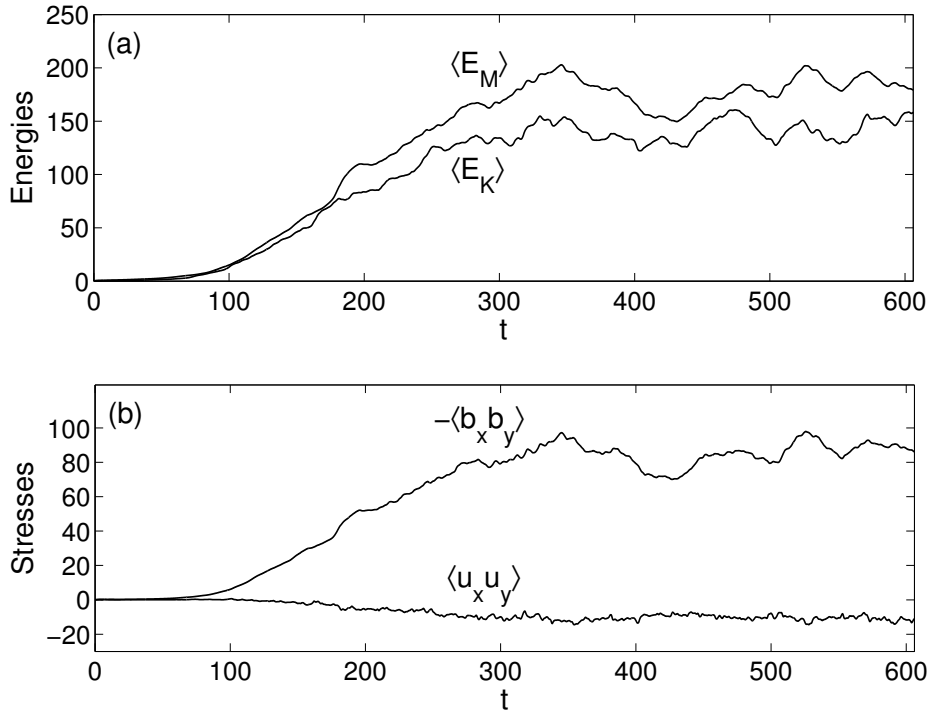

Figure 3.1: Evolution of the domain-averaged (a) perturbed kinetic, $\langle E_K \rangle$, and magnetic, $\langle E_M \rangle$, energies as well as (b) the Reynolds and Maxwell stresses in the fiducial run. Data have been boxcar-averaged over 60 shear times to make the plot readable. In the beginning, all these quantities steadily grow as a result of shear-induced transient amplification of separate SFHs. Then, at about $t = 250$, the amplification saturates to a quasi-steady turbulent state that persists till the end of the run. The magnetic energy is a bit higher than the kinetic one and the positive Maxwell stress dominates over the negative Reynolds stress.

The subsequent time-evolution with these initial conditions was followed to $t_f = 600$ (i.e., for a total of 600 shear times) by solving the basic Eqs. (3.5)-(3.10) using the spectral SNOOPY code [2]. The mean magnetic field $\mathbf{B_0}$ is conserved with time, because the domain-averaged fluctuating (turbulent) fields, as we checked, remain zero, $\langle \mathbf{u} \rangle = \langle \mathbf{b} \rangle = 0$, during the whole run thanks to the shearing box boundary conditions. The SNOOPY is a general purpose code, solving HD and MHD equations, including shear, rotation, weak compressibility and several other physical effects. It is based on a spectral (Fourier) method allowing for the drift of harmonics in $\mathbf{k}$-space due to mean flow (i.e., the shearing box boundary conditions are implemented in the code). The Fourier transforms are computed using the FFTW 3 library. Nonlinear terms are computed using a pseudo-spectral algorithm Canuto et al. (1988) and antialiasing is enforced using the "3/2" rule. Time-integration is performed by a third order Runge-Kutta scheme for nonlinear terms, whereas an implicit scheme is used for viscous and resistive terms. This spectral scheme uses a periodic remap algorithm in order to continually follow the smallest wavenumber of the system in the sheared frame moving with the flow. The code has been tested and extensively used in a number of fluid dynamical and astrophysical contexts (see e.g., Refs. Lesur & Longaretti (2011, 2007); Lesur & Ogilvie (2008); Lesur & Papaloizou (2010); Longaretti & Lesur (2010); Rempel et al. (2010); Herault et al. (2011)).

$\mathrm{Re}^* = \mathrm{Rm}^* = 2.0 \times 10^5$

[2] The code is available for download at G. Lesur's web page `http://ipag.obs.ujf-grenoble.fr/~lesurg/snoopy.html`

Figure 3.1 shows the time-development of the domain-averaged perturbed kinetic, $\langle E_K \rangle$, and magnetic, $\langle E_M \rangle$, energies as well as the Reynolds, $\langle u_x u_y \rangle$, and Maxwell $-\langle b_x b_y \rangle$ stresses. At the early stage of evolution, they all increase as a result of linear transient growth of separate SFHs contained in the initial conditions. Then, after about 250 shear times, on reaching sufficient amplitudes in the nonlinear regime, the energies and stresses settle down to a quasi-steady state of sustained turbulence (see Fig. 3.2) that does not decay and persists until the end of the simulation at $t_f = 600$.

In this state, the kinetic and magnetic energies are comparable – a ratio of their domain- and time-averaged over the whole quasi-steady state (denoted here and below, for the stresses, with double brackets) values is $\langle\langle E_M \rangle\rangle / \langle\langle E_K \rangle\rangle = 1.28$, that is, there is a near equipartition of the energy between kinetic and magnetic components. The Maxwell stress is much larger than the Reynolds stress, indicating that the turbulent transport and energy extraction from the mean flow are dominated by the magnetic field perturbations. The average of the domain-averaged Maxwell stress over the last 350 shear times is positive $\langle\langle -b_x b_y \rangle\rangle = 84.5$, while that of the domain-averaged Reynolds stress is negative $\langle\langle u_x u_y \rangle\rangle = -10.4$. As is seen from Eq. (3.13), the domain-averaged total stress must necessarily be positive for maintenance of turbulence and therefore it is the Maxwell stress that plays a decisive role in this process – counteracting dissipation, it ensures continuous feeding and sustenance of the turbulence at the expense of the mean shear flow.

The structure of the velocity and magnetic field in the quasi-steady

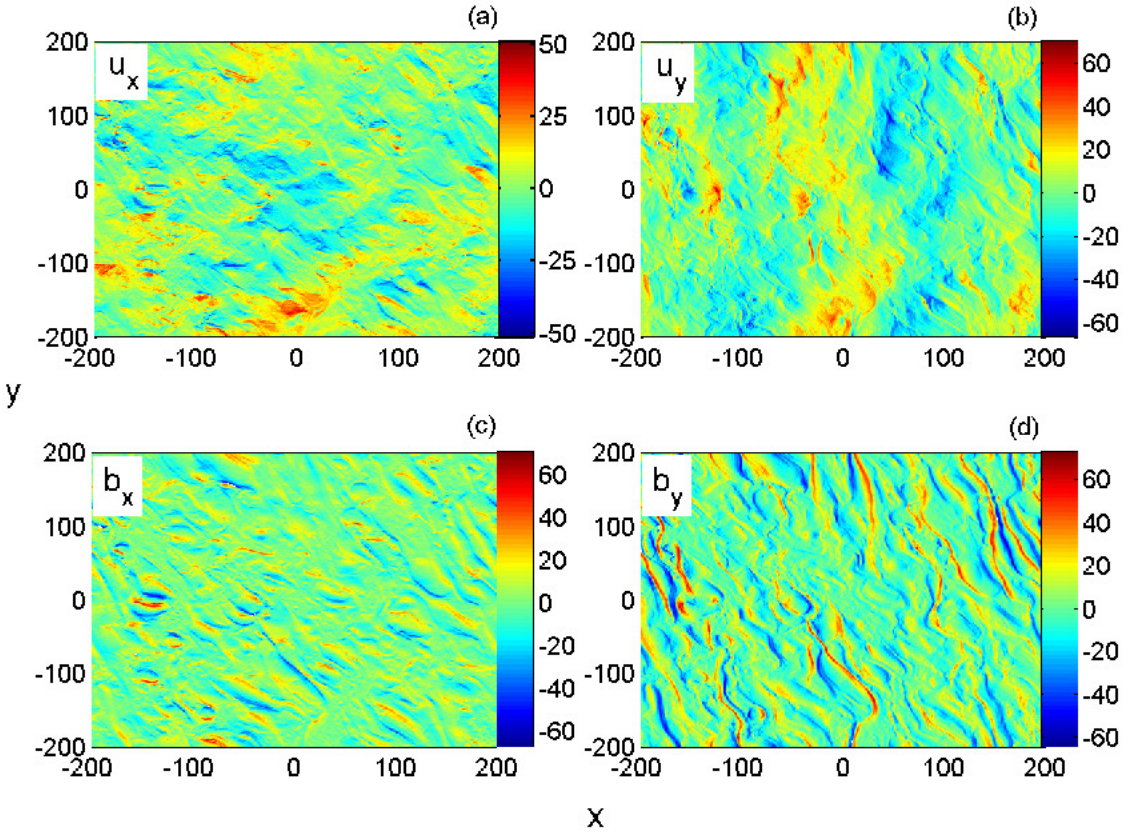

Figure 3.2: (Color online) Distribution of (a),(b) the velocity and (c),(d) the magnetic field components in $(x, y)-$plane in the fully developed quasi-steady turbulence at $t = 490$. This state is fairly nonlinear: u_x and u_y vary within limits comparable to the domain-averaged velocity of the background flow (in non-dimensional units $\langle |U_0| \rangle = L_x/4 = 100$), while b_x and b_y are much larger than the background magnetic field $B_{0y} = 1$. Structures in the u_y and b_y fields are elongated in the $y-$direction due to shear.

turbulent state (at $t = 490$) is depicted in Fig. 2. These fields are chaotic with u_y and b_y [Figs. 3.2(b) and 3.2(d)] having more elongated features in the $y-$direction due to shear compared to u_x and b_x [Figs. 3.2(a) and 3.2(c)]. At this time, the normalized fluctuating velocity and magnetic field are comparable, $\langle u_x^2 \rangle = 87.68$, $\langle u_y^2 \rangle = 178.73$, $\langle b_x^2 \rangle = 113.17$, $\langle b_y^2 \rangle = 238.64$ and are much larger than their corresponding initial values. Also, the $y-$components are larger than the x-ones: $\langle u_x^2 \rangle < \langle u_y^2 \rangle$, $\langle b_x^2 \rangle < \langle b_y^2 \rangle$, which holds throughout the run. Within the domain, u_x and u_y reach maximum values $|u_x|_{\max} = 51.53$ and $|u_y|_{\max} = 70.15$ comparable to the average background flow velocity, $\langle |U_0| \rangle = L_x/4 = 100$, and the b_x and b_y have grown much larger, $|b_x|_{\max} = 70.61$ and $|b_y|_{\max} = 72.78$, than the mean field $B_{0y} = 1$. So, this quasi-steady MHD turbulence can be viewed as being strongly nonlinear and weakly magnetized, since $\langle \mathbf{b}^2 \rangle^{1/2} \gg B_{0y}$.

The general behavior of the domain-averaged kinetic and magnetic energies and stresses with time obtained here in the 2D case is qualitatively consistent with that typically found in similar, but 3D simulations of MHD turbulence driven by the magnetorotational instability (MRI) in local models of accretion disks with a net toroidal magnetic field along the disk flow Hawley et al. (1995); Guan et al. (2009); Simon & Hawley (2009), as in the present setup. In both cases, there are no exponentially growing modes in the considered unbounded constant shear flows in the classical sense of linear stability analysis Stern (1963); Ogilvie & Pringle (1996), i.e., the flows are spectrally stable. In such flows, perturbations can grow only transiently during finite

times Balbus & Hawley (1992); Chagelishvili et al. (1997); Dimitrov et al. (2011), which is thought to be a key factor for the onset of subcritical turbulence Grossmann (2000); Chapman (2002); Eckhardt et al. (2007). One of the basic characteristics of subcritical transition is its sensitivity to the initial perturbation amplitude (e.g., Refs. Baggett et al. (1995); Schmid & Henningson (2001); Lesur & Papaloizou (2010); Duguet et al. (2010)), which is also observed here. We found that there exists a critical amplitude for initial velocity and magnetic field perturbations (at a given L_x, Re and Rm) below which turbulence is absent – there is only transient amplification insufficient to trigger transition, which eventually decays due to dissipation. By contrast, for initial amplitudes larger than the critical value a turbulent transition does occur after a phase of large enough transient growth, as is also evident from Fig. 3.1. Specifically, at Re = Rm = 5 adopted here, the critical amplitude turned out to be $\langle \mathbf{u}^2 \rangle_{crit}^{1/2} = \langle \mathbf{b}^2 \rangle_{crit}^{1/2} = 0.34$ (for the same type of initial noise spectrum for both velocity and magnetic field perturbations), and in the fiducial run we accordingly selected the initial rms amplitudes (=0.84) larger than this in order to achieve turbulent regime. This confirms that the turbulence we study here is subcritical, however, we have not explored the transition process, that is, have not pinned down the critical transition amplitude for different values of the system parameters (domain size, Reynolds numbers, etc.) in more detail. The problem of subcritical transition in MHD shear flows deserves a special investigation in its own right, but in the present analysis we are mainly interested in the properties of the resulting self-sustaining turbulence itself once it has

settled into quasi-steady state. The underlying physics of the onset and sustenance of subcritical turbulence in spectrally stable hydrodynamic shear flows – the bypass concept – has been extensively studied previously in a number of papers (see e.g., Refs. Grossmann (2000); Eckhardt et al. (2007) for a review), but extension to MHD turbulence in spectrally stable magnetized shear flows, to the best of our knowledge, has not been systematically investigated yet. The equilibrium flow considered here with a linear spanwise shear of mean velocity and streamwise magnetic field is the simplest but important example of such spectrally stable magnetized shear flows that allows us to grasp specific processes determining the onset, self-sustenance and spectral characteristics of MHD turbulence in this kind of flow. Deeper insight into the dynamics of such subcritical MHD turbulence can be gained by performing an analysis in spectral space.

3.4 Turbulence behavior in spectral plane

In this section, we focus on the analysis of the dynamics of the quasi-steady turbulent state in Fourier plane. We now explicitly calculate the individual terms in Eqs. (3.21) and (3.22), which were classified and described in Sec. II, using the simulation data. The SNOOPY code, being of the spectral type, is particularly useful for this purpose, as it allows us to directly extract Fourier transforms from the data.

Before proceeding to spectral analysis, we note that generally a turbulent field and hence its Fourier transform are quite noisy. To remove this noise

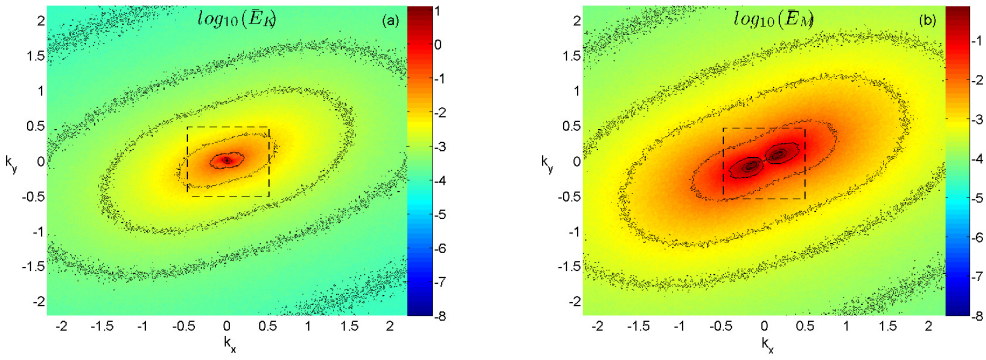

Figure 3.3: (Color online) Time-averaged (a) kinetic and (b) magnetic energies' spectra in $\mathbf{k}-$plane pertaining to the quasi-steady turbulent state. These time-averages are done over 80 shear times, as described in the text. The isolines correspond to the values $-4, -3.5, -3, -2, -1, 0$ of $log_{10}(\bar{E}_K)$ in panel (a) and to the values $-4, -3.5, -3, -2, -1, -0.5, -0.3, 0$ of $log_{10}(\bar{E}_M)$ in panel (b). Both spectra are anisotropic, having larger power at the $k_x/k_y > 0$ side. The kinetic energy spectra is more concentrated at smaller wavenumbers than the magnetic one. The dashed rectangle in each plot encloses the region of major activity of the dynamical terms in Eqs. (3.21) and (3.22), which are shown in Fig. 3.5.

and extract valuable information on the trends in the turbulence dynamics, all Fourier transforms (spectra) presented below are averaged over 80 shear times. The interval between two successive dumps in the code was set to 1 shear time, so the averaging is represented by 80 snapshots. From now on we concentrate on the evolution after the quasi-steady saturated nonlinear state has set in (i.e., at $t \gtrsim 250$), so we can choose the starting moment for averaging arbitrarily over the duration of this state, since the result is practically independent of this moment by virtue of the quasi-steadiness of the process.

3.4.1 Energy spectra

Figure 3.3 shows the time-averaged spectra of the kinetic and magnetic energies in $\mathbf{k}-$plane that have been established in the quasi-steady turbulent state. Note that both spectra are strongly anisotropic, with the magnetic energy spectrum being broader than the kinetic energy one. For $k \gtrsim 0.5$, they have a similar elliptical shape inclined to the k_x-axis, whereas at $k \lesssim 0.5$ these spectra differ in structure: isolines for the magnetic energy divide into two sets of ellipses near the center with the same inclination. This indicates that SFHs with $k_x/k_y > 0$ have more energy than those with $k_x/k_y < 0$ at fixed k_y. Since $\beta \gg 1$, the effect of the mean flow shear prevails over that of the mean magnetic field that leads us to suppose that the anisotropy of these spectra might be primarily due to shear. [3] These features of the kinetic and magnetic energy spectra, which clearly distinguish them from typical turbulent spectra in the classical shearless case Biskamp (2003), arise as a consequence of the specific way in which the terms of linear and nonlinear origin in Eqs. (3.21) and (3.22) operate in $\mathbf{k}-$plane. We show below that these terms are anisotropic over wavenumbers due to shear, resulting in a new phenomenon – the transverse cascade of power in spectral plane – compared to the classical (isotropic) case.

The above time-averaged 2D spectra integrated over the angle in $\mathbf{k}-$plane, $\bar{E}^{(k)}_{K,M} = k \int_0^{2\pi} \bar{E}_{K,M} d\phi$, and represented as a function of k are shown in Fig.

[3] Similar anisotropic spectra were also observed in the simulations of MHD turbulence driven by the MRI in the presence of shear Hawley et al. (1995); Lesur & Longaretti (2011).

3.4. From intermediate wavenumbers $k \sim 0.2$ up to dissipation wavenumbers $k \sim k_D = 2.24$, both one-dimensional (1D) spectra exhibit power-law dependence on k, however, with different spectral indices – the kinetic energy spectrum is well fitted by $k^{-1.4}$ and the magnetic energy spectrum by k^{-2}. At these wavenumbers, the spectral density of the magnetic energy is larger than that of the kinetic one, but at smaller $k \lesssim 0.2$ it decreases and becomes less than the kinetic one, both deviating from the power-law. These power-law parts of the spectra clearly differ from the typical Iroshnikov-Kraichnan (IK) spectrum, $k^{-1.5}$, characteristic of classical 2D and 3D MHD turbulence without background shear flow Biskamp (2003), though the kinetic energy spectrum is still close to it. Different spectra of kinetic and magnetic energies, following approximately power-laws (though, with kinetic energy spectrum somewhat coincident with the IK one), are also present in analogous 3D simulations of MRI-driven MHD turbulence in the shearing box model of a disk Simon et al. (2009); Fromang (2010); Lesur & Longaretti (2011). However, it was pointed out in those studies that in the presence of differential rotation (shear) and weak magnetization ($\beta \gg 1$) associated with disk flows, which are in fact also shared by the 2D MHD shear flow considered here, classical Kolmogorov or IK phenomenology is generally *not* applicable to turbulence dynamics, because due to shear, energy injection from the mean flow into turbulence can occur over a broad range of length-scales available in the flow, from the largest scale down to the dissipation scale, that in turn prevents the development of the proper inertial range of a spectrum in the classical sense (see also Refs. Fro-

mang & Papaloizou (2007); Lesur & Longaretti (2011)). So, the spectra obtained in those disk simulations, despite being of the power-law type, are in fact determined by interplay between injection terms due to the linear MRI, operating over a range of wavenumbers, and nonlinear terms in spectral space. The situation is similar in the present problem. As shown below, the action of the energy injection terms I_K and, especially, of I_M extends over a range of wavenumbers in $\mathbf{k}-$plane and is remarkably anisotropic [see Figs. 3.5(a), 3.5(b) and 3.6]. As noted above, these terms are responsible for the linear transient amplification of SFHs and energy extraction from the mean flow, so in this respect they play a similar role of supplying turbulence with energy in our nonrotating case as the (transient) azimuthal MRI in rotating disk flows. Moreover, we demonstrate that there exists a new phenomenon – the transverse nonlinear cascade of spectral energy density – resulting from this anisotropy and, ultimately, from shear. These new features are not common to shearless MHD turbulence and hence it is not surprising that Kolmogorov or IK theory cannot adequately describe shear flow turbulence.

We have presented the energy spectra from two perspectives: fully in $\mathbf{k}-$plane in Fig. 3.3 and their angle-integrated (over shells of constant $|\mathbf{k}|$) versions in Fig. 3.4, the former is obviously more informative than the latter. We emphasize that angle-integration of turbulent spectra and transfer functions when they are anisotropic in wavenumber plane might lead to the loss of essential information on the detailed nonlinear dynamics, so we take a more general strategy of Ref. Horton et al. (2010) and represent energy spectra

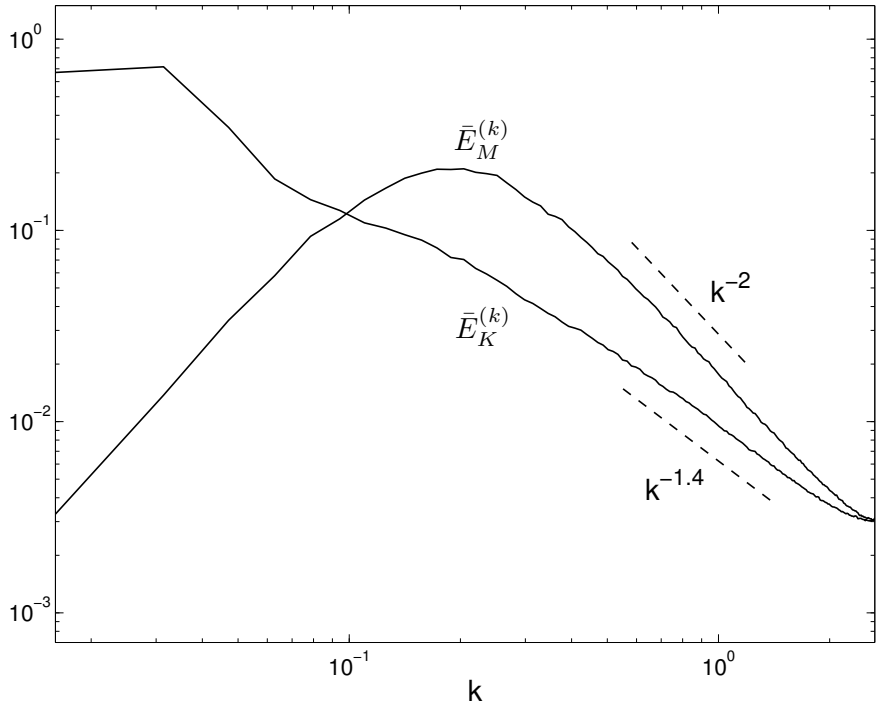

Figure 3.4: Kinetic and magnetic energy spectra from Fig. 3.3 integrated over the angle in $\mathbf{k}-$plane and plotted as a function of k. From intermediate, $k \sim 0.2$, to dissipation, $k \sim k_D = 2.24$, wavenumbers a power-law behavior is observed in both spectra, though with different spectral indices: $k^{-1.4}$ for the kinetic and k^{-2} for the magnetic energies.

as well as injection and nonlinear transfer terms in full in $\mathbf{k}-$plane, in contrast to previous related studies of MHD turbulence in shear flows considering either such angle-integrated or reduced 1D spectra (e.g., Refs. Fromang & Papaloizou (2007); Simon et al. (2009); Davis et al. (2010); Lesur & Longaretti (2011)). This allows us to obtain a complete dynamical picture and understanding of the nature of subcritical MHD turbulence in the presence of mean flow shear.

3.4.2 Spectra of energy injection: I_K and I_M

To better understand the character of the above anisotropic kinetic and magnetic energy spectra and nonlinear transfers, in Fig. 3.5 we present the distribution of the time-averaged kinetic and magnetic injection functions, I_K and I_M, cross terms, I_{K-M} and I_{M-K}, and nonlinear transfer terms, N_K and N_M, in $\mathbf{k}-$plane in the quasi-steady turbulent state. From this figure it is seen that these terms differ in magnitude and, like the spectral energies, all exhibit anisotropy over wavenumbers, that is, depend on the wavevector angle. I_K is mostly concentrated at small wavenumbers, $k \lesssim 0.1$ [Fig. 3.5(a)], being positive at $k_x/k_y < 0$ (red and yellow regions), where it increases the kinetic energy of SFH, and negative at $k_x/k_y > 0$ (blue regions), where it takes kinetic energy from SFH and gives it back to the flow. A net contribution of I_K over all wavenumbers is, however, negative (i.e., $\langle u_x u_y \rangle < 0$). On the other hand, I_M mostly operates at larger wavenumbers, $0.05 \lesssim k \lesssim 0.5$ [Fig. 3.5(b)], and is dominant and positive on the $k_x/k_y > 0$ side (red and yellow regions), where it supplies SFH with magnetic energy. The net result of I_M over all wavenumbers is a positive energy gain for perturbations (i.e., $\langle -b_x b_y \rangle > 0$), which prevails over the net negative effect of I_K, as is also evident from Fig. 3.1(b), and maintains turbulence. So, energy input for perturbation SFHs is provided by the magnetic source term I_M, which operates over a much broader region in $\mathbf{k}$-plane than I_K does. We checked that such a dependence of kinetic and magnetic energy injection terms on wavenumbers, in fact, is also seen for the linear evolution of SFH, i.e., when the SFH drifts along the k_x-axis

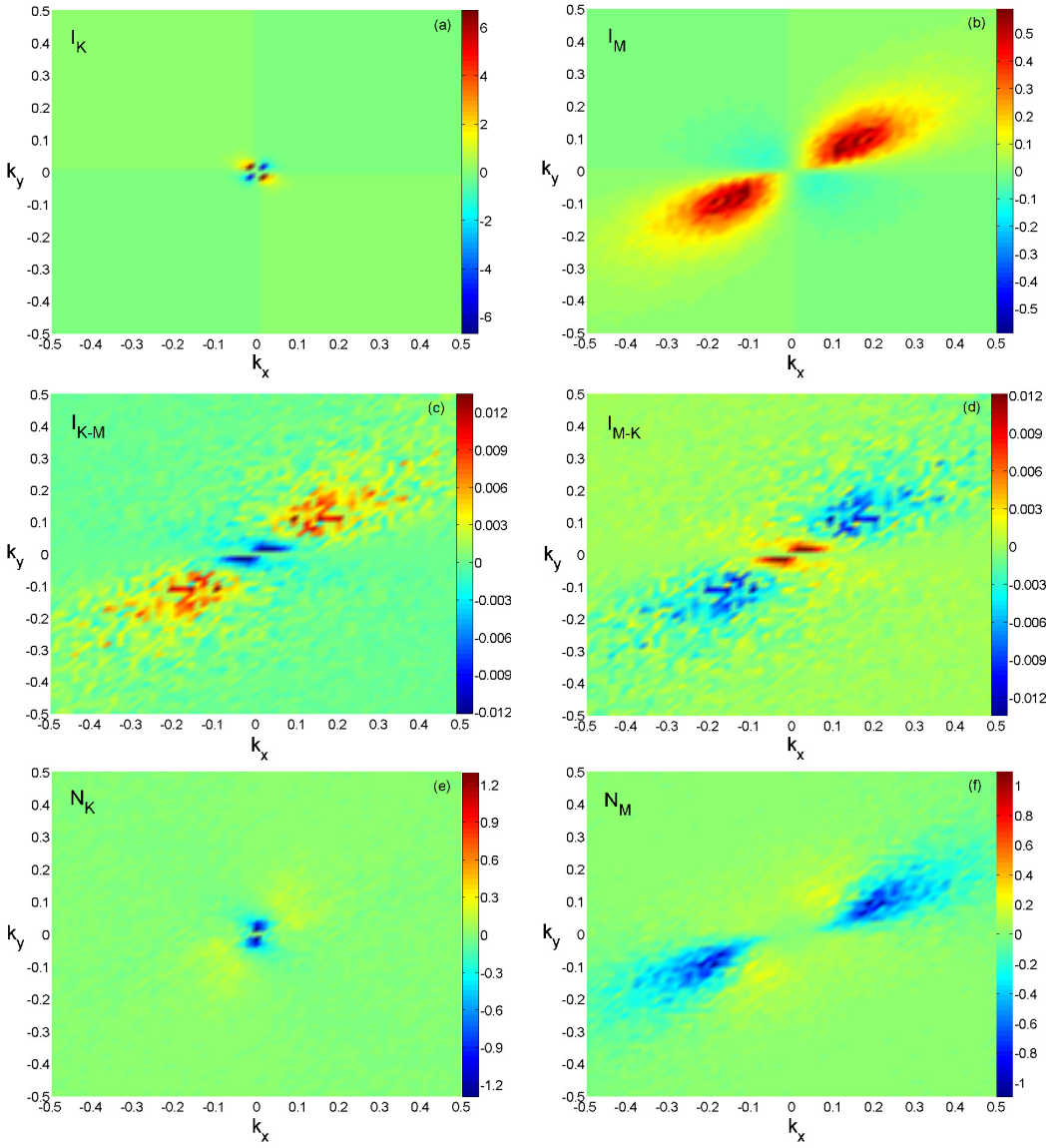

Figure 3.5: (Color online) Maps of the time-averaged (a) kinetic, I_K, and (b) magnetic, I_M, energy injection terms, (c) and(d) the cross terms I_{K-M}, I_{M-K} and the (e) kinetic, N_K, and (f) magnetic, N_M, nonlinear transfer terms in $\mathbf{k}-$plane in the state of quasi-steady turbulence. The time averages are obtained over an interval of 80 shear times (from 472 to 552 shear times), as described in the text. Kinetic energy injection mostly occurs at small wavenumbers, $k \lesssim 0.1$, and on the $k_x/k_y < 0$ side where $I_K > 0$, while magnetic energy injection occurs mostly at intermediate wavenumbers, $0.05 \lesssim k \lesssim 0.5$, on the $k_x/k_y > 0$ side where $I_M > 0$, overall it is dominant over I_K, i.e, energy injection into turbulence appears to be due mainly to the Maxwell stresses. The N_K and N_M terms transfer, respectively, the spectral kinetic and magnetic energies anisotropically (transversely) in wavenumber plane, away from regions where they are negative $N_K < 0$, $N_M < 0$ (blue) to regions where they are positive $N_K > 0$, $N_M > 0$ (yellow). The nonlinear terms are comparable to the injection terms and both are about two orders of magnitude larger than the cross terms.

due to shear, its kinetic energy first increases at $k_x/k_y < 0$, then decreases after crossing the point $k_x = 0$, while its magnetic energy starts to increase at $k_x/k_y > 0$ during a few shear times and then continues to oscillate with Alfvén frequency, $\omega_A = u_A k_y$, and constant amplitude (provided dissipation is neglected).

The linear cross terms, I_{K-M} and I_{M-K} [Figs. 3.5(c) and 3.5(d)], are small compared to both I_K, I_M and nonlinear N_K, N_M terms. In spectral plane, the action of these terms is somewhat opposite to that of the corresponding injection terms. I_{K-M} lowers the kinetic energy at small wavenumbers, but increases at intermediate and large wavenumbers on the $k_x/k_y > 0$ side, while I_{M-K} lowers the magnetic energy at intermediate and large wavenumbers in the same quadrant and increases it at small wavenumbers. As noted above, these cross terms cancel out in the total energy Eq. (3.24) and because they are much smaller than the other dynamical terms, do not play any major role in the energy balance in Eqs. (3.21) and (3.22) too.

The difference between the injection wavenumbers for the kinetic and magnetic energies is demonstrated more clearly in Fig. 3.6, showing these injection, nonlinear transfer, and dissipation terms angle-integrated in $\mathbf{k}-$plane, $I_K^{(k)}, N_K^{(k)}, D_K^{(k)}$ [Fig. 3.6(a)] and $I_M^{(k)}, N_M^{(k)}, D_M^{(k)}$ [Fig. 3.6(b)], and represented as a function of k. It is seen from this figure that the range of wavenumbers, where the injection terms are at work, extends from the smallest wavenumbers in the domain, $k_{x,min}$, up to $k \sim 1$, comparable to the dissipation wavenumber k_D. $I_K^{(k)}$ is positive at small wavenumbers, reaching a maximum at $k \approx 0.05$,

then becomes negative and vanishing at $k > 0.12$ (i.e., no longer injects kinetic energy). On the other hand, $I_M^{(k)}$ is positive and hence creates the turbulence's magnetic energy at all wavenumbers, reaching a maximum at $k \approx 0.2$, which is about twice as large as that of $I_K^{(k)}$. Note in Fig. 3.6 that these injection and nonlinear transfer terms $N_K^{(k)}$ and $N_M^{(k)}$ widely overlap. This implies that in the presence of shear, there is not a single injection scale in the flow, as is usually assumed in classical turbulence theory, but instead energy injection occurs all the way from the largest length-scales down to the dissipation scale.

Therefore, although power-law spectra for both the kinetic and the magnetic energies are found at $0.2 \lesssim k \lesssim 2$ (Fig. 3.4), they still cannot be considered as being a proper inertial range, since energy is injected at these intermediate scales (see also Refs. Fromang & Papaloizou (2007); Lesur & Longaretti (2011) for a similar situation in the MRI-driven turbulence, where the injection of energy, drawn from the mean flow, into turbulence occurs over a range of scales at which nonlinear transfers operate as well). From Fig. 3.6, it is also seen that in this wavenumber range, the dissipation terms are much smaller than the injection and nonlinear transfer terms, so this part of the energy spectra are in fact formed mainly as a result of the combined action of the linear injection and nonlinear cascade.

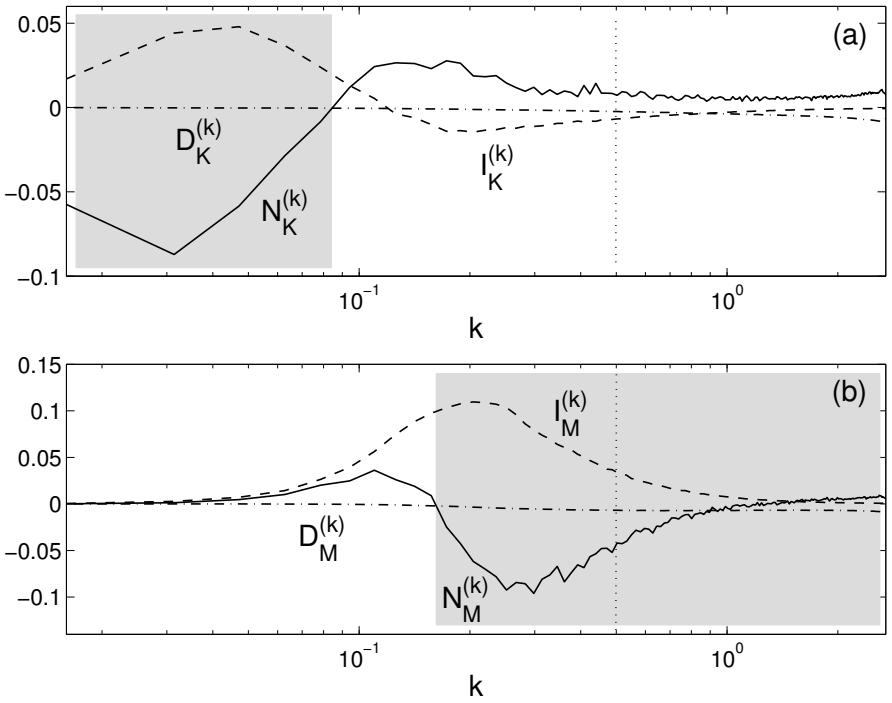

Figure 3.6: (Color online) Kinetic and magnetic injection and nonlinear transfer terms from Fig. 3.5 as well as dissipation terms integrated over the angle in $\mathbf{k}-$plane, (a) $I_K^{(k)}, N_K^{(k)}, D_K^{(k)}$ and (b) $I_M^{(k)}, N_M^{(k)}, D_M^{(k)}$, and represented as a function of k. Injection terms (dashed lines) operate over a range of wavenumbers, overlapping with nonlinear terms (solid lines). The magnetic energy injection is larger than the kinetic one. Both viscous and resistive dissipation (dot-dashed lines) are relatively important only at $k > k_D = 2.24$. The reference dotted vertical line marks the maximum wavenumber $k = 0.5$ of the domains in Fig. 3.5. Shaded (gray) regions correspond to wavenumbers at which $N_K^{(k)} < 0, N_M^{(k)} < 0$ and hence the kinetic and magnetic energies, respectively, are transferred, on average, away from these wavenumbers due to nonlinearity.

3.4.3 Nonlinear transfers N_K and N_M – the essence of the transverse cascade

We now move to describing the nonlinear kinetic and magnetic transfer functions. As noted above, they do not represent a new source of total energy for turbulence, but only act to redistribute kinetic and magnetic spectral energies, which are extracted from the mean flow, over wavenumbers and, in cooperation with injection terms, determine the characteristics of spectra. So, our primary goal is to understand how the nonlinear transfer terms work and, consequently, in which directions energies cascade in Fourier plane in the presence of background shear. As mentioned in Introduction, for a purely HD constant shear (Couette) flow, which is spectrally stable, it was shown in Ref. Horton et al. (2010) that nonlinear transfer function is anisotropic in $\mathbf{k}-$plane, i.e., depends on the polar angle due to shear and, as a consequence, leads to redistribution of the spectral energy over wavevector angles. This relatively new process termed the angular, or transverse cascade of energy has been shown to be essential for the maintenance of the subcritical nonlinear state in this flow via the bypass mechanism.

Actually, identification of the transverse cascade of energy has been made possible by virtue of representation of the dynamics fully in 2D spectral plane, without performing angle-integration that would result in washing out a key element of this process – the angular dependence (anisotropy) of the transfer functions' spectra. The findings in that paper indicate that in HD shear flows, along with the direct and inverse cascades quite well established in

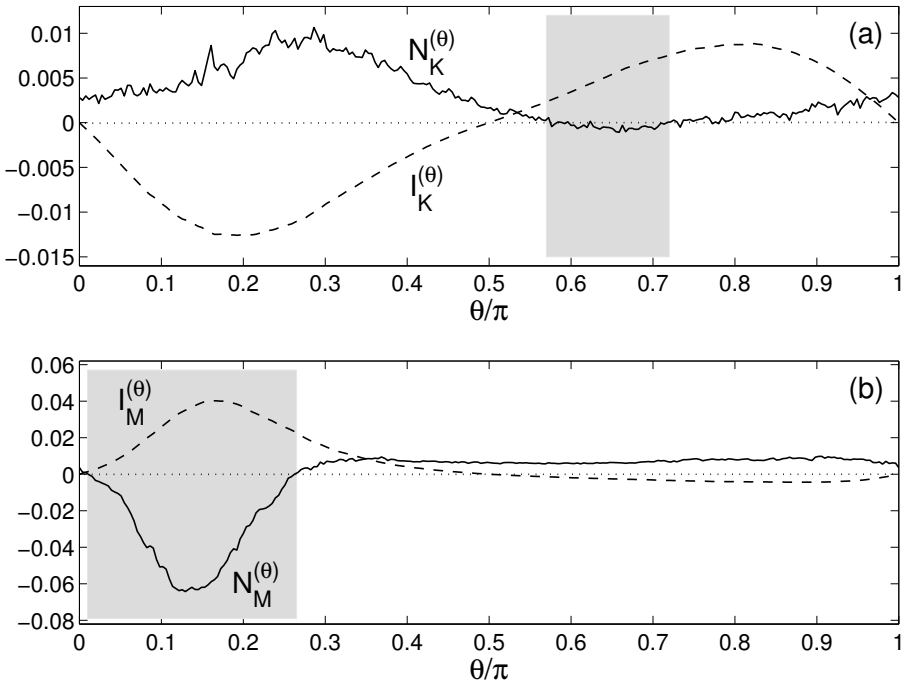

Figure 3.7: (Color online) Kinetic and magnetic injection and nonlinear transfer terms from Fig. 3.5 integrated over k, (a) $I_K^{(\theta)}, N_K^{(\theta)}$ and (b) $I_M^{(\theta)}, N_M^{(\theta)}$, and represented as a function of the wavevector polar angle θ (angles $\pi < \theta < 2\pi$ correspond to complex conjugates and are not shown here). These plots clearly demonstrate the angular dependence (anisotropy) of both the injection (dashed lines) and the nonlinear transfer (solid lines) terms. Shaded (gray) regions correspond to angles at which $N_K^{(\theta)} < 0, N_M^{(\theta)} < 0$ and hence kinetic and magnetic energies, respectively, are transferred from these angles to other angles due to nonlinearity, that is, a new phenomenon – the transverse (angular) cascade of energy – takes place.

turbulence theory, a new, transverse type of cascade can also take place which, in fact, appears to be as important as the former. Based on these results, in the present Chapter we generalize a spectral analysis of nonlinear dynamics given in Horton et al. (2010) for the HD constant shear flow to the MHD constant shear flow considered here, with the aim of understanding the mechanism responsible for the sustenance of the subcritical MHD turbulence in question. Specifically, we will examine whether there exists a cooperative action of any kind between energy-injecting linear and nonlinear transfer terms, like that occurring in HD shear flows, capable of sustaining perturbations in spectrally stable MHD shear flows.

Figures 3.5(e) and 3.5(f) show the distribution of the time-averaged kinetic, N_K, and magnetic, N_M, nonlinear transfer functions with wavenumbers in the quasi-steady turbulence, alongside the injection terms, in order to easily see their cooperative (correlated) action with the latter. As mentioned above, both N_K and N_M are strongly anisotropic, i.e., depend on the polar angle in $\mathbf{k}-$plane. This anisotropy has qualitatively the same character as that of I_K, I_M, I_{K-M} and the 2D energy spectra in Fig. 3.3, that is, the spectra of all these are inclined towards the k_x-axis due to shear. To bring out this angular dependence more clearly, we integrated I_K, I_M and N_K, N_M over k, from the smallest $k_{min} = k_{x,min}$ to the largest $k_{max} = k_{x,max}$ values in the domain,

$$I_{K,M}^{(\theta)} = \int_{k_{min}}^{k_{max}} I_{K,M} k dk, \quad N_{K,M}^{(\theta)} = \int_{k_{min}}^{k_{max}} N_{K,M} k dk$$

and represent them as functions of the polar angle θ in Fig. 3.7. While the above-defined $N_K^{(k)}$ and $N_M^{(k)}$ describe energy transfers in the direction

of $\mathbf{k}$, $N_K^{(\theta)}$ and $N_M^{(\theta)}$ describe energy transfer along the azimuthal direction, perpendicular to $\mathbf{k}$.

As shown in Figs. 3.5-3.7, the distributions of N_K and N_M over wavenumbers differ, leading to different types of cascades for the kinetic and magnetic spectral energies. Since these quantities are symmetric with respect to a change $\mathbf{k} \to -\mathbf{k}$, without loss of generality, everywhere below we concentrate on the upper part ($k_y > 0$) of $\mathbf{k}-$plane. N_K mainly operates in two regions of $\mathbf{k}-$plane: at small wavenumbers, $k \lesssim 0.1$, where it is negative [blue region with $N_K < 0$ in Fig.3.5(e) corresponding to gray-shaded area with $N_K^{(k)} < 0$ in Fig. 3.6(a)], and at intermediate wavenumbers $0.1 \lesssim k \lesssim 0.5$ on the $k_x/k_y > 0$ side ($0 \leq \theta \leq \pi/2$), where it is positive (yellow region with $N_K > 0$); at all other wavenumbers the kinetic transfer function is nearly zero. On the other hand, N_M mainly operates at $0.05 \lesssim k \lesssim 1$ [see also Fig. 3.6(b)], is positive at $0.3\pi \lesssim \theta \leq \pi$ [yellow region with $N_M > 0$ in Fig. 3.5(f)] and negative at $0 \leq \theta \lesssim 0.3\pi$ (blue region with $N_M < 0$); at all other wavenumbers the magnetic transfer term is nearly zero. Note also that the distributions of N_K and N_M look somewhat similar to those of the linear exchange terms I_{K-M} and I_{M-K}, respectively, but, as noted above, the latter are two orders of magnitude smaller than the former.

By definition, these nonlinear transfer functions redistribute the corresponding spectral energies away from the regions in $\mathbf{k}-$plane where they are negative to the regions where they are positive. The kinetic energy injection due to I_K occurs, as described above, at small wavenumbers ($k \lesssim 0.1$) with

$\pi/2 < \theta < \pi$ where $I_K > 0$ [see also Figs. 3.6(a) and 3.7(a)], but the N_K term is negative there, transferring kinetic energy away from these injection wavenumbers to intermediate wavenumbers, $k \gtrsim 0.1$, with $0 \leq \theta \leq \pi/2$, where $N_K > 0$. This picture of spectral kinetic energy transfer, or cascade towards larger wavenumbers is also evident from Fig. 3.6(a), where the angle-integrated $N_K^{(k)}$ changes from negative to positive at about $k = 0.1$, consistent with the flow of kinetic energy away from $k \lesssim 0.1$ to $k \gtrsim 0.1$. The cascade behavior for the turbulent magnetic energy is different from that of the kinetic energy. The magnetic energy injection due to I_M occurs at intermediate wavenumbers ($0.05 \lesssim k \lesssim 1$) for $0 < \theta < \pi/2$, where $I_M > 0$ [see also Figs. 3.6(b) and 3.7(b)], but the N_M term, which is mostly negative there, transfers the magnetic energy away from this injection region to its neighboring region on the left with slightly smaller wavenumbers but larger polar angles $0.3\pi \lesssim \theta \leq \pi$, where N_M is positive. This cascade of magnetic energy to smaller wavenumbers is more clearly seen from Fig. 3.6(b), where the angle-integrated $N_M^{(k)}$ changes from positive to negative at around $k = 0.17$, indicating the flow of magnetic spectral energy from $k \gtrsim 0.1$ to $k \lesssim 0.1$.

Thus, in shear MHD turbulence, the kinetic and magnetic energies are transferred both along the wavevector, corresponding to familiar direct and inverse cascades, and transversely (perpendicular) to it (i.e., over angles θ). Just this second type of nonlinear cascade, better characterized by $N_K^{(\theta)}$ and $N_M^{(\theta)}$ (Fig. 3.7), is a new effect of shear and is discussed more in the next subsection; it is absent in classical shearless MHD turbulence.

As stressed in Ref. Horton et al. (2010), the transverse cascade of energy appears to be a generic feature of nonlinear dynamics of perturbations in spectrally stable shear flows, so the conventional description of shear flow turbulence solely in terms of direct and inverse cascades, which leaves such nonlinear transverse cascade out of consideration, might be incomplete and misleading. We emphasize that in the present case revealing the complete picture of these nonlinear cascade processes has become largely possible due to carrying out the analysis in spectral plane. Because of the shear-induced anisotropy of cascade directions, only angle-integrated transfer functions in Fig. 6 (that are in fact typically used in most numerical studies of shear MHD turbulence, e.g., Refs. Fromang & Papaloizou (2007); Simon et al. (2009); Davis et al. (2010); Lesur & Longaretti (2011)), clearly, are not fully representative of the actual, more general nonlinear redistribution of the spectral energies in $\mathbf{k}-$plane, which also includes transfer with respect to wavevector angles – the transverse cascade.

3.4.4 Interplay of the linear injection and nonlinear transverse cascade

We have seen above that the nonlinear redistributions of spectral kinetic and magnetic energies over the wavevector polar angle, θ, in $\mathbf{k}-$plane, termed the transverse cascade, are due to shear-induced dependence of the nonlinear transfer functions N_M and N_M on this angle. This can be better appreciated from Fig. 3.7 showing the $N_K^{(\theta)}$ and $N_M^{(\theta)}$ introduced in previous subsection. They exhibit different dependencies over θ, resulting in different characters of

the transverse cascade for the kinetic and magnetic energies. Note the opposite relative trends between $I_K^{(\theta)}$ and $N_K^{(\theta)}$ [Fig. 3.7(a)] and between $I_M^{(\theta)}$ and $N_M^{(\theta)}$ [Fig. 3.7(b)] with respect to θ:

$$I_K^{(\theta)} \leq 0 \;\; and \;\; N_K^{(\theta)} > 0 \;\; at \;\; 0 \leq \theta \leq \pi/2,$$

$$I_K^{(\theta)} \geq 0 \;\; and \;\; N_K^{(\theta)} \approx 0 \;\; at \;\; \pi/2 < \theta \leq \pi.$$

On the other hand,

$$I_M^{(\theta)} \geq 0 \;\; and \;\; N_M^{(\theta)} \leq 0 \;\; at \;\; 0 \leq \theta \lesssim 0.3\pi,$$

$$I_M^{(\theta)} \approx 0 \;\; and \;\; N_M^{(\theta)} > 0 \;\; at \;\; 0.3\pi \lesssim \theta \leq \pi.$$

This implies that the region of $\mathbf{k}-$plane, where SFHs are replenished with kinetic energy by nonlinearity (i.e., where $N_K > 0$), lies on the right side of the kinetic energy injection region with $I_K > 0$, whereas the region where SFHs are replenished with magnetic energy by nonlinearity (i.e., where $N_M > 0$) lies on the left side of the magnetic energy injection region with $I_M > 0$, as also seen in Fig. 5. As explained below, this specific arrangement of the injection and nonlinear redistribution areas for the magnetic energy in spectral plane appears to be crucial to the sustenance of the turbulence.

After characterizing the specific activity of the linear injection and nonlinear transfer terms in $\mathbf{k}-$plane associated with the presence of shear, we now consider the evolution of SFHs in the quasi-steady turbulence and identify a mechanism sustaining this state. As noted above, apart from these terms, Eqs. (3.21) and (3.22) also contain terms describing drift of SFHs in spectral plane

due to shear flow. In the upper half-plane ($k_y > 0$) we focus on, all SFHs drift along the k_x-axis direction and cross the injection and transfer regions in succession. Since the turbulence is quasi-steady, these three basic processes involved in the spectral Eqs. (3.21) and (3.22): linear drift of SFHs, energy injection and nonlinear transfer, together with viscous and resistive dissipation, are in subtle balance, or cooperation, resulting in the closed (positive) feedback loop that energetically maintains this state. We interpret the workings of this loop as follows. Let us start the loop cycle. The nonlinear transfer functions N_K and N_M supply (from a previous cycle) SFHs with kinetic energy mainly at wavenumbers with polar angles $0 \leq \theta \lesssim 0.6\pi$ and $0.7\pi \lesssim \theta \leq \pi$, where $N_K > 0, N_K^{(\theta)} > 0$, and magnetic energy at $0.3\pi \lesssim \theta \leq \pi$, where $N_M, N_M^{(\theta)} > 0$ [see Figs. 3.5(e), 3.5(f) and 3.7]. Then, these SFHs drift along the k_x-direction and enter the injection regions, where $I_K > 0$ and $I_M > 0$. As a result, the kinetic energy of those SFHs with $k_y \lesssim 0.1$ and the magnetic energy of those SFHs with $k_y \gtrsim 0.05$ grow at the expense of the mean flow – just at this stage the kinetic and magnetic energies are being injected into the turbulence due to I_K and I_M from the mean flow. Then, the SFHs move into the regions where $N_K < 0$ and $N_M < 0$ and hence these nonlinear terms now act to transfer part of the kinetic and magnetic energies from the amplified SFHs back, respectively, to the regions where $N_K > 0$ and $N_M > 0$, from which these SFHs started off, in this way regenerating new SFHs there (positive nonlinear feedback). Towards the end of the cycle, part of the original SFH's kinetic energy is returned to the mean flow, since $I_K \leq 0$ at $0 \leq \theta \leq \pi/2$, so effectively there

is no net gain of the turbulent kinetic energy from the mean shear flow; the second part, which goes into the new SFHs, is taken from the magnetic energy via the nonlinear exchange by positive N_K (at $k_y \gtrsim 0.1$) and the third part is gradually dissipated due to viscosity as the SFH drifts further towards larger wavenumbers ($k \gtrsim k_D$). So, during each cycle, the SFHs gain primarily the magnetic energy from the mean flow due to the injection term I_M. Part of this magnetic energy is transformed by nonlinearity into the kinetic, as mentioned above, and the other part into magnetic energies of the newly created SFHs. The rest of the magnetic energy is dissipated due to resistivity. As seen from Figs. 3.5(f) and 3.7(b), in $\mathbf{k}-$plane, the magnetic injection region lies on the right side of the region of its nonlinear regeneration where $N_M > 0$. As a consequence, these new (regenerated) SFHs will drift through the same cycle and the whole process of (magnetic) energy extraction from the mean flow will be repeated. In this way, a positive feedback loop – a cooperative interplay of the linear transient amplification and nonlinear transverse redistribution of the magnetic spectral energy is established, ensuring the sustenance of a quasi-steady turbulent state at the expense of the background flow energy.

We have seen that a principal role in the above-described MHD self-sustaining mechanism is played by magnetic field perturbations that actually feed turbulence – SFHs, which are able to extract energy from the shear flow by means of the Maxwell stresses (i.e., by I_M), are continuously repopulated by the nonlinear magnetic transfer term. This nonlinear positive feedback for the magnetic perturbations is probably related to the fact that the Maxwell

stress has the "right" positive sign to supply turbulence [Fig. 3.1(b)]. By contrast, the injection region for the kinetic energy in $\mathbf{k}-$plane lies to the left and below the main region of its nonlinear regeneration [at $0 \leq \theta \leq \pi/2$ where $N_K > 0$, see Figs. 3.5(e) and 3.7(a)]. As a result, the majority of new SFHs, drifting along the k_x-axis, cannot cross the injection region and thus continuously gain the kinetic energy from the flow; even the small fraction of new SFHs that can cross this region eventually returns the kinetic energy to the flow where $I_K < 0$. In other words, the nonlinear feedback for the kinetic energy does not operate in a similar, constructive, manner as that for the magnetic energy. This may be related to the Reynolds stress being negative [Fig. 3.1(b)] and hence ineffective in feeding turbulence with kinetic energy. So, in the 2D MHD shear turbulence considered here, unlike the Maxwell stress, the Reynolds stress cannot provide the right sign for transport.

3.5 Discussion and summary

In this Chapter, we have studied the characteristics and self-sustaining mechanism of subcritical MHD turbulence in incompressible magnetized spectrally stable shear flows via DNS using the spectral code SNOOPY. We have examined how the background shear flow interacts with the turbulent fluctuations of the incompressible 2D MHD equations to produce a self-sustained turbulence. The analysis of the turbulence dynamics was carried out in Fourier plane. To keep the problem as manageable as possible and at the same time not to omit key effects of shear on the dynamics of turbulence, as the base

flow we took the simplest but important case of plane MHD Couette flow with linear shear and an imposed background uniform, weak, magnetic field parallel to it. This flow configuration is linearly stable (with decaying linear perturbations at long times) according to classical (modal) stability theory and hence the only cause of transition to turbulence can be a linear transient amplification of (magnetic field) perturbations due to the nonnormality associated with shear at streamwise wavenumbers $k_y < S/u_A$. Consequently, the considered 2D MHD turbulence is subcritical by nature. To understand its sustaining mechanism, we Fourier transformed basic MHD equations and derived evolution equations for the perturbed kinetic and magnetic spectral energies in wavenumber plane. In these spectral equations, using the simulation results, we calculated individual terms, which are divided into two types – terms of linear and nonlinear origin. The terms of linear origin – the Maxwell and Reynolds stresses – are responsible for energy exchange between the turbulence and the mean flow through transient amplification of perturbation harmonics due to shear. However, as we have shown, only the positive Maxwell stress appears to be a dominant (magnetic) energy injector for the turbulence; it is much larger than the Reynolds stress, which has a negative sign and therefore does not contribute to the turbulent kinetic energy gain. Another linear term due to shear in these equations makes the spectral energies drift in the spectral plane parallel to the k_x-axis. The nonlinear terms, which do not directly draw the mean flow energy, act to transversely redistribute this energy in Fourier plane, continually repopulating perturbation harmonics

that can undergo transient growth. Thus, we have demonstrated that in spectrally stable shear flows, the subcritical MHD turbulent state is sustained by the interplay of linear and nonlinear processes – the first supplies energy for turbulence via shear-induced transient growth mechanism of magnetic field perturbations (characterized by the Maxwell stresses) and the second plays an important role of providing a positive feedback that makes this transient growth process recur over long times and compensate for high-k dissipation due to viscosity and resistivity.

This picture is consistent with the bypass scenario of subcritical turbulence in spectrally stable shear flows and differs fundamentally from a usual (supercritical) turbulence scenario, which is based on exponentially growing perturbations in a system that permanently supply turbulent energy and do not require nonlinear (positive) feedback for its sustenance. Such a cooperative action of linear transient growth and nonlinear transfer mechanisms relies on anisotropy of the energy spectra, injection and nonlinear cascades in spectral plane (see Fig. 3.5), which is ultimately attributable to the flow shear. This shear-induced anisotropy, i.e., the dependence of spectra and nonlinear transfers on polar angle in $\mathbf{k}-$plane, as we found and analyzed here in the case of MHD flows, appears to be inherent in shear flow turbulence; a similar anisotropy exists in HD shear flows (see Ref. Horton et al. (2010) for details). It differs from the typical anisotropy of classical (shearless) MHD turbulence in the presence of a (strong) background magnetic field (e.g., Ref. Goldreich & Sridhar (1995)) and changes the classical view on nonlinear cascade processes:

traditionally, the net action of nonlinear turbulent processes is interpreted as either a direct or an inverse cascade (e.g., Ref. Biskamp (2003)). Our analysis demonstrates, however, that in MHD shear flows, like HD ones, the dominant nonlinear process, resulting from the spectral anisotropy, is in fact the redistribution of perturbation spatial Fourier harmonics over the wavevector *angles*. (Probably for this reason, in our simulations with background shear we did not observe the typical 2D coherent magnetic structures that grow via merging due to inverse cascade of magnetic helicity Biskamp & Welter (1989); Wu & Chang (2001)). These anisotropic energy transfers in Fourier space have been termed *nonlinear transverse redistribution*, or the transverse cascade. In the considered flow, the nonlinear transverse cascade plays a vital role in the long-term sustenance of turbulence – it redistributes mainly magnetic spectral energy over different angles in $\mathbf{k}-$plane such that to continually regenerate those harmonics which, drifting in spectral plane, have the potential to undergo transient growth, extracting energy from the mean flow. This indicates that the transverse cascade of spectral (magnetic) energy appears to be characteristic of MHD turbulence in shear flows, so the conventional characterization of nonlinear MHD cascade processes in the presence of the flow shear in terms of direct and inverse cascades, which ignores the transverse cascade, should be generally incomplete and misleading. Identification of this new – transverse – type of nonlinear cascades and its role in the maintenance of shear MHD turbulence represents one of our main results.

We showed that as a result of anisotropy of nonlinear transfers in

$\mathbf{k}-$plane, kinetic and magnetic energy spectra are also highly anisotropic (see Fig. 3.3). These spectra integrated over wavevector angle exhibit power-law behavior for intermediate wavenumbers, though with different spectral indices: $k^{-1.4}$ for the kinetic and k^{-2} for the magnetic energies. Despite this, the angle-averaged spectra we found should not be regarded as truly inertial ranges, because the stresses inject kinetic and magnetic energies into turbulence over a broad range of wavenumbers – from the largest scales in the domain down to the shortest scales comparable to dissipation scale – well overlapping with the nonlinear transfer terms (see Figs. 3.6 and 3.7). So, these spectra are determined by the combined effect of linear injection and nonlinear transfer terms. This is in contrast to the usual forced turbulence case, where energy is injected (by external forcing) in a narrow wavenumber band and subsequent development of spectra is due to nonlinearity only (e.g., Refs. Biskamp (2003); Douglas et al. (2008); Newton & Kim (2009)). As noted above, the energy injection by the stresses occurs through the transient amplification of perturbation Fourier harmonics due to shear, implying that the shear plays an important dynamical role at large and intermediate scales ($\gtrsim u_A/S$). However, the angle-averaging of anisotropic spectra (and also of transfer functions) in shear flows, as often done in similar cases, might result in the loss of essential information about the spectral characteristics of shear turbulence because of its angular dependence too.

In the context of the spectral indices, it is interesting to point out that in some regions of the Earth's magnetotail, a magnetic energy spectrum with

a slope close to that obtained here, k^{-2}, is observed Zimbardo et al. (2010). It is hard to attribute this observational result to either the Kolmogorov or the IK spectra. This may suggest the influence of shear flow on the dynamics of the magnetotail turbulence and formation of its spectrum. The way we see it, definite conclusions can be drawn by performing a numerical analysis similar to that presented here for a specific 3D model configuration of the magnetotail.

In this Chapter, we have considered 2D dynamics and a brief discussion of 3D MHD turbulence in magnetized shear flows is in order. According to the classical view, there is a fundamental difference in the nonlinear dynamics of 2D versus 3D HD processes: 3D ones are characterized by a direct cascade of energy, while 2D ones by inverse cascade. By contrast, in MHD, the nonlinear dynamics of 2D and 3D processes are similar in the sense that cascade directions of characteristic quantities (energy, helicity, etc.) are identical (see e.g., Ref. Biskamp (2003)). As for the transverse cascade analyzed in this Chapter, it occurs in HD as well as in MHD shear flows. It is well-known that in HD shear flows, 2D turbulence is not maintained and dies out (without external forcing), i.e., inverse cascade modified by transverse cascade is unable to sustain turbulence (HD turbulence in shear flows is usually 3D). The present study demonstrates that, unlike HD shear flows, self-sustained 2D turbulence can do exist in MHD shear flows owing to the transverse cascade. Being dependent on the shear, the transverse cascade is expected to occur and play an important role in the dynamics of 3D MHD shear turbulence too. But further studies should clarify, whether the nonlinear dynamics with the third $z-$direction

(perpendicular to the flow plane) represents just a mere extension of the basic self-sustaining process described here in 2D or introduces a qualitatively new contribution. In any case, the transverse cascade will remain a vital ingredient in the self-sustenance of turbulence in 3D too. Although our analysis is limited to 2D, since these are the streamwise and shearwise directions, it allows us to bring out a basic mechanism underlying the self-sustenance (via interplay of linear transient amplification and nonlinear transverse cascade processes) and properties of subcritical MHD shear turbulence.

Chapter 4

Nonlinear transverse cascade and sustenance of MRI-turbulence in Keplerian disks with an azimuthal magnetic field

4.1 Introduction

The problem of the onset and sustenance of turbulence in accretion disks lies at the basis of understanding different aspects of disk dynamics and evolution: secular redistribution of angular momentum yielding observationally obtained accretion rates, dynamo action and generation of magnetic fields and outflows, possibility of appearance of coherent structures (e.g., vortices, zonal flows, pressure bumps) that can form sites for planet formation. Investigations in this direction acquired new impetus and became more active since Balbus & Hawley (1991) demonstrated the relevance and significance of the magnetorotational instability (MRI) for disks. Today the MRI is considered as the most likely cause of magnetohydrodynamic (MHD) turbulence in disks and hence a driver agent of the above phenomena. Starting from the 1990s a vast number of analytical and numerical studies have investigated different aspects of linear and nonlinear evolution of the MRI in three-dimensional (3D) Keplerian disks using both local shearing box and global approaches for different configurations (unstratified and stratified, incompressible and compress-

ible, with vertical and/or azimuthal magnetic fields having zero and nonzero net fluxes) at different domain sizes and resolutions (see e.g., Armitage, 2011; Fromang, 2013, for a review).

In this Chapter (related to (Gogichaishvili et al., 2017)), we consider a local model of a disk threaded by a nonzero net azimuthal/toroidal magnetic field. The linear stability analysis showed that only non-axisymmetric perturbations can exhibit the MRI for this orientation of the background field (Balbus & Hawley, 1992; Ogilvie & Pringle, 1996; Terquem & Papaloizou, 1996; Papaloizou & Terquem, 1997; Brandenburg & Dintrans, 2006; Salhi et al., 2012; Shtemler et al., 2012). Such perturbations are, however, sheared by the disk's differential rotation (shear) and as a result the MRI acquires a transient nature, while the flow stays exponentially, or spectrally stable. Nevertheless, as early seminal numerical simulations by Hawley et al. (1995) revealed, the transient MRI in the presence of an azimuthal field in fact causes transition to MHD turbulence. However, the transient growth itself, which in this case is the only available source of energy for turbulence, cannot ensure a long-term sustenance of the latter without appropriate nonlinear feedback. In other words, the role of nonlinearity becomes crucial: it lies at the heart of the sustenance of turbulence. Thus, the transition to turbulence in the presence of azimuthal field fundamentally differs from that in the case of the vertical field, where the MRI grows exponentially forming a channel flow, which, in turn, breaks down into turbulence due to secondary (parasitic) instabilities (Goodman & Xu, 1994; Hawley et al., 1995; Bodo et al., 2008; Pessah & Goodman, 2009;

Latter et al., 2009; Pessah, 2010; Longaretti & Lesur, 2010; Murphy & Pessah, 2015).

The first developments of the MRI in magnetized disks in the 1990s coincided with the period of the breakthrough of the fluid dynamical community in understanding the dynamics of spectrally stable (i.e., without exponentially growing eigenmodes) hydrodynamic (HD) shear flows (see e.g., Reddy et al., 1993; Trefethen et al., 1993; Farrell & Ioannou, 1996; Schmid & Henningson, 2001; Schmid, 2007). The nonnormality of these flows, i.e., the nonorthogonality of the eigenfunctions of classical modal approach, had been demonstrated and its consequences – the transient/nonmodal growth of perturbations and the transition to turbulence were thoroughly analyzed. There are no exponentially growing modes in such flows and the turbulence is energetically supported only by the linear nonmodal growth of perturbations due to the shear flow nonnormality.

Differentially rotating disks represent special case of shear flows and hence the effects of nonnormality inevitably play a key role in their dynamics (e.g., Chagelishvili et al., 2003; Mukhopadhyay et al., 2005; Zhuravlev & Razdoburdin, 2014; Razdoburdin & Zhuravlev, 2017). In particular, in magnetized disks, the nonmodal/transient growth of the MRI over intermediate (dynamical) times can be actually more relevant in many situations than its modal growth (Mamatsashvili et al., 2013; Squire & Bhattacharjee, 2014). Since in the present case of azimuthal field, the MRI exhibits only transient rather than exponential growth, the resulting turbulence, like in spectrally stable HD

shear flows, is expected to be governed by a subtle cooperation of this non-modal growth and nonlinear processes. As is shown in previous Chapter, this is indeed the case for an analogous two-dimensional (2D) MHD flow with linear shear and magnetic field parallel to it and the flow configuration considered here in fact represents its 3D generalization. So, our main goal is to investigate the spectral properties and sustaining dynamics of MHD turbulence driven by the transient amplification of the MRI in disks with a net nonzero azimuthal field.

The dynamics and statistics of MRI-driven MHD turbulence in Keplerian disk flows have been commonly analyzed and interpreted in physical space rather than in Fourier space. This also concerns studies of disks with nonzero net azimuthal magnetic field. Below we cite the most relevant ones. Hawley et al. (1995); Guan et al. (2009); Guan & Gammie (2011); Nauman & Blackman (2014); Ross et al. (2016) in the shearing box, and Fromang & Nelson (2006); Beckwith et al. (2011); Flock et al. (2011, 2012a); Sorathia et al. (2012); Hawley et al. (2013); Parkin & Bicknell (2013) in global disk simulations extensively investigated the dependence of the dynamics and saturation of the MRI-turbulence without explicit dissipation on the domain size, resolution and imposed azimuthal field strength. Fleming et al. (2000) in local model and Flock et al. (2012b) in global model addressed the influence of resistivity and established a critical value of magnetic Reynolds number for the existence of turbulence. Simon & Hawley (2009) and Meheut et al. (2015) included also viscosity together with resistivity and showed that at fixed field strength the

saturation amplitude mainly depends on the magnetic Prandtl number, that is, the ratio of viscosity to resistivity, if the latter is larger than unity and the Reynolds number is high enough. On the other hand, at Prandtl numbers smaller than unity the turbulence sustenance is more delicate: it appears to be independent of the Prandtl number and mainly determined by the magnetic Reynolds number. Simon & Hawley (2009) attributed this behavior to the small-scale resistive dissipation processes (reconnection), which are thought to be central in the saturation process.

Part of these papers based on the local approximation (Hawley et al., 1995; Fleming et al., 2000; Nauman & Blackman, 2014; Meheut et al., 2015) do present analysis of energy density power spectrum, but in somewhat restricted manner by considering either averaging over wavevector angle, i.e., averages over spherical shells of constant $|\mathbf{k}|$, or slices along different directions in Fourier space. However, there are several studies of MRI turbulence also in the local approximation, but with nonzero net vertical magnetic flux (Lesur & Longaretti, 2011) and with zero net flux (Fromang & Papaloizou, 2007; Simon et al., 2009; Davis et al., 2010), which go beyond energy spectrum and describe the dynamics of MRI- turbulence and associated energy injection (stresses) and nonlinear transfer processes in Fourier space, but again in a restricted manner by using shell-averaging procedure and/or reduced one-dimensional (1D) spectrum along a certain direction in Fourier space by integrating in the other two. However, as demonstrated by Hawley et al. (1995); Lesur & Longaretti (2011); Murphy & Pessah (2015) for MRI-turbulence (with net vertical field)

and in previous Chapter related to 2D MHD shear flow turbulence in Fourier space, the power spectra and underlying dynamics are notably anisotropic due to shear, i.e., depend quite strongly also on the orientation of wavevector $\mathbf{k}$ in Fourier space rather than only on its magnitude $|\mathbf{k}|$. This is in contrast to a classical isotropic forced turbulence without background velocity shear, where energy cascade proceeds along $\mathbf{k}$ only (Biskamp, 2003). This shear-induced anisotropy also differs from the typical anisotropy of classical shearless MHD turbulence in the presence of a (strong) background magnetic field (Goldreich & Sridhar, 1995). It leads to anisotropy of nonlinear processes and particularly to the nonlinear transverse cascade (see below) that play a central role in the sustenance of turbulence in the presence of transient growth. Consequently, the shell-averaging done in the above studies is misleading, because it completely leaves out shear-induced spectral anisotropy, which is thus an essential ingredient of the dynamics of shear MHD turbulence. The recent works by Meheut et al. (2015) and Murphy & Pessah (2015) share a similar point of view, emphasizing the importance of describing anisotropic shear MRI-turbulence using a full 3D spectral analysis instead of using spherical shell averaging in Fourier space, which is applicable only for isotropic turbulence without shear. Such a generalized treatment is a main goal of this Chapter. In particular, Murphy & Pessah (2015) employ a new approach that consists in using invariant maps for characterizing anisotropy of MRI-driven turbulence in physical space and dissecting the 3D Fourier spectrum along the most relevant planes, as defined by the type of anisotropy of the flows.

As for the global disk studies cited above, relatively little attention is devoted to the dynamics of MRI-turbulence in Fourier space. This is, however, understandable, since in contrast to the cartesian shearing box model, global disk geometry makes it harder to perform Fourier analysis in all three, radial, azimuthal and meridional directions, so that these studies only consider azimuthal spectra integrated in other two directions.

Recently, we have numerically studied a cooperative interplay of linear transient growth and nonlinear processes ensuring the sustenance of nonlinear perturbations in hydrodynamic and 2D MHD plane spectrally stable constant shear flows (Horton et al., 2010; Mamatsashvili et al., 2014, 2016). Performing the analysis of dynamical processes in Fourier space, we showed that the shear-induced spectral anisotropy gives rise to a new type of nonlinear cascade process that leads to transverse redistribution of modes in $\mathbf{k}$-space, i.e. to a redistribution over wavevector angles. This process, referred to as *the nonlinear transverse cascade*, originates ultimately from flow shear and fundamentally differs from the canonical (direct and inverse) cascade processes accepted in classical Kolmogorov or Iroshnikov-Kraichnan (IK) theories of turbulence (see e.g., Biskamp, 2003). The new approach developed in these studies and the main results can be summarized as follows:

– identifying modes that play a key role in the sustaining process of the turbulence;

– defining a wavenumber area in Fourier space that is vital in the sustenance of turbulence;

– defining a range of aspect ratios of the simulation domain for which the dynamically important modes are fully taken into account;
– revealing the dominance of the nonlinear transverse cascade in the dynamics;
– showing that the turbulence is sustained by a refined interplay between the linear transient (nonmodal) growth and the nonlinear transverse cascade.

In this Chapter, with the same spirit and goals in mind, we take the approach of Chapter 3 to investigate the dynamics and sustenance of MHD turbulence driven by the transient growth of MRI with a net nonzero azimuthal field in a Keplerian disk flow. We adopt the shearing box model of the disk (see e.g., Hawley et al., 1995), where the flow is characterized by constant shear rate, as that considered in that paper, except it is 3D, including rotation (Coriolis force) and vertical thermal stratification. To capture the spectral anisotropy of the MRI-turbulence, we analyze the linear and nonlinear dynamical processes and their interplay in 3D Fourier space in full *without* using the above-mentioned procedure of averaging over spherical shells of constant $k = |\mathbf{k}|$. So, our study is intended to be more general than the above-mentioned studies that also addressed the spectral dynamics of MRI-turbulence. One of our goals is to demonstrate the realization and efficiency of the transverse cascade and its role in the turbulence dynamics also in the 3D case, as we did for 2D MHD shear flow. Although in 3D perturbation modes are more diverse and, of course, modify the dynamics, still the essence of the cooperative interplay of linear (transient) and nonlinear (transverse cascade) processes should be preserved.

We pay particular attention to the choice of the aspect ratio of the simulation box, so as to encompass as full as possible the modes exhibiting the most effective amplification due to the transient MRI. To this aim, we apply the method of optimal perturbations, widely used in fluid dynamics for characterizing the nonmodal growth in spectrally stable shear flows (see e.g., Farrell & Ioannou, 1996; Schmid & Henningson, 2001; Zhuravlev & Razdoburdin, 2014), to the present MRI problem (see also Squire & Bhattacharjee, 2014). These are perturbations that undergo maximal transient growth during the dynamical time. In this framework, we define areas in Fourier space, where the transient growth is more effective – these areas cover small wavenumber modes. On the other hand, the simulation box includes only a discrete number of modes and minimum wavenumbers are set by its size. A dense population of modes in these areas of the effective growth in **k**-space is then achieved by suitably choosing the box sizes. In particular, we show that simulations with elongated in the azimuthal direction boxes (i.e., with azimuthal size larger than radial one), do not fully account for this nonmodal effects, since the discrete wavenumbers of modes contained in such boxes scarcely cover the areas of efficient transient growth.

This Chapter is organized as follows. The physical model and derivation of dynamical equations in Fourier space is given in Section 4.2. Selection of the suitable aspect ratio of the simulation box based on the optimal growth calculations is made in Section 4.3. Numerical simulations of the MRI-turbulence at different aspect ratios of the simulation box are done in Section 4.4. In

this Section we present also energy spectra, we determine dynamically active modes and delineate the vital area of turbulence, where the active modes and hence the sustaining dynamics are concentrated. The analysis of the interplay of the linear and nonlinear processes in Fourier space and the sustaining mechanism of the turbulence is described in Section 4.5. In this Section we also reveal the basic subcycle of the sustenance, describe the importance of the magnetic nonlinear term in the generation and maintenance of the zonal flow, examine the effect of the box aspect ratio and demonstrate the universality of the sustaining scheme. A summary and discussion are given in Section 4.6.

4.2 Physical model and equations

We consider the motion of an incompressible conducting fluid with constant kinematic viscosity ν, thermal diffusivity χ and Ohmic resistivity η, in the shearing box centered at a radius r_0 and rotating with the disk at angular velocity $\Omega(r_0)$. Adopting the Boussinesq approximation for vertical thermal stratification (Balbus & Hawley, 1991; Lesur & Ogilvie, 2010), the governing equations of the non-ideal MHD become

$$\frac{\partial \mathbf{U}}{\partial t}+(\mathbf{U}\cdot\nabla)\mathbf{U} = -\frac{1}{\rho}\nabla P+\frac{(\mathbf{B}\cdot\nabla)\,\mathbf{B}}{4\pi\rho}-2\mathbf{\Omega}\times\mathbf{U}+2q\Omega^2 x\mathbf{e}_x-\Lambda N^2\theta\ \mathbf{e}_z+\nu\nabla^2\mathbf{U}, \tag{4.1}$$

$$\frac{\partial \theta}{\partial t}+\mathbf{U}\cdot\nabla\theta = \frac{u_z}{\Lambda}+\chi\nabla^2\theta, \tag{4.2}$$

$$\frac{\partial \mathbf{B}}{\partial t} = \nabla\times(\mathbf{U}\times\mathbf{B})+\eta\nabla^2\mathbf{B}, \tag{4.3}$$

$$\nabla\cdot\mathbf{U} = 0, \tag{4.4}$$

$$\nabla \cdot \mathbf{B} = 0, \tag{4.5}$$

where $\mathbf{e}_x$, $\mathbf{e}_y$, $\mathbf{e}_z$ are the unit vectors, respectively, along the radial (x), azimuthal (y) and vertical (z) directions, ρ is the density, $\mathbf{U}$ is the velocity, $\mathbf{B}$ is the magnetic field, P is the total pressure, equal to the sum of the thermal and magnetic pressures, $\theta \equiv \delta\rho/\rho$ is the perturbation of the density logarithm (or entropy, since pressure perturbations are neglected in the Boussinesq approximation). Finally, N^2 is the Brunt-Väisälä frequency squared that controls the stratification. It is assumed to be positive and spatially constant, equal to $N^2 = 0.25\Omega^2$, formally corresponding to a stably stratified (i.e., convectively stable) local model along the vertical z-axis (Lesur & Ogilvie, 2010). For dimensional correspondence with the usual Boussinesq approximation, we define a stratification length $\Lambda \equiv g/N^2$, where g is the vertical component of the gravity. Note, however, that Λ cancels out from the equations if we normalize the density logarithm by $\Lambda\theta \to \theta$, which will be used henceforth. So, here we take into account the effects of thermal stratification in a simple way. Bodo et al. (2012, 2013) studied more sophisticated models of stratified MRI-turbulence in the shearing box, treating thermal physics self-consistently with dynamical equations. The shear parameter $q = -d\ln\Omega/d\ln r$ is set to $q = 3/2$ for a Keplerian disk.

Equations (4.1)-(4.5) have a stationary equilibrium solution – an azimuthal flow along the y-direction with linear shear of velocity in the the radial x-direction, $\mathbf{U}_0 = (0, -q\Omega x, 0)$, with the total pressure P_0, density ρ_0 and threaded by an azimuthal uniform background magnetic field, $\mathbf{B}_0 =$

$(0, B_{0y}, 0), B_{0y} > 0$. This simple, but important configuration, which corresponds to a local version of a Keplerian flow with toroidal field, allows us to grasp the key effects of the shear on the perturbation dynamics and ultimately on a resulting turbulent state.

Consider perturbations of the velocity, total pressure and magnetic field about the equilibrium, $\mathbf{u} = \mathbf{U} - \mathbf{U}_0, p = P - P_0, \mathbf{b} = \mathbf{B} - \mathbf{B}_0$. Substituting them into Equations (4.1)-(4.5) and rearranging the nonlinear terms with the help of divergence-free conditions (4.4) and (4.5), we arrive to the system (A.1)-(A.9) governing the dynamics of perturbations with arbitrary amplitude that is given in Appendix A. These equations are solved within a box with sizes (L_x, L_y, L_z) and resolutions (N_x, N_y, N_z), respectively, in the $x, y, z-$directions. We use standard for the shearing box boundary conditions: shearing-periodic in x and periodic in y and z (Hawley et al., 1995). For stratified disks, outflow boundary conditions in the vertical direction are more appropriate, however, in the present study, as mentioned above, we adopt a local approximation in z with spatially constant N^2 that justifies our choice of the periodic boundary conditions in this direction (Lesur & Ogilvie, 2010). This does not affect the main dynamical processes in question.

4.2.1 Energy equation

The perturbation kinetic, thermal and magnetic energy densities are defined, respectively, as

$$E_K = \frac{1}{2}\rho_0 \mathbf{u}^2, \quad E_{th} = \frac{1}{2}\rho_0 N^2 \theta^2, \quad E_M = \frac{\mathbf{b}^2}{8\pi}.$$

From the main Equations (A.1)-(A.9) and the shearing box boundary conditions, after some algebra, we can readily derive the evolution equations for the volume-averaged kinetic, thermal and magnetic energy densities

$$\frac{d}{dt}\langle E_K\rangle = q\Omega\,\langle\rho_0 u_x u_y\rangle - N^2\,\langle\rho_0\theta u_z\rangle + \frac{1}{4\pi}\,\langle\mathbf{B}_0\mathbf{u}\otimes\nabla\mathbf{b}\rangle - \frac{1}{4\pi}\,\langle\mathbf{b}\mathbf{b}\otimes\nabla\mathbf{u}\rangle - \rho_0\nu\langle(\nabla\mathbf{u})^2\rangle, \tag{4.6}$$

$$\frac{d}{dt}\langle E_{th}\rangle = N^2\,\langle\rho_0\theta u_z\rangle - \rho_0 N^2\chi\langle(\nabla\theta)^2\rangle, \tag{4.7}$$

$$\frac{d}{dt}\langle E_M\rangle = q\Omega\left\langle -\frac{b_x b_y}{4\pi}\right\rangle + \frac{1}{4\pi}\,\langle\mathbf{B}_0\mathbf{b}\otimes\nabla\mathbf{u}\rangle + \frac{1}{4\pi}\,\langle\mathbf{b}\mathbf{b}\otimes\nabla\mathbf{u}\rangle - \frac{\eta}{4\pi}\langle(\nabla\mathbf{b})^2\rangle, \tag{4.8}$$

where the angle brackets denote an average over the box. Adding up Equations (4.6)-(4.8), the cross terms of linear origin on the right hand side (rhs), proportional to N^2 and $\mathbf{B}_0$ (which describe kinetic-thermal and kinetic-magnetic energy exchange, respectively) and the nonlinear terms cancel out because of the boundary conditions. As a result, we obtain the equation for the total energy density $E = E_K + E_{th} + E_M$,

$$\frac{d\langle E\rangle}{dt} = q\Omega\left\langle \rho_0 u_x u_y - \frac{b_x b_y}{4\pi}\right\rangle - \rho_0\nu\langle(\nabla\mathbf{u})^2\rangle - \rho_0 N^2\chi\langle(\nabla\theta)^2\rangle - \frac{\eta}{4\pi}\langle(\nabla\mathbf{b})^2\rangle. \tag{4.9}$$

The first term on the rhs of Equation (4.9) is the flow shear, $q\Omega$, multiplied by the volume-averaged total stress. The total stress is a sum of the Reynolds, $\rho_0 u_x u_y$, and Maxwell, $-b_x b_y/4\pi$, stresses that describe, respectively, exchange of kinetic and magnetic energies between perturbations and the background flow in Equations (4.6) and (4.8). Note that they originate from the linear

terms proportional to shear in Equations (A.2) and (A.6). The stresses also determine the rate of angular momentum transport (e.g., Hawley et al., 1995; Balbus, 2003) and thus are one of the important diagnostics of turbulence. The negative definite second, third and fourth terms describe energy dissipation due to viscosity, thermal diffusivity and resistivity, respectively. Note that a net contribution from the nonlinear terms has canceled out in the total energy evolution Equation (4.9) after averaging over the box. Thus, only Reynolds and Maxwell stresses can supply perturbations with energy, extracting it from the background flow due to the shear. In the case of the MRI-turbulence studied below, these stresses ensure energy injection into turbulent fluctuations. The nonlinear terms, not directly tapping into the flow energy and therefore not changing the total perturbation energy, act only to redistribute energy among different wavenumbers as well as among components of velocity and magnetic field (see below). In the absence of shear ($q = 0$), the contribution from the Reynolds and Maxwell stresses disappears in Equation (4.9) and hence the total perturbation energy cannot grow, gradually decaying due to dissipation.

4.2.2 Spectral representation of the equations

Before proceeding further, we normalize the variables by taking Ω^{-1} as the unit of time, the disk scale height H as the unit of length, ΩH as the unit of velocity, $\Omega H\sqrt{4\pi\rho_0}$ as the unit of magnetic field and $\rho_0\Omega^2H^2$ as the unit of pressure and energy. Viscosity, thermal diffusivity and resistivity are measured, respectively, by Reynolds number, Re, Péclet number, Pe, and

magnetic Reynolds number, Rm, defined as

$$\mathrm{Re} = \frac{\Omega H^2}{\nu}, \quad \mathrm{Pe} = \frac{\Omega H^2}{\chi}, \quad \mathrm{Rm} = \frac{\Omega H^2}{\eta}.$$

All the simulations share the same Re = Pe = Rm = 3200 (i.e., the magnetic Prandtl number Pm = Rm/Re = 1). The strength of the imposed background uniform azimuthal magnetic field is measured by a parameter $\beta = 2\Omega^2 H^2/v_A^2$, which we fix to $\beta = 200$, where $v_A = B_{0y}/(4\pi\rho_0)^{1/2}$ is the corresponding Alfvén speed. In the incompressible case, this parameter is a proxy of the usual plasma β parameter (Longaretti & Lesur, 2010), since the sound speed in thin disks is $c_s \sim \Omega H$. In this non-dimensional units, the mean field becomes $B_{0y} = \sqrt{2/\beta} = 0.1$.

Our primary interest lies in the spectral aspect of the dynamics, so we start with decomposing the perturbations $f \equiv (\mathbf{u}, p, \theta, \mathbf{b})$ into spatial Fourier harmonics/modes

$$f(\mathbf{r}, t) = \int \bar{f}(\mathbf{k}, t) \exp\left(\mathrm{i}\mathbf{k}\cdot\mathbf{r}\right) d^3\mathbf{k} \tag{4.10}$$

where $\bar{f} \equiv (\bar{\mathbf{u}}, \bar{p}, \bar{\theta}, \bar{\mathbf{b}})$ denotes the corresponding Fourier transforms. Substituting decomposition (4.10) into perturbation Equations (A.1)-(A.9), taking into account the above normalization and eliminating the pressure (see derivation in Appendix B), we obtain the following evolution equations for the quadratic forms of the spectral velocity, logarithmic density (entropy) and magnetic field:

$$\frac{\partial}{\partial t}\frac{|\bar{u}_x|^2}{2} = -qk_y\frac{\partial}{\partial k_x}\frac{|\bar{u}_x|^2}{2} + \mathcal{H}_x + \mathcal{I}_x^{(u\theta)} + \mathcal{I}_x^{(ub)} + \mathcal{D}_x^{(u)} + \mathcal{N}_x^{(u)}, \tag{4.11}$$

$$\frac{\partial}{\partial t}\frac{|\bar{u}_y|^2}{2} = -qk_y\frac{\partial}{\partial k_x}\frac{|\bar{u}_y|^2}{2} + \mathcal{H}_y + \mathcal{I}_y^{(u\theta)} + \mathcal{I}_y^{(ub)} + \mathcal{D}_y^{(u)} + \mathcal{N}_y^{(u)}, \tag{4.12}$$

$$\frac{\partial}{\partial t}\frac{|\bar{u}_z|^2}{2} = -qk_y\frac{\partial}{\partial k_x}\frac{|\bar{u}_z|^2}{2} + \mathcal{H}_z + \mathcal{I}_z^{(u\theta)} + \mathcal{I}_z^{(ub)} + \mathcal{D}_z^{(u)} + \mathcal{N}_z^{(u)}, \tag{4.13}$$

$$\frac{\partial}{\partial t}\frac{|\bar{\theta}|^2}{2} = -qk_y\frac{\partial}{\partial k_x}\frac{|\bar{\theta}|^2}{2} + \mathcal{I}^{(\theta u)} + \mathcal{D}^{(\theta)} + \mathcal{N}^{(\theta)}, \tag{4.14}$$

$$\frac{\partial}{\partial t}\frac{|\bar{b}_x|^2}{2} = -qk_y\frac{\partial}{\partial k_x}\frac{|\bar{b}_x|^2}{2} + \mathcal{I}_x^{(bu)} + \mathcal{D}_x^{(b)} + \mathcal{N}_x^{(b)}, \tag{4.15}$$

$$\frac{\partial}{\partial t}\frac{|\bar{b}_y|^2}{2} = -qk_y\frac{\partial}{\partial k_x}\frac{|\bar{b}_y|^2}{2} + \mathcal{M} + \mathcal{I}_y^{(bu)} + \mathcal{D}_y^{(b)} + \mathcal{N}_y^{(b)}, \tag{4.16}$$

$$\frac{\partial}{\partial t}\frac{|\bar{b}_z|^2}{2} = -qk_y\frac{\partial}{\partial k_x}\frac{|\bar{b}_z|^2}{2} + \mathcal{I}_z^{(bu)} + \mathcal{D}_z^{(b)} + \mathcal{N}_z^{(b)}. \tag{4.17}$$

These seven dynamical equations in Fourier space, which are the basis for the subsequent analysis, describe processes of linear, $\mathcal{H}_i(\mathbf{k},t)$, $\mathcal{I}_i^{(u\theta)}(\mathbf{k},t)$, $\mathcal{I}^{(\theta u)}(\mathbf{k},t)$, $\mathcal{I}_i^{(ub)}(\mathbf{k},t)$, $\mathcal{I}_i^{(bu)}(\mathbf{k},t)$, $\mathcal{M}(\mathbf{k},t)$, and nonlinear, $\mathcal{N}_i^{(u)}(\mathbf{k},t)$, $\mathcal{N}^{(\theta)}(\mathbf{k},t)$, $\mathcal{N}_i^{(b)}(\mathbf{k},t)$, origin, where the index $i = x, y, z$ henceforth. $\mathcal{D}_i^{(u)}(\mathbf{k},t)$, $\mathcal{D}^{(\theta)}(\mathbf{k},t)$, $\mathcal{D}_i^{(b)}(\mathbf{k},t)$ describe the effects of viscous, thermal and resistive dissipation as a function of wavenumber and are negative definite. These terms come from the respective linear and nonlinear terms in main Equations (A.1)-(A.7) and their explicit expressions are derived in Appendix B. In the turbulent regime, these basic linear and nonlinear processes are subtly intertwined, so before embarking on calculating and analyzing these terms from the simulation data, we first describe them in more detail below. Equations (4.11)-(4.17) serve as a mathematical basis for our main goal – understanding the character of the interplay of the dynamical processes sustaining the MRI-turbulence. Since we consider a finite box in physical space, the perturbation dynamics also depends

on the smallest wavenumber available in the box (see Section 3), which is set by its sizes L_x, L_y, L_z and is a free parameter in the shearing box.

To get a general feeling, as in Simon et al. (2009); Lesur & Longaretti (2011), we derive also equations for the spectral kinetic energy, $\mathcal{E}_K = (|\bar{u}_x|^2 + |\bar{u}_y|^2 + |\bar{u}_z|^2)/2$, by combining Equations (4.11)-(4.13),

$$\frac{\partial \mathcal{E}_K}{\partial t} = -qk_y \frac{\partial \mathcal{E}_K}{\partial k_x} + \mathcal{H} + \mathcal{I}^{(u\theta)} + \mathcal{I}^{(ub)} + \mathcal{D}^{(u)} + \mathcal{N}^{(u)}, \tag{4.18}$$

where

$$\mathcal{H} = \sum_i \mathcal{H}_i = \frac{q}{2}(\bar{u}_x \bar{u}_y^* + \bar{u}_x^* \bar{u}_y),$$

$$\mathcal{I}^{(u\theta)} = \sum_i \mathcal{I}_i^{(u\theta)}, \quad \mathcal{I}^{(ub)} = \sum_i \mathcal{I}_i^{(ub)},$$

$$\mathcal{D}^{(u)} = \sum_i \mathcal{D}_i^{(u)} = -\frac{2k^2}{\mathrm{Re}} \mathcal{E}_K, \quad \mathcal{N}^{(u)} = \sum_i \mathcal{N}_i^{(u)}$$

and for the spectral magnetic energy, $\mathcal{E}_M = (|\bar{b}_x|^2 + |\bar{b}_y|^2 + |\bar{b}_z|^2)/2$, by combining Equations (4.15)-(4.17),

$$\frac{\partial \mathcal{E}_M}{\partial t} = -qk_y \frac{\partial \mathcal{E}_M}{\partial k_x} + \mathcal{M} + \mathcal{I}^{(bu)} + \mathcal{D}^{(b)} + \mathcal{N}^{(b)}, \tag{4.19}$$

where

$$\mathcal{M} = -\frac{q}{2}(\bar{b}_x \bar{b}_y^* + \bar{b}_x^* \bar{b}_y), \quad \mathcal{I}^{(bu)} = \sum_i \mathcal{I}_i^{(bu)} = -\mathcal{I}^{(ub)},$$

$$\mathcal{D}^{(u)} = \sum_i \mathcal{D}_i^{(u)} = -\frac{2k^2}{\mathrm{Rm}} \mathcal{E}_M, \quad \mathcal{N}^{(b)} = \sum_i \mathcal{N}_i^{(b)}.$$

The equation of the thermal energy, $\mathcal{E}_{th} = N^2|\theta|^2/2$, is straightforward to derive by multiplying Equation (4.14) just by N^2, so we do not write it here.

Besides, we will see below that the thermal energy is much less than the magnetic and kinetic energies, so the thermal processes have a minor contribution in forming the final picture of the turbulence. Similarly, we get the equation for the total spectral energy of perturbations, $\mathcal{E} = \mathcal{E}_K + \mathcal{E}_{th} + \mathcal{E}_M$,

$$\frac{\partial \mathcal{E}}{\partial t} = -qk_y \frac{\partial \mathcal{E}}{\partial k_x} + \mathcal{H} + \mathcal{M} + \mathcal{D}^{(u)} + N^2\mathcal{D}^{(\theta)} + \mathcal{D}^{(b)} + \mathcal{N}^{(u)} + N^2\mathcal{N}^{(\theta)} + \mathcal{N}^{(b)}. \tag{4.20}$$

One can distinguish six basic processes, five of linear and one of nonlinear origin, in Equations (4.11) and (4.17) (and therefore in energy Equations 4.18 and 4.19) that underlie the perturbation dynamics:

1. The first terms on the rhs of Equations (4.11)-(4.17), $-qk_y\partial(.)/\partial k_x$, describe the linear "drift" of the related quadratic forms parallel to the k_x-axis with the normalized velocity qk_y. These terms are of linear origin, arising from the convective derivative on the lhs of the main Equations (A.1)-(A.7) and therefore correspond to the advection by the background flow. In other words, background shear makes the spectral quantities (Fourier transforms) drift in $\mathbf{k}-$space, non-axisymmetric harmonics with $k_y > 0$ and $k_y < 0$ travel, respectively, along and opposite the k_x-axis at a speed $|qk_y|$, whereas the ones with $k_y = 0$ are not advected by the flow. This drift in Fourier space is equivalent to the time-varying radial wavenumber, $k_x(t) = k_x(0) + q\Omega k_y t$, in the linear analysis of non-axisymmetric shearing waves in magnetized disks (e.g., Balbus & Hawley, 1992; Johnson, 2007; Pessah & Chan, 2012).

In the energy Equations (4.18) and (4.19), the spectral energy drift, of course, does not change the total kinetic and magnetic energies, since $\int d^3\mathbf{k}\partial(k_y\mathcal{E}_{K,M})/\partial k_x = 0$.

2. The second rhs terms of Equations (4.11)-(4.13), $\mathcal{H}_i$, and Equation (4.16), $\mathcal{M}$, are also of linear origin associated with the shear (Equations B.20-B.22 and B.34), i.e., originate from the linear terms proportional to the shear parameter in Equations (A.2) and (A.6). They describe the interaction between the flow and individual Fourier modes, where the velocity components $|\bar{u}_i|^2$ and the azimuthal field perturbation $|\bar{b}_y|^2$ can grow, respectively, due to $\mathcal{H}_i$ and $\mathcal{M}$, at the expense of the flow. In the present case, such amplification is due to the linear azimuthal MRI fed by the shear. In the presence of the mean azimuthal field, only non-axisymmetric modes exhibit the MRI and since they also undergo the drift in $\mathbf{k}-$space, their amplification acquires a transient nature (Balbus & Hawley, 1992; Papaloizou & Terquem, 1997; Brandenburg & Dintrans, 2006; Salhi et al., 2012; Shtemler et al., 2012). From the expressions (B.20)-(B.22) and (B.34), we can see that $\mathcal{H}_i$ and $\mathcal{M}$ are related to the volume-averaged nondimensional Reynolds and Maxwell stresses entering energy Equations (4.6) and (4.8) through

$$q\langle u_x u_y\rangle = \int \mathcal{H} d^3\mathbf{k}, \qquad q\langle -b_x b_y\rangle = \int \mathcal{M} d^3\mathbf{k},$$

where $\mathcal{H} = \sum_i \mathcal{H}_i$, and hence represent, respectively, the spectra of the Reynolds and Maxwell stresses, acting as the source, or injection of ki-

netic and magnetic energies for perturbation modes at each wavenumber (see Equations 4.18 and 4.19) (see also Fromang & Papaloizou, 2007; Simon et al., 2009; Davis et al., 2010; Lesur & Longaretti, 2011).

3. the cross terms, $\mathcal{I}_i^{(u\theta)}$ and $\mathcal{I}^{(\theta u)}$ (Equations B.23 and B.28) describe, respectively, the effect of the thermal process on the i-component of the velocity, $\bar{u}_i$, and the effect of the z-component of the velocity on the logarithmic density (entropy) for each mode. These terms are also of linear origin, related to the Brunt-Väisälä frequency squared N^2, and come from the corresponding linear terms in Equations (A.3) and (A.4). They are not a source of new energy, as $\sum_i \mathcal{I}_i^{(u\theta)} + N^2 \mathcal{I}^{(\theta u)} = 0$, but rather characterize exchange between kinetic and thermal energies (Equation 4.14 and 4.18), so they cancel out in the total spectral energy Equation (4.20).

4. the second type of cross terms, $\mathcal{I}_i^{(ub)}$ and $\mathcal{I}_i^{(bu)}$ (Equations B.24 and B.35), describe, respectively, the influence of the i-component of the magnetic field, $\bar{b}_i$, on the same component of the velocity, $\bar{u}_i$, and vice versa for each mode. These terms are of linear origin too, proportional to the mean field B_{0y}, and originate from the corresponding terms in Equations (A.1)-(A.3) and (A.5)-(A.7). From the definition it follows that $\mathcal{I}_i^{(ub)} = -\mathcal{I}_i^{(bu)}$ and hence these terms also do not generate new energy for perturbations, but rather exchange between kinetic and magnetic energies (Equations 4.18 and 4.19). They also cancel out in the total spectral energy equation.

5. The terms $\mathcal{D}_i^{(u)}$, $\mathcal{D}^{(\theta)}$ and $\mathcal{D}_i^{(b)}$ (Equations B.25, B.29 and B.36) describe, respectively, dissipation of velocity, logarithmic density (entropy) and magnetic field for each wavenumber. They are obviously of linear origin and negative definite. Comparing these dissipation terms with the energy-supplying terms $\mathcal{H}_i$ and $\mathcal{M}$, we see that the dissipation is at work at large wavenumbers $k \gtrsim k_D \equiv \min(\sqrt{\mathrm{Re}}, \sqrt{\mathrm{Pe}}, \sqrt{\mathrm{Rm}})$.

6. The terms $\mathcal{N}_i^{(u)}$, $\mathcal{N}^{(\theta)}$ and $\mathcal{N}_i^{(b)}$ (Equations B.26, B.30 and B.37) originate from the nonlinear terms in main Equations (A.1)-(A.7) and therefore describe redistributions, or transfers/cascades of the squared amplitudes, respectively, of the i-component of the velocity, $|\bar{u}_i|^2$, entropy, $|\bar{\theta}|^2$, and the i-component of the magnetic field, $|\bar{b}_i|^2$, over wavenumbers in $\mathbf{k}-$space as well as among each other via nonlinear triad interactions. Similarly, the above-defined $\mathcal{N}^{(u)}$, $N^2\mathcal{N}^{(\theta)}$, $\mathcal{N}^{(b)}$ describe nonlinear transfers of kinetic, thermal and magnetic energies, respectively. It follows from the definition of these terms that their sum integrated over an entire Fourier space is zero,

$$\int [\mathcal{N}^{(u)}(\mathbf{k},t) + N^2\mathcal{N}^{(\theta)}(\mathbf{k},t) + \mathcal{N}^{(b)}(\mathbf{k},t)]d^3\mathbf{k} = 0, \tag{4.21}$$

which is, in fact, a direct consequence of cancelation of the nonlinear terms in the total energy Equation (4.9) in physical space. This implies that the main effect of nonlinearity is only to redistribute (scatter) energy (drawn from the background flow by Reynolds and Maxwell stresses) of the kinetic, thermal and magnetic components over wavenumbers and

among each other, while leaving the total spectral energy summed over all wavenumbers unchanged. The nonlinear transfer functions ($\mathcal{N}^{(u)}$, $\mathcal{N}^{(\theta)}$, $\mathcal{N}^{(b)}$) play a central role in MHD turbulence theory – they determine cascades of energies in **k**-space, leading to the development of their specific spectra (e.g., Verma, 2004; Alexakis et al., 2007; Teaca et al., 2009; Sundar et al., 2017). These transfer functions are one of the main focus of the present analysis. One of our main goals is to explore how they operate in the presence of the azimuthal field MRI in disks and ultimately of the shear. Specifically, below we will show that, like in 2D HD and MHD shear flows we studied before (Horton et al., 2010; Mamatsashvili et al., 2014), energy spectra, energy-injection as well as nonlinear transfers are also anisotropic in the quasi-steady MRI-turbulence, resulting in the redistribution of power among wavevector angles in $\mathbf{k}-$space, i.e., the *nonlinear transverse cascade*.

Having described all the terms in spectral equations, we now turn to the total spectral energy Equation (4.20). Each mode drifting parallel to the k_x-axis, go through a dynamically important region in Fourier space, which we call the *vital area*, where *energy-supplying* linear terms, $\mathcal{H}$ and $\mathcal{M}$, and *redistributing* nonlinear terms, $\mathcal{N}^{(u)}$, $\mathcal{N}^{(\theta)}$, $\mathcal{N}^{(b)}$ operate. The net effect of the nonlinear terms in the total spectral energy budget over all wavenumbers is zero according to Equation (4.21). Thus, the only source for the total perturbation energy is the integral over an entire **k**-space $\int(\mathcal{H}+\mathcal{M})d^3\mathbf{k}$ that extracts energy from a vast reservoir of shear flow and injects it into perturbations.

Since the terms $\mathcal{H}$ and $\mathcal{M}$, as noted above, are of linear origin, the energy extraction and perturbation growth mechanisms (the azimuthal MRI) are essentially linear by nature. The role of nonlinearity is to continually provide, or regenerate those modes in **k**-space that are able to undergo the transient MRI, drawing on mean flow energy, and in this way feed the nonlinear state over long times.

4.3 Optimization of the box aspect ratio – linear analysis

It is well known from numerical simulations of MRI-turbulence that its dynamics (saturation) generally depends on the aspect ratio (L_y/L_x, L_x/L_z) of a computational box (e.g., Hawley et al., 1995; Bodo et al., 2008; Guan et al., 2009; Johansen et al., 2009; Shi et al., 2016). In order to understand this dependence and hence appropriately select the aspect ratio in simulations, in our opinion, one should take into account as fully as possible the nonmodal growth of the MRI during intermediate (dynamical) timescales, because it can ultimately play an important role in the turbulence dynamics (Squire & Bhattacharjee, 2014). However, this is often overlooked in numerical studies. So, in this Section, we identify the aspect ratios of the preselected boxes that better take into account the linear transient growth process.

In fluid dynamics, the linear transient growth of perturbations in shear flows is usually quantified using the formalism of optimal perturbations (Farrell & Ioannou, 1996; Schmid & Henningson, 2001; Schmid, 2007). This approach

has already been successfully applied to (magnetized) disk flows (Mukhopadhyay et al., 2005; Zhuravlev & Razdoburdin, 2014; Squire & Bhattacharjee, 2014; Razdoburdin & Zhuravlev, 2017). Such perturbations yield maximum linear nonmodal growth during finite times and therefore are responsible for most of the energy extraction from the background flow. So, in this framework, we quantify the linear nonmodal optimal amplification of the azimuthal MRI as a function of mode wavenumbers for the same parameters adopted in the simulations.

In the shearing box, the radial wavenumber of each non-axisymmetric perturbation mode (shearing wave) changes linearly with time due to shear, $k_x(t) = k_x(0) + q\Omega k_y t$. The maximum possible amplification of the total energy $\mathcal{E} = \mathcal{E}_K + \mathcal{E}_{th} + \mathcal{E}_M$ of a shearing wave, with an initial wavenumber $\mathbf{k}(0) = (k_x(0), k_y, k_z)$ by a specific (dynamical) time t_d is given by

$$G(\mathbf{k}(t_d)) = \max_{\bar{f}(0)} \frac{\mathcal{E}(\mathbf{k}(t_d))}{\mathcal{E}(\mathbf{k}(0))}, \tag{4.22}$$

where the maximum is taken over all initial conditions $\bar{f}(0)$ with a given energy $\mathcal{E}(\mathbf{k}(0))$. The final state at t_d and the corresponding energy $\mathcal{E}(\mathbf{k}(t_d))$ are found from the initial state at $t = 0$ by integrating the linearized version of spectral Equations (B.1)-(B.9) in time for each shearing wave and finding a propagator matrix connecting the initial and final states. Then, expression (4.22) is usually calculated by means of the singular value decomposition of the propagator matrix. The square of the largest singular value then gives the optimal growth factor G for this set of wavenumbers. The corresponding

initial conditions, leading to this highest growth at t_d are called optimal perturbations. (A reader interested in the details of these calculations is referred to Squire & Bhattacharjee (2014), where the formalism of optimal growth and optimal perturbations in MRI-active disks, which is adopted here, is described to a greater extent.) Reference time, during which to calculate the nonmodal growth, is generally arbitrary. We choose it equal to the characteristic (e-folding) time of the most unstable MRI mode, $t_d = 1/\gamma_{max} = 1.33\Omega^{-1}$, where $\gamma_{max} = 0.75\Omega$ is its growth rate (Balbus, 2003; Ogilvie & Pringle, 1996), since it is effectively a dynamical time as well.

Figure 4.1 shows G in $(k_x, k_y)-$plane at fixed k_z as well as its value maximized over the initial $k_x(0)$, $G_{max} = \max_{k_x(0)} G$, represented as a function of k_y, k_z. Because of the k_x-drift, the optimal mode with some initial radial wavenumber $k_x(0)$, at t_d will have the wavenumber $k_x(t_d) = k_x(0) + qk_y t_d$. In the top panel, G is represented as a function of this final wavenumber $k_x(t_d)$. Because of the shear, the typical distribution at fixed k_z is inclined towards the k_x-axis, having larger values on the $k_x/k_y > 0$ side (red region). The most effective nonmodal MRI amplification occurs at smaller wavenumbers, in the areas marked by dark red in both (k_x, k_y) and (k_y, k_z)-planes in Figure 4.1. Thus, the growth of the MRI during the dynamical time appears to favor smaller k_z (see also Squire & Bhattacharjee, 2014), as opposed to the transient growth of the azimuthal MRI often calculated over times much longer than the dynamical time, which is the more effective the larger is k_z (Balbus & Hawley, 1992; Papaloizou & Terquem, 1997). Obviously, the growth over such

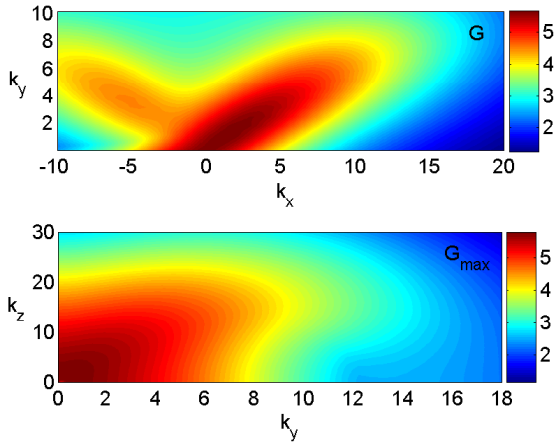

Figure 4.1: (upper panel) Optimal nonmodal growth factor, G, in (k_x, k_y)-plane at $t_d = 1.33$ and $k_z/2\pi = 1$ (which is the same as $k_z = 1$ in new mode number notations used in the next Sections). (lower panel) Maximized over initial $k_x(0)$ growth factor, G_{max}, as a function of k_y and k_z.

long timescales is irrelevant for the nonlinear (turbulence) dynamics.

In the simulation box, however, the wavenumber spectrum is inherently discrete, with smallest wavenumbers being defined by the box size (L_x, L_y, L_z) as $k_{i,min} = 2\pi/L_i$, while other wavenumbers being multiples of them. We take $L_z = 1$ (i.e., $L_z = H$ in dimensional units) and mainly consider four aspect ratios $(L_x, L_y, L_z) = (4, 4, 1),\ (2, 4, 1),\ (1, 4, 1),\ (4, 2, 1)$. Figure 4.2 shows the modes (black dots) in each box superimposed on the map of G in (k_x, k_y)-plane from Figure 4.1 for the first vertical harmonics with $k_{z,min}$, or equivalently $k_z = 1$ (in new notations used below). We see that from among these four boxes, the box $(4, 4, 1)$ contains the largest possible number of modes in the area of the effective transient growth and therefore best accounts for

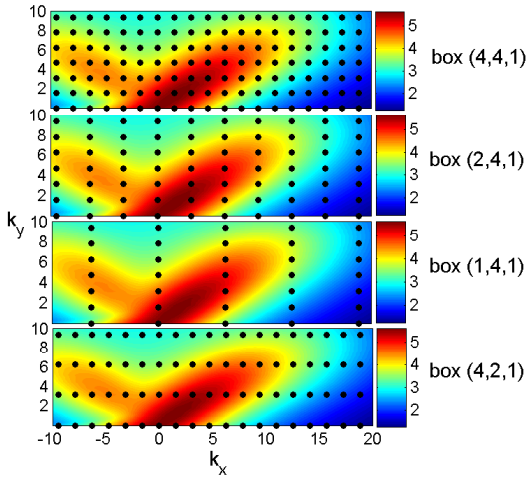

Figure 4.2: Discrete modes (black dots) contained in each simulation box superimposed on the distribution of G in (k_x, k_y)-plane from the upper panel of Figure 4.1. From all the selected boxes, the box $(4, 4, 1)$ contains most of the effectively amplified modes.

the role of the nonmodal effects in the energy exchange processes in the case of turbulence. Of course, further increasing L_x and L_y leads to larger number of modes in the area of effective growth, however, as also seen from Figure 4.2, already for the box $(4, 4, 1)$ this area appears to be sufficiently well populated with modes, i.e., enough resolution (measured in terms of $\Delta k_i = 2\pi/L_i$) is achieved in Fourier space to adequately capture the nonmodal effects. To ascertain this, we also carried out a simulation for the box $(8, 8, 1)$ and found that the ratio of the number of the active modes (i.e., the number in the growth area) to the total number of modes in this larger box is almost the same as for the box $(4, 4, 1)$. Consequently, these boxes should give qualitatively similar dynamical pictures in Fourier space. For this reason, below we choose the box $(4, 4, 1)$ as fiducial and present only some results for other boxes for comparison

at the end of Section 5.

4.4 Simulations and general characteristics

The main Equations (A.1)-(A.9) are solved using the pseudo-spectral code SNOOPY (Lesur & Longaretti, 2007). It is a general-purpose code, solving HD and MHD equations, including shear, rotation, stratification and several other physical effects in the shearing box model. Fourier transforms are computed using the FFTW library, taking also into account the drift of radial wavenumber $k_x(t)$ in $\mathbf{k}$-space due to shear in order to comply with the shearing-periodic boundary conditions. Nonlinear terms are computed using a pseudo-spectral algorithm (Canuto et al., 1988), and antialiasing is enforced using the 2/3-rule. Time integration is done by a standard explicit third-order Runge-Kutta scheme, except for viscous and resistive terms, which are integrated using an implicit scheme. The code has been extensively used in the shearing box studies of disk turbulence (e.g., Lesur & Ogilvie, 2010; Lesur & Longaretti, 2011; Herault et al., 2011; Meheut et al., 2015; Murphy & Pessah, 2015; Riols et al., 2017).

We carry out simulations for boxes with different radial and azimuthal sizes $(L_x, L_y, L_z) = (4, 4, 1)$, $(2, 4, 1)$, $(1, 4, 1)$, $(4, 2, 1)$, $(8, 8, 1)$ and resolution of 64 grid points per scale height $H = 1$ (Table 1). The numerical resolution adopted ensures that the dissipation wavenumber, k_D, is smaller than the maximum wavenumber, $k_{i,max} = 2\pi N_i/3L_i$, in the box (taking into account the 2/3-rule). The initial conditions consist of small amplitude ran-

Table 4.1: Simulation characteristics: box size, number of grid points, volume- and time-averaged values (denoted by double brackets) of the perturbed kinetic, E_K, magnetic, E_M, and thermal, E_{th}, energy densities as well as the rms values of the magnetic field components and the Reynolds, $u_x u_y$, and Maxwell, $-b_x b_y$, stresses in the fully developed turbulence.

(L_x, L_y, L_z)	(N_x, N_y, N_z)	$\langle\langle E_K\rangle\rangle$	$\langle\langle E_M\rangle\rangle$	$\langle\langle E_{th}\rangle\rangle$	$\langle\langle b_x^2\rangle\rangle^{1/2}$	$\langle\langle b_y^2\rangle\rangle^{1/2}$	$\langle\langle b_z^2\rangle\rangle^{1/2}$	$\langle\langle u_x u_y\rangle\rangle$	$\langle\langle -b_x b_y\rangle\rangle$
$(8, 8, 1)$	$(512, 512, 64)$	0.0173	0.0422	0.0022	0.101	0.266	0.06	0.0037	0.0198
$(4, 4, 1)$	$(256, 256, 64)$	0.0125	0.03	0.0019	0.086	0.224	0.05	0.0028	0.0146
$(2, 4, 1)$	$(128, 256, 64)$	0.0116	0.0298	0.0019	0.085	0.223	0.05	0.0028	0.0144
$(1, 4, 1)$	$(64, 256, 64)$	0.0111	0.0295	0.0018	0.085	0.222	0.05	0.0027	0.0143
$(4, 2, 1)$	$(256, 128, 64)$	0.0056	0.012	0.0011	0.053	0.14	0.03	0.0013	0.0059

dom noise perturbations of velocity on top of the Keplerian shear flow. A subsequent evolution is followed up to $t_f = 630$ (about 100 orbits). The wavenumbers k_x, k_y, k_z are normalized, respectively, by the grid cell sizes of Fourier space, $\Delta k_x = 2\pi/L_x, \Delta k_y = 2\pi/L_y$ and $\Delta k_z = 2\pi/L_z$, that is, $(k_x/\Delta k_x, k_y/\Delta k_y, k_z/\Delta k_z) \rightarrow (k_x, k_y, k_z)$. As a result, the normalized azimuthal and vertical wavenumbers are integers $k_y, k_z = 0, \pm 1, \pm 2, ...$, while k_x, although changes with time due to drift, is integer at discrete moments $t_n = nL_y/(q|k_y|L_x)$, where n is a positive integer.

In all the boxes, initially imposed small perturbations start to grow as a result of the nonmodal MRI amplification of the constituent Fourier modes. Then, after several orbits, the perturbation amplitude becomes high enough, reaching the nonlinear regime and eventually the flow settles down into a quasi-steady sustained MHD turbulence. Figure 4.3 shows the time-development of the volume-averaged perturbed kinetic, $\langle E_K\rangle$, thermal, $\langle E_{th}\rangle$, and magnetic, $\langle E_M\rangle$, energy densities as well as the Reynolds, $\langle u_x u_y\rangle$, and Maxwell $-\langle b_x b_y\rangle$ stresses for the fiducial box $(4, 4, 1)$. For completeness, in

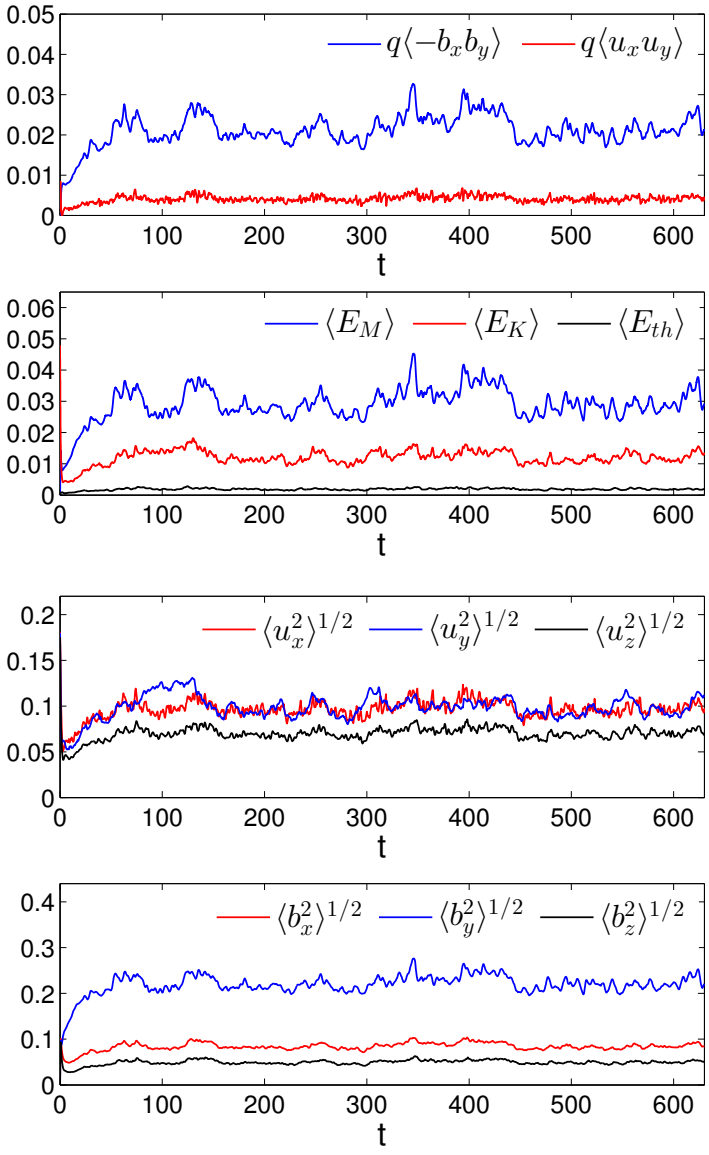

Figure 4.3: Evolution of volume-averaged Reynolds and Maxwell stresses (top row), kinetic, thermal and magnetic energy densities (second row), rms of velocity (third row) and magnetic field (bottom row) components for the fiducial box $(4, 4, 1)$. Turbulence sets in after several orbits, with the magnetic energy dominating kinetic and thermal energies, and the Maxwell stress the Reynolds one. The azimuthal component of the turbulent magnetic field is larger than the other two ones due to the shear. It is also about twice larger than the mean field $B_{0y} = 0.1$ (Table 4.1).

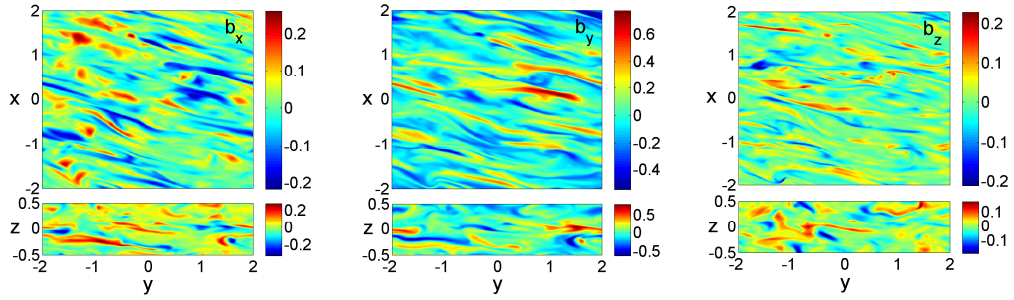

Figure 4.4: Typical structure of the magnetic field in the fully developed quasi-steady turbulent state at $t = 550$ for the box $(4, 4, 1)$. Shown are the sections in (y, x) and (y, z)-planes.

this figure, we also show the evolution of the rms values of the turbulent velocity and magnetic field components. The magnetic energy dominates the kinetic and thermal ones, with the latter being much smaller than the former two, while the Maxwell stress is about 5 times larger than the Reynolds one. This indicates that the magnetic field perturbations are primarily responsible for energy extraction from the mean flow by the Maxwell stress, transporting angular momentum outward and sustaining turbulence. In contrast to the 2D plane case (Mamatsashvili et al., 2014), the Reynolds stress in this 3D case is positive and also contributes to the outward transport. The temporal behavior of the volume-averaged kinetic and magnetic energy densities and stresses is consistent with analogous studies of MRI-turbulence in disks with a net azimuthal field (Hawley et al., 1995; Guan et al., 2009; Simon & Hawley, 2009; Meheut et al., 2015). For all the models, the time- and volume-averaged quantities over the whole quasi-steady state, between $t = 100$ and the end of the run at t_f, are listed in Table 4.1. For the fiducial model, the ratios of the

magnetic energy to kinetic and thermal ones are $\langle\langle E_M\rangle\rangle/\langle\langle E_K\rangle\rangle = 2.4$ and $\langle\langle E_M\rangle\rangle/\langle\langle E_{th}\rangle\rangle = 15.8$, respectively, and the ratio of the Maxwell stress to the Reynolds stress is $\langle\langle -b_x b_y\rangle\rangle/\langle\langle u_x u_y\rangle\rangle = 5.21$. For other boxes, similar ratios hold between magnetic and hydrodynamic quantities, as can be read off from Table 4.1, with the magnetic energy and stresses being always dominant over respective hydrodynamic ones. Interestingly, for all boxes in the quasi-steady turbulent state, $\langle E_M\rangle$ and $\langle -b_x b_y\rangle$ closely follow each other at all times, with the ratio being nearly constant, $\langle E_M\rangle/\langle -b_x b_y\rangle \approx 2$ (see also Hawley et al., 1995; Guan et al., 2009). From Table 4.1, we can also see how the level (intensity) of the turbulence varies with the radial and azimuthal sizes of the boxes. For fixed $L_y = 4$, the saturated values of the energies and stresses increase with L_x, but only very little, so they can be considered as nearly unchanged, especially after $L_x > 1$. By contrast, at fixed $L_x = 4$, these quantities are more sensitive to the azimuthal size L_y, increasing more than twice with the increase of the latter from $L_y = 2$ to $L_y = 4$. However, after $L_y = 4$ the increase of the turbulence strength with the box size is slower, as evident from the box $(8, 8, 1)$. This type of dependence of the azimuthal MRI-turbulence characteristics on the horizontal sizes of the simulation box is consistent with that of Guan et al. (2009).

The structure of the turbulent magnetic field in the fully developed quasi-steady turbulence in physical space is presented in Figure 4.4. It is chaotic and stretched along the y-axis due to the shear, with b_y achieving higher values than b_x and b_z. At this moment, the rms values of these com-

ponents are, $\langle b_x^2 \rangle^{1/2} = 0.079$, $\langle b_z^2 \rangle^{1/2} = 0.044$, while $\langle b_y^2 \rangle^{1/2} = 0.2$ and is twice larger than the background field $B_{0y} = 0.1$. These values, as expected, are consistent with the bottom panel of Figure 4.3. So, the turbulent field satisfies $\langle b_z^2 \rangle^{1/2} < \langle b_x^2 \rangle^{1/2} < B_{0y} < \langle b_y^2 \rangle^{1/2}$, which in fact holds throughout the evolution for all models (Table 4.1).

4.4.1 Analysis in Fourier space – an overview

A deeper insight into the nature of the turbulence driven by the azimuthal MRI can be gained by performing analysis in Fourier space. So, following Horton et al. (2010); Mamatsashvili et al. (2014, 2016), we examine in detail the specific spectra and sustaining dynamics of the quasi-steady turbulent state by explicitly calculating and visualizing the individual linear and nonlinear terms in spectral Equations (4.11)-(4.17), which have been classified and described in Section 2, based on the simulation data. These equations govern the evolution of the quadratic forms (squared amplitudes) of Fourier transforms of velocity, thermal and magnetic field perturbations and are more informative than Equations (4.18) and (4.19) for spectral kinetic and magnetic energies. In the latter equations a lot of essential information is averaged and lost. Therefore, energy equations alone are insufficient for understanding intertwined linear and nonlinear processes that underlie the sustaining dynamics of the turbulence. For this reason, we rely largely on Equations (4.11)-(4.17), enabling us to form a complete picture of the turbulence dynamics. So, we divide our analysis in Fourier space into several steps:

I. Three-dimensionality, of course, complicates the analysis. Therefore, initially, we find out which vertical wavenumbers are important by integrating the spectral energies and stresses in (k_x, k_y)-plane (Figure 4.5). As will be evident from such analysis, mostly the lower vertical harmonics, $|k_z| = 0, 1, 2$, (i.e., with vertical scales comparable to the box size L_z) engage in the turbulence maintaining process.

II. Next, concentrating on these modes with lower vertical wavenumber, we present the spectral magnetic energy in (k_x, k_y)-plane (Figure 4.6) and identify the energy-carrying modes in this plane (Figure 4.7). From these modes, we delineate a narrower set of dynamically important active ones, which are central in the sustenance process. Based on this, we identify a region in Fourier space – *the vital area* – where the basic linear and nonlinear processes for these modes operate. Despite a limited extent of the vital area, the number of the dynamically important modes within it appears to be quite large and they are distributed anisotropically in Fourier space.

III. Integrating in (k_x, k_y)-plane the quadratic forms of the spectral velocity and magnetic field components ($|\bar{u}_i|^2$ and $|\bar{b}_i|^2$) as well as the corresponding linear and nonlinear terms on the rhs of Equations 4.11-4.17), we obtain a first idea about the importance of each of them in the dynamics as a function of k_z (Figure 4.8). Note that the action of the linear drift terms vanishes after the integration. Nevertheless, the universality and importance of the linear drift is obvious in any case.

IV. Finally, we analyze the interplay of these processes/terms that de-

termines the turbulence dynamics (Figures 4.9-4.14). As a result, we construct the turbulence sustaining picture/mechanism by revealing the transverse nature of the nonlinear processes – the nonlinear transverse cascade – and demonstrating its key role in the sustenance.

Fromang & Papaloizou (2007); Simon et al. (2009); Davis et al. (2010); Lesur & Longaretti (2011) took a similar approach of representing the MHD equations in Fourier space and analyzing individual linear and nonlinear (transfer) terms in the dynamics of MRI-turbulence. They derived evolution equations for the kinetic and magnetic energy spectra, which are similar to our Equations (4.18)-(4.19) except for notation and mean field direction. As mentioned above, we do not make the shell-averages in Fourier space, as done in these studies, that completely wipes out spectral anisotropy due to the shear crucial to the turbulence dynamics.

Since our analysis primarily focuses on the spectral aspect of the dynamics, the SNOOPY code, being of spectral type, is particularly convenient for this purpose, as it allows us to directly extract Fourier transforms. From now on we consider the evolution after the quasi-steady turbulence has set in, so all the spectral quantities/terms in Equations (4.11)-(4.17) are averaged in time over an entire saturated turbulent state between $t = 200$ and the end of the run. Below we concentrate on the fiducial box $(4, 4, 1)$. Comparison of the spectral dynamics in other boxes and the effects of the box aspect ratio will be presented in the next Section.

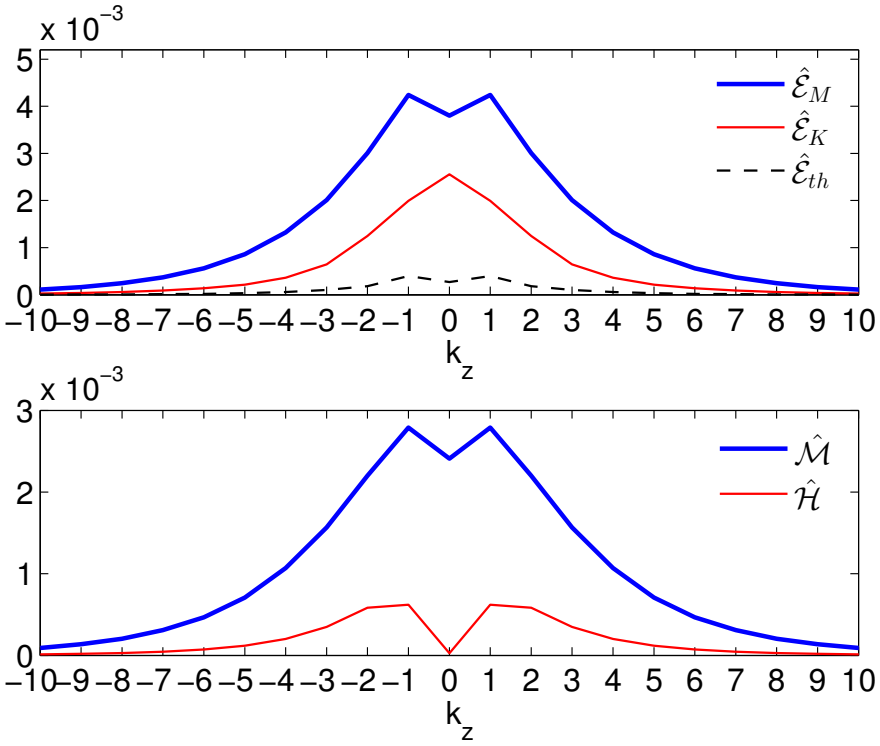

Figure 4.5: Integrated in (k_x, k_y)-plane time-averaged kinetic, $\hat{\mathcal{E}}_K$, magnetic, $\hat{\mathcal{E}}_M$ and thermal $\hat{\mathcal{E}}_{th}$ energy spectra (upper panel) as well as Reynolds, $\hat{\mathcal{H}}$, and Maxwell, $\hat{\mathcal{M}}$, stresses (lower panel) as a function of k_z for the box $(4, 4, 1)$.

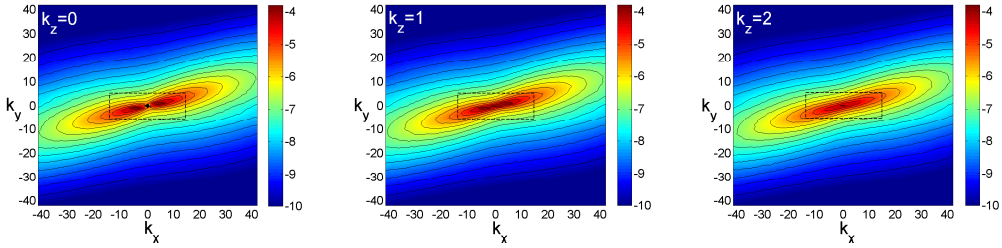

Figure 4.6: Logarithm of the spectral magnetic energy, $log_{10}\mathcal{E}_M$, in (k_x, k_y)-plane at $k_z = 0, 1, 2$ for the box $(4, 4, 1)$. The spectra is strongly anisotropic due to the shear, having larger power on the $k_x/k_y > 0$ side at a given k_y. Dashed rectangles delineate the vital area of turbulence, where the sustaining process is concentrated (see Figures 4.9-4.14).

4.4.2 Energy spectra, active modes and the vital area

Figure 4.5 shows the time-averaged spectra of the kinetic, magnetic and thermal energies as well as the Reynolds and Maxwell stresses integrated in (k_x, k_y)-plane, $\hat{\mathcal{E}}_{K,M,th}(k_z) = \int \mathcal{E}_{K,M,th} dk_x dk_y$ and $(\hat{\mathcal{H}}(k_z), \hat{\mathcal{M}}(k_z)) = \int (\mathcal{H}, \mathcal{M}) dk_x dk_y$ as a function of k_z. The magnetic energy is the largest and the thermal energy the smallest, while the Maxwell stress dominates the Reynolds one, at all k_z. All the three energy spectra and stresses reach a maximum at small $|k_z|$ – the magnetic and thermal energies as well as the stresses at $|k_z| = 1$, while the kinetic energy at $k_z = 0$ – and rapidly decrease with increasing $|k_z|$. As a result, in particular, the magnetic energy injection into turbulence due to the Maxwell stress takes place mostly at small k_z, which is consistent with our linear optimal

growth calculations (Section 3) and also with Squire & Bhattacharjee (2014), but is in contrast to the accepted view that the purely azimuthal field MRI is stronger at high k_z (Balbus & Hawley, 1992; Hawley et al., 1995). The

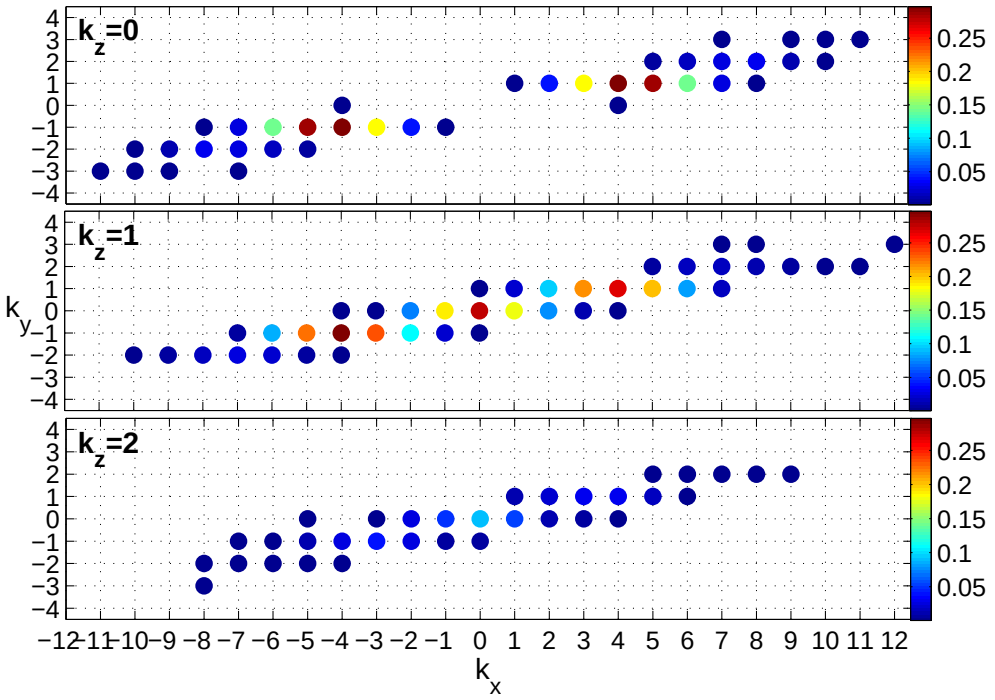

Figure 4.7: Distribution of the active modes in **k**-space at $k_z = 0, 1, 2$ for the box $(4, 4, 1)$. The color dots represent the modes whose magnetic energy, $\mathcal{E}_M$, grows more than 50% of the maximum spectral magnetic energy, $\mathcal{E}_{M,max}$, and the colors indicate the fraction of time each mode contains this higher energy during the quasi-steady state until the end of the simulation.

main reason for this difference, as mentioned above, is that the latter is usually calculated over much longer times (spanning from tens to hundred dynamical times), following the evolution of the shearing waves from initial tightly leading to final tightly trailing orientation, whereas the optimal growth is usually calculated over a finite (dynamical) time, which seems more appropriate in the case of turbulence. Thus, the large-scale modes with the first few k_z contain most of the energy and hence play a dynamically important role.

To have a fuller picture of the energy spectra, in Figure 4.6 we present sections of $\mathcal{E}_M$ in (k_x, k_y)-plane again at first three vertical wavenumbers $k_z = 0, 1, 2$, for which it is higher (see Figure 4.5). The spectrum is highly anisotropic due to the shear with the same elliptical shape and inclination towards the k_x-axis irrespective of k_z. This indicates that modes with $k_x/k_y > 0$ have more energy than those with $k_x/k_y < 0$ at fixed k_y. The kinetic energy spectrum shares similar properties and is not shown here. A similar anisotropic spectrum was already reported in the shearing-box simulations of MRI-turbulence with a nonzero net vertical field (Hawley et al., 1995; Lesur & Longaretti, 2011; Murphy & Pessah, 2015). This energy spectrum, which clearly differs from a typical turbulent spectrum in the classical case of forced MHD turbulence without shear (Biskamp, 2003), arises as a consequence of a specific anisotropy of the linear and nonlinear terms of Equations (4.11)-(4.17) in $\mathbf{k}-$space. These new features are not common to shearless MHD turbulence and hence it is not surprising that Kolmogorov or IK theory cannot adequately describe shear flow turbulence.

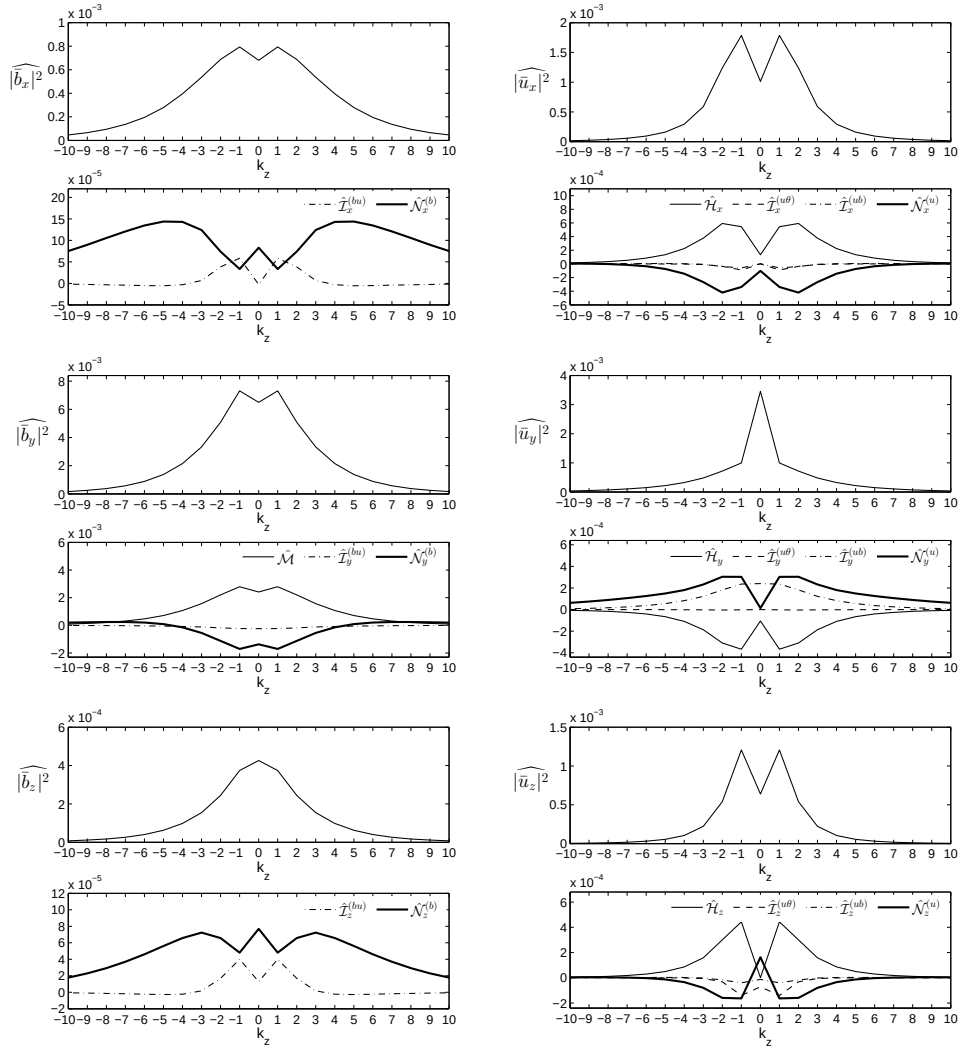

Figure 4.8: Integrated in (k_x, k_y)-plane the quadratic forms of the spectral velocity and magnetic field components together with the corresponding linear and nonlinear terms from corresponding Equations (4.11)-(4.17) as a function of k_z.

Having described the energy spectrum, we now look at how energy-carrying modes, most actively participating in the dynamics, are distributed in (k_x, k_y)-plane. We refer to modes whose magnetic energy reaches values higher than 50% of the maximum spectral magnetic energy as active modes. Although this definition is somewhat arbitrary, it gives an idea on where the dynamically important modes are located in Fourier space. Figure 4.7 shows these modes in (k_x, k_y)-plane at $k_z = 0, 1, 2$ with color dots. They are obtained by following the evolution of all the modes in the box during an entire quasi-steady state and selecting those modes whose magnetic energy becomes higher than the above threshold. The color of each mode indicates the fraction of time, from the onset of the quasi-steady state till the end of the simulation, during which it contains this higher energy. We have also checked that Figure 4.7 is not qualitatively affected upon changing the 50% threshold to either 20% or 70%. Like the energy spectrum, the active modes with different duration of "activity" are distributed quite anisotropically in (k_x, k_y)-plane, occupying a broader range of radial wavenumbers $|k_x| \lesssim 12$ than that of azimuthal ones $|k_y| \lesssim 3$. This main, energy-containing area in $\mathbf{k}$-space represents *the vital area* of turbulence. Essentially, the active modes in the vital area take part in the sustaining dynamics of turbulence. The other modes with larger wavenumbers lie outside the vital area and always have energies and stresses less than 50% of the maximum value, therefore, not playing as much a role in the energy-exchange process between the background flow and turbulence. Note that the total number of the active modes (color dots) in Figure 4.7 is equal to 114,

implying that the dynamics of the MRI-turbulence, strictly speaking, cannot be reduced to low-order models of the sustaining processes, involving only a small number of active modes (e.g., Herault et al., 2011; Riols et al., 2017).

4.4.3 Vertical spectra of the dynamical terms

Having identified the vital area, we now examine the significance of each of the linear and nonlinear terms in this area first along the vertical k_z-direction in Fourier space. For this purpose, we integrate in (k_x, k_y)-plane the quadratic forms of the spectral velocity and magnetic field components as well as the rhs terms of Equations (4.11)-(4.13) and (4.15)-(4.17), as we have done for the spectral energies and stresses above. We do not apply this procedure to the linear drift term (which vanishes after such integration) and dissipation terms, as their action is well known. The results are presented in Figure 4.8 (the spectral quantities integrated in (k_x, k_y)-plane are all denoted by hats), which shows that:

I. The dynamics of $\widehat{|\bar{b}_x|^2}$ is governed by $\hat{\mathcal{I}}_x^{(bu)}$ and $\hat{\mathcal{N}}_x^{(b)}$, which are both positive and therefore act as a source for the radial field at all k_z.

II. The dynamics of $\widehat{|\bar{b}_y|^2}$ is governed by $\hat{\mathcal{M}}$ and $\hat{\mathcal{N}}_y^{(b)}$, the action of $\hat{\mathcal{I}}_y^{(bu)}$ is negligible compared with these terms. The effect of $\hat{\mathcal{M}}$ is positive for all k_z, reaching a maximum, as we have seen before, at $|k_z| = 1$. This implies that the energy injection into turbulence from the background flow due to the MRI occurs over a range of length scales, preventing the development of the proper inertial range in the classical sense (see also Lesur & Longaretti, 2011). On

the other hand, $\hat{\mathcal{N}}_y^{(b)}$ is negative and hence acts as a sink for low/active k_z, but positive at large $|k_z|$. So, the nonlinear term transfers the azimuthal field component from these wavenumbers to large $|k_z|$ as well as (which is more important) to other components.

III. The dynamics of $\widehat{|\bar{b}_z|^2}$ is governed by $\hat{\mathcal{I}}_z^{(bu)}$ and $\hat{\mathcal{N}}_z^{(b)}$, which are both positive, with the latter being larger than the former at all k_z. Note that $\widehat{|\bar{b}_z|^2}$ is smaller compared to the other two components, while $\widehat{|\bar{b}_y|^2}$ is the largest.

IV. The dynamics of $\widehat{|\bar{u}_x|^2}$ is governed by $\hat{\mathcal{H}}_x$ and $\hat{\mathcal{N}}_x^{(u)}$, the action of the exchange terms, $\hat{\mathcal{I}}_x^{(u\theta)}$ and $\hat{\mathcal{I}}_x^{(ub)}$, are negligible compared to these terms. The effect of $\hat{\mathcal{H}}_x$ is positive for all k_z, acting as the only source for $\bar{u}_x$. By contrast, $\hat{\mathcal{N}}_x^{(u)}$ is negative (sink), opposing $\hat{\mathcal{H}}_x$, with a similar dependence of its absolute value on k_z. So, the nonlinear term transfers the radial velocity to other components.

V. The dynamics of $\widehat{|\bar{u}_y|^2}$ is governed by $\hat{\mathcal{H}}_y$, $\hat{\mathcal{I}}_y^{(ub)}$ and $\hat{\mathcal{N}}_y^{(u)}$, the action of $\hat{\mathcal{I}}_y^{(u\theta)}$ is negligible. The effects of $\hat{\mathcal{N}}_y^{(u)}$ and $\hat{\mathcal{I}}_y^{(ub)}$ are positive for all k_z, while $\hat{\mathcal{H}}_y$ is negative. Special attention deserves the sharp peak of $\widehat{|\bar{u}_y|^2}$ at $k_z = 0$. This peak is related to the formation of the zonal flow with $|k_x| = 1$ and $k_y = 0$ in the MRI-turbulence (Johansen et al., 2009), which will be analyzed below.

VI. The dynamics of $\widehat{|\bar{u}_z|^2}$ is governed by $\hat{\mathcal{H}}_z$, $\hat{\mathcal{I}}_z^{(u\theta)}$ and $\hat{\mathcal{N}}_z^{(u)}$, the action of $\hat{\mathcal{I}}_z^{(ub)}$ is negligible. $\widehat{|\bar{u}_z|^2}$ is the only term that explicitly depends on the thermal processes. Note also that $\hat{\mathcal{N}}_z^{(u)}$ is negative at $|k_z| \geq 1$, but becomes positive at $k_z = 0$, implying inverse transfer towards small k_z. We do not go

into the details of this dependence, as $\widehat{|\bar{u}_z|^2}$ is anyway smaller compared to the other components. Besides, the thermal processes do not play a major role in the overall dynamics, since their energy is much smaller than the magnetic end kinetic energies (see also Figure 4.3).

It is seen from Figure 4.8 that all the dynamical terms primarily operate at small vertical wavenumbers $|k_z| = 0, 1, 2$. Some of them ($\hat{\mathcal{N}}_x^{(b)}$ and $\hat{\mathcal{N}}_z^{(b)}$) may extend up to $|k_z| = 3 - 6$, but eventually decay at large $|k_z|$. Similarly, the spectra of the velocity and magnetic field have relatively large values also at small $|k_z|$. So, $|k_z| = 2$ can be viewed as an upper vertical boundary of the vital area in Fourier space.

4.5 Interplay of the linear and nonlinear processes in the sustenance of the turbulence

We have seen above that the sustaining dynamics of turbulence is primarily concentrated at small vertical wavenumbers, so now we present the distribution of the time-averaged amplitudes of the spectral quantities $\bar{u}_i$, $\bar{b}_i$ as well as the linear (k_x-drift, $\mathcal{H}_i, \mathcal{I}_i, \mathcal{M}$) and nonlinear ($\mathcal{N}_i$) dynamical terms in (k_x, k_y)-plane again at $k_z = 0, 1, 2$ in Figures 4.9-4.14 (as noted before, we omit here the thermal processes, $\bar{\theta}$, which play a minor role). These figures give quite a detailed information and insight about all the linear and nonlinear processes involved in Equations (4.11)-(4.17) and allow us to properly understand their interplay leading to the turbulence sustenance. We start the analysis of this interplay with a general outline of the figures. We do not show here

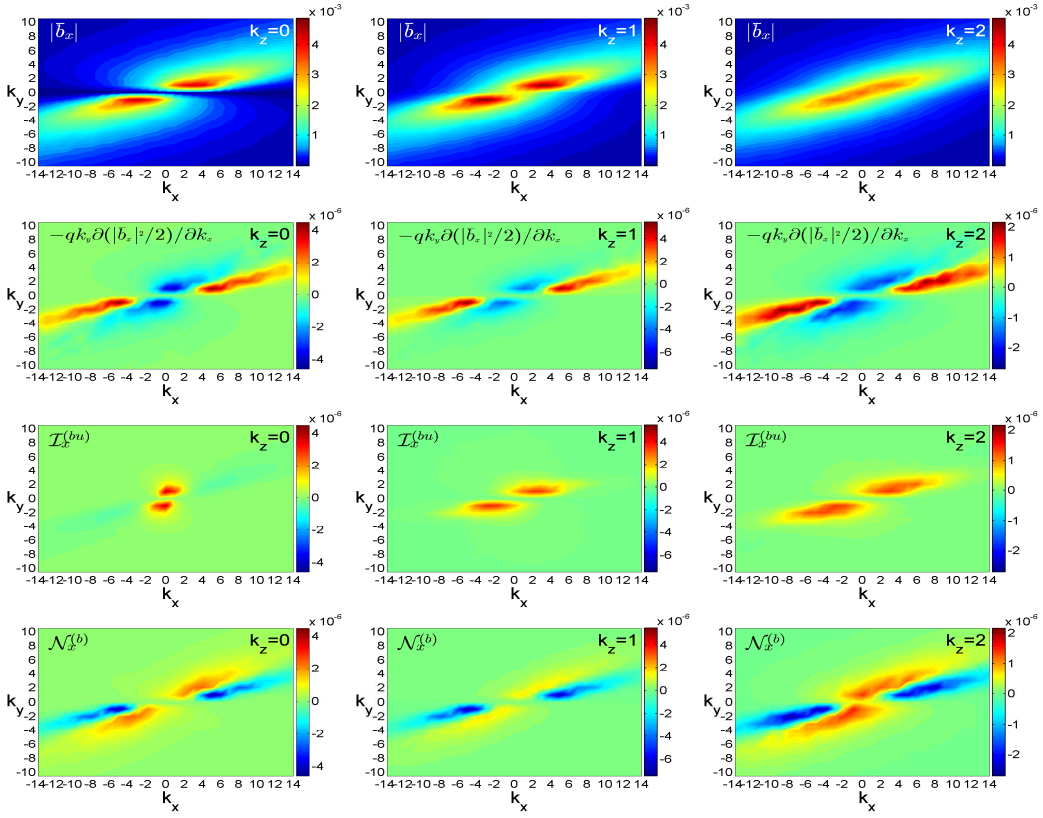

Figure 4.9: Spectrum of the radial field, $|\bar{b}_x|$, and the maps of the corresponding linear and nonlinear terms, governing its dynamics (Equation 4.15), in (k_x, k_y)-plane at $k_z = 0(left),\ \ 1(middle),\ \ 2(right)$. The spectrum as well as the action of these terms are highly anisotropic, (i.e., depend on the wavevector azimuthal angle) due to the shear. These terms are appreciable and primarily operate in the vital area $|k_x| \lesssim 12, |k_y| \lesssim 3$. The red and yellow (blue and dark blue) regions in each panel correspond to wavenumbers where respective dynamical terms are positive (negative) and hence act as a source (sink) for $|\bar{b}_x|^2$. In light green regions, outside the vital area, these terms are small, although, as we checked, preserve the same anisotropic shape. In particular, the nonlinear transfer term $\mathcal{N}_x^{(b)}$ transversely redistributes $|\bar{b}_x|^2$ from the blue and dark blue regions, where $\mathcal{N}_x^{(b)} < 0$, to the red and yellow regions, where $\mathcal{N}_x^{(b)} > 0$. These regions exhibit considerable variations with the azimuthal angle of the wavevector and also depend on k_z.

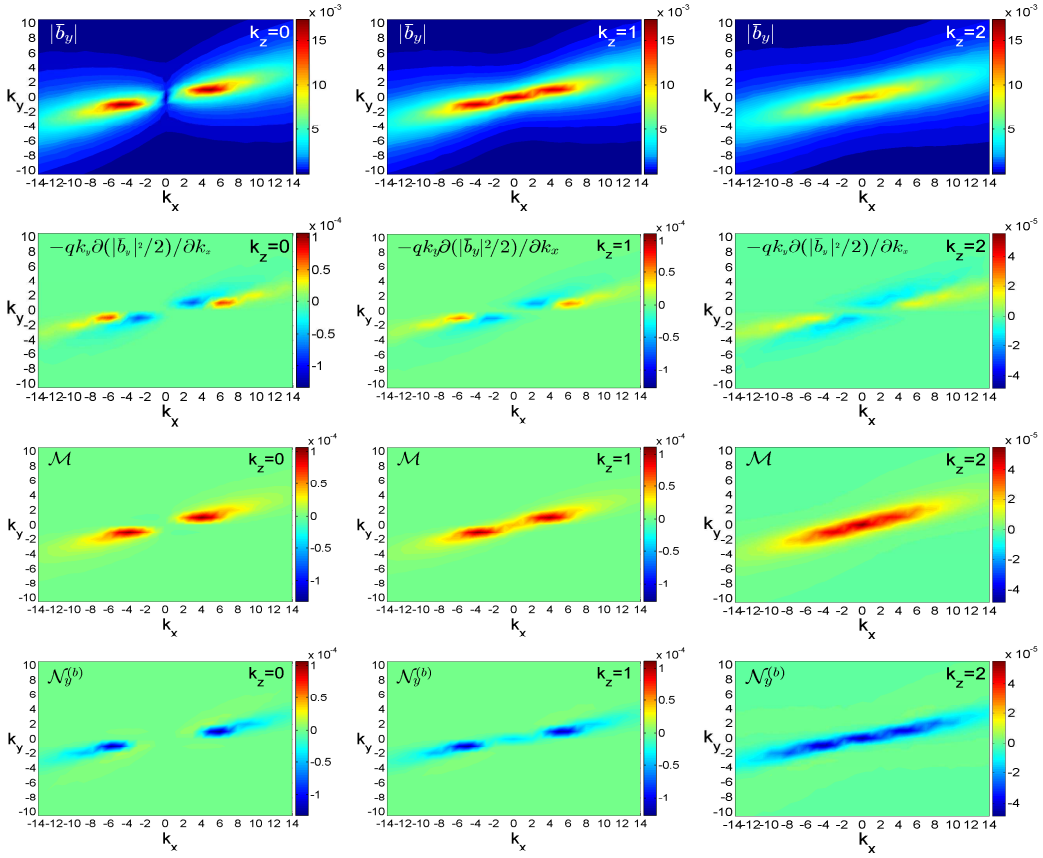

Figure 4.10: Same as in Figure 4.9, but for the azimuthal field $\bar{b}_y$ with the corresponding dynamical terms from Equation (4.16). The dynamics of this component is primarily determined by the combined action of the drift, the Maxwell stress $\mathcal{M}$, which is positive (energy injection) and the nonlinear term $\mathcal{N}_y^{(b)}$, which is negative (sink) in the vital area. The linear exchange term $\mathcal{I}_y^{(bu)}$ is negligible compared with the above terms and is not shown here.

the viscous ($\mathcal{D}_i^{(u)}$) and resistive $\mathcal{D}_i^{(b)}$ terms, since their action is quite simple – they are always negative and reduce the corresponding quantities, thereby opposing the sustenance process. They increase with k, but in the vital area are too small to have any influence on the dynamics.

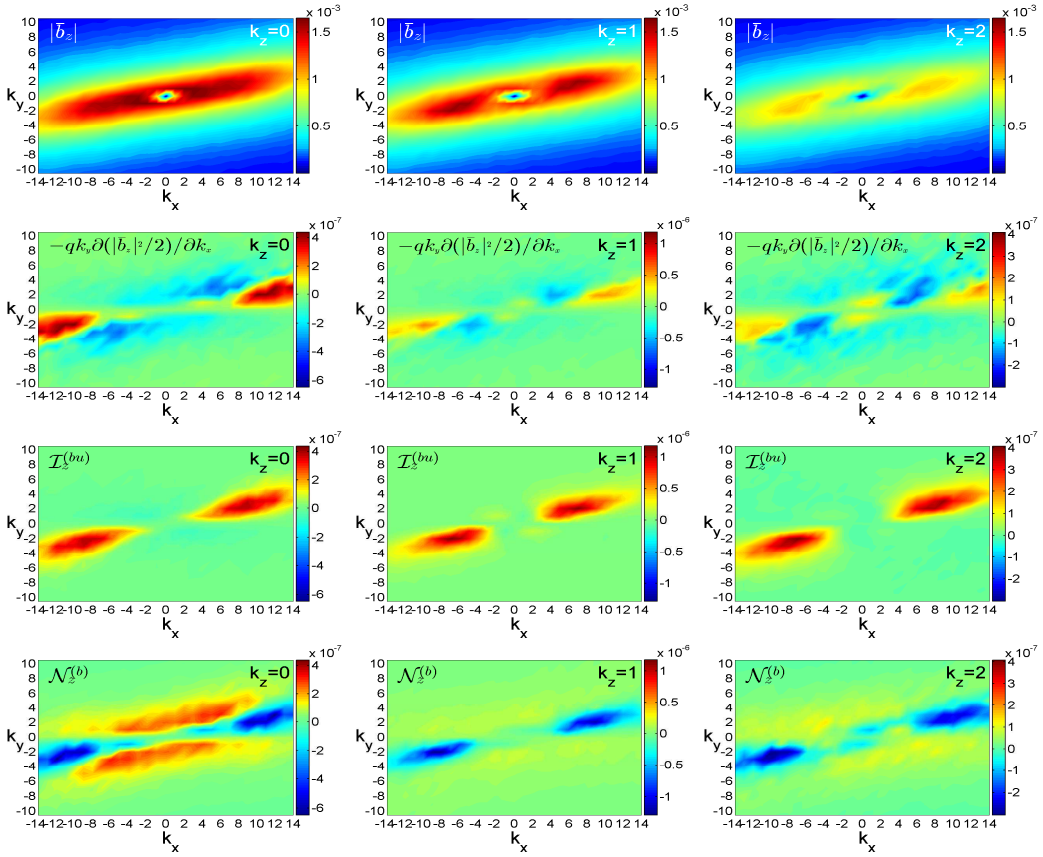

Figure 4.11: Same as in Figure 4.9, but for $\bar{b}_z$ with the corresponding dynamical terms from Equation (4.17). The transverse character of the nonlinear redistribution, $\mathcal{N}_z^{(b)}$, is also evident. $|\bar{b}_z|$ is small in comparison with $|\bar{b}_x|$ and $|\bar{b}_y|$.

A first glance at the plots makes it clear that all the spectra of the physical quantities and processes are highly anisotropic due to the shear, i.e., strongly depend on the azimuthal angle in (k_x, k_y)-planes as well as vary with k_z, with a similar type of anisotropy and inclination towards the k_x-axis, as the energy spectrum in Figure 4.6. For the nonlinear processes represented by $\mathcal{N}_i^{(u)}$ and $\mathcal{N}_i^{(b)}$ (bottom row in Figures 4.9-4.14), this anisotropy can not

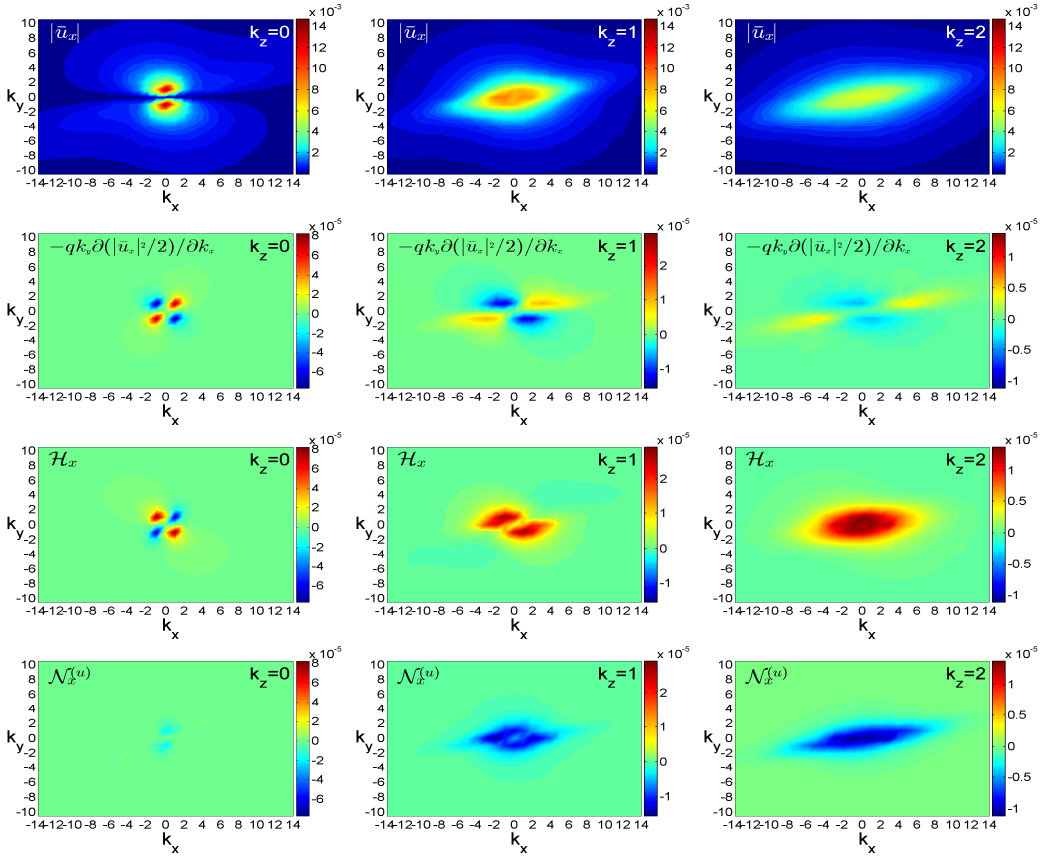

Figure 4.12: Spectra of $|\bar{u}_x|$ and the maps of the corresponding linear and nonlinear terms governing its dynamics (Equation 4.11) in (k_x, k_y)-plane at $k_z = 0(left), 1(middle), 2(right)$. The dynamics of this velocity component is primarily determined by $\mathcal{H}_x$ (source) and $\mathcal{N}_x^{(u)}$ (sink), the linear exchange terms, $\mathcal{I}_x^{(u\theta)}$ and $\mathcal{I}_x^{(ub)}$, are negligible compared with the above terms and are not shown here.

be put within the framework of commonly considered forms of nonlinear – direct and inverse – cascades, since its main manifestation is the transverse (among wavevector angles) nonlinear redistribution of modes in (k_x, k_y)-plane as well as among different k_z. In these figures, the nonlinear terms transfer the

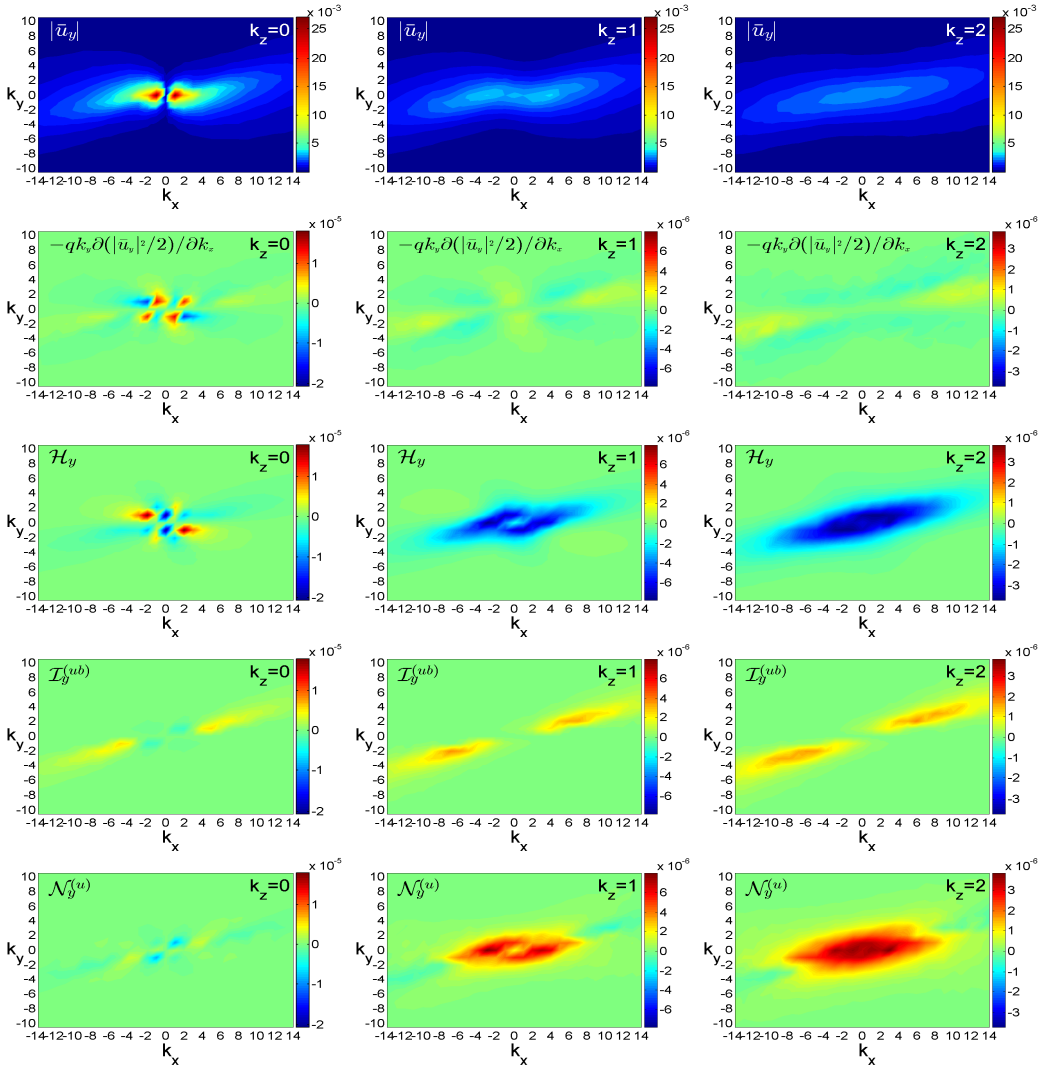

Figure 4.13: Same as in Figure 4.12, but for $\bar{u}_y$ with the corresponding dynamical terms from Equation (4.12). The influence of the thermal process, $\mathcal{I}_y^{(u\theta)}$, is negligible and not shown here. The spectrum of $|\bar{u}_y|$ reaches a maximum at $k_x = \pm 1, k_y = k_z = 0$, which corresponds to the zonal flow in physical space.

corresponding quadratic forms of the velocity and magnetic field components transversely away from the regions where they are negative ($\mathcal{N}_i^{(u)} < 0, \mathcal{N}_i^{(b)} <$

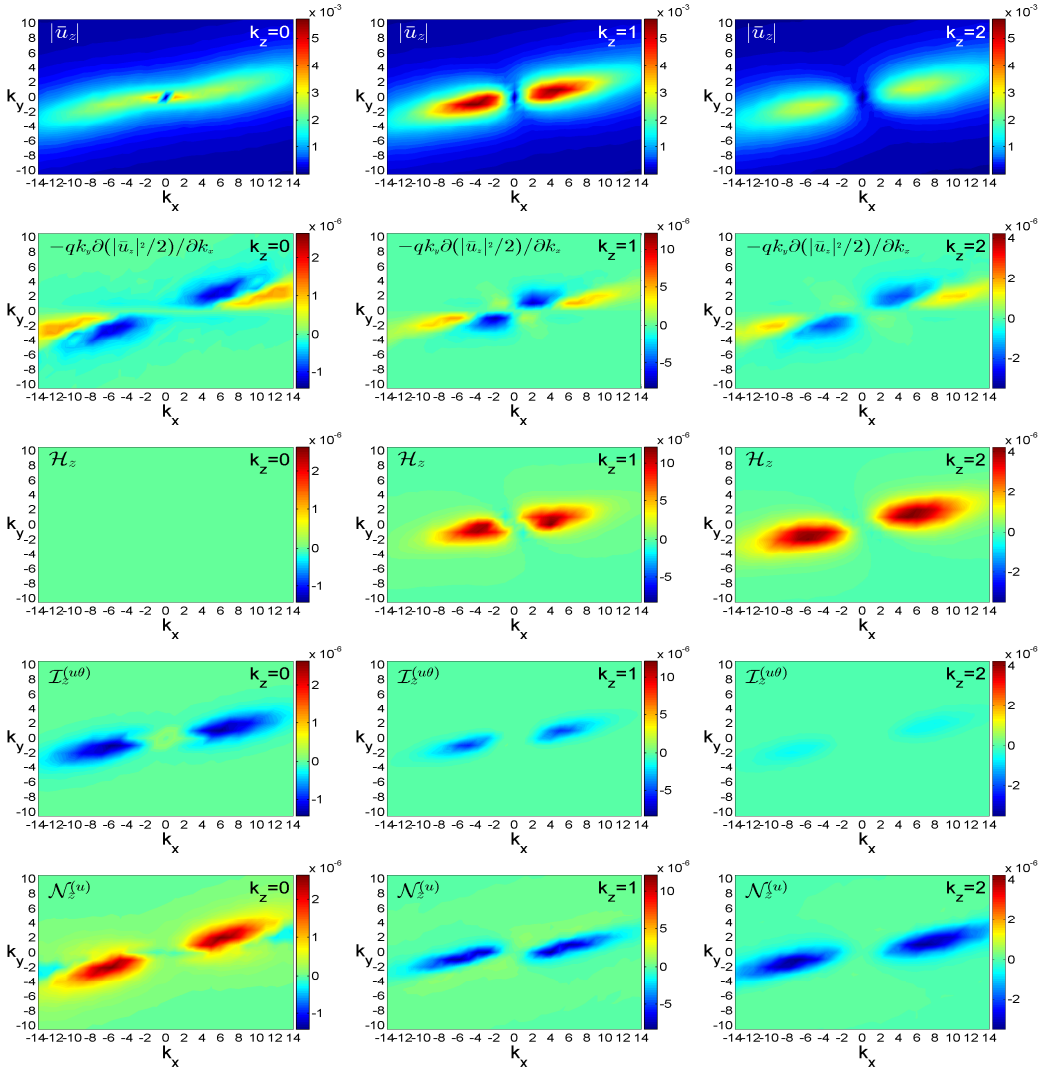

Figure 4.14: Same as in Figure 4.12, but for $\bar{u}_z$ with the corresponding dynamical terms from Equation (4.13). The influence of the linear magnetic exchange term $\mathcal{I}_z^{(ub)}$ is negligible and is not shown here. The nonlinear term $\mathcal{N}_z^{(u)}$ transfers $|\bar{u}_z|^2$ towards small k_z (as it also seen in the corresponding panel of Figure 4.8).

0, blue and dark blue) towards the regions where they are positive ($\mathcal{N}_i^{(u)} > 0, \mathcal{N}_i^{(b)} > 0$, yellow and red). These regions display quite a strong angular

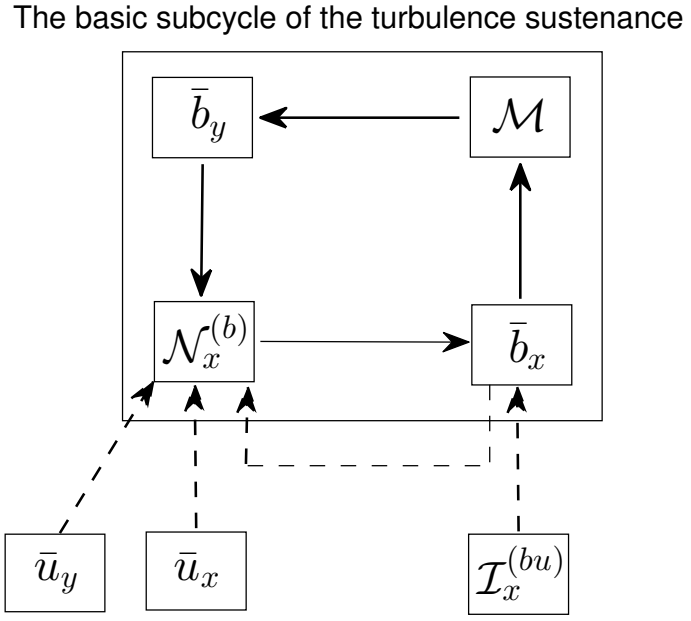

Figure 4.15: Sketch of the basic subcycle of the sustaining process (the solid arrows within the rectangle): (i) generation of $\bar{b}_x$ by the nonlinearity $\mathcal{N}_x^{(b)}$, (ii) subsequent production of $\mathcal{M}$ from $\bar{b}_x$ and (iii) of the azimuthal field energy $|\bar{b}_y|^2$ by $\mathcal{M}$ (the linear MRI stage) and finally (iv) the nonlinear feedback – contribution of $\bar{b}_y$ to $\mathcal{N}_x^{(b)}$. The other contributions (dashed arrows) of $\mathcal{I}_x^{(bu)}$ to the production of $\bar{b}_x$ and the feedback of $\bar{u}_x, \bar{u}_y, \bar{b}_x$ to $\mathcal{N}_x^b$ ($\bar{u}_z$ and $\bar{b}_z$ are small and not shown), are a part of the overall sustaining scheme, but outside the basic subcycle.

variation in (k_x, k_y)-planes.

Similarly, the terms of linear origin $\mathcal{H}_i, \mathcal{I}_i, \mathcal{M}$ are strongly anisotropic in (k_x, k_y)-plane. For the corresponding quantity, they act as a source when positive (red and yellow regions) and as a sink when negative (blue and dark blue regions). The linear exchange of energy with the background shear flow (which is the central energy supply for turbulence) involves all the components of the velocity perturbation through $\mathcal{H}_i$ terms in Equations (4.11)-(4.13) and only the azimuthal y-component of the magnetic field perturbation through the Maxwell stress term, $\mathcal{M}$, in Equation (4.16). However, the other quadratic forms can grow due to the linear exchange, $\mathcal{I}_i$, and nonlinear, $\mathcal{N}_i$, terms. The growth of the quadratic forms and energy extraction from the flow as a result of the operation of all these linear terms essentially constitutes the azimuthal MRI in the flow.

The linear drift parallel to the k_x-axis is equally important for all the physical quantities. The plots depicting the drift (second row in Figures 4.9-4.14), show that this process transfers modes with velocity $|qk_y|$ along k_x-axis at $k_y > 0$ and in the opposite direction at $k_y < 0$. Namely, the drift gives the linear growth of individual harmonics a transient nature, as it sweeps them through the vital area in $\mathbf{k}$-space. One has to note that the dynamics of axisymmetric modes with $k_y = 0$ should be analyzed separately, as the drift does not affect them. Consequently, the drift can not limit the duration of their amplification and if there is any, even weak, linear or nonlinear source of growth at $k_y = 0$, these harmonics can reach high amplitudes.

Let us turn to the analysis of the route ensuring the turbulence sustenance. First of all, we point out that it should primarily rely on magnetic perturbations, as the Maxwell stress is mainly responsible for energy supply for turbulence. From Figure 4.9, it is seen that the linear exchange term $\mathcal{I}_x^{(bu)}$ and the nonlinear term $\mathcal{N}_x^{(b)}$ make comparable contributions to the generation and maintenance of the radial field component $|\bar{b}_x|$. This is also consistent with the related plots in Figure 4.8. The exchange term takes energy from the radial velocity $\bar{u}_x$ and gives to $\bar{b}_x$. The distribution of $\mathcal{N}_x^{(b)}$ clearly demonstrates transversal transfer of $|\bar{b}_x|^2$ in (k_x, k_y)-plane for all considered $k_z = 0, 1, 2$ as well as among different components. The linear drift term also participates in forming the final spectrum of $|\bar{b}_x|$ in the quasi-steady turbulent state. It opposes the action of the nonlinear term: for $k_y > 0$ ($k_y < 0$), $\mathcal{N}_x^{(b)}$, transfers modes to the left (right), from the blue and dark blue region to the red and yellow regions, while the drift transfers in the opposite direction. So, the interplay of the drift, $\mathcal{I}_x^{(bu)}$ and $\mathcal{N}_x^{(b)}$ yields the specific anisotropic spectra of $|\bar{b}_x|$ shown in the top row of this figure. Particularly noteworthy is the role of the nonlinear term at $k_y = 0, k_z = 1, 2$, because the drift and the linear magnetic-kinetic exchange terms are proportional to k_y and hence vanish. As a result, axisymmetric modes with $k_y = 0$ are energetically supported only by the nonlinear term. (At $k_y = 0$, although $\mathcal{N}_x^{(b)}$ is positive both at $k_z = 1$ and $k_z = 2$, its values at $k_z = 1$ are about an order of magnitude smaller than those at $k_z = 2$ and might not be well represented by light green color in the bottom middle panel in Figure 4.9.) So, $\bar{b}_x$, which is remarkably generated by

the nonlinear term, in turn, is a key factor in the production and distribution of the energy-injecting Maxwell stress, $\mathcal{M}$, in Fourier space. Indeed, note the correlation between the distributions of $|\bar{b}_x|$ and $\mathcal{M}$ in (k_x, k_y)-plane depicted, respectively, in the top row of Figure 4.9 and in the third row of Figure 4.10.

From Figure 4.10 it is evident that, in fact, the Maxwell stress, $\mathcal{M}$, which is positive in (k_x, k_y)-plane and appreciable in the vital area, is the only source for the quadratic form of the azimuthal field component, $|\bar{b}_y|^2$, and hence for the turbulent magnetic energy, which is dominated by this component. The linear exchange term, $\mathcal{I}_y^{(bu)}$, appears to be much smaller with this stress term (and hence is not shown in this figure). The nonlinear term, $\mathcal{N}_y^{(b)}$, is negative in the vital area (blue regions in the bottom row of Figure 4.10), draining $|\bar{b}_y|^2$ there and transferring it to large wavenumbers as well as among different components. Thus, the sustenance of the magnetic energy is of linear origin, due solely to the Maxwell stress that, in turn, is generated from the radial field component. This stage constitutes the main (linear) part of the sustenance scheme, which will be described in the next subsection, and is actually a manifestation of the azimuthal MRI.

The dynamics of the vertical field component $\bar{b}_z$ is shown in 4.11. This components is smaller than $\bar{b}_x$ and $\bar{b}_y$. The linear exchange term, $\mathcal{I}_z^{(bu)}$, acts as a source, supplying $\bar{b}_z$ from the vertical velocity $\bar{u}_z$. The nonlinear term, $\mathcal{N}_z^{(b)}$, also realizes the transverse cascade and scatters the modes in different areas of (k_x, k_y)-plane (from the yellow and red to blue and dark blue areas in the bottom row of Figure 4.11). However, as it is seen from the related plot

in Figure 4.8, the cumulative effect of $\mathcal{N}_z^{(b)}$ in (k_x, k_y)-plane is positive and even prevails over the positive cumulative contribution of $\mathcal{I}_z^{(bu)}$ in this plane at every k_z. As it is clearly seen from Figure 4.11, the linear drift term opposes the action of the nonlinear term for $\bar{b}_z$, similar to that in the case of $\bar{b}_x$.

Figure 4.12 shows that the linear term $\mathcal{H}_x$ can be positive and act as a source for the radial velocity $|\bar{u}_x|^2$ at the expense of the mean flow, while the nonlinear term $\mathcal{N}_x^{(u)}$ is negative and drains it. The exchange terms $\mathcal{I}_x^{(u\theta)}$, $\mathcal{I}_x^{(ub)}$ are also negative, giving the energy of the radial velocity, respectively, to $\bar{\theta}$ and $\bar{b}_x$, but their contributions are negligible compared with $\mathcal{H}_x$ and $\mathcal{N}_x^{(u)}$ and hence not shown in this figure. So, the sustenance of $|\bar{u}_x|$ is ensured by the interplay of the linear drift and $\mathcal{H}_x$ terms. Indeed, shifting the result of the action of $\mathcal{H}_x$ by the linear drift to the right (left) for $k_y > 0$ ($k_y < 0$) gives the spectrum of $|\bar{u}_x|$ presented in the top row this figure.

Figure 4.13 shows that the dynamics of the azimuthal velocity $\bar{u}_y$ is governed primarily by $\mathcal{H}_y$, $\mathcal{I}_y^{(ub)}$ and $\mathcal{N}_y^{(u)}$. The action of $\mathcal{I}_y^{(u\theta)}$ is negligible compared with these terms, in agreement with the corresponding plot of Figure 4.8, and is not shown in this figure. The contributions of $\mathcal{I}_y^{(ub)}$ and $\mathcal{N}_y^{(u)}$ can be positive and hence these terms act as a source for $|\bar{u}_y|^2$. The distribution of $\mathcal{H}_y$ at $k_z = 0$ is quite complex with alternating positive and negative areas in (k_x, k_y)-plane, while it is negative for $k_z = 1, 2$. A interplay between these three terms yields the spectrum of $|\bar{u}_y|$ shown in the top row of Figure 4.13. From this spectrum, the harmonic with $k_x = 1, k_y = k_z = 0$ has the highest amplitude. Translating this result in physical space, it implies that the turbulence forms

quite powerful azimuthal/zonal flow, which will be examined in more detail in the next subsection.

Figure 4.14 shows that the contribution of the thermal $\mathcal{I}_z^{(u\theta)}$ in the dynamics of the quadratic form of vertical velocity, $|\bar{u}_z|^2$, is mostly negative (sink), but not so strong. The magnetic exchange term $\mathcal{I}_z^{(ub)}$ also acts as a sink, but is much smaller than $\mathcal{I}_z^{(u\theta)}$ and can be neglected. Of course, the role of the linear drift term is standard and similar to those for other components described above. The sustenance of $|\bar{u}_z|$ at $k_z = 0$ is ensured by the combination of the linear drift and the positive nonlinear term $\mathcal{N}_z^{(u)}$, while at $k_z = 1, 2$ it is maintained by the interplay of the linear drift and $\mathcal{H}_z$, which provides a source, now the nonlinear term $\mathcal{N}_z^{(u)}$ acts as a sink.

4.5.1 The basic subcycle of the turbulence sustenance

As we already mentioned, the sustenance of the turbulence is the result of a subtle intertwining of the anisotropic linear transient growth and nonlinear transverse cascade processes, which have been described in the previous section. The intertwined character of these processes is too complex for a vivid schematization. Nevertheless, based on the insight into the turbulence dynamics gained from Figures 4.9-4.14, we can bring out the *basic subcycle* of the sustenance that clearly shows the equal importance of the linear and nonlinear processes. The azimuthal and radial magnetic field components are most energy-containing in this case. The basic subcycle of the turbulence sustenance, which is concentrated in the vital area in Fourier space, is sketched

in Figure (4.15) (solid arrows within a rectangle) and can be understood as follows. The nonlinear term $\mathcal{N}_x^{(b)}$ contributes to the generation of the radial field $\bar{b}_x$ through the transverse cascade process. In other words, $\mathcal{N}_x^{(b)}$ provides a positive feedback for the continual regeneration of the radial field, which, in turn, is a seed/trigger for the linear growth of the MRI – $\bar{b}_x$ creates and amplifies the Maxwell stress, $\mathcal{M}$, due to the shear (via linear term in Equation B.6 proportional to q). The positive stress then increases the dominant azimuthal field energy $|\bar{b}_y|^2/2$ at the expense of the mean flow, opposing the negative nonlinear term $\mathcal{N}_y^{(b)}$ (and resistive dissipation). Thus, this central energy gain process for turbulence, as mentioned before, is of linear nature and a consequence of the azimuthal MRI. The linearly generated $\bar{b}_y$ gives a dominant contribution – positive feedback – to the nonlinear term $\mathcal{N}_x^{(b)}$, closing the basic subcycle.

This is only a main part of the complete and more intricate sustaining scheme that involves also the velocity components. In this sketch, the dashed arrows denote the other, extrinsic to the basic subcycle, processes. Namely, $\bar{b}_x$, together with the nonlinear term, is fueled also by the linear exchange term, $\mathcal{I}_x^{(bu)}$, which takes energy from the radial velocity $\bar{u}_x$, while the azimuthal velocity $\bar{u}_y$ gets energy from $\bar{b}_y$ via the linear exchange term $\mathcal{I}_y^{(ub)}$. These are all linear processes, part of the MRI. (The vertical velocity does not explicitly participate in this case.) All These components of the velocity $\bar{u}_x$, $\bar{u}_y$, $\bar{u}_z$ and the magnetic field $\bar{b}_x$, $\bar{b}_z$ then contribute to the nonlinear feedback through the nonlinear term for the radial field, $\mathcal{N}_x^{(b)}$, which is the most important

one in the sustenance (see Equations B.37), but still the contribution of $\bar{b}_y$ in this nonlinear term is dominant. This feedback process is essentially 3D: we verified that modes with $|k_z| = 1, 2$ give the largest contribution to the horizontal integral in the expression for the nonlinear term $\mathcal{N}_x^{(b)}$ (not shown here).

It is appropriate here to give a comparative analysis of the dynamical processes investigated in this Chapter and those underlying sustained 3D MRI-dynamo cycles reported in Herault et al. (2011) and Riols et al. (2015, 2017), despite the fact that these papers considered a magnetized Keplerian flow with different, zero net vertical flux, configuration and different values of parameters (smaller resolution, box aspect ratio, smaller Reynolds numbers) than those adopted here. These apparently resulted in the resistive processes penetrating into the vital area (in our terms) and reducing a number of active modes to only first non-axisymmetric ones (shearing waves) with the minimal azimuthal and vertical wavenumbers, $k_y = 2\pi/L_y, k_z = 0, 2\pi/L_z$, which undergo the transient MRI due to the mean axisymmetric azimuthal (dynamo) field. By contrast, the number of the active modes in our turbulent case is more than hundred (Figure 4.7). Regardless of these differences, we can trace the similarities in the sustenance cycles – the energy budget equations for these modes derived in those papers in fact show that a similar scheme underlies the sustenance as in the present case. The energy of the radial field $\bar{b}_x$ of new leading non-axisymmetric modes is supplied by the joint action of the induction term (i.e., $\mathcal{I}_x^{(bu)}$ in our notations) and redistribution by the nonlinear term, however, a

summation over k_x as used in those energy budget equations does not permit to see how this nonlinear redistribution of modes over k_x due to the transverse cascade actually occurs in their analysis. As for the energy of $\bar{b}_y$, it is amplified by the Maxwell stress during the transient MRI phase (also called the Ω-effect) and is drained by the corresponding nonlinear term. Since in the turbulent state considered here there are much more active modes, representing various linear and nonlinear dynamical terms in (k_x, k_y)-plane has a definite advantage over such low-mode-number models in that gives a more general picture of nonlinear triad interactions among all active modes. Such a comparison raises one more point for thought: for a correct consideration of nonlinear triad interactions, we gave preference to boxes symmetrical in (x, y)-plane, while, all simulations in those papers are carried out in azimuthally elongated boxes.

4.5.2 Zonal flow

Excitation of zonal flows by the MRI-turbulence was previously observed by Johansen et al. (2009) and Bai & Stone (2014) in the case of zero and nonzero net vertical magnetic flux, respectively. We also observe it here in the case of the net azimuthal field. As noted above, the mode corresponding to the zonal flow is axisymmetric and vertically constant, $k_y = k_z = 0$, with large scale variation in the radial direction, $|k_x| = 1$. The divergence-free (incompressibility) condition (B.8) implies that the radial velocity is zero, $\bar{u}_x = 0$, for this mode and hence $\mathcal{H}_y = 0$ at all times, also the magnetic exchange term is identically zero at $k_y = 0$, $\mathcal{I}_y^{(ub)} = 0$. Therefore, a source of the zonal flow

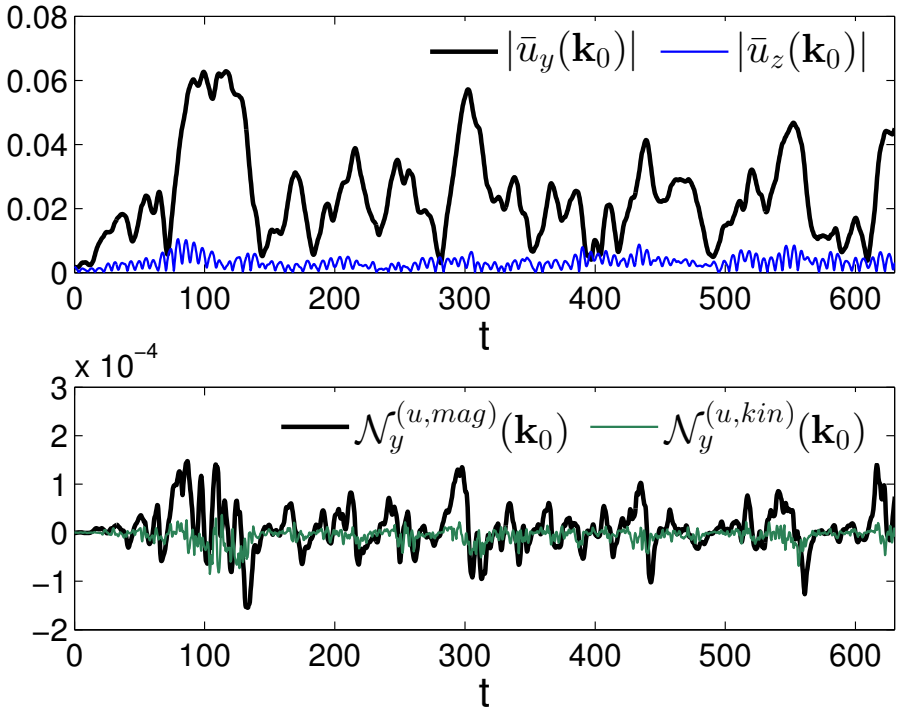

Figure 4.16: Evolution of the large-scale mode $\mathbf{k}_0 = (1, 0, 0)$, which corresponds to the axisymmetric zonal flow. Shown are the amplitudes of the azimuthal $|\bar{u}_y|$ (black) and the vertical $|\bar{u}_z|$ (blue) velocities (upper panel) as well as the magnetic $\mathcal{N}_y^{(u,mag)}$ (black) and hydrodynamic $\mathcal{N}_y^{(u,kin)}$ (green) parts of the nonlinear term $\mathcal{N}_y^{(u)}$ (lower panel). The dominant azimuthal velocity (i.e., zonal flow) is driven by the magnetic part of the nonlinear term and is characterized by remarkably slower time variations.

can be only the nonlinear term $\mathcal{N}_y^{(u)}$ in Equation (4.12). We can divide this term into the magnetic, $\mathcal{N}_y^{(u,mag)}$, and hydrodynamic, $\mathcal{N}_y^{(u,kin)}$, parts,

$$\mathcal{N}_y^{(u)} = \mathcal{N}_y^{(u,mag)} + \mathcal{N}_y^{(u,kin)}. \tag{4.23}$$

For the dominant mode $\mathbf{k_0} = (1, 0, 0)$, these two parts in Equation (4.23) have the forms:

$$\mathcal{N}_y^{(u,mag)}(\mathbf{k}_0, t) = \frac{\mathrm{i}}{2}\bar{u}_y^*(\mathbf{k}_0, t) \int d^3\mathbf{k}' \bar{b}_y(\mathbf{k}', t)\bar{b}_x(\mathbf{k}_0 - \mathbf{k}', t) + c.c.,$$

with the integrand composed of the turbulent magnetic stresses and

$$\mathcal{N}_y^{(u,kin)}(\mathbf{k}_0, t) = -\frac{\mathrm{i}}{2}\bar{u}_y^*(\mathbf{k}_0, t) \int d^3\mathbf{k}' \bar{u}_y(\mathbf{k}', t)\bar{u}_x(\mathbf{k}_0 - \mathbf{k}', t) + c.c.,$$

with the integrand composed of the turbulent hydrodynamic stresses. To understand the nature of the zonal flow, in Figure 4.16 we present the time-development of the azimuthal and vertical velocities as well as the driving nonlinear terms for this mode. $|u_y(\mathbf{k_0}, t)|$ is characterized by remarkably longer timescale (tens of orbits) variations and prevails over rapidly oscillating $|u_z(\mathbf{k_0}, t)|$, i.e., the dominant harmonic indeed forms a slowly varying in time axisymmetric zonal flow. Comparing the time-development of $|\bar{u}_y(\mathbf{k}_0, t)|$ with that of the corresponding nonlinear terms in the lower panel of Figure 4.16, we clearly see that it is driven primarily by the magnetic nonlinear term, $\mathcal{N}_y^{(u,mag)}(\mathbf{k_0}, t)$, which physically describes the effect of the total azimuthal magnetic tension (random forcing) exerted by all other smaller-scale modes on the large-scale $\mathbf{k}_0$ mode, whereas $\mathcal{N}_y^{(u,kin)}(\mathbf{k_0}, t)$, corresponding to the net effect

of the hydrodynamic stresses, is much smaller than the magnetic one. The important role of the magnetic perturbations in launching and maintaining the zonal flow is consistent with the findings of Johansen et al. (2009).

4.5.3 Effect of the aspect ratio and the universality of the turbulence sustenance scheme

The main advantage of the box $(4, 4, 1)$ analyzed in the previous subsection is that (i) it is symmetric in physical (x, y)-and Fourier (k_x, k_y)-planes, where the effects of shear are most important, (ii) the modes contained in this box densely cover the vital area in (k_x, k_y)-plane and sufficiently comprise effectively growing (optimal) harmonics (see the panel for the box $(4, 4, 1)$ in Figure 4.2). In the three asymmetric boxes – $(1, 4, 1)$, $(2, 4, 1)$ and $(4, 2, 1)$ – the modes less densely cover the vital area (Figure 4.2). As for the box $(8, 8, 1)$, as mentioned above, the results qualitatively similar to the box $(4, 4, 1)$ are expected. In this subsection, we examine how the box aspect ratio influences the turbulence dynamics, and in particular, the distribution of the linear and nonlinear process in Fourier space.

A general temporal behavior of the volume-averaged energies, stresses and rms values of the velocity and magnetic field components is similar to that for the box $(4, 4, 1)$ represented in Figure 4.3 (see also Table 4.1) and we do not show it here, but concentrate instead on the differences in Fourier space. Figure 4.17 juxtaposes the spectra of the magnetic energy, Maxwell stress and the magnetic nonlinear term $\mathcal{N}_x^{(b)}$ for all the boxes. From this figure it is

evident that the skeleton of the balances of the various linear and nonlinear processes and, in particular the basic subcycle, underlying the sustenance of the azimuthal MRI-turbulence are qualitatively the same in all the simulated boxes and quite robust – the variations in box sizes do not affect its effectiveness. Changes in box aspect ratios lead to variation of the inclinations, shapes and intensities of the energy spectra as well as the distribution of linear and nonlinear dynamical terms in (k_x, k_y)-plane. It is seen in Figure 4.17 that this variation is minimal between the symmetric in (x, y)-plane boxes $(4, 4, 1)$ and $(8, 8, 1)$ – they have similar spectral characteristics with identical inclination angles – but is more remarkable among the asymmetric boxes, $(4, 2, 1)$, $(2, 4, 1)$, $(1, 4, 1)$. Specifically, in the latter boxes, the spectral characteristics are somewhat deformed and have different inclinations compared to those in the symmetric boxes. The reason for this is the reduction of the active modes' number/density along the k_x- and k_y-axis in these boxes in contrast to the symmetric ones (see Figure 4.2).

4.6 Summary and discussion

In this Chapter, we elucidated the essence of the sustenance of MRI-driven turbulence in Keplerian disks threaded by a nonzero net azimuthal field by means of a series of shearing box simulations and analysis in 3D Fourier (**k**-)space. It is well known that in the linear regime the MRI in the presence of a azimuthal field has a transient nature and eventually decays without an appropriate nonlinear feedback. We studied in detail the linear and

nonlinear dynamical processes and their interplay in Fourier space that ensure such a feedback. Our first key finding is the pronounced anisotropy of the nonlinear processes in **k**-space. This anisotropy is a natural consequence of the anisotropy of linear processes due to the shear and cannot be described in the framework of direct and inverse cascades, commonly considered in the classical theory of HD and MHD turbulence without shear, because the main activity of the nonlinear processes is transfer of modes over wavevector orientation (angle) in **k**-space, rather than along wavevector that corresponds to direct/inverse cascades. This new type of nonlinear process – *the transverse cascade* – plays a decisive role in the long-term maintenance of the MRI-turbulence. Our second key result is that the sustenance of the turbulence in this case is ensured as a result of a subtle interplay of the linear transient MRI growth and nonlinear transverse cascade. This interplay is intrinsically quite complex and refined. Nevertheless, one can isolate the basic subcycle of the turbulence sustenance, which is as follows. The linear exchange of energy between the magnetic field and the background flow, realized by the Maxwell stress, $\mathcal{M}$, supplies only the azimuthal field component $\bar{b}_y$. As for the radial field $\bar{b}_x$, it is powered by the linear exchange $\mathcal{I}_x^{(bu)}$ and the nonlinear $\mathcal{N}_x^{(b)}$ terms. So, $\bar{b}_x$ and $\bar{b}_y$ have sources of different origin. However, one should bear in mind that these processes are intertwined with each other: the source of $\bar{b}_y$ (i.e., the Maxwell stress, $\mathcal{M}$) is created by $\bar{b}_x$. In its turn, the production of the nonlinear source of $\bar{b}_x$ (i.e., $\mathcal{N}_x^{(b)}$) is largely due to $\bar{b}_y$. Similarly intertwined are the dynamics of other spectral magnetic and kinematic components. This sustaining dynamics of

the turbulence is concentrated mainly in a small wavenumber area of **k**-space, i.e., involves large scale modes, and is appropriately called the *vital area*.

The spectra of the kinetic and magnetic energies that are established in the turbulent state as a result of such interplay are consequently also anisotropic and fundamentally differ from classical Kolmogorov or IK spectra. So, the conventional characterization of nonlinear MHD cascade processes in shear flows in terms of direct and inverse cascades, which ignores the shear-induced spectral anisotropy and the resulting important transverse cascade process, is generally incomplete and misleading. For this reason, we examined the dynamical processes in 3D Fourier space in full without making the shell-averaging, which has been commonly done in previous studies of MRI-turbulence and smears out the anisotropy. We also showed that the turbulence is accompanied by a large scale and slowly varying in time zonal (azimuthal) flow, which is driven by the turbulent magnetic stresses.

The proposed scheme of the turbulence sustenance based on the intertwined cooperated action of the linear and nonlinear processes in the vital area is quite robust – it is effective for different aspect ratios of the simulation box. For all the box configurations considered, $(4, 4, 1)$, $(1, 4, 1)$, $(2, 4, 1)$, $(4, 2, 1)$ and $(8, 8, 1)$, the scheme is essentially universal, although there are quantitative differences. The anisotropy of the box in (k_x, k_y)-plane is superposed on the intrinsic shear-induced anisotropy of the dynamical process and somewhat deforms the picture of the turbulence, but the sustaining scheme is not changed. In any case, an isotropic distribution of modes in (k_x, k_y)-plane

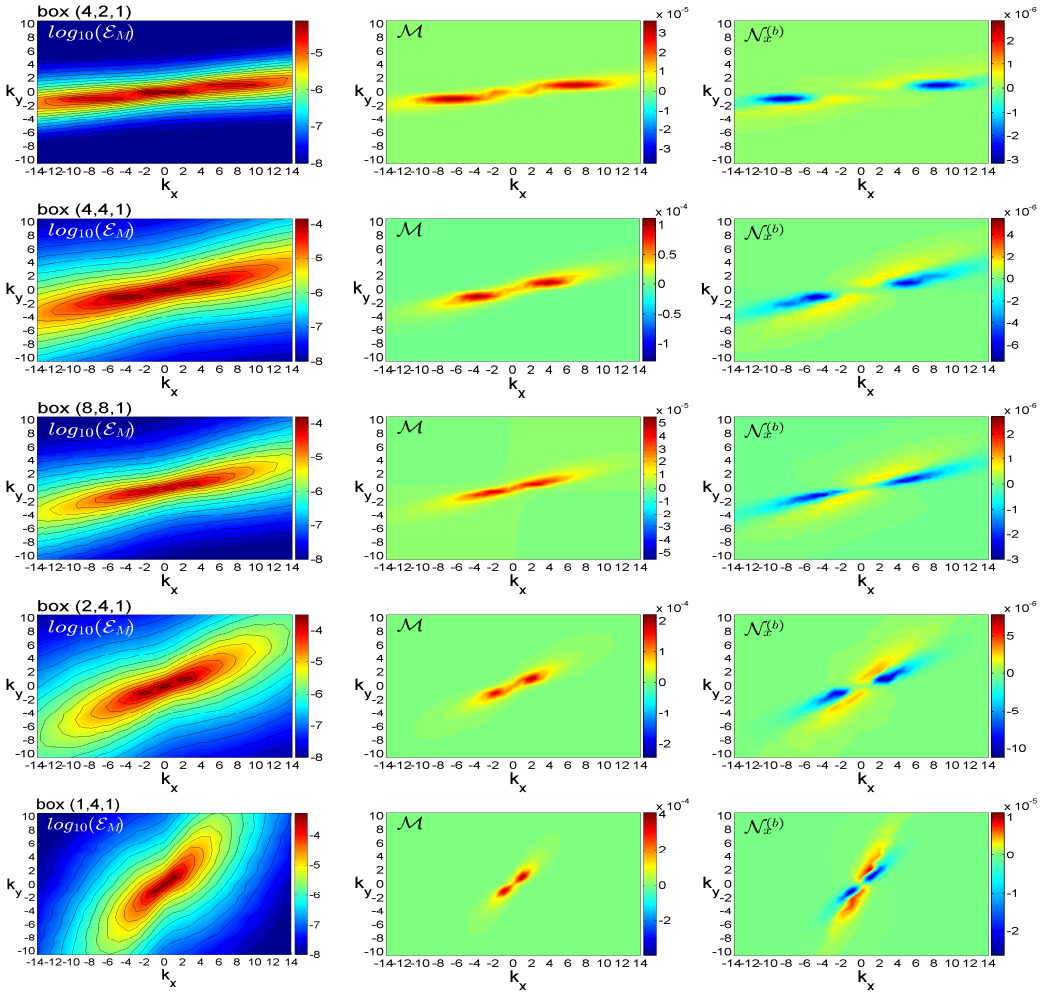

Figure 4.17: Spectra of $\mathcal{E}_M$, $\mathcal{M}$ and $\mathcal{N}_x^{(b)}$ in (k_x, k_y)-plane at $k_z = 1$ for all the boxes: $(4, 2, 1)$ (top row), $(4, 4, 1)$ (second row), $(8, 8, 1)$ (third row), $(2, 4, 1)$ (fourth row) and $(1, 4, 1)$ (bottom row). In all the panels, the general structure of these spectral terms is quite similar, that indicates the universality and the robust character of the turbulence sustaining scheme. At the same time, the symmetric boxes $(4, 4, 1)$ and $(8, 8, 1)$ have similar spectral pictures with identical inclinations, while in the asymmetric in (x, y)-plane boxes, the spectral characteristics are somewhat deformed and have different inclinations compared to the symmetric boxes.

seems preferable for studying the own anisotropy of the shear flow system, which is naturally achieved for equal radial and azimuthal sizes, $L_x = L_y$, of the box.

In this Chapter, we considered a spectrally stable (i.e., without purely exponential MRI) magnetized disk flow with an azimuthal field, where the energy for turbulence can only be supplied via linear transient growth of the MRI. Being associated with shear, it seems obvious that the vital area and nonlinear transverse cascade should be also present in disk flows with a nonzero net vertical magnetic field, which can give rise to the exponentially growing MRI (Balbus & Hawley, 1991; Goodman & Xu, 1994; Pessah & Goodman, 2009). In this case, besides purely exponentially growing axisymmetric (channel) modes, energy supply and transport via (transient) growth of non-axisymmetric ($k_y \neq 0$) modes are also important (Longaretti & Lesur, 2010; Mamatsashvili et al., 2013; Squire & Bhattacharjee, 2014). The latter, leading to anisotropic nonlinear dynamics (Murphy & Pessah, 2015), can inevitably effect the nonlinear transverse cascade process. However, as it is shown in Chapter 5, the presence of the purely exponentially growing modes alter the scheme of the interplay of the dynamical processes that we studied here in the case of the azimuthal field.

Chapter 5

Active modes and dynamical balances in MRI-turbulence of Keplerian disks with a net vertical magnetic field

5.1 Introduction

Anisotropic turbulence offers a means of enhanced transport of angular momentum in astrophysical disks (Shakura & Sunyaev, 1973; Lynden-Bell & Pringle, 1974), whereas isotropic turbulence is unable to ensure such a transport. It is not surprising that from the 1980s, research in astrophysical disks focused on identifying sources of turbulence and understanding its statistical characteristics. The turning point was the beginning of the 1990s, when a linear instability mediated by a weak vertical magnetic field in differentially rotating conducting fluids (Velikhov, 1959; Chandrasekhar, 1960) was rediscovered for sufficiently ionized astrophysical disks by Balbus & Hawley (1991) and subsequently named as the magnetorotational instability (MRI). MRI is a robust dynamical instability that leads to exponential growth of axisymmetric perturbations, gives rise to and steadily supplies with energy magnetohydrodynamic (MHD) turbulence, as was demonstrated in earlier numerical simulations shortly after the importance of linear MRI in disks had been realized (e.g., Hawley & Balbus, 1991, 1992; Hawley et al., 1995; Brandenburg et al.,

1995; Balbus & Hawley, 1998).

The generic nonnormality (non-self-adjointness) of a strongly sheared Keplerian flow of astrophysical disks provides an additional important linear mechanism of energy supply to the turbulence - transient, or nonmodal growth of perturbations (Lominadze et al., 1988; Chagelishvili et al., 2003; Yecko, 2004; Afshordi et al., 2005; Tevzadze et al., 2008; Shtemler et al., 2011; Salhi et al., 2012; Pessah & Chan, 2012; Mamatsashvili et al., 2013; Zhuravlev & Razdoburdin, 2014; Squire & Bhattacharjee, 2014; Razdoburdin & Zhuravlev, 2017). Although the latter is generally less powerful than the classical (exponentially growing) MRI, it is nevertheless capable of driving quite robust MHD turbulence in the absence of the classical MRI, for instance, in disks threaded by a purely azimuthal/toroidal magnetic field (e.g., Hawley et al., 1995; Fromang & Nelson, 2006; Simon & Hawley, 2009; Guan et al., 2009; Guan & Gammie, 2011; Flock et al., 2012b; Nauman & Blackman, 2014; Meheut et al., 2015; Gogichaishvili et al., 2017). In such spectrally, or modally stable magnetized disk flows lacking exponentially growing MRI modes, nonlinear processes are vital for turbulence sustenance. In this situation, the canonical – direct and inverse – cascade processes (accepted in classical Kolmogorov or Iroshnikov-Kraichnan theories of turbulence) are not capable of sustaining the turbulence – this role is taken over by a new type of the cascade processes, so-called *the nonlinear transverse cascade* (Horton et al., 2010; Mamatsashvili et al., 2014). What is the physical reason for the emergence of the transverse cascade in shear flows and its specific nature? The thing is that the anisotropy

of the nonnormality/shear-induced linear dynamics entails the anisotropy of the nonlinear processes: transverse, or angular redistribution of perturbation harmonics in Fourier (wavenumber) space. In spectrally stable shear flows, in which the only mechanism for the energy supply to perturbations is the linear transient growth process, the nonlinear transverse cascade continually repopulates with perturbation harmonics those areas in Fourier space, where they can undergo transient amplification, and in this way ensures a long-term sustenance of the turbulence (Mamatsashvili et al., 2014, 2016). In the absence of such a feedback, non-axisymmetric modes that undergo in this case the most effective nonmodal growth, get later sheared away and eventually decay. In the context of disks, this process was studied in detail in paper (Gogichaishvili et al., 2017) (see Chapter 4) for a Keplerian flow with a net azimuthal magnetic field by combining direct numerical simulations and, based on them, the subsequent analysis of the dynamical processes in Fourier space. It was shown that the nonlinear transverse cascade does ensure continual regeneration of transiently growing harmonics, thereby yielding sustained robust subcritical turbulence in the disk flow. Thus, in spectrally stable MHD shear flows, the existence of turbulence is due to a subtle interplay of linear transient growth and the nonlinear transverse cascade processes.

In this Chapter, we consider a local model of a weakly ionized Keplerian disk threaded by a net vertical magnetic field, where there exists classical MRI with a steady exponential growth of axisymmetric modes (Balbus & Hawley, 1991, 1998; Wardle, 1999; Pessah et al., 2006; Lesur & Longaretti,

2007; Pessah & Chan, 2008; Longaretti & Lesur, 2010; Latter et al., 2015; Shakura & Postnov, 2015). Because of this, there is no deficit in energy supply and the role of nonlinearity in the sustenance of perturbations is not as vital as in the case of azimuthal field. However, at the same time, MRI also owes its existence to the shear of disk flow and therefore is inevitably subject to nonmodal effects (Mamatsashvili et al., 2013; Squire & Bhattacharjee, 2014). As demonstrated in this Chapter (related to (Gogichaishvili et al., 2018)), this has two important consequences. First, the nonmodal MRI growth of both axisymmetric and non-axisymmetric modes during finite times are in fact more relevant and important in the energy supply process of turbulence, because the time scales involved are of the order of dynamical/orbital time (Walker et al., 2016), than the modal (exponential) growth of axisymmetric modes prevalent at large times (see also Squire & Bhattacharjee, 2014). Second, underlying nonlinear processes are necessarily anisotropic in Fourier space as a result of the inherent anisotropy of linear nonmodal dynamics due to the shear. This anisotropy above all gives rise to the nonlinear transverse cascade and one of the main goals of the present Chapter is to vividly demonstrate its importance in forming the overall dynamical picture of net vertical field MRI-turbulence.

Recently, Murphy & Pessah (2015) investigated the saturation of MRI in disks with a net vertical field and the properties of the resulting MHD turbulence both in physical and Fourier space. Their study was mainly devoted to characterizing the anisotropic nature of this turbulence. They also pointed out a general lack of analysis of the anisotropy in the existing stud-

ies of MRI-turbulence: "Although there have been many studies of the linear phase of the MRI and its nonlinear evolution, only a fraction have explored the mechanism responsible for its saturation in detail, and none have focused explicitly on the evolution of the degree of anisotropy exhibited by the magnetized flow as it evolves from the linear regime of the instability to the ensuing turbulent state". The main reason for overlooking the anisotropic nature of MRI-driven turbulence in most of previous works focusing on its spectral dynamics (e.g., Fromang & Papaloizou, 2007; Simon et al., 2009; Davis et al., 2010; Lesur & Longaretti, 2011) was a somewhat misleading mathematical treatment, specifically, spherical shell-averaging procedure in Fourier space (borrowed from forced MHD turbulence studies without shear flow, see e.g., Verma, 2004; Alexakis et al., 2007), which had been employed to extract statistical information about the properties of MRI-turbulence. Obviously, the use of the shell-averaging, which, in fact, smears out the transverse cascade, is, strictly speaking, justified for isotropic turbulence, but by no means for shear flow turbulence and therefore for, its special case, MRI-turbulence "nourished" in a sheared environment of disk flow. Thus, the shell-averaging is not an optimal tool for analyzing spectral energy distributions as well as dynamical processes in MRI-driven turbulence that is far from isotropic due to the shear (see also Hawley et al., 1995; Nauman & Blackman, 2014; Lesur & Longaretti, 2011; Murphy & Pessah, 2015; Gogichaishvili et al., 2017). This fact also calls into question investigations based on the shell-averaging that aim to identify a power-law character and associated slopes of turbulent energy spectrum, be-

cause the anisotropy of the energy spectrum itself, a direct consequence of the transverse cascade, is wiped out in these cases. This is probably the reason why the kinetic and magnetic energy spectra do not generally display a well-defined power-law behavior in MRI-turbulence in disk flows with a net vertical field (Simon et al., 2009; Lesur & Longaretti, 2011; Meheut et al., 2015; Walker et al., 2016).

In view of the above, in this work we focus on the dynamics and balances of MRI-turbulence in disks with a net vertical/poloidal magnetic field. We adopt the local shearing box model of the disk with constant vertical thermal stratification. The analysis is performed in three-dimensional (3D) Fourier space in full, i.e., without doing the above-mentioned averaging of spectral quantities over spherical shells of constant wavenumber magnitude $k = |\mathbf{k}|$. This allows us to capture the spectral anisotropy of MRI-turbulence due to the shear and the resulting nonlinear angular redistribution of perturbation modes in Fourier space, i.e., transverse cascade, thereby getting a deeper understanding of spectral and statistical properties of the turbulence. In previous relevant studies on a net vertical field MRI (e.g., Goodman & Xu, 1994; Hawley et al., 1995; Sano & Inutsuka, 2001; Lesur & Longaretti, 2007; Bodo et al., 2008; Latter et al., 2009, 2010; Simon et al., 2009; Pessah & Goodman, 2009; Longaretti & Lesur, 2010; Pessah, 2010; Bai & Stone, 2014; Murphy & Pessah, 2015), this angular redistribution (scatter) of modes in Fourier space was attributed to secondary, or parasitic instabilities. Specifically, the most unstable, exponentially growing axisymmetric MRI modes (channels) are sub-

ject to secondary instabilities of non-axisymmetric modes with growth rates proportional to the amplitude of these channel solutions. In this way, the parasitic instabilities redistribute the energy from the primary axisymmetric channel modes to non-axisymmetric parasitic ones, halting the exponential growth of the former and leading to the saturation of MRI. Several approximations are made in this description: 1. the large amplitude channel mode is a time-independent background off which the small-amplitude parasitic modes feed and 2. the effects of the imposed vertical field, the Coriolis force, and the basic Keplerian shear are all usually neglected. These assumptions clearly simplify the analysis of the excitation and dynamics of the non-axisymmetric parasitic modes, but, more importantly, because of neglecting the basic flow shear, omit independent from the primary MRI modes source of their support - the transient/nonmodal growth of non-axisymmetric modes, which, as discussed above, is an inevitable linear process in shear (disk) flows.

To keep an analysis general and self-consistent, together with the general nonmodal growth process, we employ the concept of the nonlinear transverse cascade in the present problem of MRI with a net vertical magnetic field that naturally encompasses the secondary instabilities. This unifying framework enables us to correctly describe the interaction between the channel and non-axisymmetric parasitic modes when the above assumptions break down – the amplitudes of these two mode types become comparable, so that it is no longer possible to clearly distinguish between the channel as a primary background and parasites as small perturbations on top of that. This is the

case in the developed turbulent state of vertical field MRI, where channels undergo recurrent amplifications (bursts) and decays (e.g., Sano & Inutsuka, 2001; Lesur & Longaretti, 2007; Bodo et al., 2008; Simon et al., 2009; Murphy & Pessah, 2015). This decay phase is usually attributed to the linear non-axisymmetric parasitic instabilities, however, in the fully developed turbulent state it is more likely governed by nonlinearity. As is shown in this Chapter, the transverse cascade accounts for the transfer of energy from the axisymmetric channel modes to a broad spectrum of non-axisymmetric ones (referred to as the rest modes here) as well as to the axisymmetric zonal flow mode, which appears to commonly accompany MRI-turbulence (Johansen et al., 2009; Simon et al., 2012; Bai & Stone, 2014). The nonlinear transverse cascade may not be the vital source of the energy supply to turbulence in the presence of purely exponentially growing MRI, but still it shapes the dynamics, sets the saturation level/strength and determines the overall "design" of the turbulence the "building blocks" of which are these three types of perturbation modes analyzed in this Chapter.

In the spirit of works (Horton et al., 2010; Mamatsashvili et al., 2014, 2016; Gogichaishvili et al., 2017, 2018), here we investigate in detail the roles of underlying different anisotropic linear and nonlinear dynamical processes shaping the net vertical field MRI-turbulence. Namely, we first perform direct numerical simulations of the turbulence and then, using the simulation data, explicitly calculate individual linear and nonlinear terms in spectral equations and analyze them and their interplay in detail. The present study is a gen-

eralization of the related works by Simon et al. (2009); Lesur & Longaretti (2011), where the dynamics of vertical field MRI-turbulence – the spectra of energy, injection and nonlinear transfers – were analyzed in Fourier space, however, using a restrictive approach of shell-averaging, which misses out the shear-induced anisotropy of the turbulence and hence the interaction of axisymmetric channel and non-axisymmetric modes. It also extends the study of Murphy & Pessah (2015), who focused on the anisotropy of vertical field MRI-turbulence in both physical and Fourier space and examined, in particular, anisotropic spectra of the magnetic energy and Maxwell stress during the linear growth stage of the channel solutions and after saturation, but not the action of the linear and nonlinear terms governing their evolution.

This Chapter is organized as follows. The physical model and derivation of dynamical equations in Fourier space is given in Section 5.2. The linear nonmodal growth of MRI with a net vertical field is analyzed in Section 5.3. Numerical simulations of the ensuing MRI-turbulence and its general characteristics, such as time-development, energy spectra and the classification of dynamically active modes are given in Section 5.4. In this section we also give the main analysis of the individual dynamics of the active modes and their interdependence in Fourier space that underlie the dynamics of the turbulence. Conclusions are given in Section 5.5.

5.2 Physical model and basic equations

We use a shearing box model to investigate the essence of MHD turbulence driven by the classical MRI in Keplerian disks. The shearing box represents a local Cartesian coordinate frame centered at a fiducial point that co-rotates with the disk at angular velocity Ω (Hawley et al., 1995). In this frame, we consider the flow of an incompressible conducting fluid with constant kinematic viscosity ν, thermal diffusivity χ and Ohmic resistivity η. The flow is thermally stratified in the vertical direction. Adopting the Boussinesq approximation for the vertical stratification (Balbus & Hawley, 1991; Lesur & Ogilvie, 2010), the basic equations of non-ideal MHD become

$$\frac{\partial \mathbf{U}}{\partial t}+(\mathbf{U}\cdot\nabla)\mathbf{U} = -\frac{1}{\rho}\nabla P+\frac{(\mathbf{B}\cdot\nabla)\,\mathbf{B}}{4\pi\rho}-2\mathbf{\Omega}\times\mathbf{U}+2q\Omega^2 x\mathbf{e}_x-\Lambda N^2\theta\ \mathbf{e}_z+\nu\nabla^2\mathbf{U}, \tag{5.1}$$

$$\frac{\partial \theta}{\partial t}+\mathbf{U}\cdot\nabla\theta = \frac{u_z}{\Lambda}+\chi\nabla^2\theta, \tag{5.2}$$

$$\frac{\partial \mathbf{B}}{\partial t} = \nabla\times(\mathbf{U}\times\mathbf{B})+\eta\nabla^2\mathbf{B}, \tag{5.3}$$

$$\nabla\cdot\mathbf{U} = 0, \tag{5.4}$$

$$\nabla\cdot\mathbf{B} = 0, \tag{5.5}$$

where $\mathbf{e}_x,\ \mathbf{e}_y,\ \mathbf{e}_z$ are the unit vectors along the cartesian coordinates (x, y, z), respectively, in the radial, azimuthal and vertical directions, ρ is the density, $\mathbf{U}$ is the velocity, $\mathbf{B}$ is the magnetic field, P is the total pressure, equal to the sum of the thermal and magnetic pressures, $\theta \equiv \delta\rho/\rho$ is the perturbation of the density logarithm, or entropy. The shear parameter $q = -d\ln\Omega/d\ln r$ is

set to $q = 3/2$ for a Keplerian disk. N^2 is the Brunt-Väisälä frequency squared that controls the stratification in the Boussinesq approximation. The effects of thermal stratification are taken into account here in a simple manner, that is, N^2 is assumed to be positive and spatially constant, equal to $0.25\Omega^2$, in the considered stably stratified local model along the z-axis (Lesur & Ogilvie, 2010). We define a stratification length $\Lambda \equiv g/N^2$, where g is the vertical component of the gravity. This length cancels out from the main equations if we normalize the density logarithm by $\Lambda\theta \to \theta$, which is used henceforth.

Equations (5.1)-(5.5) have a stationary equilibrium solution – an azimuthal flow along the y-direction with linear shear of velocity in the the radial x-direction, $\mathbf{U}_0 = -q\Omega x\mathbf{e}_y$, with the total pressure P_0, density ρ_0 and threaded by a vertical uniform magnetic field, $\mathbf{B}_0 = B_{0z}\mathbf{e}_z, B_{0z} = const > 0$. Consider now perturbations of the velocity, total pressure and magnetic field about the equilibrium, $\mathbf{u} = \mathbf{U} - \mathbf{U}_0, p = P - P_0, \mathbf{b} = \mathbf{B} - \mathbf{B}_0$. Substituting them into Equations (5.1)-(5.5) and rearranging the nonlinear terms with the help of divergence-free conditions (5.4) and (5.5), we arrive at the system (C.1)-(C.9) governing the dynamics of perturbations with arbitrary amplitude that is given in Appendix C. These equations form the basis for our numerical simulations below to get a complete data set of the perturbation evolution in the turbulent state.

We normalize the variables by taking Ω^{-1} as the unit of time, the disk thickness H as the unit of length, ΩH as the unit of the velocity, $\Omega H\sqrt{4\pi\rho_0}$ as the unit of the magnetic field and $\rho_0\Omega^2H^2$ as the unit of the pressure and

energy. Viscosity, thermal diffusivity and resistivity are measured, respectively, by the Reynolds number, Re, Péclet number, Pe, and magnetic Reynolds number, Rm, which are defined as

$$\mathrm{Re} = \frac{\Omega H^2}{\nu}, \quad \mathrm{Pe} = \frac{\Omega H^2}{\chi}, \quad \mathrm{Rm} = \frac{\Omega H^2}{\eta},$$

which are taken to be equal $\mathrm{Re} = \mathrm{Pe} = \mathrm{Rm} = 3000$ (i.e., the magnetic Prandtl number $\mathrm{Pm} = \mathrm{Rm}/\mathrm{Re} = 1$). The strength of the background uniform vertical magnetic field is measured by the parameter $\beta = 2\Omega^2 H^2/v_A^2$, which we fix to $\beta = 10^3$, where $v_A = B_{0z}/(4\pi\rho_0)^{1/2}$ is the corresponding Alfvén speed. In the incompressible case, this parameter is a proxy of the usual plasma β parameter, since sound speed in thin disks is $c_s \sim \Omega H$ (Longaretti & Lesur, 2010). In this non-dimensional units, the mean field is $B_{0z} = \sqrt{2/\beta} = 0.0447$.

We carry out numerical simulations of the main Equations (C.1)-(C.9) using the publicly available pseudo-spectral code SNOOPY (Lesur & Longaretti, 2007). It is a general-purpose code, solving HD and MHD equations with various physical effects, such as shear, rotation, stratification, etc. The code is based on a spectral implementation of the shearing box model with the standard boundary conditions: periodic in the y- and z-directions, but shear-periodic in the x-direction. Fourier transforms are computed using the FFTW library, taking also into account the drift of modes in $\mathbf{k}$-space for consistency with these boundary conditions. Nonlinear terms are computed using a pseudo-spectral algorithm (Canuto et al., 1988), and antialiasing is enforced using the 2/3-rule. Time-integration is done by a third-order Runge-Kutta

scheme, except for viscous and resistive terms, which are integrated using an implicit scheme. The code has been extensively used in the shearing box studies of disk turbulence (e.g., Lesur & Ogilvie, 2010; Longaretti & Lesur, 2010; Lesur & Longaretti, 2011; Herault et al., 2011; Meheut et al., 2015; Murphy & Pessah, 2015).

Our numerical box has sizes $(L_x, L_y, L_z) = (4, 4, 1)$ (in units of H) and resolutions $(N_x, N_y, N_z) = (256, 256, 128)$, respectively, in the x, y, z-directions. This chosen aspect ratio of the box is most preferable, as it is itself isotropic in the (x, y)-plane and avoids "numerical deformation" of the generic anisotropic dynamics of MRI-turbulence. (Such a numerical deformation at different aspect ratios, L_y/L_x, is analyzed in detail in Gogichaishvili et al. (2017) for disk flows with a net azimuthal field). Boxes with the same aspect ratio was adopted also in other related studies of a net nonzero vertical field MRI-turbulence (Bodo et al., 2008; Longaretti & Lesur, 2010; Lesur & Longaretti, 2011; Bai & Stone, 2014; Meheut et al., 2015) to diminish the recurrent bursts of the channel mode, however, as we show below, they still play an important role in the turbulence dynamics even in this extended box. The initial conditions consist of small amplitude random noise perturbations of velocity on top of the Keplerian shear flow. A subsequent evolution was followed up to $t_f = 700$ (about 111 orbits). The data accumulated from the simulations, in fact, represents complete information about the MRI-turbulence in the considered flow system. We analyze this data in Fourier ($\mathbf{k}$-) space in order to grasp the interplay of linear and nonlinear processes underlying the turbu-

lence dynamics. Obtaining the simulation data is just the first, preparatory stage of the main part of our study that focuses on the dynamics in Fourier space. This second stage involves derivation of evolution equations for physical quantities (for the amplitudes of velocity and magnetic field) in Fourier space and subsequent analysis of the right hand side terms of these spectral dynamical equations.

5.2.1 Equations in Fourier space

We start the analysis of the spectral dynamics by decomposing the perturbations $f \equiv (\mathbf{u}, p, \theta, \mathbf{b})$ into spatial Fourier harmonics/modes

$$f(\mathbf{r}, t) = \int \bar{f}(\mathbf{k}, t) \exp\left(\mathrm{i}\mathbf{k} \cdot \mathbf{r}\right) d^3\mathbf{k} \tag{5.6}$$

where $\bar{f} \equiv (\bar{\mathbf{u}}, \bar{p}, \bar{\theta}, \bar{\mathbf{b}})$ denotes the corresponding Fourier transforms. The derivation of spectral equations of perturbations is a technical task and presented in Appendix C: substituting decomposition (5.6) into perturbation Equations (C.1)-(C.9), we obtain the evolution equations for the spectral velocity (Equations C.25-C.27), logarithmic density (entropy, Equation C.13) and magnetic field (Equations C.14-C.16). Below we give the final set of the equations for the quadratic forms of these quantities in Fourier space. Multiplying Equations (C.25)-(C.27), respectively, by $\bar{u}_x^*$, $\bar{u}_y^*$, $\bar{u}_z^*$, and adding up with their complex conjugates, we obtain

$$\frac{\partial}{\partial t}\frac{|\bar{u}_x|^2}{2} = -qk_y\frac{\partial}{\partial k_x}\frac{|\bar{u}_x|^2}{2} + \mathcal{H}_x + \mathcal{I}_x^{(u\theta)} + \mathcal{I}_x^{(ub)} + \mathcal{D}_x^{(u)} + \mathcal{N}_x^{(u)}, \tag{5.7}$$

$$\frac{\partial}{\partial t}\frac{|\bar{u}_y|^2}{2} = -qk_y\frac{\partial}{\partial k_x}\frac{|\bar{u}_y|^2}{2} + \mathcal{H}_y + \mathcal{I}_y^{(u\theta)} + \mathcal{I}_y^{(ub)} + \mathcal{D}_y^{(u)} + \mathcal{N}_y^{(u)}, \tag{5.8}$$

$$\frac{\partial}{\partial t}\frac{|\bar{u}_z|^2}{2} = -qk_y\frac{\partial}{\partial k_x}\frac{|\bar{u}_z|^2}{2} + \mathcal{H}_z + \mathcal{I}_z^{(u\theta)} + \mathcal{I}_z^{(ub)} + \mathcal{D}_z^{(u)} + \mathcal{N}_z^{(u)}, \tag{5.9}$$

where the terms of linear origin are

$$\mathcal{H}_x = \left(1 - \frac{k_x^2}{k^2}\right)(\bar{u}_x\bar{u}_y^* + \bar{u}_x^*\bar{u}_y) + 2(1-q)\frac{k_xk_y}{k^2}|\bar{u}_x|^2, \tag{5.10}$$

$$\mathcal{H}_y = \frac{1}{2}\left[q - 2 - 2(q-1)\frac{k_y^2}{k^2}\right](\bar{u}_x\bar{u}_y^* + \bar{u}_x^*\bar{u}_y) - 2\frac{k_xk_y}{k^2}|\bar{u}_y|^2 \tag{5.11}$$

$$\mathcal{H}_z = (1-q)\frac{k_yk_z}{k^2}(\bar{u}_x\bar{u}_z^* + \bar{u}_x^*\bar{u}_z) - \frac{k_xk_z}{k^2}(\bar{u}_y\bar{u}_z^* + \bar{u}_y^*\bar{u}_z), \tag{5.12}$$

$$\mathcal{I}_i^{(u\theta)} = N^2\left(\frac{k_ik_z}{k^2} - \delta_{iz}\right)\frac{\bar{\theta}\bar{u}_i^* + \bar{\theta}^*\bar{u}_i}{2}, \tag{5.13}$$

$$\mathcal{I}_i^{(ub)} = \frac{\mathrm{i}}{2}k_zB_{0z}(\bar{u}_i^*\bar{b}_i - \bar{u}_i\bar{b}_i^*), \tag{5.14}$$

$$\mathcal{D}_i^{(u)} = -\frac{k^2}{\mathrm{Re}}|\bar{u}_i|^2, \tag{5.15}$$

and the modified nonlinear transfer functions for the quadratic forms of the velocity components are

$$\mathcal{N}_i^{(u)} = \frac{1}{2}(\bar{u}_iQ_i^* + \bar{u}_i^*Q_i). \tag{5.16}$$

Here the index $i = x, y, z$ henceforth, δ_{iz} is the Kronecker delta and Q_i (given by Equation C.28) describes the nonlinear transfers via triad interactions for the spectral velocities $\bar{u}_i$ in Equations (C.25)-(C.27). It is readily shown that the sum of $\mathcal{H}_i$ is equal to the Reynolds stress spectrum multiplied by the shear parameter q, $\mathcal{H} = \mathcal{H}_x + \mathcal{H}_y + \mathcal{H}_z = q(\bar{u}_x\bar{u}_y^* + \bar{u}_x^*\bar{u}_y)/2$.

Next, multiplying Equation (C.13) by $\bar{\theta}^*$ and adding up with its complex conjugate, we get

$$\frac{\partial}{\partial t}\frac{|\bar{\theta}|^2}{2} = -qk_y\frac{\partial}{\partial k_x}\frac{|\bar{\theta}|^2}{2} + \mathcal{I}^{(\theta u)} + \mathcal{D}^{(\theta)} + \mathcal{N}^{(\theta)}, \tag{5.17}$$

where the terms of linear origin are

$$\mathcal{I}^{(\theta u)} = \frac{1}{2}(\bar{u}_z \bar{\theta}^* + \bar{u}_z^* \bar{\theta}), \tag{5.18}$$

$$\mathcal{D}^{(\theta)} = -\frac{k^2}{\mathrm{Pe}} |\bar{\theta}|^2 \tag{5.19}$$

and the modified nonlinear transfer function for the quadratic form of the entropy is

$$\mathcal{N}^{(\theta)} = \frac{\mathrm{i}}{2} \bar{\theta}^* (k_x N_x^{(\theta)} + k_y N_y^{(\theta)} + k_z N_z^{(\theta)}) + c.c., \tag{5.20}$$

where $N_i^{(\theta)}$ (given by Equation C.20) describes the nonlinear transfers for the entropy $\bar{\theta}$ in Equation (C.13).

Finally, multiplying Equations (C.14)-(C.16), respectively, by $\bar{b}_x^*$, $\bar{b}_y^*$, $\bar{b}_z^*$, and adding up with their complex conjugates, we obtain

$$\frac{\partial}{\partial t} \frac{|\bar{b}_x|^2}{2} = -q k_y \frac{\partial}{\partial k_x} \frac{|\bar{b}_x|^2}{2} + \mathcal{I}_x^{(bu)} + \mathcal{D}_x^{(b)} + \mathcal{N}_x^{(b)} \tag{5.21}$$

$$\frac{\partial}{\partial t} \frac{|\bar{b}_y|^2}{2} = -q k_y \frac{\partial}{\partial k_x} \frac{|\bar{b}_y|^2}{2} + \mathcal{M} + \mathcal{I}_y^{(bu)} + \mathcal{D}_y^{(b)} + \mathcal{N}_y^{(b)} \tag{5.22}$$

$$\frac{\partial}{\partial t} \frac{|\bar{b}_z|^2}{2} = -q k_y \frac{\partial}{\partial k_x} \frac{|\bar{b}_z|^2}{2} + \mathcal{I}_z^{(bu)} + \mathcal{D}_z^{(b)} + \mathcal{N}_z^{(b)}, \tag{5.23}$$

where $\mathcal{M}$ is the Maxwell stress spectrum multiplied by q,

$$\mathcal{M} = -\frac{q}{2}(\bar{b}_x \bar{b}_y^* + \bar{b}_x^* \bar{b}_y), \tag{5.24}$$

$$\mathcal{I}_i^{(bu)} = -\mathcal{I}_i^{(ub)} = \frac{\mathrm{i}}{2} k_z B_{0z} (\bar{u}_i \bar{b}_i^* - \bar{u}_i^* \bar{b}_i) \tag{5.25}$$

$$\mathcal{D}_i^{(b)} = -\frac{k^2}{\mathrm{Rm}} |\bar{b}_i|^2 \tag{5.26}$$

and the modified nonlinear terms for the quadratic forms of the magnetic field components are

$$\mathcal{N}_x^{(b)} = \frac{\mathrm{i}}{2}\bar{b}_x^*[k_y\bar{F}_z - k_z\bar{F}_y] + c.c., \tag{5.27}$$

$$\mathcal{N}_y^{(b)} = \frac{\mathrm{i}}{2}\bar{b}_y^*[k_z\bar{F}_x - k_x\bar{F}_z] + c.c., \tag{5.28}$$

$$\mathcal{N}_z^{(b)} = \frac{\mathrm{i}}{2}\bar{b}_z^*[k_x\bar{F}_y - k_y\bar{F}_x] + c.c., \tag{5.29}$$

where $\bar{F}_x, \bar{F}_y, \bar{F}_z$ (given by Equations C.21-C.23) are the fourier transforms of the respective components of the perturbed electromotive force and describe nonlinear transfers for the spectral magnetic field components in Equations (C.14)-(C.16).

Our analysis is based on Equations (5.7)-(5.9), (5.17) and (5.21)-(5.23), which describe the processes of linear $[\mathcal{H}_i(\mathbf{k},t), \mathcal{I}_i^{(u\theta)}(\mathbf{k},t), \mathcal{I}^{(\theta u)}(\mathbf{k},t), \mathcal{I}_i^{(ub)}(\mathbf{k},t), \mathcal{I}_i^{(bu)}(\mathbf{k},t),\ \mathcal{M}(\mathbf{k},t)]$ and nonlinear $[\mathcal{N}_i^{(u)}(\mathbf{k},t),\ \mathcal{N}^{(\theta)}(\mathbf{k},t),\ \mathcal{N}_i^{(b)}(\mathbf{k},t))$ origin. $\mathcal{D}_i^{(u)}(\mathbf{k},t),\ \mathcal{D}^{(\theta)}(\mathbf{k},t),\ \mathcal{D}_i^{(b)}(\mathbf{k},t)$ describe, respectively, the effects of viscous, thermal and resistive dissipation as a function of wavenumber and are negative definite. These basic dynamical equations in Fourier space and, hence the above terms, formally coincide with the corresponding ones in the case of a net azimuthal magnetic field derived in Chapter 4 (Equations 4.11-4.17), which also gives the description/meaning of each dynamical term in these spectral equations. The only difference is in the kinetic-magnetic cross terms $\mathcal{I}_i^{(ub)}(\mathbf{k},t) = -\mathcal{I}_i^{(bu)}(\mathbf{k},t)$, however, this difference drastically changes the dynamical processes. This cross terms describe, respectively, the influence of the i-component of the magnetic field ($\bar{b}_i$) on the same component of the velocity

($\bar{u}_i$) and vice versa for each mode. These terms are of linear origin and in the present case with vertical magnetic field, $\mathcal{I}_i^{(ub)}(\mathbf{k},t) \propto k_z B_{0z}$, while in the case with azimuthal magnetic field, $\mathcal{I}_i^{(ub)}(\mathbf{k},t) \propto k_y B_{0y}$. Consequently, in the presence of vertical field, this mutual influence is nonzero for axisymmetric (with $k_y = 0$) modes, which are not sheared by the flow, leading to their exponential growth, i.e., to the classical MRI. As discussed in Introduction, in the given magnetized disk shear flow, in addition to this exponential growth, which dominates in fact at large times, there exists shear-induced linear nonmodal growth of non-axisymmetric (with $k_y \neq 0$) as well as axisymmetric modes themselves, which dominates instead at finite (dynamical) times (Mamatsashvili et al., 2013; Squire & Bhattacharjee, 2014). Assessment of relative roles of the axisymmetric and non-axisymmetric modes in the vertical field MRI problem is a key question of our study. We note in advance that despite the transient nature of the nonmodal growth, it is not of secondary importance in the maintenance of the turbulence and in forming its spectral characteristics. In the case of azimuthal magnetic field, the course of events is somewhat different: the cross terms for axisymmetric modes vanish that leads to the disappearance of the classical MRI and the only source of energy for the turbulence maintenance remains linear transient growth of non-axisymmetric modes (see also Balbus & Hawley, 1992; Papaloizou & Terquem, 1997; Brandenburg & Dintrans, 2006).

Although our analysis is based on the above dynamical equations for quadratic forms of physical quantities in Fourier space, for completeness, as in

Simon et al. (2009); Lesur & Longaretti (2011); Gogichaishvili et al. (2017), we also present equation for the normalized spectral kinetic energy of modes/harmonics, $\mathcal{E}_K = (|\bar{u}_x|^2 + |\bar{u}_y|^2 + |\bar{u}_z|^2)/2$:

$$\frac{\partial \mathcal{E}_K}{\partial t} = -qk_y \frac{\partial \mathcal{E}_K}{\partial k_x} + \mathcal{H}_E + \mathcal{I}_E^{(u\theta)} + \mathcal{I}_E^{(ub)} + \mathcal{D}_E^{(u)} + \mathcal{N}_E^{(u)}, \tag{5.30}$$

which is obtained by summing of Equations (5.7)-(5.9). Right hand side terms of the above equation is the sum of the related terms:

$$\mathcal{H}_E = \sum_i \mathcal{H}_i = q(\bar{u}_x \bar{u}_y^* + \bar{u}_x^* \bar{u}_y)/2,$$

$$\mathcal{I}_E^{(u\theta)} = \sum_i \mathcal{I}_i^{(u\theta)}, \quad \mathcal{I}_E^{(ub)} = \sum_i \mathcal{I}_i^{(ub)},$$

$$\mathcal{D}_E^{(u)} = \sum_i \mathcal{D}_i^{(u)} = -\frac{2k^2}{\mathrm{Re}} \mathcal{E}_K, \quad \mathcal{N}_E^{(u)} = \sum_i \mathcal{N}_i^{(u)}.$$

Similarly, we can get equation for the normalized spectral magnetic energy of modes, $\mathcal{E}_M = (|\bar{b}_x|^2 + |\bar{b}_y|^2 + |\bar{b}_z|^2)/2$, by summing Equations (5.21)-(5.23),

$$\frac{\partial \mathcal{E}_M}{\partial t} = -qk_y \frac{\partial \mathcal{E}_M}{\partial k_x} + \mathcal{M} + \mathcal{I}_E^{(bu)} + \mathcal{D}_E^{(b)} + \mathcal{N}_E^{(b)}, \tag{5.31}$$

where

$$\mathcal{M} = -q(\bar{b}_x \bar{b}_y^* + \bar{b}_x^* \bar{b}_y)/2, \quad \mathcal{I}_E^{(bu)} = \sum_i \mathcal{I}_i^{(bu)} = -\mathcal{I}_E^{(ub)},$$

$$\mathcal{D}_E^{(b)} = \sum_i \mathcal{D}_i^{(b)} = -\frac{2k^2}{\mathrm{Rm}} \mathcal{E}_M, \quad \mathcal{N}_E^{(b)} = \sum_i \mathcal{N}_i^{(b)}.$$

The equation of the normalized thermal energy of modes, $\mathcal{E}_{th} = N^2|\theta|^2/2$, is straightforward to derive by multiplying Equation (5.17) just by N^2. We do not give it here, as the thermal energy is always small compared to the kinetic and magnetic energies (see below).

One can easily write also the equation for the total normalized spectral energy of modes, $\mathcal{E} = \mathcal{E}_K + \mathcal{E}_{th} + \mathcal{E}_M$,

$$\frac{\partial \mathcal{E}}{\partial t} = -qk_y \frac{\partial \mathcal{E}}{\partial k_x} + \mathcal{H}_E + \mathcal{M} + \mathcal{D}_E^{(u)} + N^2\mathcal{D}^{(th)} + \mathcal{D}_E^{(b)} + \mathcal{N}_E^{(u)} + N^2\mathcal{N}^{(\theta)} + \mathcal{N}_E^{(b)}. \tag{5.32}$$

In the simulation box, wavenumbers are inherently discrete, with the smallest wavenumbers being defined by the box size L_i as $k_{i,min} = 2\pi/L_i$ and the largest one by the resolution $k_{i,max} = 2\pi N_i/3L_i$ (taking into account the 2/3-rule used in pseudo-spectral codes), while other wavenumbers being multiples of $k_{i,min}$, where the index $i = x, y, z$. For convenience, we normalize wavenumbers by the grid cell sizes of Fourier space, $\Delta k_i = 2\pi/L_i$, that is, $k_i/\Delta k_i \rightarrow k_i$. As a result, the normalized azimuthal and vertical wavenumbers are integers $k_y, k_z = 0, \pm 1, \pm 2, ...$, while k_x changes with time due to drift (Hawley et al., 1995) and is integer only at discrete moments $t_n = nL_y/(q|k_y|L_x)$, where n is a positive integer.

5.3 Linear dynamics – optimal nonmodal growth

Before embarking on the nonlinear study, we first outline the characteristic features of the linear dynamics of nonzero vertical flux MRI based on the linearized set of spectral Equations (C.10-C.18). As distinct from the related linear studies with classical modal treatment (e.g., Balbus & Hawley, 1991; Lesur & Longaretti, 2007; Pessah & Chan, 2008; Longaretti & Lesur, 2010), the main goal of our linear analysis is to quantify the nonmodal growth of

axisymmetric and non-axisymmetric modes during dynamical (characteristic nonlinear, of the order of orbital) time and thereby to identify dynamically active modes which have the highest influence on the balances in the turbulence. These energy-carrying active modes naturally form *the vital area* in Fourier space, i.e., the region of wavenumbers where most of the energy supply from the basic flow to perturbation modes occurs. It is this nonmodal physics of the MRI, taking place at finite times, that is more relevant for turbulence dynamics and its energy supply process, because they have characteristic timescales of the order of orbital time (see also Squire & Bhattacharjee, 2014). Following Chapter 4, where is done a similar nonmodal analysis for the azimuthal field MRI, here for this purpose we also use the nonmodal approach combined with the formalism of optimal perturbations (Farrell & Ioannou, 1996; Schmid & Henningson, 2001; Zhuravlev & Razdoburdin, 2014). This approach is more general than the modal one, capturing the evolution of perturbation modes at all times, from intermediate (dynamical) times, when nonnormality/shear-induced nonmodal effects (growth) dominate, to large times when modal (exponential) MRI growth of axisymmetric modes prevails. The optimal perturbations yield maximum, or optimal nonmodal growth during finite times and therefore are responsible for most of the energy extraction from the background flow. This analysis is useful in nonlinear simulations for understanding energy supply processes and balances in the turbulence.

In the shearing box, the radial wavenumber of each non-axisymmetric mode (shearing wave) changes linearly with time, $k_x(t) = k_x(0) + q\Omega k_y t$, due

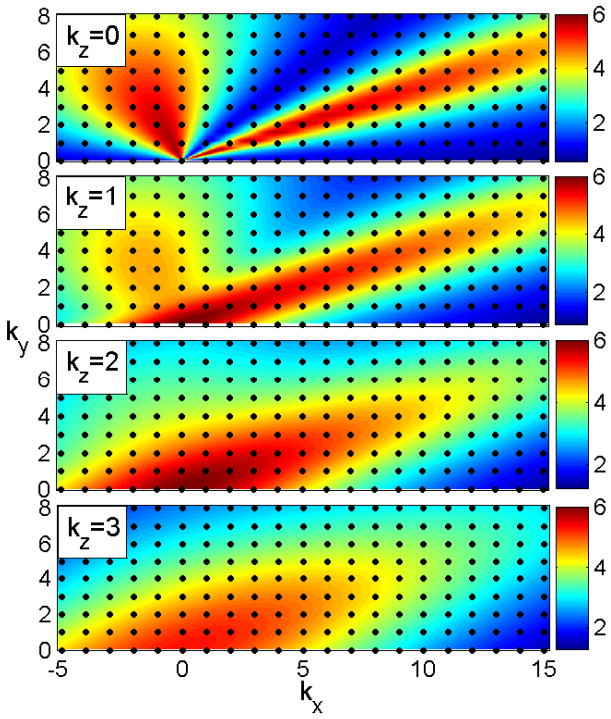

Figure 5.1: Optimal nonmodal growth factor, G, in (k_x, k_y)-plane at $t_d = 1.33$ and different $k_z = 0, 1, 2, 3$ calculated with the linearized version of the main Equations (C.1)-(C.9). The superimposed black dots represent discrete modes contained in the simulation box. The chosen box size $(4, 4, 1)$ ensures that the vital area of wavenumbers, where the most effective nonmodal growth occurs (red and yellow), is sufficiently densely populated with the modes contained in the simulation box.

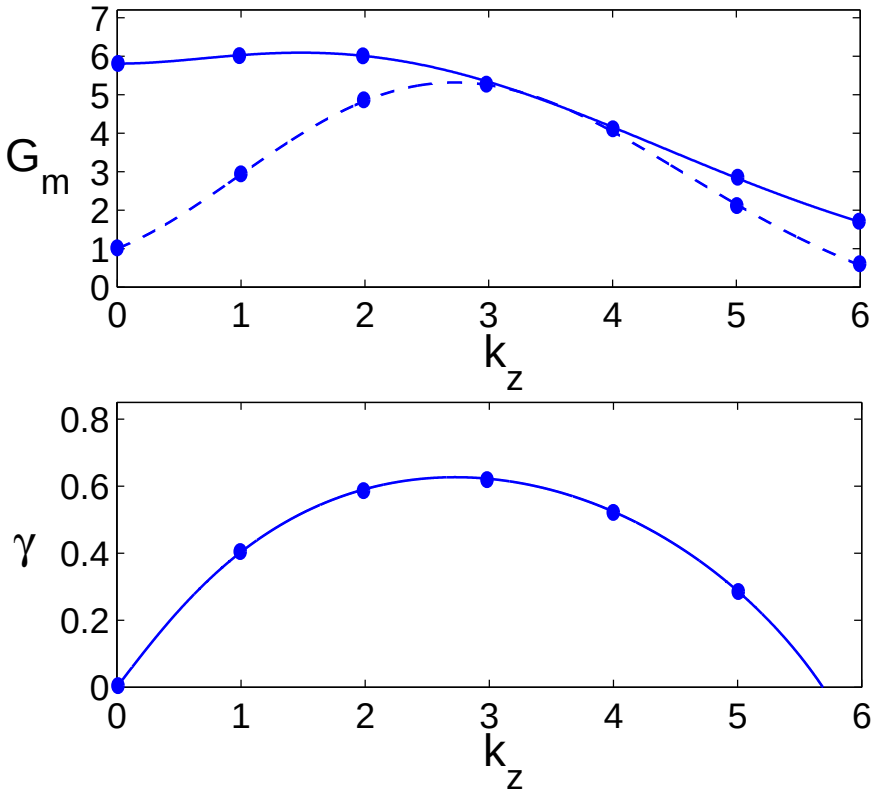

Figure 5.2: The upper panel shows the nonmodal growth factor, G_m (solid line), of the axisymmetric and radially uniform ($k_x = k_y = 0$) modes vs. k_z at $t_d = 1.33$ together with the modal growth factor of the energy, $\exp(2\gamma t_d)$ (dashed line), of these modes for the same time. Here γ is the corresponding *modal* (exponential) growth rate at $k_x = k_y = 0$ and the same values of $\beta, \mathrm{Re}, \mathrm{Rm}$, which is plotted in the lower panel vs. k_z. In both panels, k_z is in units of 2π and dots indicate the growth factors and growth rate at discrete $k_z = 1, 2, 3, ...$ present in the box.

to the shear, but is constant for axisymmetric modes, $k_x(t) = k_x(0)$. The maximum possible amplification of the total energy, $\mathcal{E}$, for a mode with wavenumbers $(k_x(0), k_y, k_z)$ by a specific time t_d is given by

$$G(t_d) = \max_{\bar{f}(0)} \frac{\mathcal{E}(t_d)}{\mathcal{E}(0)}, \tag{5.33}$$

where the maximum is taken over all initial conditions $\bar{f}(0)$ with a given total energy $\mathcal{E}(0)$. The final state at t_d with the energy $\mathcal{E}(t_d)$ are found from the initial state at $t = 0$ by solving the linearized evolution equations. Then, expression (5.33) is usually calculated by means of the singular value decomposition of the propagator, which transfers the initial state into final one (see Farrell & Ioannou, 1996; Schmid & Henningson, 2001, for details). The corresponding initial conditions, leading to this highest growth at t_d are called optimal perturbations. The reference time, t_d, during which to calculate the nonmodal growth, is usually of the order of the orbital time. For definiteness, here we take it equal to the characteristic (e-folding) time of the most unstable MRI mode in the ideal case, $t_d = 1/\gamma_{max} = 1.33$ (in units of Ω^{-1}), where $\gamma_{max} = 0.75\Omega$ is its growth rate (Balbus & Hawley, 1991), since it is effectively of the order of the dynamical time as well.

Figure 5.1 shows the optimal nonmodal growth factor G in (k_x, k_y)-plane at different vertical wavenumbers $k_z = 0, 1, 2, 3$ and the dynamical time $t_d = 1.33$. It is represented as a function of the final wavenumber $k_x(t_d) = k_x(0) + qk_y t_d$, which an optimal mode with some initial radial wavenumber $k_x(0)$ has at time t_d. Although the maximum of the nonmodal amplification in (k_x, k_y)-plane, G_m, at fixed k_z, comes at axisymmetric modes with

$k_x = k_y = 0$, there is a broad range of non-axisymmetric modes achieving comparable growth (red and yellow areas). These regions are inclined towards the k_x-axis due to the shear. At $k_z = 0$, the linear magnetic and velocity perturbations are decoupled: there are two separate amplification regions, the right corresponding to magnetic perturbations and the left to kinetic ones, both with growth factors smaller than that at $k_z = 1$. This maximum non-modal growth, G_m, as a function of k_z is shown in Figure 5.2. For the sake of comparison, this figure also shows the modal (exponential) growth rate, γ, of these horizontally uniform $k_z = k_y = 0$ modes, which are known to exhibit the fastest growth also in the modal theory of MRI (e.g., Pessah & Chan, 2008)[1], and the corresponding modal growth factor at t_d, $\exp(2\gamma t_d)$, as a function of k_z for the same values of $\beta, \mathrm{Re}, \mathrm{Rm}$. It is evident that the nonmodal and modal growths exhibit different dependencies on k_z: G_m achieves a maximum at around $k_z = 1$ and decreases with increasing k_z, whereas γ and the related modal growth factor reaches a maximum near $k_z = 3$ and decrease at small and large k_z. Note also in the upper panel of Figure 5.2 that the nonmodal growth is always larger than the modal one at all k_z, especially at the dynamically active small $k_z = 0, 1$. We will see below that the axisymmetric mode $k_x = k_y = 0, k_z = 1$, which exhibits the largest nonmodal amplification and is referred to as *the channel mode*, is in fact the most active participant in the nonlinear (turbulence) dynamics as well. Of course, in the turbulent state,

[1]Here, this growth rate has been found by solving a standard dispersion relation of non-ideal MRI with viscosity and Ohmic resistivity (see e.g., Pessah & Chan, 2008; Longaretti & Lesur, 2010).

the nonlinear terms qualitatively modify the dynamical picture, resulting in a somewhat different behavior with k_z (see e.g., Figure 5.4), still the linear analysis presented here gives a preliminary feeling/insight into process of the energy exchange with the basic flow and, most importantly, vividly shows substantial influence of the disk flow nonnormality on the growth factors of spectrally/modally unstable modes.

We stress that the nonmodal growth phenomenon – mathematically the nonnormality (non-self-adjointness) of linear evolution operators – is inherently caused by shear and, according to the above calculations, is significant for both non-axisymmetric and axisymmetric (channel) modes in MRI-active disks with a net vertical field. Specifically, the channel modes, which are stronger in this case, grow purely exponentially only at asymptotically large times, whereas their growth during finite/dynamical time is governed by nonmodal physics and can have growth factors larger than the modal one during these times (Figure 5.2). In the case of (net vertical flux) MRI-turbulence, the characteristic timescales of dynamical processes are evidently of the order of orbital/shear time (Walker et al., 2016). Therefore, it is necessary to take into account nonmodal effects on the channel mode dynamics and not rely solely on its modal growth in order to properly understand saturation and energy balance processes of the turbulence. This point regarding the importance of nonmodal physics in the dynamics of (axisymmetric) modes in MRI-turbulence was also emphasized by Squire & Bhattacharjee (2014). So, it is important that simulation box sufficiently well encompasses these nonmodally

most amplified modes for a complete representation of the dynamical picture. In the simulation box, however, the wavenumber spectrum is inherently discrete, with smallest wavenumbers being defined by the box size (L_x, L_y, L_z) as $k_{i,min} = 2\pi/L_i$, with other wavenumbers being multiples of them. These discrete modes contained in the adopted box $(4, 4, 1)$ are shown as black dots superimposed on the map of G in Figure 5.1. It is seen that they sufficiently densely cover the yellow and red areas of efficient nonmodal growth. Therefore, the box $(4, 4, 1)$ can well account for the nonmodal effects in the energy exchange processes in the case of turbulence, which, in turn, justifies its choice.

5.4 Numerical simulations and characteristic features of the turbulence

Random small perturbations imposed at the beginning on the flow start to grow mainly as a result of the nonmodal mechanism, which later continues into the exponential growth. Consequently, after several orbits, the flow settles into a fully developed MHD turbulence that persists till the end of the run. Figure 5.3 shows the evolution of the volume-averaged perturbed kinetic, $\langle E_K \rangle$, thermal, $\langle E_{th} \rangle$, and magnetic, $\langle E_M \rangle$, energy densities as well as the Reynolds, $\langle u_x u_y \rangle$, and Maxwell $-\langle b_x b_y \rangle$ stresses. In this figure, we also show the rms of the turbulent velocity and magnetic field components as a function of time. The magnetic energy is on average larger than the kinetic one by a factor of about 2 and both dominate the thermal energy, while the Maxwell stress is about 5.5 times larger than the Reynolds one. The azimuthal compo-

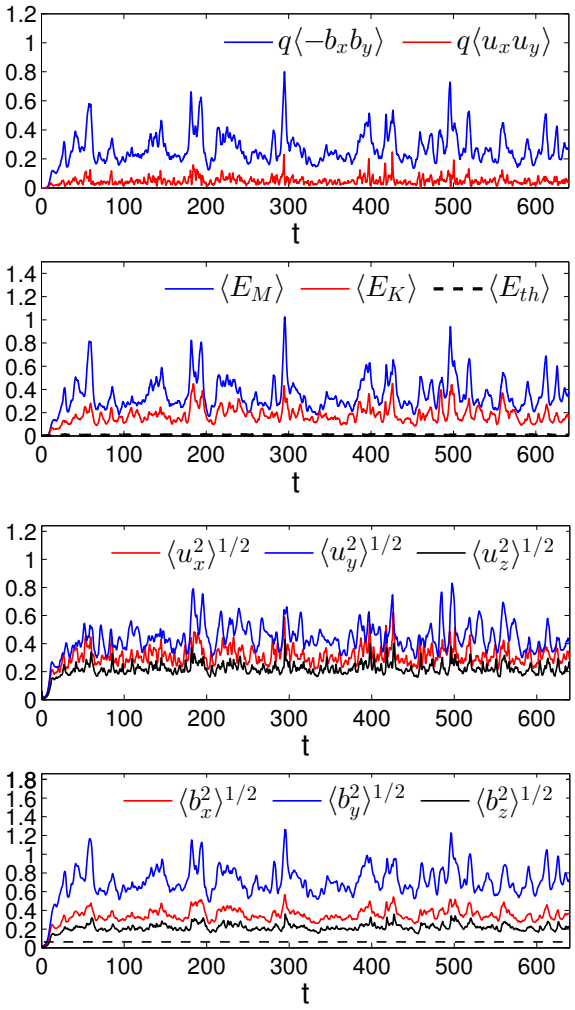

Figure 5.3: Evolution of volume-averaged Reynolds and Maxwell stresses (top row), kinetic, thermal and magnetic energy densities (second row), rms of velocity (third row) and magnetic field (bottom row) components. After several orbits, sustained turbulence sets in, characterized by recurrent bursts of these quantities all along the evolution, as is characteristic for vertical field MRI-turbulence. Magnetic energy is on average about twice larger than the kinetic one and both dominate the thermal energy, while the Maxwell stress dominates the Reynolds one on average by a factor of 5.5. The azimuthal components of the turbulent velocity and magnetic field are larger due to the shear and exhibit more pronounced bursts with peaks higher than those for the respective other two components. For reference, dashed line in the bottom panel corresponds to the background vertical field $B_{0z} = 0.0447$.

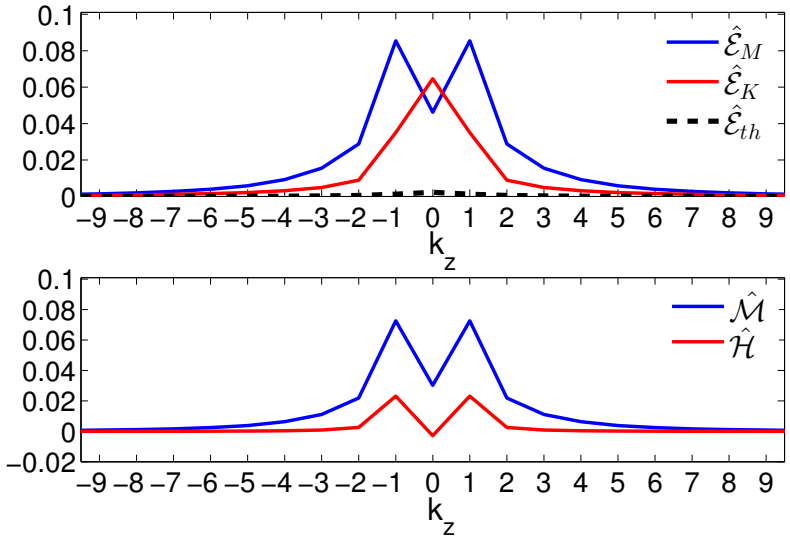

Figure 5.4: Integrated in (k_x, k_y)-plane time-averaged kinetic, $\hat{\mathcal{E}}_K$, magnetic, $\hat{\mathcal{E}}_M$, and thermal, $\hat{\mathcal{E}}_{th}$, spectral energy densities (upper panel) as well as spectral Reynolds, $\hat{\mathcal{H}}$, and Maxwell, $\hat{\mathcal{M}}$, stresses (lower panel) as a function of k_z.

nents of the velocity and magnetic field are always larger than the other two respective ones due to shear; the imposed vertical field is dominated by the turbulent magnetic field with the time-averaged rms values $\langle b_x^2 \rangle^{1/2} = 8B_{0z}$, $\langle b_y^2 \rangle^{1/2} = 16B_{0z}$, $\langle b_z^2 \rangle^{1/2} = 4.9B_{0z}$. As seen in Figure 5.3, the main characteristic feature of the temporal evolution of all these volume-averaged quantities is a burst-like behavior with intermittent peaks and quiescent intervals, as is typical of MRI-turbulence in disks with a net vertical field (Lesur & Longaretti, 2007; Bodo et al., 2008; Longaretti & Lesur, 2010; Murphy & Pessah, 2015). The peaks are most pronounced/intensive in the azimuthal velocity and magnetic field, inducing corresponding peaks in the magnetic energy and Maxwell stress. As a result, these bursts yield enhanced rates of angular momentum

transport. On a closer examination, one can notice that the peaks in the rms of u_z and b_z follow just after the respective stronger peaks in the rms of u_y and b_y (see also Murphy & Pessah, 2015). We show below that these bursts are in fact closely related to the manifestations of the dynamics of two modes:
– the channel mode with wavenumber $\mathbf{k}_c = (0, 0, \pm 1)$, which is horizontally uniform varying only on the largest z-vertical scale in the domain, and
– the zonal flow mode with wavenumber $\mathbf{k}_{zf} = (\pm 1, 0, 0)$ varying only on the largest x-radial scale in the domain.
Namely, the burst-like growth of the channel mode due to MRI amplifies x- and, especially, y-components of velocity and magnetic field (the channel mode itself does not have the z-components of these quantities). In turn, its nonlinear interaction with other dynamically active non-axisymmetric modes (referred to as parasitic modes in the literature) shortly afterwards gives rise to the peaks of the z-components of these quantities. Below we show that this nonlinear interaction is mainly manifested as the transverse cascade in $\mathbf{k}$-space.

The role of the channel mode and hence the intensity of bursts depend on the box aspect ratio L_x/L_z, being more pronounced when the aspect ratio is around unity, but becoming weaker as it increases (Bodo et al., 2008). Nevertheless, as we demonstrate in this Chapter, the channel mode is a key participant in the dynamics of a net vertical field MRI-turbulence. In particular, the adopted here box $(4, 4, 1)$ would exhibit only relatively weak bursts according to Bodo et al. (2008), while as we found here, the amplification of the channel mode can nevertheless influence the behavior of other active

modes and ultimately the total stress and energy.

5.4.1 Energy spectra

Figure 5.4 shows the spectra of the kinetic, magnetic and thermal energies as well as the Reynolds and Maxwell stresses integrated in (k_x, k_y)-plane, $\hat{\mathcal{E}}_{K,M,th}(k_z) = \int \mathcal{E}_{K,M,th} dk_x dk_y$ and $(\hat{\mathcal{H}}(k_z), \hat{\mathcal{M}}(k_z)) = \int (\mathcal{H}, \mathcal{M}) dk_x dk_y$ as a function of k_z, which have been averaged over time from $t = 100$ till $t = 650$ in the fully developed turbulent state. At all k_z, the spectral magnetic energy is larger than the kinetic one except at $k_z = 0$, where they are comparable, and both dominate the spectral thermal energy, while the spectral Maxwell stress is larger than the Reynolds one. The maximum of the magnetic energy as well as both stresses comes at $|k_z| = 1$, corresponding to the channel mode $\mathbf{k}_c = (0, 0, 1)$. Thus, most of magnetic and kinetic energy injection due to the stresses takes place at small $|k_z|$ rather than at $|k_z| = 3$ that corresponds to the most unstable axisymmetric mode of MRI in the modal approach (lower panel of Figure 5.2). This is consistent with the above linear nonmodal growth calculations, which have demonstrated how the nonnormality eliminates the dominance of the $|k_z| = 3$ mode in preference to lower k_z modes during finite times (Figures 5.1 and 5.2). This result supports again the statement made above that the nonmodal growth over short, dynamical/orbital time is more relevant for energy exchange processes in the turbulence. A maximum of the kinetic energy spectrum is at $k_z = 0$ and is a bit higher than the magnetic energy at this k_z. It corresponds to the axisymmetric zonal flow mode with

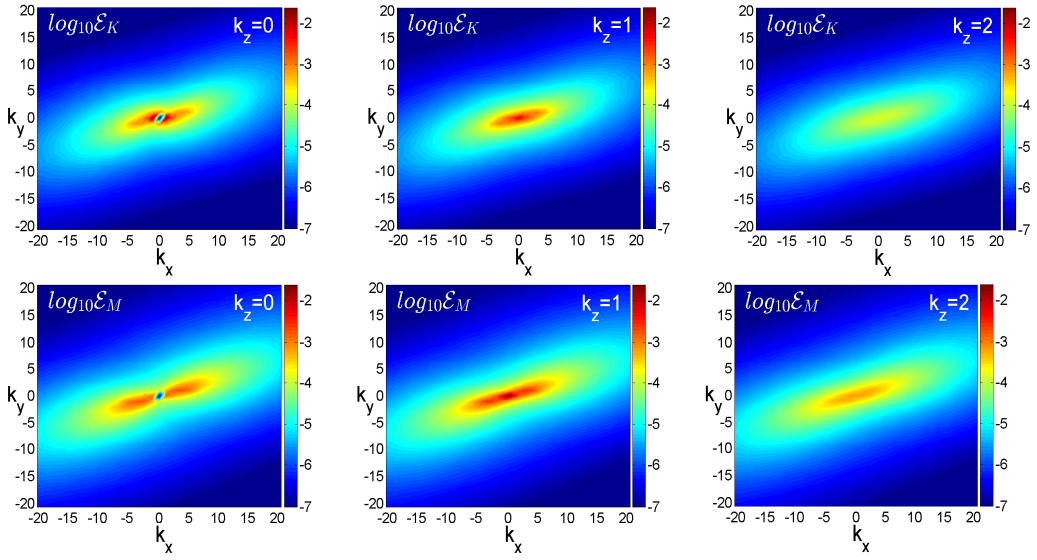

Figure 5.5: Slices of the logarithmic 3D spectra of the kinetic, $log_{10}\mathcal{E}_K$ (upper row), and magnetic, $log_{10}\mathcal{E}_M$ (lower row), energies in (k_x, k_y)-plane at $k_z = 0, 1, 2$. Both spectra are strongly anisotropic due to the shear with similar overall shape and inclination towards k_x-axis. The maximum of the kinetic energy spectrum comes at the zonal flow mode $\mathbf{k}_{zf} = (\pm 1, 0, 0)$, while that of the magnetic energy spectrum at the channel mode $\mathbf{k}_c = (0, 0, \pm 1)$.

$\mathbf{k}_{zf} = (\pm 1, 0, 0)$. Thus, the large-scale modes with the first few k_z contain most of the energy and hence play a dynamically important role.

Having examined the dependence of the energy and stress spectra on the vertical wavenumber, we now present in Figure 5.5 slices of the 3D spectra of the kinetic, $\mathcal{E}_K$, and magnetic, $\mathcal{E}_M$, energies in (k_x, k_y)-plane at first three vertical wavenumbers $k_z = 0, 1, 2$, for which these energies are relatively high (see Figure 5.4). Both spectra are highly anisotropic due to the shear with a similar overall elliptical shape and inclination towards the k_x-axis at these k_z. This inclination implies that for a given k_y, trailing waves $(k_x/k_y > 0)$ have

larger power than leading ($k_x/k_y < 0$) ones. We checked that this spectral anisotropy in fact extends to larger wavenumbers, up to dissipation scale. The maximum of the kinetic energy spectrum comes at the wavenumber $\mathbf{k}_{zf} = (\pm 1, 0, 0)$ of the zonal flow mode, while that of the magnetic energy spectrum at the channel mode wavenumber $\mathbf{k}_c = (0, 0, \pm 1)$. These spectra also demonstrate that there is a broad range of trailing non-axisymmetric modes (red areas) with energies, on average, comparable to that of the channel mode and hence taking an active part in the turbulence dynamics (see also Longaretti & Lesur, 2010). A more detailed analysis of the relative roles and dynamics of the channel, zonal flow and other (non-axisymmetric) modes is made below. Although not shown here, the slices of the 3D spectrum of the Maxwell stress in (k_x, k_y)-plane have a similar shape and type of anisotropy as the magnetic energy spectrum in Figure 5.5. Similar anisotropic energy spectra were already reported in the shearing box simulations of MRI-turbulence with a nonzero net vertical field (Hawley et al., 1995; Lesur & Longaretti, 2011; Murphy & Pessah, 2015). These spectra, which clearly differ from a typical turbulent spectrum in the classical case of forced MHD turbulence without shear (Biskamp, 2003), arise as a consequence of a specific anisotropy of the linear and nonlinear terms of Equations (5.30) and (5.31) in $\mathbf{k}$-space in the presence of the shear.

5.4.2 Active modes in k-space

The dynamically important modes with most effective amplification have been identified above based on the optimal nonmodal growth calculations

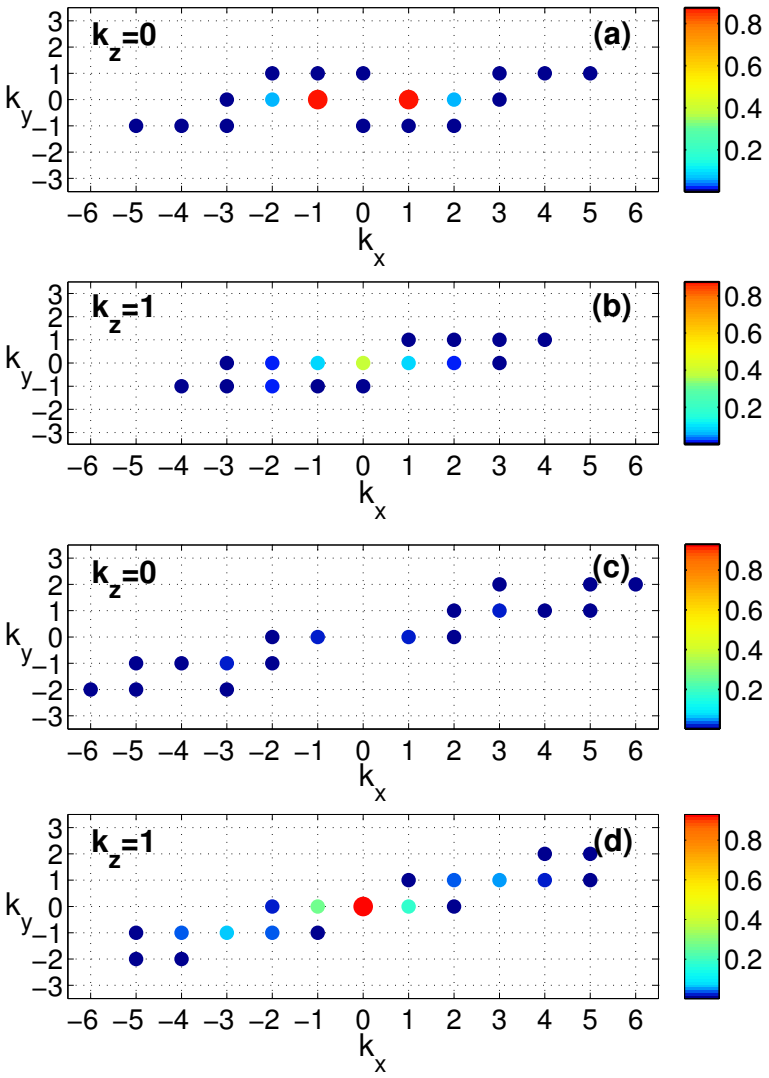

Figure 5.6: Distribution of the active modes in **k**-space at $k_z = 0, 1$ computed separately for the kinetic [panels (a) and (b)] and magnetic [panels (c) and (d)] components. The color dots in these panels represent the modes whose spectral kinetic (magnetic) energy reaches more than 50% of the maximum value of the kinetic $\mathcal{E}_{K,max}$ (magnetic $\mathcal{E}_{M,max}$) energy at the same time. The colors indicate the fraction of time each mode maintains this higher energy compared to the entire duration of the turbulence in the simulation. The zonal flow mode $\mathbf{k}_{zf} = (\pm 1, 0, 0)$ and the channel mode $\mathbf{k}_c = (0, 0, \pm 1)$ [denoted by bigger red dots, respectively, in panels (a) and (d)] clearly stand out against other modes, as they retain, respectively, higher kinetic and magnetic energies most of the time.

(Figure 5.1), i.e., on the analysis of the linear dynamics. However, the overall dynamical picture of the turbulence is formed as a result of the refined interplay of linear and nonlinear processes. So, it is reasonable to introduce the notion of *active modes* in **k**-space – energy-carrying modes playing a major role in the dynamics – separately for the kinetic and magnetic components. The active kinetic (magnetic) modes are labeled those modes whose spectral kinetic (magnetic) energy grows more than 50% of the maximum spectral kinetic energy $\mathcal{E}_{K,max}$ (magnetic energy $\mathcal{E}_{M,max}$) at the same time. Both types of active modes in Fourier space at $k_z = 0, 1$ are shown in Figure 5.6 with color dots. They are obtained by following the evolution of all the modes in the box during the whole simulation and selecting out those modes whose kinetic or magnetic energy becomes higher than the above threshold. The color of each mode indicates the fraction of the total evolution time t_f during which it retains this higher energy. These dynamically active modes, with different "periods of activity", are distributed anisotropically in (k_x, k_y)-plane and concentrated in the region of small wavenumbers, $|k_x| \leq 6, |k_y| \leq 2$, of **k**-space, constituting the so-called *vital area* of the turbulence. In this area, the most powerful dynamical processes are concentrated that define the strength and statistical characteristics of the turbulence. There are two – the channel $\mathbf{k}_c$ and the zonal flow $\mathbf{k}_{zf}$ – modes (bigger red dots, respectively, in panels (a) and (d) of Figure 5.6) that clearly stand out against other modes, as they retain, respectively, higher magnetic (the channel mode) and kinetic (the zonal flow mode) energies most of the time. As a result, these two modes play a key

role in shaping the turbulence dynamics and deserve a more detailed separate analysis, which is given in the following subsections. Apart from the channel and zonal flow modes, there are a sufficient number other active modes (blue dots in Figure 5.6) that individually are not so significant, since they retain the higher kinetic or magnetic energies for much less a time than the channel and zonal flow modes. However, the combined action of the multitude of these modes is competitive to the channel and zonal flow modes. We label them as *the rest modes* and devoted to them a subsection 5.4.5 below. The other modes with larger wavenumbers, including those with $|k_z| \geq 2$ (not shown in Figure 5.6), lie outside the vital area and always carry energies and stresses smaller than 50% of the maximum value (or even much less). Therefore, they do not play as much a role in the energy-exchange process between the background flow and turbulence.

5.4.3 The channel mode

We have seen above that the channel mode – the harmonic with wavenumber $\mathbf{k}_c = (0, 0, \pm 1)$ that is uniform in the horizontal (x, y)-plane and has the largest vertical wavelength (correspondingly, the smallest wavenumber, $k_z = \pm 1$) in the domain – is a key participant in the turbulence dynamics. It carries higher energy most of the time in the turbulent state among other active modes in the vital area and corresponds to the maximum of the spectral magnetic energy and stresses in Fourier space at each moment (see Figure 5.9 below). So, first we analyze the dynamics of this mode and then move to the

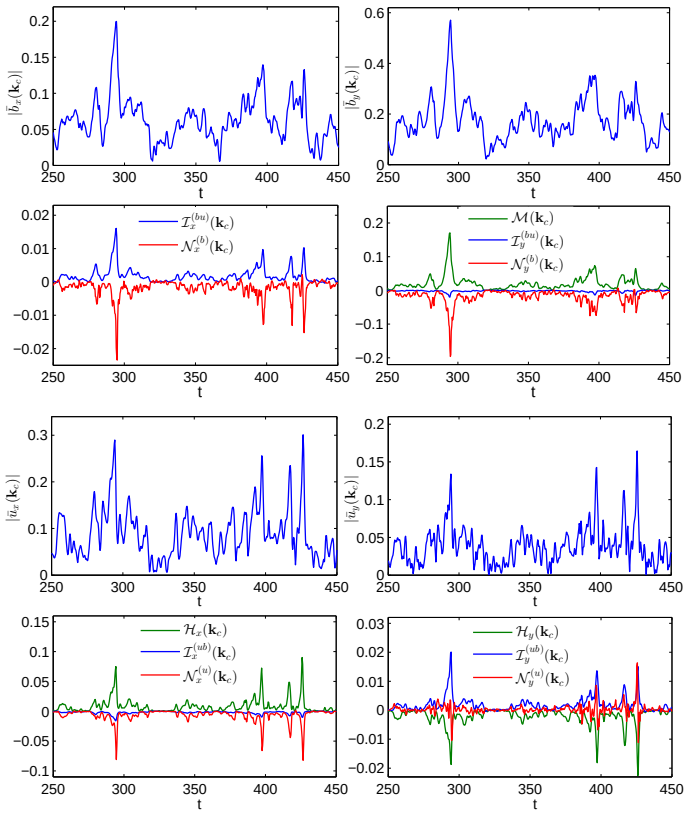

Figure 5.7: Evolution of the main spectral amplitudes of the magnetic field, $|\bar{b}_x(\mathbf{k}_c)|, |\bar{b}_y(\mathbf{k}_c)|$, and velocity, $|\bar{u}_x(\mathbf{k}_c)|$, $|\bar{u}_y(\mathbf{k}_c)|$, of the channel mode with $\mathbf{k}_c = (0, 0, \pm 1)$ as well as the corresponding time-histories of the linear – stresses, $\mathcal{M}(\mathbf{k}_c)$, $\mathcal{H}(\mathbf{k}_c)$, and exchange, $\mathcal{I}^{(ub)}(\mathbf{k}_c)$, $\mathcal{I}^{(bu)}(\mathbf{k}_c)$ – and nonlinear, $\mathcal{N}^{(u)}(\mathbf{k}_c)$, $\mathcal{N}^{(b)}(\mathbf{k}_c)$, terms, which govern the dynamics of this mode. The channel mode is supported by the linear processes – the action of the stresses and the linear exchange terms describe its amplification due to MRI, while the nonlinear terms mostly oppose this growth, resulting in the recurrent bursts in the evolution of the magnetic field and velocity. $|\bar{b}_x|$ and $|\bar{b}_y|$ are amplified, respectively, by $\mathcal{I}_x^{(bu)}$ and $\mathcal{M}$, as they are always positive, and then drained, respectively, by the nonlinear terms $\mathcal{N}_x^{(b)}$ and $\mathcal{N}_y^{(b)}$, which are always negative, transferring energy to other wavenumbers and components (see Figures 5.10 and 5.12). Consequently, the negative peaks of these terms a bit lag the corresponding peaks of the linear terms. This azimuthal field component is also drained to a lesser degree by $\mathcal{I}_y^{(bu)}$, giving its energy to $|\bar{u}_y|$. $|\bar{u}_x|$ is amplified by positive $\mathcal{H}_x$ and drained by negative $\mathcal{N}_x^{(u)}$ and, to a lesser degree, by $\mathcal{I}_x^{(ub)}$ – the peaks of the latter two sink terms lag those of the linear source term $\mathcal{H}_x$. $|\bar{u}_y|$ is amplified by $\mathcal{I}_y^{(ub)}$ and drained by always negative $\mathcal{H}_y$. $\mathcal{N}_y^{(u)}$ alternates sign, as distinct from the other nonlinear terms, providing for $|\bar{u}_y|$ either source, when positive, or sink, when negative. The influence of the nonlinear terms is maximal at the peaks of $|\bar{b}_x(\mathbf{k}_c)|$ and $|\bar{b}_y(\mathbf{k}_c)|$ – they halt the MRI-growth and lead to a fast drain of the channel mode over a few orbital times.

zonal flow and the rest modes.

Figure 5.7 shows the evolution of the main spectral amplitudes of the magnetic field, $|\bar{b}_x(\mathbf{k}_c)|, |\bar{b}_y(\mathbf{k}_c)|$, and velocity, $|\bar{u}_x(\mathbf{k}_c)|$, $|\bar{u}_y(\mathbf{k}_c)|$ of the channel mode. Also plotted are the time-histories of the corresponding linear – stresses, $\mathcal{M}(\mathbf{k}_c)$, $\mathcal{H}(\mathbf{k}_c)$ and exchange $\mathcal{I}^{(ub)}(\mathbf{k}_c)$, $\mathcal{I}^{(bu)}(\mathbf{k}_c)$ – and nonlinear, $\mathcal{N}^{(u)}(\mathbf{k}_c)$, $\mathcal{N}^{(b)}(\mathbf{k}_c)$, terms in the above spectral Equations (5.7)-(5.8) and (5.21)-(5.22), which govern the dynamics of this mode. The action of the stresses $\mathcal{M}(\mathbf{k}_c)$, $\mathcal{H}(\mathbf{k}_c)$ and exchange terms, $\mathcal{I}^{(ub)}(\mathbf{k}_c)$, $\mathcal{I}^{(bu)}(\mathbf{k}_c)$ describe together the (non-modal) effect of MRI on the channel mode and are mainly responsible for its amplification. The action of the nonlinear terms, $\mathcal{N}^{(u)}(\mathbf{k}_c)$, $\mathcal{N}^{(b)}(\mathbf{k}_c)$, describe, in turn, interaction of the channel mode with other active modes with different wavenumbers and components (this process is covered in detail in subsection 5.4.6, see also Figures 5.10 and 5.12 below). These linear and nonlinear terms jointly determine the temporal evolution of the channel mode's velocity and magnetic field with characteristic recurrent bursts seen in Figure 5.7. It is clear from this figure that the typical variation, or dynamical time of the nonlinear terms is indeed of the order of the orbital time, indicating again that the non-modal physics of MRI is more relevant in the state of developed turbulence. Analysis of these terms allows us to understand nuances of the channel mode dynamics and ultimately the behavior of the total stress and the energy (Figure 5.3), because, as we will see below (subsection 5.4.5), the channel mode bursts manifest themselves in the time-development of the volume-averaged magnetic energy and the Maxwell stress. These terms operate differently for

velocity and magnetic fields.

Let us first consider the magnetic field components in Figure 5.7. $|\bar{b}_x|$ and $|\bar{b}_y|$ are amplified, respectively, by $\mathcal{I}_x^{(bu)}$ and $\mathcal{M}$, as they are always positive, and then drained, respectively, by the nonlinear terms $\mathcal{N}_x^{(b)}$ and $\mathcal{N}_y^{(b)}$, which are always negative, transferring energy to other wavenumbers and components. Consequently, the negative peaks of these nonlinear terms a bit lag the corresponding peaks of the linear terms. This azimuthal field, which is a dominant field component in the channel mode, is also drained to a lesser degree by the negative exchange term $\mathcal{I}_y^{(bu)}$, transferring its energy to $|\bar{u}_y|$. As for the velocity components, $|\bar{u}_x|$ is amplified by positive $\mathcal{H}_x$, then drained mostly by $\mathcal{N}_x^{(u)}$, which is always negative and, to a lesser degree, by also negative $\mathcal{I}_x^{(ub)}$ – the peaks of the latter two sink terms lag corresponding peaks of the linear source term $\mathcal{H}_x$. Finally, $|\bar{u}_y|$ is mostly amplified by $\mathcal{I}_y^{(ub)}$, taking energy from $|\bar{b}_y|$, and is drained by always negative $\mathcal{H}_y$. $\mathcal{N}_y^{(u)}$ acts differently from the above nonlinear terms – it alternates sign, providing for $|\bar{u}_y|$ either source, when positive, or sink, when negative. So, other modes via nonlinear interaction occasionally reinforce the growth of the channel mode's azimuthal velocity, which is primarily due to MRI and is represented by the exchange term $\mathcal{I}_y^{(ub)}$ which is always positive.

In conclusion, the channel mode is supported by the linear – nonmodal MRI growth – processes, while nonlinear processes mostly oppose this growth. The effect of the nonlinear terms is maximal during the peaks of $|\bar{b}_x(\mathbf{k}_c)|$ and $|\bar{b}_y(\mathbf{k}_c)|$ – they halt the growth and lead to a fast drain of the channel mode en-

ergy, redistributing this energy to other modes. Thus, in a strict self-consistent approach of the net vertical field MRI-turbulence, this redistribution of the channel mode energy to other modes is actually due to the nonlinear processes (in the form of the transverse cascade, Figures 5.10 and 5.12). However, in previous studies, the channel mode has been considered, for simplicity, not as a variable/perturbation mode itself, but as a part of the basic/stationary dynamics (see e.g., Goodman & Xu, 1994; Pessah & Goodman, 2009; Latter et al., 2009; Pessah, 2010). In those analysis, the redistribution of the channel mode energy to other modes is classified as a linear process – called *parasitic instability* – and these modes (parasites, in our terms "the rest modes"), which feed on the channel mode, are assumed to have smaller amplitudes than that of the latter. This simplified approach definitely gives a good feeling of the broadening of perturbation spectrum at the expense of the channel mode. At the same time, this simplification might somewhat suffer from inaccuracy in the case of the developed turbulence, since the channel mode, on the contrary, is not stationary and consists of a chaotically repeated processes of bursts and subsequent drains – chaotic are both the values of the peaks as well as time intervals between them.

5.4.4 The zonal flow mode

The second mode that also plays an important role in the turbulence dynamics is the zonal flow mode – the harmonic with wavenumber $\mathbf{k}_{zf} = (\pm 1, 0, 0)$ that is independent of the azimuthal and vertical coordinates (i.e.,

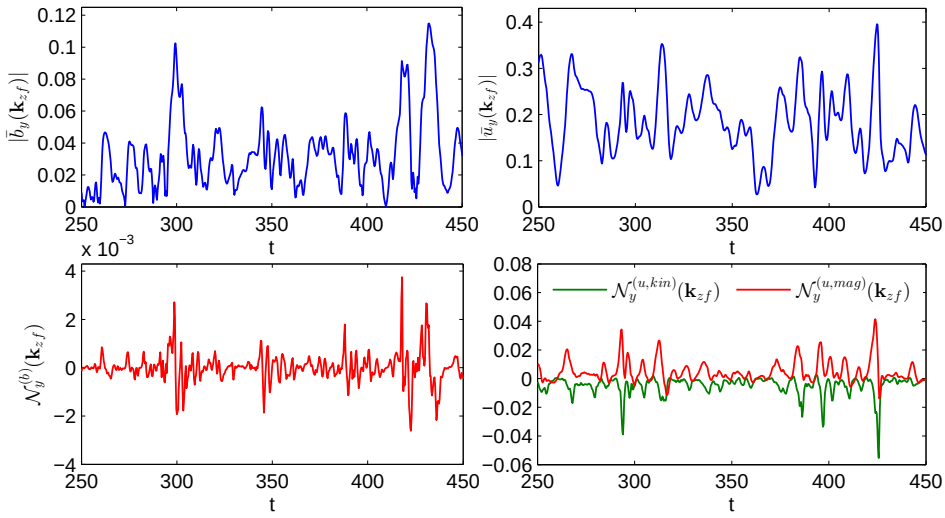

Figure 5.8: Evolution of the azimuthal magnetic field, $\bar{b}_y(\mathbf{k}_{zf})$, and velocity, $\bar{u}_y(\mathbf{k}_{zf})$, components of the zonal flow mode with $\mathbf{k}_{zf} = (\pm 1, 0, 0)$ as well as the corresponding nonlinear terms $\mathcal{N}_y^{(b)}(\mathbf{k}_{zf})$, $\mathcal{N}_y^{(u,kin)}(\mathbf{k}_{zf})$, $\mathcal{N}_y^{(u,mag)}(\mathbf{k}_{zf})$, which drive this mode. The azimuthal velocity $\bar{u}_y$ is dominant in this mode. It is produced by the magnetic part $\mathcal{N}_y^{(u,mag)}$, as it is mostly positive, and drained by the hydrodynamic part $\mathcal{N}_y^{(u,kin)}$, which is always negative.

is axisymmetric and vertically uniform) and has the largest radial wavelength (correspondingly, the smallest wavenumber, $k_x = \pm 1$) in the domain. Excitation of zonal flows in MRI-turbulence with zero and nonzero net vertical magnetic flux was previously observed by Johansen et al. (2009); Bai & Stone (2014); Simon & Armitage (2014), however, its dynamics was usually analyzed based on the simplified models. Here we trace the zonal flow evolution in Fourier space self-consistently, without invoking such models, by examining its governing dynamical terms in the main spectral equations directly from the simulation data.

We have seen in Figure 5.6 that in the turbulent state the zonal flow mode carries higher kinetic energy most of the time among other active modes and corresponds to the maximum of the spectral kinetic energy in Fourier space (see Figure 5.9 below). However, this mode does not contribute to the spectral Reynolds and Maxwell stresses, because its radial velocity and magnetic field components are identically zero, $\bar{u}_x(\mathbf{k}_{zf}) = \bar{b}_x(\mathbf{k}_{zf}) = 0$, due to incompressibility (C.17) and divergence-free (C.18) conditions. Besides, we checked that the vertical velocity, $\bar{u}_z(\mathbf{k}_{zf})$, and magnetic field, $\bar{b}_z(\mathbf{k}_{zf})$, components are also much smaller than the respective azimuthal ones. So, in Figure 5.8 we present only the evolution of the dominant spectral amplitudes of the azimuthal magnetic field, $|\bar{b}_y(\mathbf{k}_{zf})|$, and velocity, $|\bar{u}_y(\mathbf{k}_{zf})|$, of the zonal flow mode. $|u_y(\mathbf{k}_{zf})|$ is characterized by noticeably longer timescale (tens of orbits) variations, i.e., this mode indeed forms a slowly varying in time axisymmetric zonal flow in physical space, while $|b_y(\mathbf{k}_{zf})|$ together with longer timescale variations also exhibits shorter timescale changes. It is readily seen that the linear – stresses and exchange – terms are identically zero for the zonal flow mode in governing Equations (5.8) and (5.22), $\mathcal{H}_y(\mathbf{k}_{zf}) = \mathcal{M}(\mathbf{k}_{zf}) = 0$, $\mathcal{I}_y^{(ub)}(\mathbf{k}_{zf}) = \mathcal{I}_y^{(u\theta)}(\mathbf{k}_{zf}) = 0$. Thus, the linear processes (i.e., MRI) do not affect this mode. Therefore, it can be supported only by the nonlinear terms $\mathcal{N}_y^{(u)}, \mathcal{N}_y^{(b)}$. Since $\bar{u}_y$ is the dominant component in this mode, we look more into its nonlinear term in order to pin down a mechanism of zonal flow generation. This term consists of the magnetic, $\mathcal{N}_y^{(u,mag)}$, and hydrodynamic,

$\mathcal{N}_y^{(u,kin)}$, contributions,

$$\mathcal{N}_y^{(u)} = \mathcal{N}_y^{(u,mag)} + \mathcal{N}_y^{(u,kin)}, \tag{5.34}$$

which for $\mathbf{k}_{zf} = (\pm 1, 0, 0)$, have the following forms:

$$\mathcal{N}_y^{(u,mag)}(\mathbf{k}_{zf}) = \frac{\mathrm{i}}{2}\bar{u}_y^*(\mathbf{k}_{zf}) \int d^3\mathbf{k}' \bar{b}_y(\mathbf{k}')\bar{b}_x(\mathbf{k}_{zf} - \mathbf{k}') + c.c.,$$

with the integrand composed of the turbulent magnetic stresses and

$$\mathcal{N}_y^{(u,kin)}(\mathbf{k}_{zf}) = -\frac{\mathrm{i}}{2}\bar{u}_y^*(\mathbf{k}_{zf}) \int d^3\mathbf{k}' \bar{u}_y(\mathbf{k}')\bar{u}_x(\mathbf{k}_{zf} - \mathbf{k}') + c.c.,$$

with the integrand composed of the turbulent hydrodynamic stresses. The time-histories of these hydrodynamic and magnetic nonlinear parts as well as $\mathcal{N}_y^{(b)}$ are also shown in Figure 5.8. It is seen that $\mathcal{N}_y^{(b)}(\mathbf{k}_{zf})$ changes sign, acting for $|\bar{b}_y|$ as a source, when positive, and as a sink, when negative. On the other hand, the magnetic part is positive most of the time, producing and amplifying $|\bar{u}_y|$. Thus, the zonal flow is supported by $\mathcal{N}_y^{(u,mag)}(\mathbf{k}_{zf})$, which physically describes the effect of the total azimuthal magnetic tension exerted by all the rest modes on the large-scale $\mathbf{k}_{zf}$ mode. This important role of the small-scale magnetic perturbations in launching and maintaining the zonal flow is consistent with the findings of Johansen et al. (2009). By contrast, the hydrodynamic part $\mathcal{N}_y^{(u,kin)}(\mathbf{k}_{zf})$, describing the effect of the total azimuthal hydrodynamic tension exerted by all other modes on the zonal flow mode, is always negative and drains $|\bar{u}_y|$. As a result, its peaks a bit lag the peaks of the magnetic part, which initiates the growth of the azimuthal velocity.

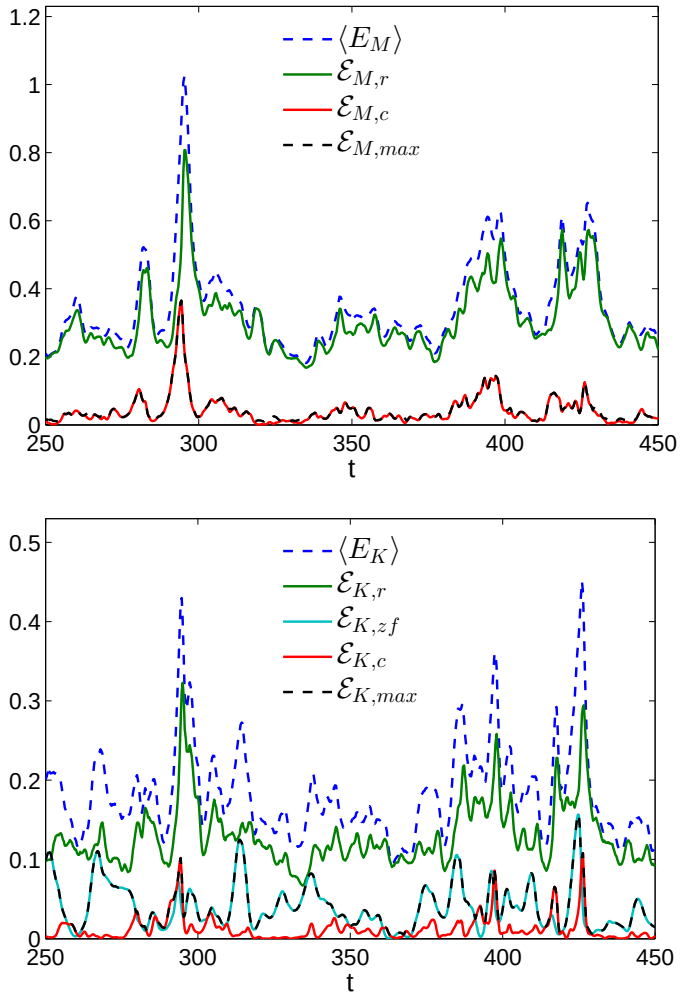

Figure 5.9: The left panel shows the evolution of the total magnetic energy, $\langle E_M \rangle$ (dashed blue), the magnetic energy of the channel mode, $\mathcal{E}_{M,c}$ (red), the total magnetic energy of the rest modes, $\mathcal{E}_{M,r} \approx \langle E_M \rangle - \mathcal{E}_{M,c}$ (green) and the maximum value of the spectral magnetic energy, $\mathcal{E}_{M,max}$ (dashed black), which always coincides with the energy of the channel mode. The right panel shows the evolution of the total kinetic energy, $\langle E_K \rangle$ (dashed blue), the kinetic energy of the channel mode, $\mathcal{E}_{K,c}$ (red), and of the zonal flow mode, $\mathcal{E}_{K,zf}$ (cyan) the total kinetic energy of the rest modes, $\mathcal{E}_{K,r} \approx \langle E_K \rangle - \mathcal{E}_{K,c} - \mathcal{E}_{K,zf}$ (green) and the maximum value of the spectral kinetic energy, $\mathcal{E}_{K,max}$ (dashed black), which always coincides with either the kinetic energy of the channel mode or the zonal flow mode, whichever is larger in a given time. It is also seen that the peaks of the magnetic (kinetic) energy of the rest modes tend to mainly follow the respective peaks of the magnetic (kinetic) energy of the channel mode, because, this mode nonlinearly transfers energy to the rest modes (Figure 5.10), causing their subsequent amplification (peak). Note also that often the zonal flow energy increases when the channel mode energy decreases and vice versa.

5.4.5 The rest modes

So far we have identified and described two – the channel and zonal flow – modes that are the main participants of the dynamical processes. In addition to these modes, as classified in subsection 5.4.2, there are a sufficient number of active modes in the system (blue dots in Figure 5.6), which are not individually significant, but collectively have sufficiently large kinetic and magnetic energies - more than channel or/and zonal flow modes. Consequently, the combined influence of these modes on the overall dynamics of the turbulence becomes important. This set of active modes has been labeled as *the rest modes*, which, as mentioned above, are also called parasitic modes in the studies of net vertical field MRI-turbulence. As we checked, the contribution of other larger wavenumber modes, whose kinetic (magnetic) energy always remains less than 50% of the maximum spectral kinetic (magnetic) energy, in the energy balances is small compared to that of these three main types of modes and therefore is neglected below.[2] Figure 5.9 allows us to compare the total magnetic, $\mathcal{E}_{M,r}$ (left panel), and kinetic, $\mathcal{E}_{K,r}$ (right panel), energies of the rest modes with the corresponding energies of the channel and zonal flow modes at different stages of the evolution. The magnetic energy of the zonal flow mode, $\mathcal{E}_{M,zf} = \mathcal{E}_M(-\mathbf{k}_{zf}) + \mathcal{E}_M(\mathbf{k}_{zf}) \approx 0$, is small compared to that of the channel and the rest modes and is not shown in the left plot. In this case, the total volume-averaged magnetic energy is approximately the sum of the

[2]For this reason, in this subsection, these energy balances are written with approximate equality sign.

magnetic energies of the channel mode, $\mathcal{E}_{M,c} = \mathcal{E}_M(-\mathbf{k}_c) + \mathcal{E}_M(\mathbf{k}_c)$, and the rest modes, $\langle E_M \rangle \approx \mathcal{E}_{M,c} + \mathcal{E}_{M,r}$ (neglecting the very small contribution from the zonal flow mode), whereas in the total kinetic energy, all the three types of modes contribute: $\langle E_K \rangle \approx \mathcal{E}_{K,c} + \mathcal{E}_{K,zf} + \mathcal{E}_{K,r}$ with $\mathcal{E}_{K,c} = \mathcal{E}_K(-\mathbf{k}_c) + \mathcal{E}_K(\mathbf{k}_c)$ and $\mathcal{E}_{K,zf} = \mathcal{E}_K(-\mathbf{k}_{zf}) + \mathcal{E}_K(\mathbf{k}_{zf})$ being the kinetic energies of the channel and zonal flow modes, respectively. In Figure 5.9, $\mathcal{E}_{M,max}$ and $\mathcal{E}_{K,max}$ are, respectively, the maximum values of the spectral magnetic and kinetic energies[3]. The left panel shows that this maximum value of the magnetic energy falls on the channel mode, i.e., $\mathcal{E}_{M,max} = \mathcal{E}_{M,c}$, during an entire course of the evolution. In other words, the channel mode is always magnetically the strongest among all the active rest modes, although the total magnetic energy of the latter modes dominates the magnetic energy of the channel mode, $\mathcal{E}_{M,r} > \mathcal{E}_{M,c}$, especially in the quiescent intervals between the bursts, when the magnetic energy of the channel mode is relatively low. This points to the importance of the rest modes in the turbulence dynamics. Despite this dominance, however, it is seen in the left panel of Figure 5.9 that the peaks of the rest modes' magnetic energy always occur shortly after the corresponding peaks of the channel mode's magnetic energy, indicating that the former increases, or is driven by the latter (see subsection 5.4.6). Thus, the typical burst-like behavior of the nonzero the net vertical field MRI-turbulence is closely related to the manifestation of the channel mode dynamics.

[3] Actually, Figure 5.9 shows these maximum energies with factor 2 to match the definition of the channel and zonal flow mode energies.

The role of the rest modes is also seen in the evolution of the kinetic energies in the right panel of Figure 5.9. As is in the case of the magnetic energy, the contribution of the total kinetic energy of the rest modes, $\mathcal{E}_{K,r}$, in the volume-averaged total kinetic energy is always dominant. The kinetic energy of the zonal flow mode, $\mathcal{E}_{K,zf}$, is comparable to the kinetic energy of the rest modes only occasionally, while the contribution of the kinetic energy of the channel mode, $\mathcal{E}_{K,c}$, in the overall balance of the total kinetic energy is even less. However, also in this case, the maximum value of the spectral kinetic energy, $\mathcal{E}_{K,max}$, always coincides with either the kinetic energy of the channel mode or the zonal flow mode, whichever is larger at a given moment. Moreover, on a closer inspection of the kinetic energy curves, it appears that the peaks of the total kinetic energy of the rest modes in fact tends to mainly follow the corresponding peaks of the channel mode, because, as demonstrated in the next subsection, this mode transfers energy to the rest modes via the nonlinear transfers, causing their subsequent amplification. Note also that often the zonal flow energy increases and has a peak when the channel mode energy decreases and has a minimum, that is, the zonal flow tends to grow when the channel mode is at its minimum and vice versa. This anti-correlation between the zonal flow and magnetic activity, which was also reported in Johansen et al. (2009), is further explored in Fourier space in the next subsection.

5.4.6 Interdependence of the channel, zonal flow and rest modes

So far we have separately described the dynamics of the main – the channel, the zonal flow and the rest modes. Now we move to the analysis of their interlaced dynamics in Fourier space, which determines the properties and balances of MRI-turbulence with net vertical magnetic field. First of all it is a characteristic burst-like behavior of the volume-averaged energies and stresses (Figures 5.3), which is related to the manifestations of these modes' activity and nonlinear interaction. As was discussed in subsection 5.4.3, the short bursts of the channel mode arise as a result of the competition between the linear nonmodal MRI-amplification and nonlinear redistribution of the channel mode's energy in **k**-space.

Each such burst event starts with the linear amplification, which initially overwhelms the nonlinear redistribution to other modes and therefore the energy of the channel mode increases. At the same time, the effect of the nonlinear terms on the channel mode, described by $\mathcal{N}^{(b)}(\mathbf{k}_c), \mathcal{N}^{(u)}(\mathbf{k}_c)$, increases as well, as it gradually loses its energy to the rest modes due to nonlinear transfers. At a certain amplitude of the channel mode, these nonlinear terms become comparable to the linear ones responsible for MRI, halt the further growth of the channel mode and start its fast drain (Figure 5.7).

This moment, corresponding to the peak, is a critical stage in the channel mode's evolution and therefore it is important to examine in more detail how nonlinear processes redistribute/transfer the energy of the channel mode in Fourier space. For this purpose, we present the map of the nonlinear transfer

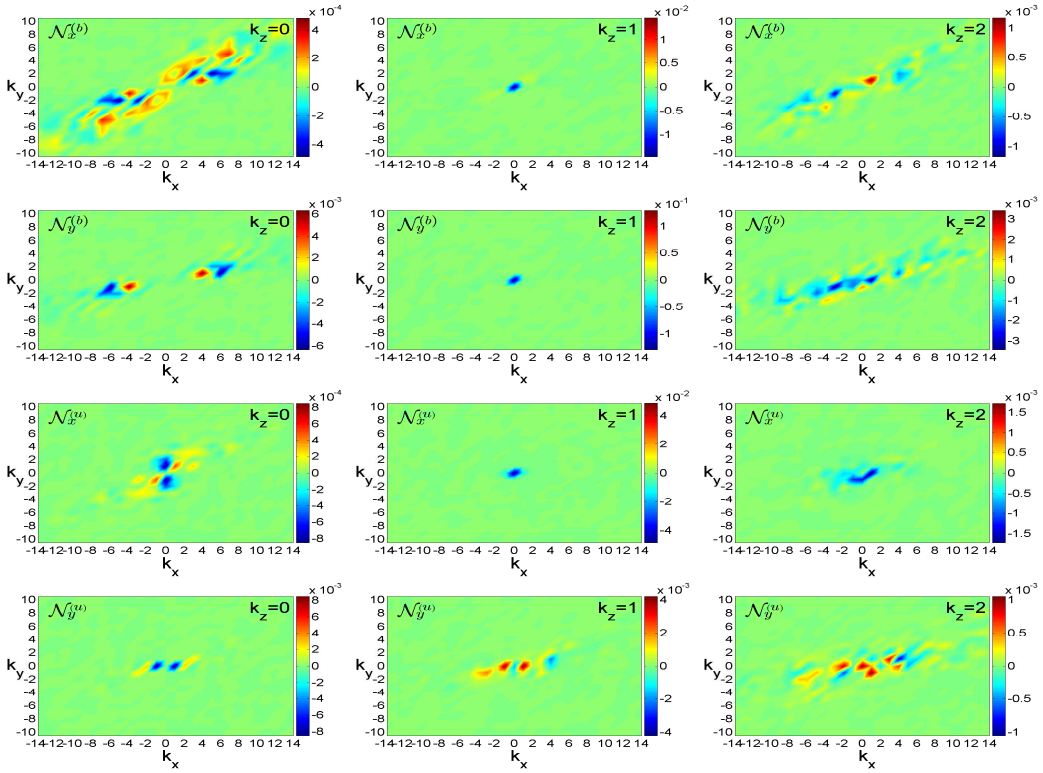

Figure 5.10: Spectra of the nonlinear transfer terms in (k_x, k_y)-plane at $k_z = 0(left), 1(middle), 2(right)$ at around $t = 294$, when the channel mode energy has a peak. At $k_z = 1$ the nonlinear transfer terms $\mathcal{N}_x^{(b)}$, $\mathcal{N}_y^{(b)}$, $\mathcal{N}_x^{(u)}$ strongly peak near $k_x = k_y = 0$ and are negative, while $\mathcal{N}_y^{(u)}$ has a positive peak at $k_x = \pm 1, k_y = 0$, but is negative for the channel mode. So, all these nonlinear terms act as a sink for the channel mode at its highest point, transferring its energy to a wide spectrum of the rest modes at $k_z = 0$ and higher $|k_z| > 1$; however, the zonal flow does not receive energy in this process. The yellow and red areas in each plot show exactly which modes receive energy and hence are being excited at this time due to the nonlinear transfers as a result of the decline of the channel mode. This set of modes belong to the class of *the rest modes*, as discussed in the text. For $k_z = 0, 2$ shown here, these transfers are notably anisotropic due to shear, i.e., depend on the polar angle of wavevector, being mainly concentrated in the first and third quadrants of (k_x, k_y)-plane and are a consequence of the transverse cascade process.

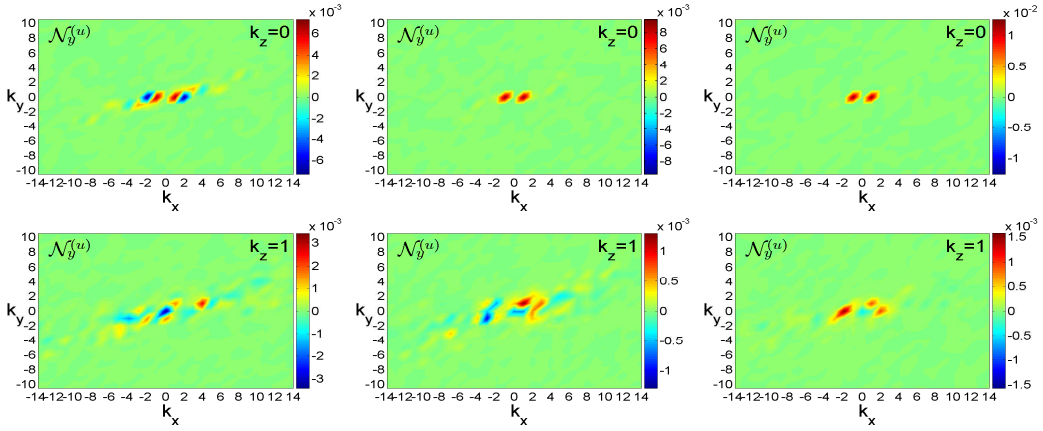

Figure 5.11: The nonlinear transfer term $\mathcal{N}_y^{(u)}$ in (k_x, k_y)-plane at $k_z = 0, 1$, when the channel mode energy is at the minimum, i.e., at the end ("bottom") of the burst at there different moments, $t = 296, 311, 383$. This term is positive at the wavenumber of the zonal flow mode, $\mathbf{k}_{zf}$, but negative at the wavenumber of the channel mode, $\mathbf{k}_c$, at all these moments. Hence, $\mathcal{N}_y^{(u)}$ at the end of the channel mode burst acts as the source for the zonal flow mode. Thus, the formation of the zonal flow mode starts after the end of the channel mode burst.

terms in (k_x, k_y)-plane at $k_z = 0, 1, 2$ at two key stages of the burst dynamics – first when the channel mode energy has a peak (Figure 5.10) and when its energy is at a minimum (Figure 5.11). The nonlinear redistribution quite differ from each other at these "top" and "bottom" points of the channel mode bursts. In both moments they are notably anisotropic due to the shear, i.e., depend on a wavenumber polar angle, being preferably concentrated in the first and third quadrants, and thus realize the transverse cascade of the modes in Fourier space. Figure 5.10, corresponding to the "top" in the vicinity of the moment $t = 294$ of the highest magnetic energy peak of the channel mode, shows strong negative peaks of the nonlinear transfer terms $\mathcal{N}_x^{(b)}$, $\mathcal{N}_y^{(b)}$, $\mathcal{N}_x^{(u)}$

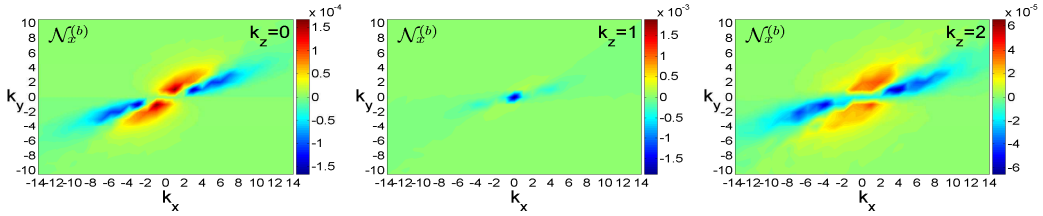

Figure 5.12: Time-averaged nonlinear term $\mathcal{N}_x^{(b)}$ in (k_x, k_y)-plane at $k_z = 0(left), 1(middle), 2(right)$. As in a single instant shown in Figure 5.10, the action of this term is highly anisotropic due to the shear, i.e., strongly depend on the wavevector polar angle. However, this time-averaged distribution is much smoother than its instantaneous counterpart and clearly shows transfer of modes over wavevector angles, that is, *the transverse cascade* of $|\bar{b}_x|^2$ from the blue regions, where $\mathcal{N}_x^{(b)} < 0$ and acts as a sink for it, to the red and yellow regions, where $\mathcal{N}_x^{(b)} > 0$ and acts as a source/production. In light green regions, these terms are small, although, as we checked, preserve the same anisotropic shape. As in Figure 5.10, at $k_z = 1$, $\mathcal{N}_x^{(b)}$ peaks again at $k_x = k_y = 0$, implying that also in the time-averaged sense, the dominant nonlinear process at $k_z = 1$ is draining of the channel mode energy and transferring it to the rest modes with other k_z (mainly $k_z = 0, 1$).

for the channel mode (i.e., at $k_x = k_y = 0, k_z = 1$), as the nonlinearity leads its fast drain at this moment. The red and yellow areas in this figure represent the subset of the rest modes, mostly with $k_z = 0, 2$, which receive energy via nonlinear transfers at this moment of the channel mode's peak activity. Note that at this time, the nonlinearity transfers the channel mode energy not to the zonal flow mode (since $\mathcal{N}_y^{(u)}(\mathbf{k}_{zf}) < 0$ at this moment), but to the rest modes. In other words, the rest modes can be considered as the main "culprits/parasites" in the decline of the channel mode in the developed turbulent state. The action of the above nonlinear terms in Fourier space during other peaks of the channel mode are qualitatively similar to that given in Figure 5.10

at around $t = 294$, however, concretely which modes, from the total set of the rest modes, receive energy is, of course, different for each burst. Thus, this unifying approach – the analysis of the dynamics and the nonlinear transfer functions in Fourier space – enables us to self-consistently describe the interaction between the channel and the rest (parasitic) modes when the standard assumptions in the usual treatment of these modes (Goodman & Xu, 1994; Pessah & Goodman, 2009) break down: the amplitudes of these two mode types become comparable, so that one can no longer separate the channel as a primary background and parasites as small perturbations on top of that. *Overall, the rest (parasitic) modes play a major role in the channel mode decline. After each its burst, the transverse cascade determines a specific spectrum of the parasitic modes in the turbulent state, which mostly gain energy as a result of draining the channel mode.*

Quite differently acts the nonlinearity at the "bottom" point when the channel mode is at its minimum. In this case, the main effect is the production of the zonal flow mode, so that in Figure 5.11 we show only the nonlinear transfer term for the azimuthal velocity, $\mathcal{N}_y^{(u)}$, at the end ("bottom") of the channel burst at there different moments. It is seen that this term is positive at the wavenumber of the zonal flow mode, $\mathbf{k}_{zf}$, at all there moments (red dots at $k_x = \pm 1, k_y = 0$ on the plots with $k_z = 0$), acting as the source for the zonal flow mode. As a result, the formation of the zonal flow mode starts after the end of the channel mode burst. For the channel mode wavenumber $\mathbf{k}_c$, $\mathcal{N}_y^{(u)}$ is negative at these moments, acting as a sink. As for the other nonlinear terms

at the "bottom" points (not shown here), they look qualitatively similar to those in Figure 5.10, except that they no longer have a prominent negative peak at $\mathbf{k}_c$, since the rest and the zonal flow modes dominate instead in the dynamics at these times.

We have seen from Figures 5.10 and 5.11 that the shear-induced anisotropy of nonlinear transfers in Fourier space lie at the basis of the balances of dynamical processes in vertical field MRI-turbulence. In particular, they determine the drain of the channel mode and the resulting anisotropic spectrum of the rest modes which gain energy from the channel mode after each peak. However, the snapshots of the spectral dynamics of the modes shown in these figures, being at separate moments, are still irregular, somewhat obscuring this generic spectral anisotropy of the MRI-turbulence due to the shear. They convey only a short-time behavior of the turbulence. The spectral anisotropy of MRI-turbulence with a net vertical field was demonstrated by Hawley et al. (1995); Lesur & Longaretti (2011) and recently in more detail by Murphy & Pessah (2015), who, however, characterized only the anisotropic spectra of the magnetic energy and Maxwell stress in $\mathbf{k}$-space, but not the nonlinear processes. This inherent anisotropic character of the dynamical process of shear flows in Fourier space is best identified and described by considering a long-term evolution of the turbulence, i.e., by averaging the spectral quantities over time, as was done in the above studies. Such an averaging in the present case with a net vertical field indeed shows the dominance of the nonlinear transverse cascade, i.e., the angular (i.e., over wavevector angles) redistribution of the power

in Fourier space in the overall dynamical balances (nonlinear interactions) between the channel and the rest modes, which is a main process underlying the turbulence. Previously, Lesur & Longaretti (2011) also investigated the nonlinear transfers in a net vertical field MRI-turbulence, however, they applied, together with time-averaging, also shell-averaging of the linear and nonlinear dynamical terms in **k**-space that naturally smears out the spectral anisotropy and hence the transverse cascade.

We demonstrate the anisotropic nature of the nonlinear transfers on longer time-scale on the example of the radial component of the magnetic field, for which it is most apparent. Figure 5.12 shows the corresponding nonlinear term $\mathcal{N}_x^{(b)}$ in (k_x, k_y)-plane at different $k_z = 0, 1, 2$ averaged in time from $t = 100$ till $t = 650$. Like in a single instant shown in Figure 5.10, the action of this term is highly anisotropic in its dependence on the azimuthal angle in (k_x, k_y)-plane due to the shear. However, this time-averaged distribution is much smoother than its instantaneous counterpart and clearly shows transfer of modes over wavevector angles, i.e., the transverse cascade of $|\bar{b}_x|^2$ from the blue regions, where $\mathcal{N}_x^{(b)} < 0$ and acts as a sink for it, to the red and yellow regions, where $\mathcal{N}_x^{(b)} > 0$ and acts as a source/production. In light green regions (outside the vital area) these terms are small, although preserve the same anisotropic shape. As in Figure 5.10, at $k_z = 1$, $\mathcal{N}_x^{(b)}$ has a pronounced negative peak again at $k_x = k_y = 0$ in Figure 5.12, implying that in this time-averaged sense too the dominant nonlinear process at $k_z = 1$ is draining of the channel mode energy. This energy is transferred transversely to the rest

modes with other k_z (mainly $k_z = 0, 1$) and a range of k_x, k_y indicated by the red and yellow areas in Figure 5.12 where $\mathcal{N}_x^{(b)} > 0$. Since time-averaging procedure spans the whole duration of the turbulence in the simulations, these smooth regions in fact enclose all the rest modes ever excited during the entire evolution.

5.4.7 On the effect of stratification

It is well-known from simulations of zero net flux MRI-turbulence that vertical stratification favors notable dynamo action in magnetized disks, where a large-scale azimuthal magnetic field is generated and exhibits a "butterfly" diagram – regular

quasi-periodic spatio-temporal oscillations (reversals) (e.g., Brandenburg et al., 1995; Johansen et al., 2009; Davis et al., 2010; Gressel, 2010; Shi et al., 2010; Simon et al., 2011; Bodo et al., 2012, 2014; Gressel & Pessah, 2015). By contrast, although large-scale azimuthal field generation can still take place in unstratified zero net flux MRI-turbulence in vertically sufficiently extended boxes, the spatio-temporal variation of this field is still more incoherent/irregular in the form of wandering patches (Lesur & Ogilvie, 2008; Shi et al., 2016). A detailed physical mechanism of how stratification brings about such an organization of the magnetic field is not fully understood and requires further studies. This is an important topical question, as it closely bears on the convergence problem in zero net flux MRI-turbulence simulations in stratified and unstratified shearing boxes, which is currently under debate (see e.g.,

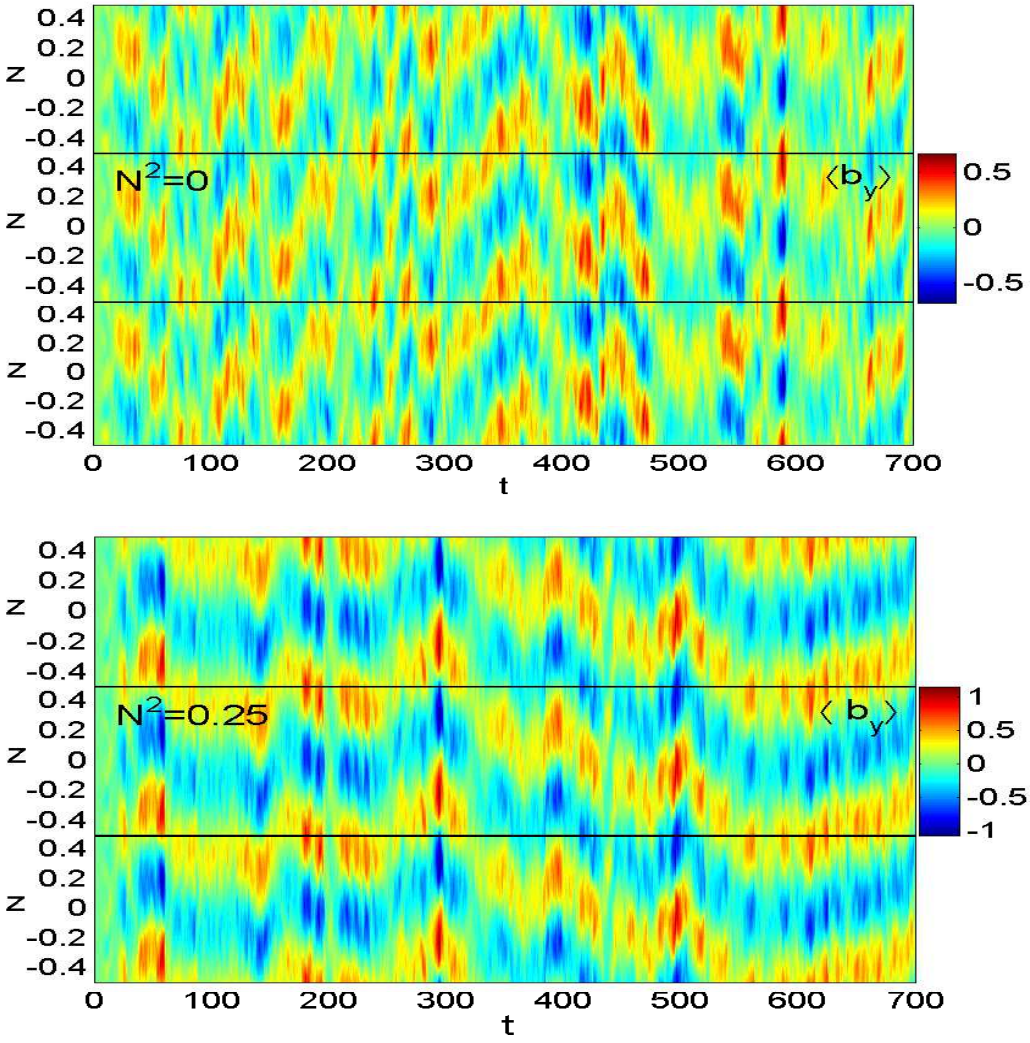

Figure 5.13: Space-time diagram of the azimuthal field averaged in the horizontal (x, y)-plane, $\langle b_y \rangle$, in the unstratified $N^2 = 0$ (top) and stratified $N^2 = 0.25$ (bottom) boxes. In contrast to the unstratified case, the stratification results in a remarkable organization of the average azimuthal field, which is dominated by the $k_z = \pm 1$ modes, into a relatively coherent pattern in the (t, z)-plane with a regular phase variation. Each box has been stacked with identical boxes from top and bottom to simplify perception of this pattern.

Bodo et al., 2014; Shi et al., 2016; Ryan et al., 2017, and references therein). Despite the fact that the present problem, containing a nonzero net vertical flux, differs from the case of zero net flux usually considered in the context of MRI-dynamo, here we also observe a notable spatio-temporal organization of the large-scale azimuthal field in the turbulent state (see below). Somewhat analogous an ordered cyclic behavior of the horizontally averaged azimuthal magnetic field was found previously in MRI-turbulence with a net vertical magnetic flux in the shearing box, but with more complex isothermal vertical stratification (Bai & Stone, 2013; Fromang et al., 2013; Simon et al., 2013; Salvesen et al., 2016).

The considered here disk flow configuration is based on the Boussinesq approximation, where vertical stratification enters the governing perturbation Equations (C.25)-(C.27) in a simpler manner than in the above studies – through buoyancy-induced terms, proportional to the vertically uniform Brunt-Väisälä frequency squared, N^2. Still, this simplification has an advantage in that one could simply put only N^2 to zero in these dynamical equations without altering other parameters and equilibrium configuration of the system. This allows us to directly compare to the unstratified case and more conveniently isolate the basic role of stratification in the dynamo action. In the linear regime, stratification has only a little influence on the dynamics of vertical field MRI (Mamatsashvili et al., 2013). Moreover, it is easily seen that the effect of stratification identically vanishes for the most effectively amplified channel mode with $k_x = k_y = 0$, whose azimuthal field, equal to the

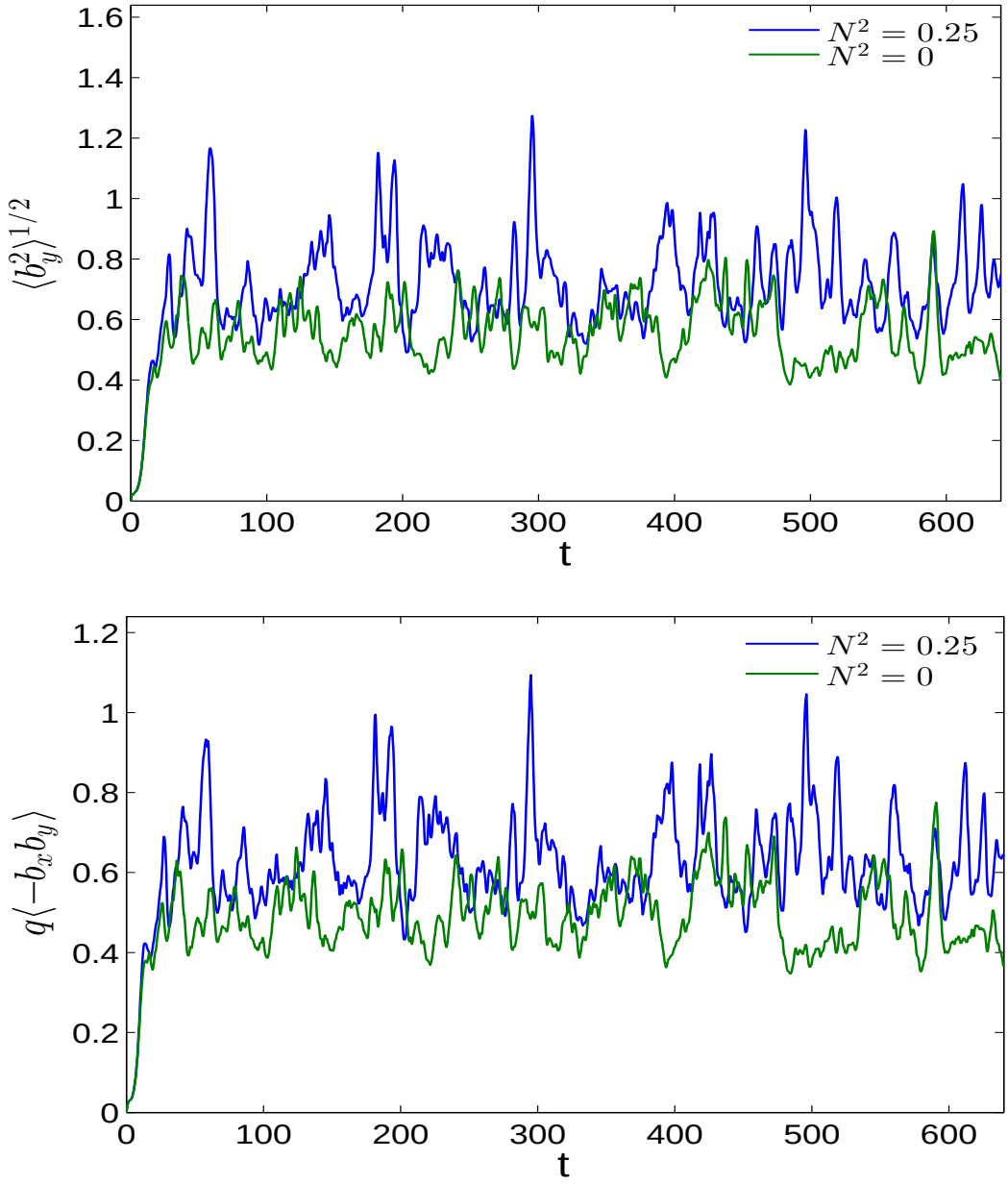

Figure 5.14: Evolution of the volume-averaged rms of b_y and Maxwell stress multiplied by q, $q\langle -b_x b_y \rangle$, in the stratified fiducial run at $N^2 = 0.25$ (blue) and unstratified $N^2 = 0$ run (green). In the presence of stratification, both these quantities are larger and exhibit more pronounced burst-like behavior compared to those in the unstratified case.

averaged in the horizontal (x, y)-plane total azimuthal field, in fact constitutes the large-scale dynamo field. So, the effect of stratification on the dynamo action is solely attributable to nonlinearity, which modifies the electromotive force.

Figure 5.13 shows the space-time diagrams of the horizontally averaged azimuthal magnetic field, $\langle b_y \rangle$, in the stratified fiducial case with $N^2 = 0.25$ as used in the Chapter and unstratified, $N^2 = 0$, case for the same other parameters. It is clearly seen that stratification causes a remarkable organization of the azimuthal field into a coherent wave-like pattern in contrast to the unstratified case. In both cases, however, this horizontally averaged field is dominated by the $k_z = \pm 1$ harmonics,[4] i.e., it is associated with the dominant channel mode analyzed above, but its phase variation with t and z in the stratified case is much more regular than that in the unstratified one. The amplitude of this averaged azimuthal field is about an order of magnitude larger than that of the background vertical field B_{0z}. Figure 5.14 shows that the rms of the azimuthal field and the volume-averaged Maxwell stress in the stratified case are larger, with stronger/higher and more frequent bursts, than those in the unstratified case. Clearly, the space-time diagram shown in Figure 5.13 in the stratified case with periodic vertical boundary conditions differs from a typical "butterfly" observed in the case of isothermal stratification in the

[4]The magnetic field of the large-scale modes $k_x = k_y = 0, k_z = \pm 1$ gives the dominant contribution to the horizontally averaged dynamo field and therefore is a central focus of study in the zero net flux MRI-dynamo problem (see e.g., Lesur & Ogilvie, 2008; Davis et al., 2010; Herault et al., 2011; Shi et al., 2016; Riols et al., 2017).

above mentioned studies. This difference can be attributable to the different nature of the buoyancy term and vertical boundary conditions used, which jointly cause elevation of the azimuthal flux from the midplane. Nevertheless, this comparison clearly demonstrates the capability of stratification to order/regularize the spatio-temporal variation of the mean azimuthal field – the main field component in accretion disk dynamo. Here, we have presented only a primary manifestation of the effect of stratification in the net vertical field MRI-turbulence. In its own right, it is a subject of a detailed and refined investigation.

5.5 Conclusion

In this Chapter, we investigated the dynamical balances underlying MRI-driven magnetohydrodynamic turbulence in Keplerian disks with a nonzero net vertical magnetic field and vertically uniform thermal stratification using shearing box simulations. Focusing on the analysis of the turbulence dynamics in Fourier (**k**-) space, we identified three key types of modes – *the channel, the zonal flow mode and the rest modes* – that are the main "players" in the turbulence dynamics. We described the dynamics of these modes separately and then their interdependence, which sets the properties of the nonzero net vertical field MRI-turbulence. The processes of linear origin are defined primarily by nonmodal, rather than modal, growth of MRI due to disk flow nonnormality/shear. This is because the dynamical time of the turbulence is of the order of the orbital/shear time during which the nonmodal effects are

important. In the turbulent state, higher values of the stresses and magnetic energy fall just on those active modes that exhibit the largest nonmodal MRI growth and *not* on the modally (exponentially) most unstable modes. In other words, the properties of the turbulence are determined mostly by nonmodal physics of MRI rather than by the modal one. From all the active modes, the one that exhibits the maximum nonmodal growth is the channel mode, which is horizontally uniform with the largest vertical scale in the domain. As for the nonlinear processes, it can be confidently stated that the decisive agent in forming and maintaining the statistical characteristics of the net vertical field MRI-turbulence is the nonlinear transverse cascade – redistribution of modes over wavevector angles in Fourier space by nonlinear transfers – arising from the presence of the shear and hence being a generic phenomenon in shear flows. Specifically, the nonlinear transverse cascade redistributes the energy of the channel mode, which is nonmodally most amplified one, to the rest modes and, subsequently, the energy of the rest modes to the zonal flow mode. (One has to note that the rest modes receive energy not only due to the nonlinear transfers, but they also undergo nonmodal MRI growth, however, less than the channel mode does). The combined action of these linear and nonlinear processes leads to the channel mode exhibiting recurrent bursts of the energy and stresses. The nonlinear transfer of its energy to the rest modes causes the decline of the channel mode after each burst and subsequent abrupt increase of the energy of the rest modes. This, in turn, induces similar, burst-like evolution of the integral characteristics of the turbulence – the total

volume-averaged energies and stresses.

The rest modes here, playing the main role in draining the channel mode, were referred to as parasitic modes in previous studies of net vertical field MRI. However, there is an important distinction. These parasitic modes are often assumed to be small compared with the channel mode and are treated as linear perturbations imposed on the latter (Goodman & Xu, 1994; Pessah & Goodman, 2009; Latter et al., 2009, 2010; Pessah, 2010). Besides, the effect of shear and hence the nonmodal physics are neglected with respect to parasitic modes. In the turbulent state, however, the rest modes can reach energies comparable to the channel mode, as has been demonstrated in this Chapter, so one can no longer separate the channel as a primary background and parasites as small perturbations on top of that. As a result, the complex interaction between these two mode types belongs to the domain of nonlinearity. Our general/unifying approach – the analysis of the dynamics in 3D Fourier space – allows us to self-consistently characterize this mode interaction. In this case, the transverse cascade defines the spectrum of the rest modes, which precipitate the decline of the channel mode after each burst.

As we found in this study, the net vertical field MRI-turbulence is robust and, in addition, multifarious – determined by the interdependent/interlaced dynamics of three qualitatively different modes. Consequently, in order to properly quantify the relative contribution of each of these modes in the turbulence characteristics, one has to capture the main aspects of their dynamics in numerical simulations. First of all, this concerns the selection of relevant

sizes (aspect ratio) of the simulation box (which is actually arbitrary in the shearing box framework) and resolutions, so that the discrete modes in the selected box densely enough cover the vital area in (k_x, k_y)-plane and maximally comprise effectively growing (optimal) modes (see Figure 5.1). Besides, one should also avoid artificial/numerical anisotropyzation of nonlinear processes. As was shown in Chapter 4, the anisotropy of the simulation box in (k_x, k_y)-plane introduces artificial anisotropy of nonlinear processes and somewhat "deforms" the overall dynamical picture of MRI-turbulence in Fourier space. In the present case, this artificial deformation could result in a change of the relative importance of the above-classified modes in the overall dynamics, for instance, could reduce the effectiveness of the channel mode compared to other modes and hence weaken its manifestation in the turbulence dynamics (see e.g., Bodo et al., 2008). In particular, changing the role of the large-scale channel mode likely affects the generation of the mean azimuthal magnetic field, or the dynamo action, since this field is directly associated with this mode. Susceptibility of the latter to specific factors of the dynamics is clearly shown in Figure 5.13: although the vertical stratification makes only negligible contribution to the turbulence energy, it remarkably enhances the generation of the mean azimuthal magnetic field and regularizes its spatiotemporal characteristics. The latter process is significant and represents the subject of a special detailed investigation.

Chapter 6

Conclusions and future work

In this thesis two key phenomena in MHD shear flows are investigated – the flows nonnormality induced linear transient dynamics/growth of perturbations and nonlinear transverse cascade – and their refined interplay ensuring onset and self-sustenance of turbulence. Nonuniform/shear flows are universally non-normal and, consequently, the flow's nonnormality induced linear transient dynamics of perturbations is inevitable. At the same time, the linear transient dynamics being anisotropic in spectral space directly results in the anisotropic nature of nonlinear processes. This circumstance gives birth to a new type of nonlinear cascade – nonlinear transverse cascade – which is fundamentally different from the known nonlinear anisotropic cascades. Overall, the nonnormality induced linear and nonlinear phenomena are inevitable in shear flows and essentially determine perturbations dynamics - "the fate of these flows". Here one should note again, that shear flows are ubiquitous both in nature and laboratory. They occur in atmospheres, oceans, solar winds, stars, astrophysical disks, pipe flows, tokamak reactors, etc. Complex dynamics of these systems is, in many respects, a consequence of their nonuniform kinematics. In the end, investigated in this thesis phenomena have quite wide range of applications.

Performed investigations have natural extensions to other configurations of astrophysical/Keplerian disks. Specifically, the study of:
– Sustenance of zero-net flux MRI-turbulence and dynamo action both in unstratified and stratified cases,
– MRI turbulence in the presence of compressibility – generation of density waves by magnetic perturbations.

All these are certainly relevant to the understanding of subcritical turbulence in other sheared engineering flows and complex environments such as MHD winds, geophysical magnetic fields, fusion plasma etc. First of all we would like to emphasize the perspective of the extension of the performed investigations to fusion plasma, specifically – to sheared mean $\mathbf{E} \times \mathbf{B}$ plasma fusion flows. Point is that the importance of nonmodal physics and the formed by the hydrodynamic community in 1990s trend have been successfully adopted in atmospheric flow and astrophysical disk flow researches. However, up to now, the trend has limited impact on the plasma and magnetic fusion communities. Filling this gap looks productive, moreover, – it seems necessary.

Appendices

Appendix A

Perturbation equations in physical and Fourier space in Keplerian disks with an azimuthal magnetic field (Chapter 4)

Equations governing the evolution of the velocity, total pressure and magnetic field perturbations, $\mathbf{u}, p, \mathbf{b}$, about the equilibrium Keplerian flow $\mathbf{U}_0 = (0, -q\Omega x, 0)$ with net azimuthal field $\mathbf{B}_0 = (0, B_{0y}, 0)$ are obtained from the basic Equations (5.1)-(5.5) and componentwise have the form:

$$\frac{Du_x}{Dt} = 2\Omega u_y - \frac{1}{\rho_0}\frac{\partial p}{\partial x} + \frac{B_{0y}}{4\pi\rho_0}\frac{\partial b_x}{\partial y} + \frac{\partial}{\partial x}\left(\frac{b_x^2}{4\pi\rho_0} - u_x^2\right) + \frac{\partial}{\partial y}\left(\frac{b_x b_y}{4\pi\rho_0} - u_x u_y\right) + \\ + \frac{\partial}{\partial z}\left(\frac{b_x b_z}{4\pi\rho_0} - u_x u_z\right) + \nu\nabla^2 u_x, \quad \text{(A.1)}$$

$$\frac{Du_y}{Dt} = (q-2)\Omega u_x - \frac{1}{\rho_0}\frac{\partial p}{\partial y} + \frac{B_{0y}}{4\pi\rho_0}\frac{\partial b_y}{\partial y} + \frac{\partial}{\partial x}\left(\frac{b_x b_y}{4\pi\rho_0} - u_x u_y\right) + \frac{\partial}{\partial y}\left(\frac{b_y^2}{4\pi\rho_0} - u_y^2\right) + \\ + \frac{\partial}{\partial z}\left(\frac{b_z b_y}{4\pi\rho_0} - u_z u_y\right) + \nu\nabla^2 u_y \quad \text{(A.2)}$$

$$\frac{Du_z}{Dt} = -\frac{1}{\rho_0}\frac{\partial p}{\partial z} - N^2\theta + \frac{B_{0y}}{4\pi\rho_0}\frac{\partial b_z}{\partial y} + \frac{\partial}{\partial x}\left(\frac{b_x b_z}{4\pi\rho_0} - u_x u_z\right) + \frac{\partial}{\partial y}\left(\frac{b_y b_z}{4\pi\rho_0} - u_y u_z\right) + \\ + \frac{\partial}{\partial z}\left(\frac{b_z^2}{4\pi\rho_0} - u_z^2\right) + \nu\nabla^2 u_z \quad \text{(A.3)}$$

$$\frac{D\theta}{Dt} = u_z - \frac{\partial}{\partial x}(u_x\theta) - \frac{\partial}{\partial y}(u_y\theta) - \frac{\partial}{\partial z}(u_z\theta) + \chi\nabla^2\theta \quad \text{(A.4)}$$

$$\frac{Db_x}{Dt} = B_{0y}\frac{\partial u_x}{\partial y} + \frac{\partial}{\partial y}\left(u_x b_y - u_y b_x\right) - \frac{\partial}{\partial z}(u_z b_x - u_x b_z) + \eta\nabla^2 b_x, \tag{A.5}$$

$$\frac{Db_y}{Dt} = -q\Omega b_x + B_{0y}\frac{\partial u_y}{\partial y} - \frac{\partial}{\partial x}\left(u_x b_y - u_y b_x\right) + \frac{\partial}{\partial z}(u_y b_z - u_z b_y) + \eta\nabla^2 b_y, \tag{A.6}$$

$$\frac{Db_z}{Dt} = B_{0y}\frac{\partial u_z}{\partial y} + \frac{\partial}{\partial x}\left(u_z b_x - u_x b_z\right) - \frac{\partial}{\partial y}(u_y b_z - u_z b_y) + \eta\nabla^2 b_z, \tag{A.7}$$

$$\frac{\partial u_x}{\partial x} + \frac{\partial u_y}{\partial y} + \frac{\partial u_z}{\partial z} = 0, \tag{A.8}$$

$$\frac{\partial b_x}{\partial x} + \frac{\partial b_y}{\partial y} + \frac{\partial b_z}{\partial z} = 0, \tag{A.9}$$

where $D/Dt = \partial/\partial t - q\Omega x\partial/\partial y$ is the total derivative along the background flow.

Appendix B

Derivation of spectral equations for quadratic terms in Keplerian disks with an azimuthal magnetic field (Chapter 4)

Here we derive evolution equations for velocity, entropy and magnetic field perturbations in Fourier space. Substituting decomposition (5.6) into Equations (A.1)-(A.9) and taking into account the normalization made in the text, we arrive at the following equations governing the dynamics of perturbation modes in Fourier space

$$\left(\frac{\partial}{\partial t}+qk_y\frac{\partial}{\partial k_x}\right)\bar{u}_x = 2\bar{u}_y - \mathrm{i}k_x\bar{p} + \mathrm{i}k_yB_{0y}\bar{b}_x - \frac{k^2}{\mathrm{Re}}\bar{u}_x + \mathrm{i}k_xN^{(u)}_{xx} + \mathrm{i}k_yN^{(u)}_{xy} + \mathrm{i}k_zN^{(u)}_{xz}, \tag{B.1}$$

$$\left(\frac{\partial}{\partial t}+qk_y\frac{\partial}{\partial k_x}\right)\bar{u}_y = (q-2)\bar{u}_x - \mathrm{i}k_y\bar{p} + \mathrm{i}k_yB_{0y}\bar{b}_y - \frac{k^2}{\mathrm{Re}}\bar{u}_y + \mathrm{i}k_xN^{(u)}_{xy} + \mathrm{i}k_yN^{(u)}_{yy} + \mathrm{i}k_zN^{(u)}_{yz}, \tag{B.2}$$

$$\left(\frac{\partial}{\partial t}+qk_y\frac{\partial}{\partial k_x}\right)\bar{u}_z = -\mathrm{i}k_z\bar{p} - N^2\bar{\theta} + \mathrm{i}k_yB_{0y}\bar{b}_z - \frac{k^2}{\mathrm{Re}}\bar{u}_z + \mathrm{i}k_xN^{(u)}_{xz} + \mathrm{i}k_yN^{(u)}_{yz} + \mathrm{i}k_zN^{(u)}_{zz}, \tag{B.3}$$

$$\left(\frac{\partial}{\partial t}+qk_y\frac{\partial}{\partial k_x}\right)\bar{\theta} = \bar{u}_z - \frac{k^2}{\mathrm{Pe}}\bar{\theta} + \mathrm{i}k_xN^{(\theta)}_x + \mathrm{i}k_yN^{(\theta)}_y + \mathrm{i}k_zN^{(\theta)}_z, \tag{B.4}$$

$$\left(\frac{\partial}{\partial t}+qk_y\frac{\partial}{\partial k_x}\right)\bar{b}_x = \mathrm{i}k_yB_{0y}\bar{u}_x - \frac{k^2}{\mathrm{Rm}}\bar{b}_x + \mathrm{i}k_y\bar{F}_z - \mathrm{i}k_z\bar{F}_y, \tag{B.5}$$

$$\left(\frac{\partial}{\partial t}+qk_y\frac{\partial}{\partial k_x}\right)\bar{b}_y = -q\bar{b}_x + \mathrm{i}k_yB_{0y}\bar{u}_y - \frac{k^2}{\mathrm{Rm}}\bar{b}_y + \mathrm{i}k_z\bar{F}_x - \mathrm{i}k_x\bar{F}_z \tag{B.6}$$

$$\left(\frac{\partial}{\partial t}+qk_y\frac{\partial}{\partial k_x}\right)\bar{b}_z=\mathrm{i}k_yB_{0y}\bar{u}_z-\frac{k^2}{\mathrm{Rm}}\bar{b}_z+\mathrm{i}k_x\bar{F}_y-\mathrm{i}k_y\bar{F}_x \tag{B.7}$$

$$k_x\bar{u}_x+k_y\bar{u}_y+k_z\bar{u}_z=0, \tag{B.8}$$

$$k_x\bar{b}_x+k_y\bar{b}_y+k_z\bar{b}_z=0, \tag{B.9}$$

where $k^2=k_x^2+k_y^2+k_z^2$ and $B_{0y}=\sqrt{2/\beta}$ is the normalized background azimuthal field. These spectral equations contain the linear as well as the nonlinear ($N_{ij}^{(u)}(\mathbf{k},t), N_i^{(\theta)}(\mathbf{k},t), \bar{F}_i(\mathbf{k},t),\ i,j=x,y,z$) terms that are the Fourier transforms of the corresponding linear and nonlinear terms in the original Equations (A.1)-(A.9). The latter are given by convolutions

$$N_{ij}^{(u)}(\mathbf{k},t)=\int d^3\mathbf{k}'\left[\bar{b}_i(\mathbf{k}',t)\bar{b}_j(\mathbf{k}-\mathbf{k}',t)-\bar{u}_i(\mathbf{k}',t)\bar{u}_j(\mathbf{k}-\mathbf{k}',t)\right], \tag{B.10}$$

$$N_i^{(\theta)}(\mathbf{k},t)=-\int d^3\mathbf{k}'\bar{u}_i(\mathbf{k}',t)\bar{\theta}(\mathbf{k}-\mathbf{k}',t) \tag{B.11}$$

where $i,j=x,y,z$ and $\bar{F}_x,\bar{F}_y,\bar{F}_z$ are the fourier transforms of the respective components of the perturbed electromotive force $\mathbf{F}=\mathbf{u}\times\mathbf{b}$,

$$\bar{F}_x(\mathbf{k},t)=\int d^3\mathbf{k}'\left[\bar{u}_y(\mathbf{k}',t)\bar{b}_z(\mathbf{k}-\mathbf{k}',t)-\bar{u}_z(\mathbf{k}',t)\bar{b}_y(\mathbf{k}-\mathbf{k}',t)\right]$$

$$\bar{F}_y(\mathbf{k},t)=\int d^3\mathbf{k}'\left[\bar{u}_z(\mathbf{k}',t)\bar{b}_x(\mathbf{k}-\mathbf{k}',t)-\bar{u}_x(\mathbf{k}',t)\bar{b}_z(\mathbf{k}-\mathbf{k}',t)\right]$$

$$\bar{F}_z(\mathbf{k},t)=\int d^3\mathbf{k}'\left[\bar{u}_x(\mathbf{k}',t)\bar{b}_y(\mathbf{k}-\mathbf{k}',t)-\bar{u}_y(\mathbf{k}',t)\bar{b}_x(\mathbf{k}-\mathbf{k}',t)\right]$$

and describe the contribution from nonlinearity to the magnetic field perturbations. In the case of classical forced MHD turbulence without background shear flow, these nonlinear transfer terms in $\mathbf{k}$-space were also derived in Verma

(2004). From Equations (B.1)-(B.3) and the divergence-free conditions (B.8) and (B.9) we can eliminate pressure

$$\bar{p} = 2\mathrm{i}(1-q)\frac{k_y}{k^2}\bar{u}_x - 2\mathrm{i}\frac{k_x}{k^2}\bar{u}_y + \mathrm{i}N^2\frac{k_z}{k^2}\bar{\theta} + \sum_{(i,j)=(x,y,z)}\frac{k_i k_j}{k^2}N_{ij}^{(u)} \tag{B.12}$$

Substituting it back into Equations (B.1)-(B.3) we get

$$\left(\frac{\partial}{\partial t} + qk_y\frac{\partial}{\partial k_x}\right)\bar{u}_x = 2\left(1-\frac{k_x^2}{k^2}\right)\bar{u}_y + 2(1-q)\frac{k_x k_y}{k^2}\bar{u}_x + N^2\frac{k_x k_z}{k^2}\bar{\theta} + \mathrm{i}k_y B_{0y}\bar{b}_x - \frac{k^2}{\mathrm{Re}}\bar{u}_x + Q_x, \tag{B.13}$$

$$\left(\frac{\partial}{\partial t} + qk_y\frac{\partial}{\partial k_x}\right)\bar{u}_y = \left[q-2-2(q-1)\frac{k_y^2}{k^2}\right]\bar{u}_x - 2\frac{k_x k_y}{k^2}\bar{u}_y + N^2\frac{k_y k_z}{k^2}\bar{\theta} + \mathrm{i}k_y B_{0y}\bar{b}_y - \frac{k^2}{\mathrm{Re}}\bar{u}_y + Q_y, \tag{B.14}$$

$$\left(\frac{\partial}{\partial t} + qk_y\frac{\partial}{\partial k_x}\right)\bar{u}_z = 2(1-q)\frac{k_y k_z}{k^2}\bar{u}_x - 2\frac{k_x k_z}{k^2}\bar{u}_y - N^2\left(1-\frac{k_z^2}{k^2}\right)\bar{\theta} + \mathrm{i}k_y B_{0y}\bar{b}_z - \frac{k^2}{\mathrm{Re}}\bar{u}_z + Q_z, \tag{B.15}$$

where

$$Q_i = \mathrm{i}\sum_j k_j N_{ij}^{(u)} - \mathrm{i}k_i\sum_{m,n}\frac{k_m k_n}{k^2}N_{mn}^{(u)}, \qquad i,j,m,n = x,y,z. \tag{B.16}$$

Multiplying Equations (B.13)-(B.15), respectively, by $\bar{u}_x^*$, $\bar{u}_y^*$, $\bar{u}_z^*$, and adding up with their complex conjugates, we obtain

$$\frac{\partial}{\partial t}\frac{|\bar{u}_x|^2}{2} = -qk_y\frac{\partial}{\partial k_x}\frac{|\bar{u}_x|^2}{2} + \mathcal{H}_x + \mathcal{I}_x^{(u\theta)} + \mathcal{I}_x^{(ub)} + \mathcal{D}_x^{(u)} + \mathcal{N}_x^{(u)}, \tag{B.17}$$

$$\frac{\partial}{\partial t}\frac{|\bar{u}_y|^2}{2} = -qk_y\frac{\partial}{\partial k_x}\frac{|\bar{u}_y|^2}{2} + \mathcal{H}_y + \mathcal{I}_y^{(u\theta)} + \mathcal{I}_y^{(ub)} + \mathcal{D}_y^{(u)} + \mathcal{N}_y^{(u)}, \tag{B.18}$$

$$\frac{\partial}{\partial t}\frac{|\bar{u}_z|^2}{2} = -qk_y\frac{\partial}{\partial k_x}\frac{|\bar{u}_z|^2}{2} + \mathcal{H}_z + \mathcal{I}_z^{(u\theta)} + \mathcal{I}_z^{(ub)} + \mathcal{D}_z^{(u)} + \mathcal{N}_z^{(u)}, \tag{B.19}$$

where the terms of linear origin are

$$\mathcal{H}_x = \left(1-\frac{k_x^2}{k^2}\right)(\bar{u}_x\bar{u}_y^* + \bar{u}_x^*\bar{u}_y) + 2(1-q)\frac{k_x k_y}{k^2}|\bar{u}_x|^2, \tag{B.20}$$

$$\mathcal{H}_y = \frac{1}{2}\left[q - 2 - 2(q-1)\frac{k_y^2}{k^2}\right](\bar{u}_x\bar{u}_y^* + \bar{u}_x^*\bar{u}_y) - 2\frac{k_x k_y}{k^2}|\bar{u}_y|^2 \tag{B.21}$$

$$\mathcal{H}_z = (1-q)\frac{k_y k_z}{k^2}(\bar{u}_x\bar{u}_z^* + \bar{u}_x^*\bar{u}_z) - \frac{k_x k_z}{k^2}(\bar{u}_y\bar{u}_z^* + \bar{u}_y^*\bar{u}_z), \tag{B.22}$$

$$\mathcal{I}_i^{(u\theta)} = N^2\left(\frac{k_i k_z}{k^2} - \delta_{iz}\right)\frac{\bar{\theta}\bar{u}_i^* + \bar{\theta}^*\bar{u}_i}{2}, \tag{B.23}$$

$$\mathcal{I}_i^{(ub)} = \frac{\mathrm{i}}{2}k_y B_{0y}(\bar{u}_i^*\bar{b}_i - \bar{u}_i\bar{b}_i^*), \tag{B.24}$$

$$\mathcal{D}_i^{(u)} = -\frac{k^2}{\mathrm{Re}}|\bar{u}_i|^2, \tag{B.25}$$

and the modified nonlinear transfer functions for the quadratic forms of the velocity components are

$$\mathcal{N}_i^{(u)} = \frac{1}{2}(\bar{u}_i Q_i^* + \bar{u}_i^* Q_i). \tag{B.26}$$

Here $i = x, y, z$ and δ_{iz} is the Kronecker delta. It is readily shown that the sum of $\mathcal{H}_i$ is equal to the Reynolds stress spectrum multiplied by the shear parameter q, $\mathcal{H} = \mathcal{H}_x + \mathcal{H}_y + \mathcal{H}_z = q(\bar{u}_x\bar{u}_y^* + \bar{u}_x^*\bar{u}_y)/2$

Similarly, multiplying Equation (B.4) by $\bar{\theta}^*$ and adding up with its complex conjugate, we get

$$\frac{\partial}{\partial t}\frac{|\bar{\theta}|^2}{2} = -qk_y\frac{\partial}{\partial k_x}\frac{|\bar{\theta}|^2}{2} + \mathcal{I}^{(\theta u)} + \mathcal{D}^{(\theta)} + \mathcal{N}^{(\theta)}, \tag{B.27}$$

where the terms of linear origin are

$$\mathcal{I}^{(\theta u)} = \frac{1}{2}(\bar{u}_z\bar{\theta}^* + \bar{u}_z^*\bar{\theta}), \tag{B.28}$$

$$\mathcal{D}^{(\theta)} = -\frac{k^2}{\mathrm{Pe}}|\bar{\theta}|^2 \tag{B.29}$$

and the modified nonlinear transfer function for the quadratic form of the entropy is

$$\mathcal{N}^{(\theta)} = \frac{\mathrm{i}}{2}\bar{\theta}^*(k_x N_x^{(\theta)} + k_y N_y^{(\theta)} + k_z N_z^{(\theta)}) + c.c. \tag{B.30}$$

Multiplying Equations (B.5)-(B.7), respectively, by $\bar{b}_x^*$, $\bar{b}_y^*$, $\bar{b}_z^*$, and adding up with their complex conjugates, we obtain

$$\frac{\partial}{\partial t}\frac{|\bar{b}_x|^2}{2} = -qk_y\frac{\partial}{\partial k_x}\frac{|\bar{b}_x|^2}{2} + \mathcal{I}_x^{(bu)} + \mathcal{D}_x^{(b)} + \mathcal{N}_x^{(b)} \tag{B.31}$$

$$\frac{\partial}{\partial t}\frac{|\bar{b}_y|^2}{2} = -qk_y\frac{\partial}{\partial k_x}\frac{|\bar{b}_y|^2}{2} + \mathcal{M} + \mathcal{I}_y^{(bu)} + \mathcal{D}_y^{(b)} + \mathcal{N}_y^{(b)} \tag{B.32}$$

$$\frac{\partial}{\partial t}\frac{|\bar{b}_z|^2}{2} = -qk_y\frac{\partial}{\partial k_x}\frac{|\bar{b}_z|^2}{2} + \mathcal{I}_z^{(bu)} + \mathcal{D}_z^{(b)} + \mathcal{N}_z^{(b)}, \tag{B.33}$$

where $\mathcal{M}$ is the Maxwell stress spectrum multiplied by q,

$$\mathcal{M} = -\frac{q}{2}(\bar{b}_x\bar{b}_y^* + \bar{b}_x^*\bar{b}_y), \tag{B.34}$$

$$\mathcal{I}_i^{(bu)} = -\mathcal{I}_i^{(ub)} = \frac{\mathrm{i}}{2}k_y B_{0y}(\bar{u}_i\bar{b}_i^* - \bar{u}_i^*\bar{b}_i) \tag{B.35}$$

$$\mathcal{D}_i^{(b)} = -\frac{k^2}{\mathrm{Rm}}|\bar{b}_i|^2 \tag{B.36}$$

and the modified nonlinear terms for the quadratic forms of the magnetic field components are

$$\mathcal{N}_x^{(b)} = \frac{\mathrm{i}}{2}\bar{b}_x^*[k_y\bar{F}_z - k_z\bar{F}_y] + c.c., \quad \mathcal{N}_y^{(b)} = \frac{\mathrm{i}}{2}\bar{b}_y^*[k_z\bar{F}_x - k_x\bar{F}_z] + c.c., \quad \mathcal{N}_z^{(b)} = \frac{\mathrm{i}}{2}\bar{b}_z^*[k_x\bar{F}_y - k_y\bar{F}_x] + c.c. \tag{B.37}$$

Appendix C

Perturbation equations in physical and Fourier space in Keplerian disks with a net vertical magnetic field (Chapter 5)

Equations governing the evolution of the velocity, total pressure and magnetic field perturbations, $\mathbf{u}, p, \mathbf{b}$, of arbitrary amplitude about the equilibrium Keplerian flow $\mathbf{U}_0 = -q\Omega x \mathbf{e}_y$ with a net vertical magnetic field $\mathbf{B}_0 = B_{0z}\mathbf{e}_z$ are obtained from the basic Equations (5.1)-(5.5) and componentwise have the form (in dimensional units):

$$\frac{Du_x}{Dt} = 2\Omega u_y - \frac{1}{\rho_0}\frac{\partial p}{\partial x} + \frac{B_{0z}}{4\pi\rho_0}\frac{\partial b_x}{\partial z} + \frac{\partial}{\partial x}\left(\frac{b_x^2}{4\pi\rho_0} - u_x^2\right) + \\ + \frac{\partial}{\partial y}\left(\frac{b_x b_y}{4\pi\rho_0} - u_x u_y\right) + \frac{\partial}{\partial z}\left(\frac{b_x b_z}{4\pi\rho_0} - u_x u_z\right) + \nu\nabla^2 u_x, \quad \text{(C.1)}$$

$$\frac{Du_y}{Dt} = (q-2)\Omega u_x - \frac{1}{\rho_0}\frac{\partial p}{\partial y} + \frac{B_{0z}}{4\pi\rho_0}\frac{\partial b_y}{\partial z} + \frac{\partial}{\partial x}\left(\frac{b_x b_y}{4\pi\rho_0} - u_x u_y\right) + \\ + \frac{\partial}{\partial y}\left(\frac{b_y^2}{4\pi\rho_0} - u_y^2\right) + \frac{\partial}{\partial z}\left(\frac{b_z b_y}{4\pi\rho_0} - u_z u_y\right) + \nu\nabla^2 u_y \quad \text{(C.2)}$$

$$\frac{Du_z}{Dt} = -\frac{1}{\rho_0}\frac{\partial p}{\partial z} - N^2\theta + \frac{B_{0z}}{4\pi\rho_0}\frac{\partial b_z}{\partial z} + \frac{\partial}{\partial x}\left(\frac{b_x b_z}{4\pi\rho_0} - u_x u_z\right) + \\ + \frac{\partial}{\partial y}\left(\frac{b_y b_z}{4\pi\rho_0} - u_y u_z\right) + \frac{\partial}{\partial z}\left(\frac{b_z^2}{4\pi\rho_0} - u_z^2\right) + \nu\nabla^2 u_z \quad \text{(C.3)}$$

$$\frac{D\theta}{Dt} = u_z - \frac{\partial}{\partial x}(u_x\theta) - \frac{\partial}{\partial y}(u_y\theta) - \frac{\partial}{\partial z}(u_z\theta) + \chi\nabla^2\theta \tag{C.4}$$

$$\frac{Db_x}{Dt} = B_{0z}\frac{\partial u_x}{\partial z} + \frac{\partial}{\partial y}\left(u_x b_y - u_y b_x\right) - \frac{\partial}{\partial z}(u_z b_x - u_x b_z) + \eta\nabla^2 b_x, \tag{C.5}$$

$$\frac{Db_y}{Dt} = -q\Omega b_x + B_{0z}\frac{\partial u_y}{\partial z} - \frac{\partial}{\partial x}\left(u_x b_y - u_y b_x\right) + \frac{\partial}{\partial z}(u_y b_z - u_z b_y) + \eta\nabla^2 b_y, \tag{C.6}$$

$$\frac{Db_z}{Dt} = B_{0z}\frac{\partial u_z}{\partial z} + \frac{\partial}{\partial x}\left(u_z b_x - u_x b_z\right) - \frac{\partial}{\partial y}(u_y b_z - u_z b_y) + \eta\nabla^2 b_z, \tag{C.7}$$

$$\frac{\partial u_x}{\partial x} + \frac{\partial u_y}{\partial y} + \frac{\partial u_z}{\partial z} = 0, \tag{C.8}$$

$$\frac{\partial b_x}{\partial x} + \frac{\partial b_y}{\partial y} + \frac{\partial b_z}{\partial z} = 0, \tag{C.9}$$

where $D/Dt = \partial/\partial t - q\Omega x\partial/\partial y$ is the total derivative along the background flow.

Next, we derive evolution equations for velocity, entropy and magnetic field perturbations in Fourier space. Substituting decomposition (5.6) into Equations (C.1)-(C.9) and taking into account the normalization made in the text, we arrive at the following equations governing the dynamics of perturbation modes in Fourier space

$$\left(\frac{\partial}{\partial t} + qk_y\frac{\partial}{\partial k_x}\right)\bar{u}_x = 2\bar{u}_y - \mathrm{i}k_x\bar{p} + \mathrm{i}k_z B_{0z}\bar{b}_x - \frac{k^2}{\mathrm{Re}}\bar{u}_x + \mathrm{i}k_x N_{xx}^{(u)} + \mathrm{i}k_y N_{xy}^{(u)} + \mathrm{i}k_z N_{xz}^{(u)}, \tag{C.10}$$

$$\left(\frac{\partial}{\partial t} + qk_y\frac{\partial}{\partial k_x}\right)\bar{u}_y = (q-2)\bar{u}_x - \mathrm{i}k_y\bar{p} + \mathrm{i}k_z B_{0z}\bar{b}_y - \frac{k^2}{\mathrm{Re}}\bar{u}_y + \mathrm{i}k_x N_{xy}^{(u)} + \mathrm{i}k_y N_{yy}^{(u)} + \mathrm{i}k_z N_{yz}^{(u)}, \tag{C.11}$$

$$\left(\frac{\partial}{\partial t} + qk_y\frac{\partial}{\partial k_x}\right)\bar{u}_z = -\mathrm{i}k_z\bar{p} - N^2\bar{\theta} + \mathrm{i}k_z B_{0z}\bar{b}_z - \frac{k^2}{\mathrm{Re}}\bar{u}_z + \mathrm{i}k_x N_{xz}^{(u)} + \mathrm{i}k_y N_{yz}^{(u)} + \mathrm{i}k_z N_{zz}^{(u)}, \tag{C.12}$$

$$\left(\frac{\partial}{\partial t} + qk_y\frac{\partial}{\partial k_x}\right)\bar{\theta} = \bar{u}_z - \frac{k^2}{\mathrm{Pe}}\bar{\theta} + \mathrm{i}k_x N_x^{(\theta)} + \mathrm{i}k_y N_y^{(\theta)} + \mathrm{i}k_z N_z^{(\theta)}, \tag{C.13}$$

$$\left(\frac{\partial}{\partial t}+qk_y\frac{\partial}{\partial k_x}\right)\bar{b}_x=\mathrm{i}k_zB_{0z}\bar{u}_x-\frac{k^2}{\mathrm{Rm}}\bar{b}_x+\mathrm{i}k_y\bar{F}_z-\mathrm{i}k_z\bar{F}_y, \tag{C.14}$$

$$\left(\frac{\partial}{\partial t}+qk_y\frac{\partial}{\partial k_x}\right)\bar{b}_y=-q\bar{b}_x+\mathrm{i}k_zB_{0z}\bar{u}_y-\frac{k^2}{\mathrm{Rm}}\bar{b}_y+\mathrm{i}k_z\bar{F}_x-\mathrm{i}k_x\bar{F}_z \tag{C.15}$$

$$\left(\frac{\partial}{\partial t}+qk_y\frac{\partial}{\partial k_x}\right)\bar{b}_z=\mathrm{i}k_zB_{0z}\bar{u}_z-\frac{k^2}{\mathrm{Rm}}\bar{b}_z+\mathrm{i}k_x\bar{F}_y-\mathrm{i}k_y\bar{F}_x \tag{C.16}$$

$$k_x\bar{u}_x+k_y\bar{u}_y+k_z\bar{u}_z=0, \tag{C.17}$$

$$k_x\bar{b}_x+k_y\bar{b}_y+k_z\bar{b}_z=0, \tag{C.18}$$

where $k^2=k_x^2+k_y^2+k_z^2$ and $B_{0z}=\sqrt{2/\beta}$ is the normalized uniform background vertical field. These spectral equations contain the linear as well as the nonlinear ($N_{ij}^{(u)}(\mathbf{k},t), N_i^{(\theta)}(\mathbf{k},t), \bar{F}_i(\mathbf{k},t)$, where $i,j=x,y,z$) terms that are the Fourier transforms of the corresponding linear and nonlinear terms in the original Equations (C.1)-(C.9). The latter are given by convolutions

$$N_{ij}^{(u)}(\mathbf{k},t)=\int d^3\mathbf{k}'\left[\bar{b}_i(\mathbf{k}',t)\bar{b}_j(\mathbf{k}-\mathbf{k}',t)-\bar{u}_i(\mathbf{k}',t)\bar{u}_j(\mathbf{k}-\mathbf{k}',t)\right], \tag{C.19}$$

$$N_i^{(\theta)}(\mathbf{k},t)=-\int d^3\mathbf{k}'\bar{u}_i(\mathbf{k}',t)\bar{\theta}(\mathbf{k}-\mathbf{k}',t) \tag{C.20}$$

and $\bar{F}_x,\bar{F}_y,\bar{F}_z$, which are the fourier transforms of the respective components of the perturbed electromotive force $\mathbf{F}=\mathbf{u}\times\mathbf{b}$,

$$\bar{F}_x(\mathbf{k},t)=\int d^3\mathbf{k}'\left[\bar{u}_y(\mathbf{k}',t)\bar{b}_z(\mathbf{k}-\mathbf{k}',t)-\bar{u}_z(\mathbf{k}',t)\bar{b}_y(\mathbf{k}-\mathbf{k}',t)\right] \tag{C.21}$$

$$\bar{F}_y(\mathbf{k},t)=\int d^3\mathbf{k}'\left[\bar{u}_z(\mathbf{k}',t)\bar{b}_x(\mathbf{k}-\mathbf{k}',t)-\bar{u}_x(\mathbf{k}',t)\bar{b}_z(\mathbf{k}-\mathbf{k}',t)\right] \tag{C.22}$$

$$\bar{F}_z(\mathbf{k},t)=\int d^3\mathbf{k}'\left[\bar{u}_x(\mathbf{k}',t)\bar{b}_y(\mathbf{k}-\mathbf{k}',t)-\bar{u}_y(\mathbf{k}',t)\bar{b}_x(\mathbf{k}-\mathbf{k}',t)\right] \tag{C.23}$$

describe the effect of nonlinearity on the magnetic field perturbations. In the case of classical forced MHD turbulence without background shear flow, these nonlinear transfer terms in **k**-space were also derived in Verma (2004). From Equations (C.10)-(C.12) and the divergence-free conditions (C.17) and (C.18) we can eliminate pressure

$$\bar{p} = 2\mathrm{i}(1-q)\frac{k_y}{k^2}\bar{u}_x - 2\mathrm{i}\frac{k_x}{k^2}\bar{u}_y + \mathrm{i}N^2\frac{k_z}{k^2}\bar{\theta} + \sum_{(i,j)=(x,y,z)} \frac{k_i k_j}{k^2} N_{ij}^{(u)} \tag{C.24}$$

Substituting it back into Equations (C.10)-(C.12) we get

$$\left(\frac{\partial}{\partial t} + qk_y\frac{\partial}{\partial k_x}\right)\bar{u}_x = 2\left(1-\frac{k_x^2}{k^2}\right)\bar{u}_y + 2(1-q)\frac{k_x k_y}{k^2}\bar{u}_x + N^2\frac{k_x k_z}{k^2}\bar{\theta} + \mathrm{i}k_z B_{0z}\bar{b}_x - \frac{k^2}{\mathrm{Re}}\bar{u}_x + Q_x, \tag{C.25}$$

$$\left(\frac{\partial}{\partial t} + qk_y\frac{\partial}{\partial k_x}\right)\bar{u}_y = \left[q-2-2(q-1)\frac{k_y^2}{k^2}\right]\bar{u}_x - 2\frac{k_x k_y}{k^2}\bar{u}_y + N^2\frac{k_y k_z}{k^2}\bar{\theta} + \mathrm{i}k_z B_{0z}\bar{b}_y - \frac{k^2}{\mathrm{Re}}\bar{u}_y + Q_y, \tag{C.26}$$

$$\left(\frac{\partial}{\partial t} + qk_y\frac{\partial}{\partial k_x}\right)\bar{u}_z = 2(1-q)\frac{k_y k_z}{k^2}\bar{u}_x - 2\frac{k_x k_z}{k^2}\bar{u}_y - N^2\left(1-\frac{k_z^2}{k^2}\right)\bar{\theta} + \mathrm{i}k_z B_{0z}\bar{b}_z - \frac{k^2}{\mathrm{Re}}\bar{u}_z + Q_z, \tag{C.27}$$

where

$$Q_i = \mathrm{i}\sum_j k_j N_{ij}^{(u)} - \mathrm{i}k_i \sum_{m,n}\frac{k_m k_n}{k^2} N_{mn}^{(u)}, \qquad i,j,m,n = x,y,z. \tag{C.28}$$

Bibliography

Afshordi, N., Mukhopadhyay, B., & Narayan, R. 2005, ApJ, 629, 373

Alexakis, A., Mininni, P. D., & Pouquet, A. 2007, New J. Phys., 9, 298

Armitage, P. J. 2011, Annu. Rev. Astron. Astrophys., 49, 195

Baggett, J. S., Driscoll, T. A., & Trefethen, L. N. 1995, Phys. Fluids, 7, 833

Bai, X.-N., & Stone, J. M. 2013, ApJ, 767, 30

—. 2014, ApJ, 796, 31

Bakas, N., Ioannou, P., & Kefaliakos, G. 2001, J. Atmos. Sci., 58, 2790

Balbus, S. A. 2003, Annu. Rev. Astron. Astrophys., 41, 555

Balbus, S. A., & Hawley, J. F. 1991, ApJ, 376, 214

—. 1992, ApJ, 400, 610

—. 1998, Rev. Mod. Phys., 70, 1

Beckwith, K., Armitage, P. J., & Simon, J. B. 2011, MNRAS, 416, 361

Biskamp, D. 2003, Magnetohydrodynamic turbulence (Cambridge University Press)

Biskamp, D., & Welter, H. 1989, Phys. Fluids B, 1, 1964

Bodo, G., Cattaneo, F., Mignone, A., & Rossi, P. 2012, ApJ, 761, 116

—. 2013, ApJ, 771, L23

—. 2014, ApJ, 787, L13

Bodo, G., Mignone, A., Cattaneo, F., Rossi, P., & Ferrari, A. 2008, A&A, 487, 1

Boldyrev, S. 2005, Astrophys. J. Lett., 626, L37

Brandenburg, A., & Dintrans, B. 2006, A&A, 450, 437

Brandenburg, A., & Lazarian, A. 2013, Space Sci. Rev., 178, 163

Brandenburg, A., Nordlund, A., Stein, R. F., & Torkelsson, U. 1995, ApJ, 446, 741

Butler, K., & Farrell, B. 1992, Phys. Fluids, 4, 1637

Canuto, C., Hussaini, M. Y., Quarteroni, A., & Zang, T. A. 1988, Spectral Methods in Fluid Dynamics (Springer)

Chagelishvili, G., Chanishvili, R., & Lominadze, J. 1996, JETP Lett., 63, 543

Chagelishvili, G., Chanishvili, R., Lominadze, J., & Tevzadze, A. 1997a, Phys. Plasmas, 5, 259

Chagelishvili, G., Tevzadze, A., Bodo, G., & Moiseev, S. 1997b, Phys. Rev. Lett., 79, 3178

Chagelishvili, G. D., Chanishvili, R. G., Hristov, T. S., & Lominadze, J. G. 2002, Sov. Phys. -JETP, 94, 434

Chagelishvili, G. D., Chanishvili, R. G., Lominadze, J. G., & Tevzadze, A. G. 1997, Phys. Plasmas, 4, 259

Chagelishvili, G. D., Zahn, J.-P., Tevzadze, A. G., & Lominadze, J. G. 2003, A&A, 402, 401

Chandrasekhar, S. 1960, Proceedings of the National Academy of Science, 46, 253

Chapman, S. J. 2002, J. Fluid Mech., 451, 35

Criminale, W. O., Jackson, T. L., & Joslin, R. D. 2003, Theory and Computation of Hydrodynamic Stability

Davis, S. W., Stone, J. M., & Pessah, M. E. 2010, ApJ, 713, 52

Dimitrov, Z. D., Maneva, Y. G., Hristov, T. S., & Mishonov, T. M. 2011, Phys. Plasmas, 18, 082110

Dmitruk, P., Matthaeus, W., Milano, L., et al. 2002, Astrophisical J., 575, 571

Douglas, J., Kim, E.-J., & Thyagaraja, A. 2008, Phys. Plasmas, 15, 052301

Duguet, Y., Schlatter, P., & Henningson, D. S. 2010, J. Fluid Mech., 650, 119

Eckhardt, B., Schneider, T. M., Hof, B., & Westerweel, J. 2007, Annu. Rev. Fluid Mech., 39, 447

Farrell, B. 1988, Phys. Fluids, 31, 2093

Farrell, B., & Ioannou, P. 1993a, Phys. Fluids A, 5, 1390

—. 1993b, J. Atmos. Sci., 50, 200

Farrell, B. F., & Ioannou, P. J. 1996, Journal of Atmospheric Sciences, 53, 2025

—. 2000, Phys. Fluids, 12, 3021

Fleming, T. P., Stone, J. M., & Hawley, J. F. 2000, ApJ, 530, 464

Flock, M., Dzyurkevich, N., Klahr, H., Turner, N., & Henning, T. 2012a, ApJ, 744, 144

Flock, M., Dzyurkevich, N., Klahr, H., Turner, N. J., & Henning, T. 2011, ApJ, 735, 122

Flock, M., Henning, T., & Klahr, H. 2012b, ApJ, 761, 95

Fromang, S. 2010, Astron. Astrophys., 514, L5

Fromang, S. 2013, in EAS Publications Series, Vol. 62, EAS Publications Series, ed. P. Hennebelle & C. Charbonnel, 95–142

Fromang, S., Latter, H., Lesur, G., & Ogilvie, G. I. 2013, A&A, 552, A71

Fromang, S., & Nelson, R. P. 2006, A&A, 457, 343

Fromang, S., & Papaloizou, J. 2007, Astron. Astrophys., 476, 1113

Gebhardt, T., & Grossmann, S. 1994, Phys. Rev. E, 50, 3705

Gogichaishvili, D., Chagelishvili, G., Chanishvili, R., & Lominadze, J. 2014, J. Plasma Phys., 80, 667

Gogichaishvili, D., Mamatsashvili, G., Horton, W., Chagelishvili, G., & Bodo, G. 2017, ApJ, 845, 70

Gogichaishvili, D. Z., Mamatsashvili, G. R., Horton, W., & Chagelishvili, G. D. 2018, ApJ, 866, 134

Goldreich, P., & Sridhar, S. 1995, ApJ, 438, 763

Goldreich, P., & Tremaine, S. 1978, Astrophysical J., 222, 850

—. 1979, Astrophysical J., 233, 857

Goodman, J., & Xu, G. 1994, ApJ, 432, 213

Gressel, O. 2010, MNRAS, 405, 41

Gressel, O., & Pessah, M. E. 2015, ApJ, 810, 59

Grossmann, S. 2000, Rev. Mod. Phys., 72, 603

Guan, X., & Gammie, C. F. 2011, ApJ, 728, 130

Guan, X., Gammie, C. F., Simon, J. B., & Johnson, B. M. 2009, ApJ, 694, 1010

Gustavsson, L. H. 1991, J. Fluid Mech., 224, 241

Hawley, J., Gammie, C., & Balbus, S. 1995, ApJ, 440, 742

Hawley, J. F., & Balbus, S. A. 1991, ApJ, 376, 223

—. 1992, ApJ, 400, 595

Hawley, J. F., Richers, S. A., Guan, X., & Krolik, J. H. 2013, ApJ, 772, 102

Heinemann, M., & Olbert, S. 1980, J. Geophysical Research: Space Physics, 85, 1311

Henningson, D. S., & Reddy, S. C. 1994, Phys. Fluids, 6, 1396

Herault, J., Rincon, F., Cossu, C., et al. 2011, Phys. Rev. E, 84, 036321

Hollweg, J., & Kaghashvili, E. 2012, Astrophysical J., 744, 114

Hollweg, J., Kaghashvili, E., & Chandran, B. 2013, Astrophisical J., 769, 142

Horton, W., Kim, J.-H., Chagelishvili, G., Bowman, J., & Lominadze, J. 2010, Phys. Rev. E., 81, 066304

Iroshnikov, P. S. 1963, Sov. Astron., 7, 566

Jimenez, J. 2013, Phys. Fluids, 25, 110814

Johansen, A., Youdin, A., & Klahr, H. 2009, ApJ, 697, 1269

Johnson, B. M. 2007, ApJ, 660, 1375

Kim, E.-J. 2006, Phys. Rev. Lett., 96, 084504

Kraichnan, R. H. 1965, Phys. Fluids, 8, 1385

Latter, H. N., Fromang, S., & Faure, J. 2015, MNRAS, 453, 3257

Latter, H. N., Fromang, S., & Gressel, O. 2010, MNRAS, 406, 848

Latter, H. N., Lesaffre, P., & Balbus, S. A. 2009, MNRAS, 394, 715

Lesur, G., & Longaretti, P.-Y. 2007, Mon. Not. R. Astron. Soc., 378, 1471

—. 2011, Astron. Astrophys., 528, A17

Lesur, G., & Ogilvie, G. I. 2008, Astron. Astrophys., 488, 451

—. 2010, MNRAS, 404, L64

Lesur, G., & Papaloizou, J. C. B. 2010, Astron. Astrophys., 513, A60

Lindzen, R. S., & Barker, J. 1985, J. Fluid Mechanics, 151, 189

Lominadze, D. G., Chagelishvili, G. D., & Chanishvili, R. G. 1988, Sov. Astron. Lett., 14, 364

Longaretti, P.-Y., & Lesur, G. 2010, Astron. Astrophys., 516, A51

Lynden-Bell, D., & Pringle, J. E. 1974, MNRAS, 168, 603

Mamatsashvili, G., Khujadze, G., Chagelishvili, G., et al. 2016, Phys. Rev. E, 94, 023111

Mamatsashvili, G. R., Chagelishvili, G. D., Bodo, G., & Rossi, P. 2013, Mon. Not. R. Astron. Soc., 435, 2552

Mamatsashvili, G. R., Gogichaishvili, D. Z., Chagelishvili, G. D., & Horton, W. 2014, Phys. Rev. E, 89, 043101

Matthaeus, W., Zank, G., Oughton, S., Mullan, D., & Dmitruk, P. 1999, Astrophisical J., 523, L93

Meheut, H., Fromang, S., Lesur, G., Joos, M., & Longaretti, P.-Y. 2015, A&A, 579, A117

Mininni, P. D. 2011, Annu. Rev. Fluid Mech., 43, 377

Moffatt, H. K. 1967, 139

Mukhopadhyay, B., Afshordi, N., & Narayan, R. 2005, ApJ, 629, 383

Murphy, G. C., & Pessah, M. E. 2015, ApJ, 802, 139

Nauman, F., & Blackman, E. G. 2014, MNRAS, 441, 1855

Newton, A. P. L., & Kim, E.-J. 2009, Phys. Rev. Lett., 102, 165002

Ogilvie, G. I., & Pringle, J. E. 1996, Mon. Not. R. Astron. Soc., 279, 152

Papaloizou, J. C. B., & Terquem, C. 1997, MNRAS, 287, 771

Parkin, E. R., & Bicknell, G. V. 2013, MNRAS, 435, 2281

Perez, J., & Chandran, B. 2013, Astrophisical J., 776, 124

Pessah, M. E. 2010, ApJ, 716, 1012

Pessah, M. E., & Chan, C.-K. 2008, ApJ, 684, 498

—. 2012, ApJ, 751, 48

Pessah, M. E., Chan, C.-K., & Psaltis, D. 2006, MNRAS, 372, 183

Pessah, M. E., & Goodman, J. 2009, ApJ, 698, L72

Razdoburdin, D. N., & Zhuravlev, V. V. 2017, MNRAS, 467, 849

Reddy, S., Schmid, P., & Henningson, D. 1993, SIAM J. Appl. Math., 53, 15

Reddy, S. C., & Henningson, D. S. 1993, J. Fluid Mech., 252, 209

Rempel, E. L., Lesur, G., & Proctor, M. R. E. 2010, Phys. Rev. Lett., 105, 044501

Riols, A., Rincon, F., Cossu, C., et al. 2015, A&A, 575, A14

—. 2017, A&A, 598, A87

Ross, J., Latter, H. N., & Guilet, J. 2016, MNRAS, 455, 526

Ryan, B. R., Gammie, C. F., Fromang, S., & Kestener, P. 2017, ApJ, 840, 6

Salhi, A., Lehner, T., Godeferd, F., & Cambon, C. 2012, Phys. Rev. E, 85, 026301

Salvesen, G., Simon, J. B., Armitage, P. J., & Begelman, M. C. 2016, MNRAS, 457, 857

Sano, T., & Inutsuka, S.-I. 2001, ApJ, 561, L179

Schmid, P. J. 2007, Annu. Rev. Fluid Mech., 39, 129

Schmid, P. J., & Henningson, D. S. 2001, Stability and Transition in Shear Flows (Springer)

Shakura, N., & Postnov, K. 2015, MNRAS, 448, 3697

Shakura, N. I., & Sunyaev, R. A. 1973, A&A, 24, 337

Shi, J.-M., Krolik, J. H., & Hirose, S. 2010, ApJ, 708, 1716

Shi, J.-M., Stone, J. M., & Huang, C. X. 2016, MNRAS, 456, 2273

Shtemler, Y. M., Mond, M., & Liverts, E. 2011, MNRAS, 413, 2957

—. 2012, MNRAS, 421, 700

Simon, J. B., & Armitage, P. J. 2014, ApJ, 784, 15

Simon, J. B., Bai, X.-N., Armitage, P. J., Stone, J. M., & Beckwith, K. 2013, ApJ, 775, 73

Simon, J. B., Beckwith, K., & Armitage, P. J. 2012, Mon. Not. R. Astron. Soc., 422, 2685

Simon, J. B., & Hawley, J. F. 2009, ApJ, 707, 833

Simon, J. B., Hawley, J. F., & Beckwith, K. 2009, ApJ, 690, 974

—. 2011, ApJ, 730, 94

Sorathia, K. A., Reynolds, C. S., Stone, J. M., & Beckwith, K. 2012, ApJ, 749, 189

Squire, J., & Bhattacharjee, A. 2014, ApJ, 797, 67

Stepanyants, Y., & Fabrikant, A. 1989, Soviet Physics Uspekhi, 32, 783

Stern, M. E. 1963, Phys. Fluids, 6, 636

Sundar, S., Verma, M. K., Alexakis, A., & Chatterjee, A. G. 2017, Phys. Plasmas, 24, 022304

Teaca, B., Verma, M. K., Knaepen, B., & Carati, D. 2009, Phys. Rev. E, 79, 046312

Terquem, C., & Papaloizou, J. C. B. 1996, MNRAS, 279, 767

Tevzadze, A. G., Chagelishvili, G. D., & Zahn, J.-P. 2008, A&A, 478, 9

Trefethen, L. 1991, Pseudospectra of matrices, Numerical Analysis, 91, 234

Trefethen, L., & Embree, M. 2005, Princeton University Press, Princeton, NJ

Trefethen, L. N., Trefethen, A. E., Reddy, S. C., & Driscoll, T. A. 1993, Science, 261, 578

Velikhov, E. 1959, Zh. Eksp. Teor. Fiz., 36, 1398

Velli, M., Grappin, R., & Mangeney, A. 1989, Phys. Rev. Lett., 63, 1807

Verdini, A., Grappin, R., Pinto, R., & Velli, M. 2012, Astrophisical J. Lett., 750, L33

Verma, M. K. 2004, Phys. Rep., 401, 229

Waleffe, F. 1995, Phys. Fluids, 7, 3060

Walker, J., Lesur, G., & Boldyrev, S. 2016, MNRAS, 457, L39

Wardle, M. 1999, MNRAS, 307, 849

Webb, G., Zank, G., Kaghashvili, E., & Ratkiewicz, R. 2005, Journal of Plasma Physics, 71, 785

Wu, C. C., & Chang, T. 2001, J. Atmos. Sol-Terr. Phys., 63, 1447

Yecko, P. A. 2004, A&A, 425, 385

Yoshida, Z. 2005, Phys. Plasmas, 12, 024503

Zaqarashvili, T. 2000, Phys. Rev. E, 62, 2745

Zaqarashvili, T., & Roberts, B. 2002, Phys. Rev. E, 66, id. 026401

Zhuravlev, V. V., & Razdoburdin, D. N. 2014, MNRAS, 442, 870

Zimbardo, G., Greco, A., Sorriso-Valvo, L., et al. 2010, Space Sci. Rev., 156, 89